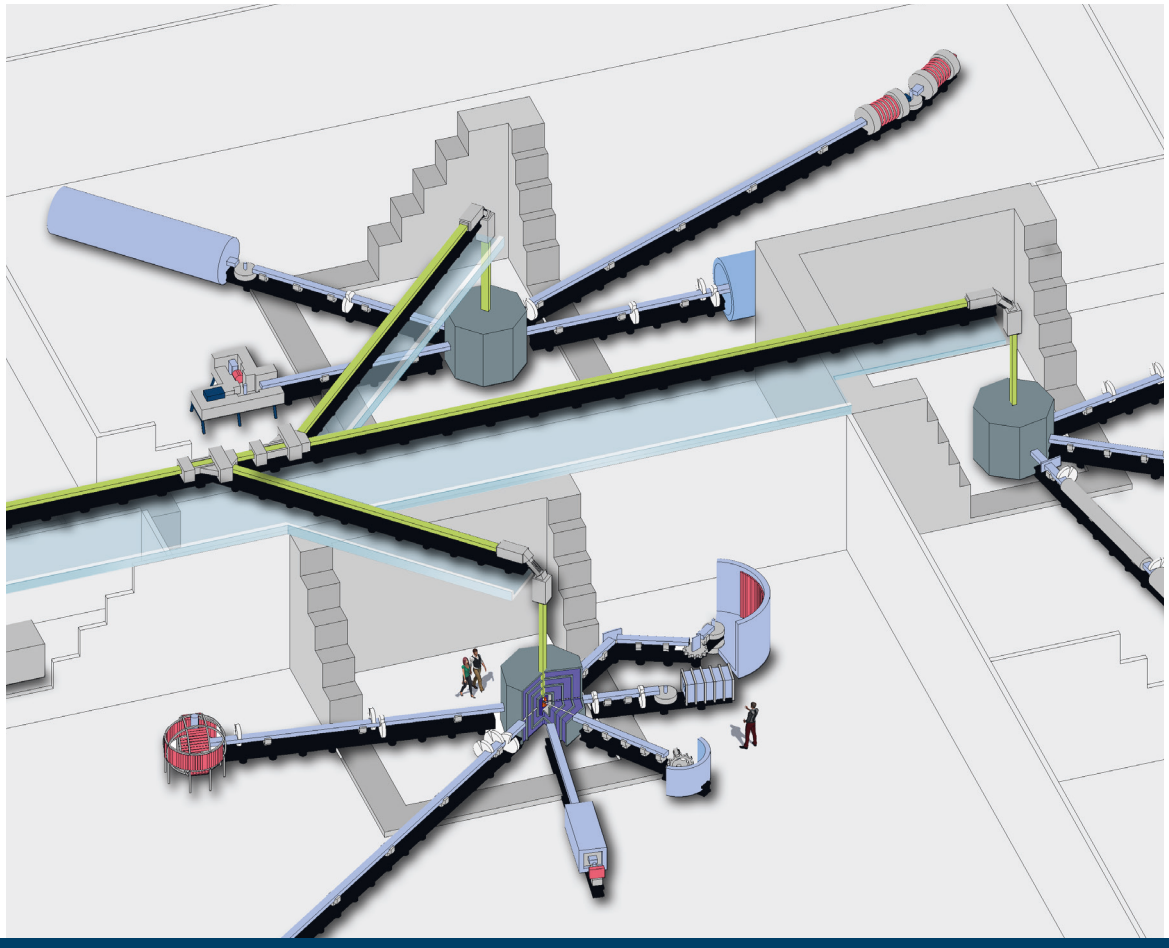

Conceptual Design Report
Jülich High Brilliance Neutron Source (HBS)

T. Brückel, T. Gutberlet (Eds.)

J. Baggemann, S. Böhm, P. Doege, J. Fenske, M. Feygenson, A. Glavic, O. Holderer, S. Jaksch, M. Jentschel, S. Kleefisch, H. Kleines, J. Li, K. Lieutenant, P. Mastinu, E. Mauerhofer, O. Meusel, S. Pasini, H. Podlech, M. Rimmler, U. Rücker, T. Schrader, W. Schweika, M. Strobl, E. Vezhlev, J. Voigt, P. Zakalek, O. Zimmer

Allgemeines / General
Band / Volume 8
ISBN 978-3-95806-501-7

Mitglied der Helmholtz-Gemeinschaft

JÜLICH
Forschungszentrum

Jülich High Brilliance Neutron Source (HBS)

1. 100 mA proton ion source
2. 70 MeV linear accelerator
3. Proton beam multiplexer system
4. Individual neutron target stations
5. Various instruments in the experimental halls

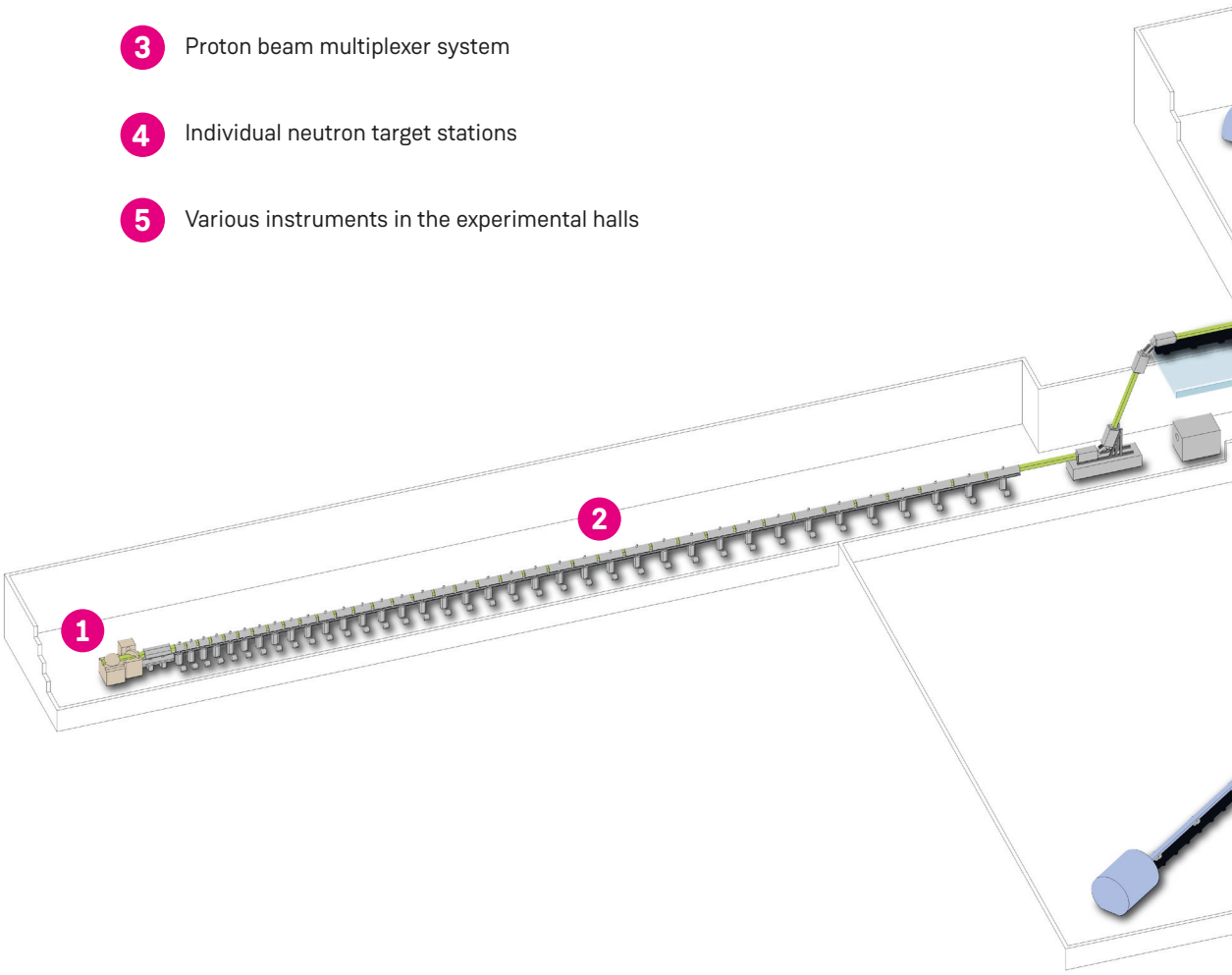

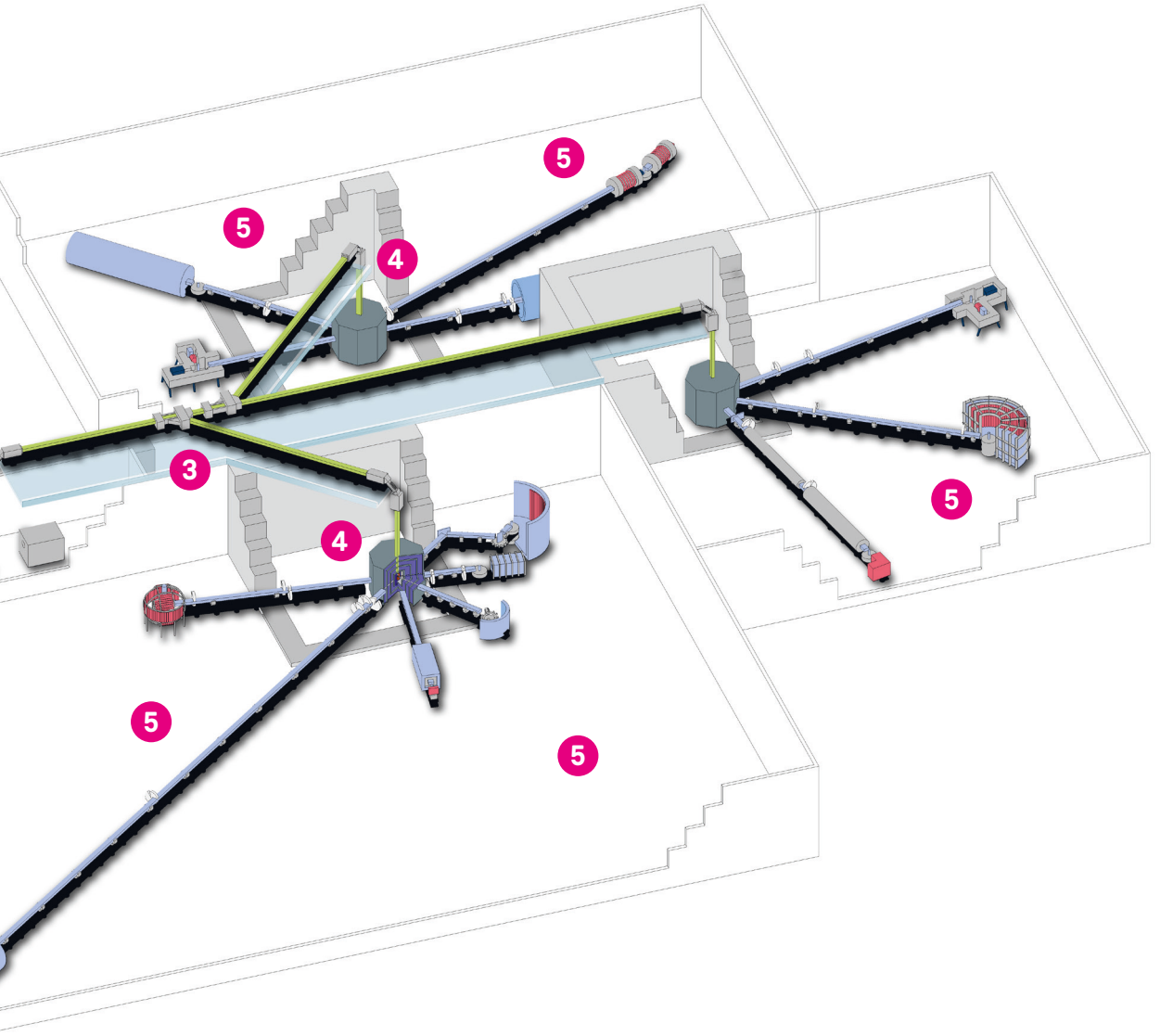
5
5
4
3
4
5
5
5

Schriften des Forschungszentrums Jülich
Reihe Allgemeines / General Band / Volume 8

Forschungszentrum Jülich GmbH
Jülich Centre for Neutron Science
JCNS

Conceptual Design Report
Jülich High Brilliance Neutron Source (HBS)

T. Brückel, T. Gutberlet (Eds.)

J. Baggemann, S. Böhm, P. Doege, J. Fenske, M. Feygenson, A. Glavic, O. Holderer, S. Jaksch, M. Jentschel, S. Kleefisch, H. Kleines, J. Li, K. Lieutenant, P. Mastinu, E. Mauerhofer, O. Meusel, S. Pasini, H. Podlech, M. Rimmler, U. Rücker, T. Schrader, W. Schweika, M. Strobl, E. Vezhlev, J. Voigt, P. Zakalek, O. Zimmer

Schriften des Forschungszentrums Jülich
Reihe Allgemeines / General Band / Volume 8

ISSN 1433-5565 ISBN 978-3-95806-501-7

Bibliografische Information der Deutschen Nationalbibliothek.
Die Deutsche Nationalbibliothek verzeichnet diese Publikation in der
Deutschen Nationalbibliografie; detaillierte Bibliografische Daten
sind im Internet über http://dnb.d-nb.de abrufbar.

Herausgeber und Vertrieb:	Forschungszentrum Jülich GmbH Zentralbibliothek, Verlag 52425 Jülich Tel.: +49 2461 61-5368 Fax: +49 2461 61-6103 zb-publikation@fz-juelich.de www.fz-juelich.de/zb
Umschlaggestaltung:	Grafische Medien, Forschungszentrum Jülich GmbH
Druck:	Grafische Medien, Forschungszentrum Jülich GmbH
Copyright:	Forschungszentrum Jülich 2020

Schriften des Forschungszentrums Jülich
Reihe Allgemeines / General, Band / Volume 8

ISSN 1433-5565
ISBN 978-3-95806-501-7

Vollständig frei verfügbar über das Publikationsportal des Forschungszentrums Jülich (JuSER)
unter www.fz-juelich.de/zb/openaccess.

CONTENT

I.

EXECUTIVE SUMMARY

- The solution of major grand challenges of humankind is largely based on progress in materials research of natural and artificial matter. Success depends critically on the availability of powerful methods being able to unravel structure and function of matter at different length and time scales.
- In this context, neutrons are indispensable microscopic probes. They are used to unravel the structure and dynamics of matter from the mesoscale to the picoscale and from seconds to femtoseconds in an ever-increasing number of disciplines and thus make essential contributions to solutions of the grand scientific and technological challenges of the future.
- Europe has the world leading neutron user community. More than 8000 users utilize the available neutron sources in Europe, requesting twice the available capacity offered per year. Within Europe, Germany has the most productive community in terms of scientific output.
- The European success of research with Neutrons is based on a hierarchical network of neutron facilities: from low flux sources, which provide the foundation by educating the next generation of neutron users and offering a platform for method development, via medium flux sources having a broader instrumentation, which provide in addition capacity and capability, to flag ship facilities (ILL and in future ESS) which are essential for the most demanding flux-hungry experiments.
- As has been pointed out by an ESFRI working group, this leading position is currently challenged by the slow dying off of older research reactors which became critical in the middle of last century. This problem has been addressed in the national strategy papers of several European neutron communities and is being tackled at present within the League of advanced European Neutron Sources (LENS).
- With the goal to reestablish a healthy ecosystem of neutron facilities within Europe and to further develop the neutron landscape for science and industry in Germany and Europe, the Jülich Centre for Neutron Science (JCNS) of Forschungszentrum Jülich GmbH has worked on a novel approach to neutron research facilities: the HBS project for a High Brilliance neutron Source. The present document summarizes the concept of such a facility in a Conceptional Design Report (CDR).
- The fresh approach of the HBS project is due to several paradigm changes:
  - the basic process for neutron release from atomic nuclei of the HBS is neither fission, nor spallation, but nuclear reactions based on the impact of low energy protons on a metal target. While this concept has already been realized in small Compact Accelerator

driven Neutron Sources (CANS), it only now becomes viable for a high-end facility by employing the latest scientific and technological advances. Such a facility avoids the need for nuclear licensing and significantly reduces the shielding requirements.

- instead of aiming at the highest source strength, HBS maximizes brilliance, the relevant physical parameter for most neutron beam instruments; "HBS produces less neutrons, but uses them more efficiently". This approach immediately translates in decreased costs for installation and operation.
- instead of providing one neutron source / moderator for all instruments, which necessarily requires compromises, HBS considers the source as an integral part of the instrument and delivers optimal pulse structure and neutron spectrum to every single instrument; "HBS delivers individually tailored beam characteristics for each instrument, instead of one fits all". This approach increases the performance of the instruments.
- instead of aiming at a certain size for a facility, the HBS concept is highly flexible and scalable from large laboratory size for local use at universities and industrial companies to full-fledged and highly competitive user facility. The conceptual design for the large laboratory facility has already been published under the name NOVA ERA. Such a neutron source has the potential to "bring neutrons to the users instead of users to neutrons".

- HBS type of sources will provide new capacity and additional capability to research with neutrons. Optimizing for brilliance makes the HBS type of sources well suited for research on small sample volumes, important e.g. in the fields of life science, nanotechnology or engineering.

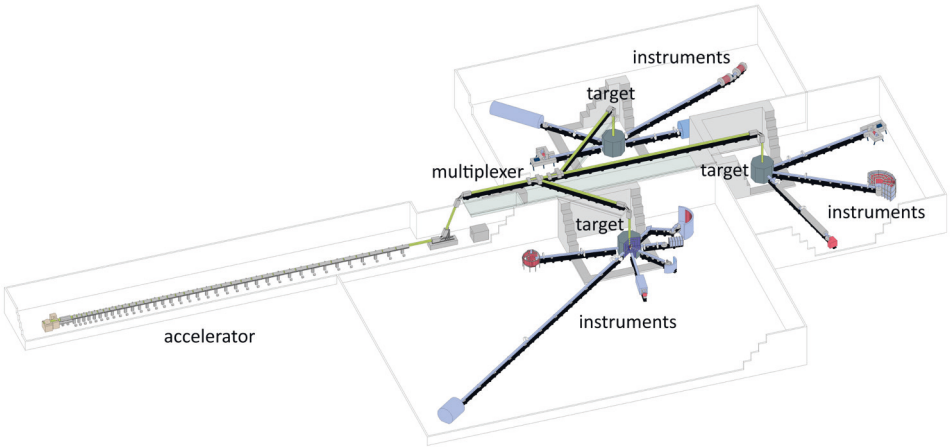

Figure I.1: *General layout of the accelerator-based high brilliance neutron source facility*

- The reference design of HBS comprises the following main components (see figure):
  - a high power linear proton accelerator with an end energy of 70 MeV, a proton beam current of 100 mA and a duty cycle of 4.3%
  - a multiplexer which distributes the proton pulses to three target stations which operate at different frequencies of 24, 96 and 384 Hz, each one optimized for a certain group of neutron beam instruments

- target-moderator-reflector assemblies that offer pulsed neutron beams at optimal frequency, pulse duration and neutron energy spectrum to fulfil the needs of each individual instrument.
- a number of instruments grouped around each target station so that they receive the optimal pulse structure while individual one dimensional "finger" moderators provide the adapted phase space volume to each individual instrument

- With this reference design, neutron beam instruments at the HBS will be highly competitive to instruments at existing medium-to high flux neutron sources thus underpinning the future flagship facility ESS. Moreover, HBS type facilities are highly flexible, can easily be adapted to the need of the respective neutron user community, do not need a nuclear license and come at significantly lower price-tag for installation and operation compared to research reactors or spallation sources.

This Conceptual Design Report represents the result of work done by the group of JCNS with support by a number of individual scientists and engineers around Europe and the rest of the world. It covers a brief review of the science case driving the project, conceptual description of the technical aspects of the facility, an outline of the operation of the facility, safety and infrastructure and an estimate on investments, costing and timeline for realization. It does not address organisational matters, nor governance matters and only in general terms financial matters, although it must be emphasised that these subjects are borne in mind in arriving at the scope of HBS and hence the specification of the facility. In a next step, work will be engaged upon which will result in a Technical Design Report (TDR) broken down in dedicated reports on the accelerator, the target and the instrumentation, being produced together with a series of other documents such as a more detailed costing report. These documents will demonstrate the sound foundation upon which such a facility could be constructed and operated.

II.

FOREWORD

Neutrons are an essential tool for science and industry for probing the structure and dynamics of matter from the mesoscale to the picoscale and from seconds to femtoseconds. In Europe research, industry and society benefit from a globally unique environment of various neutron sources with the flagship facilities ILL in Grenoble, France, and ESS in Lund, Sweden. The latter is currently under construction and will represent the world's most powerful neutron facility. The unique capabilities of neutrons and the European neutron infrastructure have been highlighted in reports by the European Neutron Scattering Association (ENSA) and the ESFRI Neutron Landscape Group recently. More than 8000 users utilize the available neutron sources in Europe, requesting nearly twice the available capacity offered per year. This high demand for research with neutrons is managed by peer review processes established to permit access to the facilities resulting in a highly competitive situation which sometimes hampers access by well-qualified applicants.

The main processes to release neutrons from atomic nuclei are: (i) fission in nuclear reactors, (ii) spallation using high-power proton accelerators, and (iii) nuclear reactions induced by low-energy protons or deuterons. The first two techniques are used very successfully in Europe and offer the highest neutron source strength with versatile options.

In view of the continuously high demand for neutron experiments by science and industry and the phasing out of existing reactor-based neutron facilities in Europe in the near future, new solutions and strategies are required to provide sustainable and effective access to neutrons in Europe. New neutron infrastructures have to provide novel capabilities not offered by the present-day facilities based on the ageing suite of research reactors in Europe. Enhanced performance does not necessarily rely on increased source strength, which goes hand-in-hand with cost increase, but can include improved flexibility and accessibility, specialization on particular important societal challenges or optimization on brilliance for small beams. In particular, cost-effective solutions are required to compensate the potential capacity loss and complement high-flux sources such as the new ESS spallation neutron source.

The High Brilliance neutron Source (HBS) project will demonstrate the technical and operational concept for a neutron infrastructure based on a low-energy proton accelerator. HBS is designed as a very flexible neutron infrastructure with neutron beams optimized for brilliance. It will host a full suite of highly competitive instruments. Thus HBS will be capable to serve as a national or regional highly attractive neutron research centre. The HBS source will benefit of state-of-the-art accelerator technology, combined with unique target-moderator concepts. HBS will mark a change in paradigm for research with neutrons where every individual neutron instrument will have its own neutron source with optimized pulse structure and a moderator adapted to the specific requirements of the instrument. Thus it will provide a unique and attractive option for achieving optimum and efficient brilliance for all neutron experiments at a lower cost compared to present-day large-scale neutron facilities.

In consequence HBS will provide a new efficient basis for harvesting and exploiting neutrons. It will offer a revolutionary route providing neutrons in a flexible and cost-effective manner to satisfy the demands of science, industry and society.

The flexibility and accessibility of an HBS type neutron source will open up and spread neutron science to include industry in its broadest sense and will enhance competitiveness in basic and applied research using neutron facilities. E.g. HBS could offer specialised target stations and access for particular areas as the development for new materials for batteries or aerospace industry. It could host analytical facilities for cultural heritage or specialize in analytical service for environmental analysis. The new accelerator-based neutron source HBS will complement and further develop the research landscape of high-end neutron facilities in Europe. In addition, HBS will provide training and preparation for the most demanding experiments at the flagship European neutron sources ILL and ESS.

The Conceptual Design Report presents a comprehensive introduction into the current landscape of neutron sources in Europe and the provision of neutrons (Chapter III). An overview on the science case using neutrons in various areas highlights the impact of neutrons on research and innovation and describes briefly the neutron methods applied (Chapter IV). Detailed outlines describe the components of the HBS starting with the accelerator system, the proton beam transport, the target stations (Chapter V) and the instrumentation considered (Chapter VI). Furthermore operation and safety aspects of the HBS facility are addressed (Chapter VII, Chapter VIII) and an outline of the required infrastructure (Chapter IX), commissioning and decommissioning (Chapter X), investment, costing and timeline (Chapter XI) is given. Additional information on certain technical aspects and detailed descriptions are provided in the added Appendices of the Conceptual Design Report.

III.
RATIONALE

III.1 Neutron provision

The use of neutrons to probe and understand matter and assess scientific theories was developed through the second half of the 20th century and neutrons have become an essential analytical tool in the scientist's toolbox. Neutrons help to provide spectacular advances in science and technology promoting the sustainable development of modern societies [1]. To produce beams of free neutrons the most suitable used processes are

- nuclear fission in research reactors,
- spallation using high-energy proton accelerators, and
- nuclear reactions with low-energy proton accelerators.

In a research reactor, neutrons released by fission of fuel atoms induce yet more fissions thus sustaining a chain reaction and providing a field of free neutrons in the moderator. Neutrons leaving the biological shielding through the provided channels are used for scattering experiments, imaging and neutron analytics. Each fission process produces on average about 1 usable neutron with an average energy of 2 MeV and a heat release of 180 MeV per neutron. High flux research reactors as the FRM II of the Heinz Maier-Leibnitz Zentrum (MLZ) in Garching, Germany, or the HFR of the Institute Laue-Langevin (ILL) in Grenoble, France, offer a neutron flux of around 10^{15} s^{-1} cm^{-2} in the thermal moderator. As fuel elements these facilities apply highly enriched uranium.

Spallation neutron sources use (pulsed) proton beams in the GeV range to hit a heavy metal target (e.g. lead, tungsten, mercury, or uranium), where around 20 to 30 neutrons per proton are evaporated with a heat release ranging between 30 and 50 MeV per neutron. The high neutron yield combined with the relatively small heat release makes spallation an ideal choice for a source optimized for high source strength, i.e. the number of produced free neutrons per second. However, the proton/target interaction zone is elongated to several 10 cm due to the high energy of the protons which hampers coupling the neutrons efficiently into a compact moderator. The high radiation level, extending to particle energies in the several 100 MeV range, requires massive shielding and a minimum distance of optical elements from the target.

Bombarding of target material such as lithium or beryllium with low or medium energy protons or deuterons in the range of 2 to 50 MeV produces neutrons by specific nuclear knock-out or stripping reactions. The neutron yield depends on the energy of the incident particles. At lower energies it is around 10^{-2} per proton (or per deuteron) with a heat release of around 1,000 MeV per neutron.

Furthermore, fusion of deuterium with deuterium or tritium in solid targets is used in small portable neutron generators, however, with low neutron yields. Here neutron yields of $4 \cdot 10^{-5}$ neutrons per 400 keV deuteron with a heat release of 10,000 MeV per neutron can be achieved.

Neutrons may also be released by photodisintegration using high-energy gamma rays or Bremsstrahlung radiation.

III.1.1 Reactor based fission neutron sources

Europe is hosting a suite of reactor based neutron facilities ranging from small facilities as the TRIGA II Vienna of the Atominstitut in Vienna, Austria, a number of middle flux neutron sources as the Budapest Research Reactor in Budapest, Hungary, and high flux neutron sources as the FRM II in Garching, Germany, or the ILL High flux Reactor in Grenoble, France. These facilities serve a user community of about 8,000 users with nearly 30,000 instrument beam days each year and are the main work horses for using neutrons in science and industry. An overview of the neutron facilities operated in Europe for neutron scattering and analytics is given in Figure III.2 below.

Most of these facilities have been build in the 60s or 70s of the last century, except of the FRM II, which came into operation in 2004. Despite continuous refurbishments and upgrades most of these reactor based neutron facilities have already reached or will reach end of their scientific lifetime within the next decade as reflected in a recent study by the European Strategy Forum on Research Infrastructures (ESFRI) [2]. This will lead to a severe reduction in the availability of neutrons for science.

Worldwide a number of reactor based neutron sources are in operation with similar performance as the mentioned European facilities. Most prominent are the JINR center in Dubna, Russia, the NIST facility in Gaithersburg, USA, and the HFIR reactor in Oak Ridge, USA. In Canada the NRU reactor in Chalk River had been in operation since the late 50s. The operation has been stopped in 2018. Smaller research reactor based neutron sources in North America are the research reactor at McMaster University in Hamilton, Canada, and the research reactor at the University of Missouri, USA.

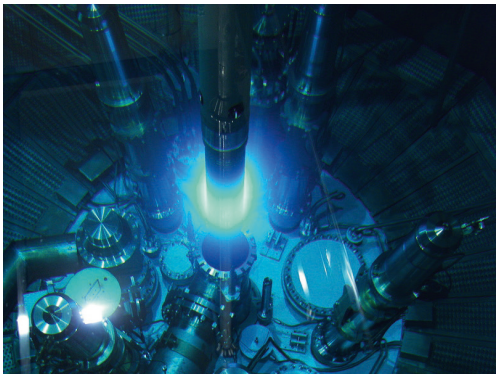

Figure III.1: *The FRM II research reactor core [3] (Picture: J. Neuhaus, FRM II / TUM)*

In Australia the ANSTO neutron facility is operated. Other reactor based neutron sources are in Japan (JRR-3), Korea (Hanaro), China (CARR), India (BARC). Most of these facilities are also in operation since the 60s or 70s. Only a few projects on new research reactors are planned world wide such as the PIK reactor in Gatchina, Russia, and the RA-10 reactor in Buenos Aires, Argentina. These reactor based sources will also be used for the production of radioisotopes for medical use to balance the investments of several 100 MEUR for construction.

III.1.2 Spallation neutron sources

Since the 70s spallation neutron sources have been developed and put into operation. In Europe the first of these kind of sources was the ISIS source in Didcot, UK, followed by SINQ in Villigen, Switzerland which came into operation in 1985 and 1996, respectively. Smaller spallation neutron sources did exist in the US with the IPNS in Argonne operated from 1982 to 2008, LANSCE in Los Alamos, USA, and KENS in Tsukuba, Japan. In addition China has recently put into operation the Chinese Spallation Neutron Source in Dongguan with a 1.6 GeV proton beam and a neutron beam intensity comparable to ISIS.

While the two spallation sources ISIS and SINQ operate with proton accelerators in the 590 to 800 MeV range, offering a comparable performance to medium flux reactors, three powerful megawatt spallation sources have been built in the last decade or are under construction to boost neutron intensity towards high flux reactors. These sources are the SNS in Oak Ridge, USA, J-PARC in Tokai-mura, Japan and the ESS in Lund Sweden. Most instruments located at the ESS will outperform instruments at the existing world leading high flux reactor ILL by an order of magnitude or more, becoming the world brightest neutron source. These megawatt spallation sources rely on powerful large proton accelerators. In case of ESS a 2 GeV linear accelerator is used and the allocated budget for construction of the facility is 1,83 Billion €.

Facility	Number of unique users	Number of instruments*	Number of experiments/year	Power	Thermal neutron flux at 1,5 Å (neutron/cm^{2}s)
ISIS	1580	31/31	850	200 kW	4.5 x 10^{15} (peak)
ILL	1433	32/37	848	58.3 MW	1.5 x 10^{15}
MLZ FRM II	965	26/26	832	20 MW	8 x 10^{14}
LLB	637	20/23	403	14 MW	3 x 10^{14}
SINQ	477	13/20	485	1 MW	4.1 x 10^{14}
BER II	302	13/17***	201	10 MW	2 x 10^{14}
BNC	145	15/15	127	10 MW	2.1 x 10^{14}
NPL	54	8/8	30	10 MW	1 x 10^{14}
TRIGA JGU	44	4/4	9	100 kW	1 x 10^{12}
JEEP II	43	5/6	65	2 MW	3 x 10^{13}
TRIGA JSI	41	8/8	**	250 kW	5 x 10^{12}
RPI	28	0/1	10	1 MW	1 x 10^{13}
ATI	15	5/5	6	250 kW	5 x 10^{12}
MARIA	13	4/6	46	30 MW	1 x 10^{14}
RID****	0	9/9	**	2 MW	3 x 10^{12}

Figure III.2: *Neutron sources in Europe [4] as of the beginning of 2019. In the meantime, by the end of 2019, three important sources have been permanently shut-down: the Orphée reactor of LLB in Saclay, France; the BER II reactor of HZB in Berlin, Germany; and the JEEP II reactor of IFE in Kjeller, Norway. The color code refers to large-scale (red), medium-scale (blue) and small-scale (grey) facilities, respectively.*

III.1.3 Accelerator driven neutron sources

Neutron sources based on nuclear reactions using low energy proton beams and light elements are in operation in USA and Japan since the 90s. The LENS facility in Indiana, USA, was build in 2003

and uses a proton accelerator with 13 MeV proton beam offering a neutron yield in the range of low flux reactors [5].

Several accelerator driven neutron sources are in operation in Japan as the RANS facility in Tokyo [6], the HUNS facility in Hokaido [7], the NUANS facility in Nagoya [8] and the KUANS source in Kyoto [9]. These university based small neutron sources use low energy proton accelerators in the energy range up to 7 MeV, except at HUNS, where an electron beam with 45 MeV is used. The performance of these sources for neutron scattering experiments is mostly an order of magnitude below small reactor based sources but allows qualified experiments on structure research (diffraction, small angle scattering) and imaging.

A compact neutron source using an electron accelerator has been in operation in Bariloche, Argentina, till recently [10]. Several projects exist in China to establish small and compact accelerator driven neutron sources.

In Europe no such kind of accelerator driven neutron source for neutron scattering applications does exist at present, but there are several projects to develop and built such neutron sources. The SONATE project in Saclay [11], France, promotes the construction of an accelerator based neutron source with a 20 MeV, 100 mA proton accelerator. At the Legnaro National Laboratory in Italy an accelerator based neutron source project is under discussion [12] as well as by ESS Bilbao in Spain. In Hungary a small compact accelerator driven neutron source will be installed by the company Mirrotron for industrial purposes. The HBS project of Forschungszentrum Jülich is the most ambitious among these projects worldwide. It aims at a source based on a low energy, high current proton accelerator to allow a neutron brilliance and flux competitive to existing medium to high flux neutron sources [13].

III.2 Neutron landscape

Historically research reactors dominate the current landscape of neutron sources. In 2018 in Europe out of 15 neutron sources 13 were research reactors (Figure III.3). For these facilities nearly 200 instruments are counted serving up to 4,800 experiments by about 5,800 unique users according to a recent survey [4]. Thanks to the versatile and broad network of neutron sources Europe has led the field for 40 years in scientific studies using neutrons. More as 4,000 publications are produced every year [14].

Two-thirds of all operational neutron sources in Europe were built in the 1960s & 1970s. Several have already been shut down and the majority of the remaining ones will close within the next ten years. In Germany, three research reactors have been shut down in the last two decades: the FRJ-2 (DIDO) reactor of Forschungszentrum Jülich in 2006, the FRG-1 reactor of Helmholtz-Zentrum Geesthacht in 2010 and the BER II reactor of Helmholtz-Zentrum Berlin in 2019. The year 2019 highlights the continuous fading away of this older generation of research reactors. Not only was BER II permanently shut down in December 2019, but two other research reactors, which were important for research with neutrons in Europe, were permanently taken out of operation: Orphée in Saclay, France and JEEP II in Kjeller, Norway. This tendency will affect the healthy position and scientific leadership of neutron science in Europe, despite the advent of the ESS, as pointed out in an ESFRI Report by the EU [2]. The report projects *"by 2025 Europe will, at best, have only 4 or 5 functioning neutron sources. Most probably these will come from ILL, FRM II (MLZ), ISIS, SINQ & ESS. … By the beginning of the 2030s a likely scenario – unless mitigating actions are taken - is that Europe will find itself with the ESS and only one or two other neutron sources. Whilst this obviously will reconfigure the scientific dynamics of neutron sources in Europe it will, even more importantly, focus the responsibility for supporting today's large scientific community and the instrumentation that it depends upon, on these few facilities. … The clear consequence of all conceivable scenarios that we foresee is that there will be a marked reduction in availability of scientific measuring capability using neutron beams in the coming years, and an undesirable loss of specialist human capital. Europe*

Figure III.3: *Neutron sources in Europe in 2018 [4]*

will lose its undisputed lead in many of the important areas of the sciences served by neutrons. … Therefore Europe's competitive edge, deriving from this pursuit, not only in science but also in the associated technological know-how, and in its medium and long-term innovation potential, will be significantly degraded, unless pro-active policies are implemented by funding bodies, the sources themselves, and the user community alike. This is the sine qua non for the continued health of this productive scientific discipline. There is a clear choice to be made between protecting and building upon Europe's investment or allowing it to wither away through indecision and inaction."

Based on the described scenario there is high risk that Europe will lose its lead in knowledge-based materials and agent design, the basis of technological progress and value creation in information and energy technologies, health and transport. With unprecedented neutron flux, the European Spallation Source ESS is expected to play an exceptional and leading role in this scenario. It will allow for entirely new types of experiments, but will not be able to offer the capacity a large and diverse user community needs. Evidently it is crucial to keep a network of national and regional neutron sources in Europe. This network must provide a co-operating eco-system ranging from low flux experiments up to European top-class sources for neutron science. Here, low energy accelerator-driven neutron sources provide a conclusive solution, as they are salable in price and performance from smaller facilities for specific applications at Universities and in industry to high-end competitive user facilities. Existing reactor based sources and spallation sources will have to be complemented by compact accelerator driven neutron sources (CANS) to secure and develop a functional and resilient network. The largest thread to research with neutrons in Europe is the loss of qualified and educated staff - scientists, engineers, technicians - due to the loss of opportunities for education following the closure of neutron facilities. Who will be able to efficiently use the European flagship ESS, a 2 B€ investment, if young people cannot be trained at smaller facilities with less user pressure? Apart of providing research capabilities, education and training can be offered through small sources, such as the one described in the Conceptual Design Report NOVA ERA, a compact accelerator based neutron source along the line of existing university based sources in Japan.

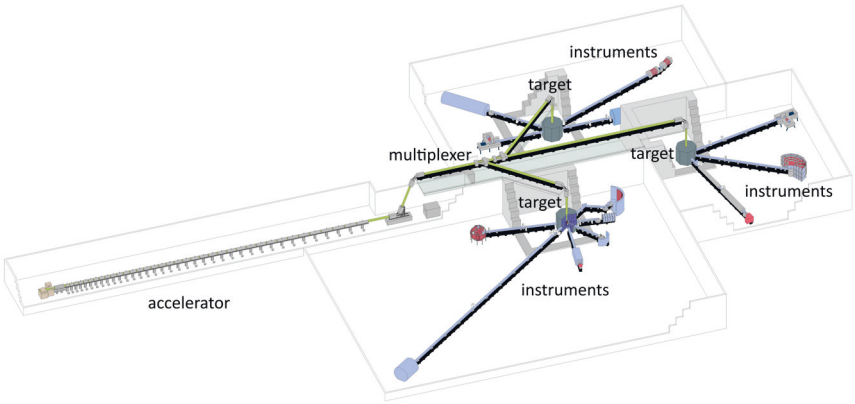

Figure III.4: *HBS baseline design*

The Jülich High Brilliance Source project HBS aims at a full-fledged medium size facility with highly competitive instruments designed to maximize beam brilliance [13]. It answers to the increased demand for experiments on small samples such as systems of biological macromolecules or nano-magnets. Together with other similar European sources, the HBS can fill the gap in instrument days anticipated with the ongoing closure of older neutron sources and open neutrons to new fields of science.

III.3 Baseline design

Accelerator-based neutron sources provide a versatile and effective opportunity to improve and spread neutron access in Europe and also a new route for supplying neutrons with leading-edge research infrastructures directly to science and industry. The HBS project pushes the performance of such sources to the current technological limits by employing state-of-the-art technologies in accelerator development, target and moderator design as well as beam extraction, beam optics and instrumentation. Based on a low energy high current proton accelerator, which produces a pulsed beam to hit a metal target (tantalum for HBS) to produce a thermal neutron flux comparable to existing medium to high flux reactor sources, a variable suite of neutron instruments can be served (Figure III.4).

Main components of the HBS are

- a dedicated proton or deuteron accelerator with optimized energy (50 to 100 MeV) and current (50 to 150 mA) that is multiplexed to feed several target stations which are operated at different frequencies.
- a target – moderator combination that offers a pulsed neutron beam at optimal frequency, pulse duration and neutron spectrum to fulfil the needs of every single instrument.
- optimized moderators according to the spectral needs of individual instruments. It is a dramatic change of paradigm in research with neutrons that in fact "every instrument has its own dedicated neutron source".
- a number of instruments at each target station, typically around 6, in order not to dilute the thermal flux maximum.

Technical outline and parameters of these components are presented in the corresponding sections.

The high brilliance compact accelerator driven neutron source aims at maximizing the brilliance of its neutron beams while maintaining their high flux. The best brilliance for a specific experiment is achieved by the optimized setup, starting from a dedicated target-moderator unit for each individual neutron instrument. Thus, the number of "useful" neutrons for the experiment in question is maximized, while minimizing the number of neutrons which have to be stopped in shielding – leading to corresponding savings in costs of the instruments and of the facility operation. Thus the HBS design follows the paradigm to "produce less thus saving costs, but waste less by maximizing brilliance, not source strength".

Brilliance

In the normal optimisation process the flux at the sample position is the last value to be known, therefore, other key parameters have to be used for the optimisation process. In this regard, Liouville's theorem [15] can be used, which states that the phase-space volume is constant along the trajectories of the system for conservative, loss-free optics. Hence, a very valid optimisation parameter is the phase-space volume given by the target / moderator / reflector (TMR) unit.

In scattering experiments a representation of the phase-space volume is the brilliance which is commonly used for any radiation source (light sources, synchrotron radiation facilities etc.). It normalises the number of emitted particles to the area they are emitted from, the wavelength band, the time interval and the solid angle. This definition of the brilliance doesn't take into account the time-of-flight possibilities a compact accelerator driven neutron source offers and therefore does not represent the phase-space volume of an experiment at such a source. The repetitiveness of the neutron beam has to be taken into account. This can be done by normalising to the number of particles hitting the target as the neutrons are produced by nuclear reactions of light ions inside a suitable target material. Hence, for such accelerator-driven neutron sources, the dimension of brilliance is chosen to be

$$[\mathrm{B}] = \frac{1}{\mathrm{scm^2sr}(1\%\Delta\lambda/\lambda)(\mathrm{mAs})}. \tag{III.1}$$

This definition of a brilliance allows the optimisation of the TMR-unit for the requirements of the instruments. A detailed description of this brilliance definition is given in the Appendix A.3.

III.3.1 Comparison to existing sources

The HBS aims to be competitive with existing neutron facilities while at the same time being more flexible, more accessible and particularly cost-efficient. On the baseline design of HBS with a 100 kW proton beam on a metal target (tantalum) the expected HBS brilliance has been simulated and compared with that of existing sources: the reactor sources HFR of the ILL in Grenoble, France, and FRM II of the MLZ in Garching, Germany, the short pulse spallation source ISIS in Didcot, England, and the long pulse spallation source ESS in Lund, Sweden.

The thermal and the cold neutron brilliance of HBS were simulated based on MCNP simulations at the transition from the moderator to the reflector. The resulting spectra were described as a sum of two (thermal) or three (bispectral) Maxwellian distributions. For the reactor sources, the wavelength dependence of the brilliance was directly taken from published data [16, 17, 18], while the peak fluxes of the pulsed sources were determined as outlined in Appendix A.2 [19, 20]. Results of these simulations are shown in Figure III.5. For thermal neutrons HBS reaches a peak brilliance of 2×10^{13} n s^{-1} cm^{-2} $Å^{-1}$ sr^{-1}, identical to the brilliance of the FRM II within errors. For cold neutrons a

brilliance of 3×10^{12} n s^{-1} cm^{-2} $Å^{-1}$ sr^{-1} at ≈ 4 Å is reached, which positions clearly HBS into the high ranks of neutron sources, surpassed only by MW spallation sources.

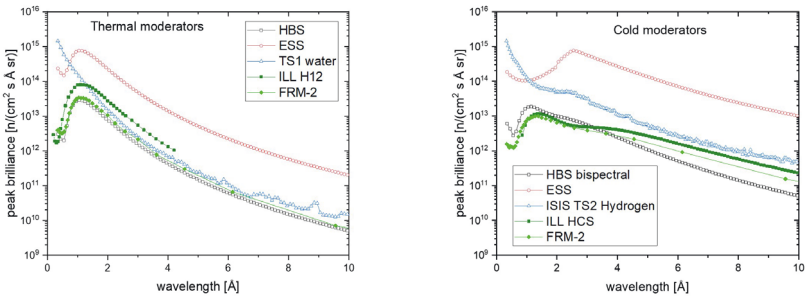

Figure III.5: *Comparison of neutron brilliance of thermal (Left) and cold (Right) neutron yield at various neutron sources*

One should note that these results rely on existing data bases for the simulation, but are being tested experimentally at a dedicated set-up at the COSY cooler synchrotron of Forschungszentrum Jülich. These experimental results will be published separately.

IV.
SCIENCE CASE

Neutrons are an essential tool in science and industry for probing structure and dynamics of matter from mesoscale to nanoscale and from seconds to nanoseconds. Especially the fact that neutrons interact strongly with hydrogen nuclei makes them a unique tool for the investigation of organic material and soft matter. The high penetration depth of neutrons allows the non-destructive investigation of large objects as e.g. engineering devices, geological samples or historical artefacts. The neutron's spin allows the determination of magnetic structures, magnetic excitations and fluctuations down to atomic length scales.

The general science case for research with neutrons has been made for many occasions (e.g. when proposing the MW spallation sources SNS and ESS) and by many organizations (e.g. ENSA [1], KFN [21] etc.). The Jülich Centre for Neutron Science JCNS organizes an annual international workshop, the "Unkel Meeting" [22], highlighting the advancements of low energy accelerator driven neutron sources. One of these meetings was specifically dedicated to the special science case of such novel neutron facilities and much of the text below is taken from the report from this event [23].

Quite general, looking at the modern trends in science, research is moving away from the investigation of simple model objects or the study of components of larger entities towards the understanding of entire complex systems, where various degrees of freedom are interacting and competing. The more elaborate and challenging these problems become, the more complementary probes, such as neutrons, nuclear magnetic resonance (NMR), electron microscopy, synchrotron radiation etc., are needed to advance our understanding. Neutrons excel in these types of studies, where information on multiple length- and time scales is mandatory to obtain a deeper insight.

- In life science, more than 160000 structures of proteins can be found in the protein data bank, mostly solved by synchrotron x-ray scattering, NMR or more recently cryo-electron microscopy. Knowledge of the structure is an important first step towards understanding functionality. The next step requires an understanding of the dynamics of these macromolecules, not only in dilute solutions, but also in the extremely crowded environment of real biological cells. Such knowledge will advance our ability to develop efficient pharmaceutical agents and thus to solve important challenges in health. Neutrons with their ability to cover the entire relevant phase space, to locate hydrogen and follow its movement, to vary the contrast between different components of such a complex system, are ideally positioned to take up this challenge to go beyond the study of the structure of single macromolecules.

- Another example concerns quantum technology, based on the unfolding of the second quantum revolution, which exploits our ability to manipulate single quantum objects. Applications require specific quantum materials, e.g. Qubits for future quantum computers have to fulfill the "DiVincenzo's criteria". The discovery of novel quantum materials with highly entangled quan-

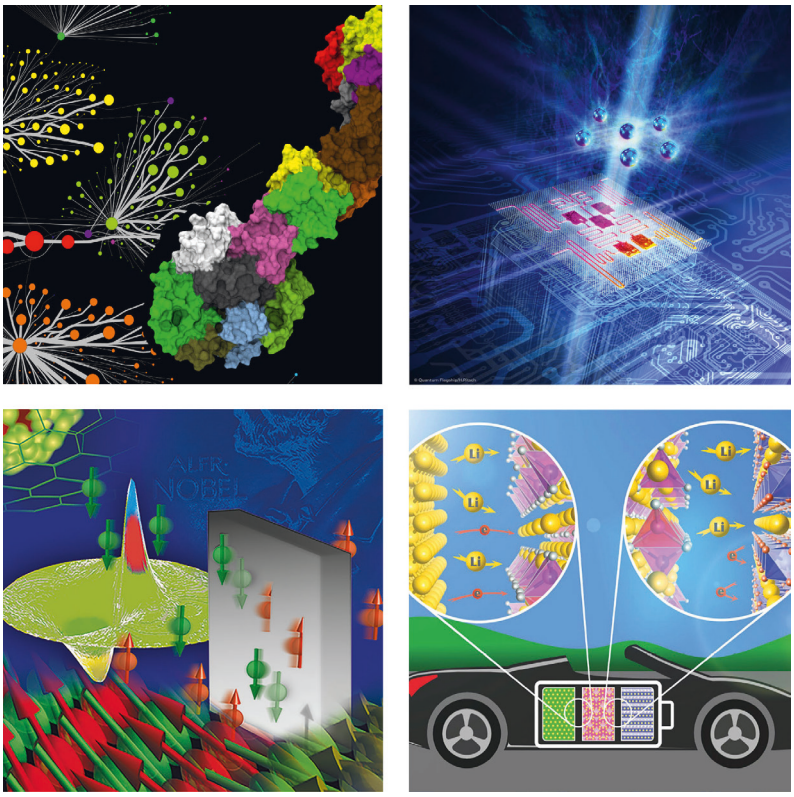

Figure IV.1: *Challenges in complex systems: crowded biological systems, quantum technology, spintronics, battery technology [24, 25, 26, 27]*

tum states and special topological properties is the realm of neutrons since the experimental setup requires complex sample environment for ultra-low temperatures, high magnetic field or high pressure, which can hardly be realized for any other microscopic probe mentioned above.

- Neutrons have already laid the foundation for the ongoing revolution in information technologies (IT), which employs the spin of the electron instead of its charge, the so-called field of spintronics. Spintronics avoids Ohm's losses and thus promises to make the dream of a Green IT come true. Again, the knowledge of the structure is the first step to manipulate functionality, here the magnetic structure of the materials combined to spintronic devices. While in macromolecular structure determination synchroton X-rays dominate the field, neutron diffraction is the unique probe for magnetic structure determination. An estimated 95% of all magnetic structures have been determined with neutrons. The next step is to understand the spin dynamics and the interface effects in thin film heterostructures making up spintronic devices. Neutrons are ideal probes also for this second step towards engineering and optimizing complex multi-component spintronic devices.

- Finally, technological devices, e.g. for energy technology, are very complex systems consisting of a combination of many different materials. The energy revolution moving towards renewable energies requires efficient energy conversion and energy storage devices, such as fuel cells and batteries. These devices are based on the movement of light elements, such as

hydrogen or lithium, which naturally makes neutrons the probe of choice. Neutrons are used to disentangle the water exchange mechanism and proton diffusion through the membrane in fuel cells or the Li migration between the electrodes in Li ion batteries. Due to the penetration ability of neutrons, these studies can be done operando, e.g. in charging and discharging cycles of batteries, and thus allow one to chose the best materials, optimize the geometry, and find and thus combat the reasons for ageing of the devices.

These examples highlight some of the strengths of neutrons. A broader description of using neutrons in all areas of science and technology is presented in the following sections of this Chapter.

However, free neutrons are rare and progress in this field can only be achieved with the provision of highly brilliant neutron beams with optimized pulse structure and energy spectrum. Such beams will be provided by the HBS, which will feature the highest ratio of beam brilliance-to-source strength, a quality criteria which will reflect in excellent signal-to-noise ratios. This will allow the investigation of small samples under optimized background conditions. The HBS is designed to be the ideal facility to solve grand challenges occurring in complex systems. It will be

- a source to solve the problems of complexity in life science, e.g. crowding in biological cells,
- a discovery machine for novel quantum materials in complex sample environment,
- a facility to optimize complex technological devices for Spintronics and for the energy revolution under realistic operation conditions.

Typical problems in science and industry mostly require a maximisation of the brilliance of a neutron beam. As an example the determination of the exact position of hydrogen atoms in protein structures needs a high flux of cold neutrons to illuminate a small protein single crystal of usually less than 1 mm^3 with a well collimated beam. The same holds for experiments in which the magnetic structure of an ordered ensemble of magnetic nanoparticles, a so called mesocrystal, is being studied. In both cases the samples available are tiny and high brilliance combined with low background is needed for a successful experiment to deliver highest flux with low divergence in a small beam diameter. This is exactly the challenge the HBS project is responding to!

The project will enable

- science with neutrons to become accessible more easily and locally in all areas mentioned, far beyond the limited access to the world-leading facilities.
- basic and applied research from material to life sciences, physics, engineering or cultural heritage to be done more flexible and timely following specific scientific and societal demand.
- the capacity of neutron beamtime to be stabilized and enlarged by the establishment of new facilities with high-quality neutron instrumentation on a level complementing the high-flux reactor and megawatt spallation sources.
- dedicated instruments for certain applications or specific scientific fields or industries to be realized on additional target stations.
- research in many fields requiring high brilliance neutron beams, e.g. for life science, engineering materials science, quantum and nanotechnology will receive a boost.

In addition, small neutron facilities at the universities or at industrial research laboratories could be made available to offer rapid access to neutron methods with instrumentation on a workhorse level [28].

IV.1 Chemistry

The synthesis of new materials is the basis of chemistry and a constant driving force in many areas in science. High temperature superconductors became available by anorganic oxide chemistry, metal organic frame works are driven by supramolecular chemistry, new battery materials, hydrogen storage systems rely on chemical synthesis of hydrogen containing materials or new lithium compounds. Improvements in photovoltaic are driven by new anorganic as well as organic materials. Organic and non-organic light emitting diodes became available by new complex and multilayered structure. Graphene evolved by sophisticated chemical synthesis. Green chemistry will require many new materials to be synthesized to minimise waste and renew feedstocks.

For the understanding of chemical reactivity, reaction kinetics and structure dynamics in energy and functional materials complementary studies using neutrons are required. They will help to develop improved structural materials, new lightweight materials, fuel cells and batteries for mobility, energy production, conversion, and storage. New or more efficient processes for material production and energy handling could be developed and improved using various neutron methods. Intermolecular forces in liquids and glasses using high pressure, temperature, or magnetic fields will be studied to understand and improve materials and systems.

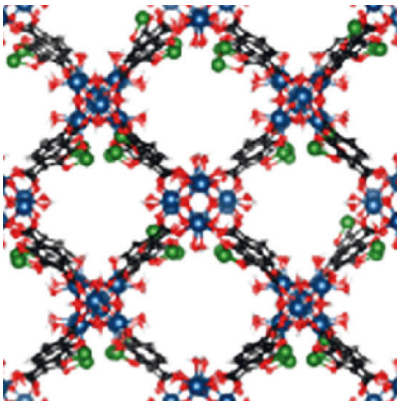

Figure IV.2: *Hydrogen loading in porous crystals [29]*

To probe the structure and dynamics of new materials neutrons are a versatile tool. Strong bonding in hard matter can be studied using total neutron scattering and neutron diffraction. Magnetic structures are probed by magnetic diffraction. Lattice dynamics, phonons and magnons are shown by inelastic neutron scattering. Weak bonding at surfaces or catalysts, colloids, liquids and solutions, self assembled aggregates and soft matter interactions in general are studied using small angle neutron scattering, neutron reflectometry and diffuse scattering.

A unique advantage of neutron scattering is the strong scattering power of light atoms, isotope contrast and the right energy scale to probe phonons. Main goals in sustainable chemistry can be approached by neutrons. The structure of novel materials can be determined and atomic vibrations of molecular crystals are accessible to probe ab initio theories. Measurements with complex sample environment are feasible due to the high penetration power of neutrons through the devices.

The current focus in chemistry using neutrons is in the areas of hydrogen storage materials using hydrides, new lithium and non-lithium containing materials for batteries, new materials in photo voltaics and renewable energy, development and understanding of white light emitting diode materials and optoelectronics, new materials for magnetic and spintronic applications, carbon based electronic materials as graphene and structural polymers to be used i.e. in 3D printing. A few examples on novel materials and system are the following.

- Ferrimagnetic double perovskites show highest remnant field values as shown for Mn_2FeReO_6 [30]. Exotic magnetoresistance or other spintronic phenomena may be generated from couplings between spin, lattice, and charge degrees of freedom in such high pressure Mn-based double perovskites. Neutron diffraction is indispensable to reveal atomic and magnetic structure of this class of materials.

- Pyrochlores are an exiting class of oxynitride materials which exhibit interesting spin glass and spin liquid behaviour. Using different cations as Ca, Sr or Ba they can be tuned for applications as phosphors in white light emitting diodes (WLED) [31]. The same can be achieved by anion clustering replacing SiN by AlO shifting emission wavelength. Structure and dynamics are examined using polarised neutron powder diffraction and inelastic neutron scattering.
- Of highest interest is the production of hydrogen by photoexcitation driven water-splitting which can be achieved with visible light using certain transition metal perovskite oxynitrides. Transition metal oxynitrides are an emerging class of materials with optical, photocatalytic, dielectric and magneto-resistive properties. A driving force in these properties seems to be the oxygen/nitrogen anion ordering in these systems. Neutron powder diffraction has been applied due to the distinct scattering contrast between oxygen and nitrogen to probe the anion ordering [32].
- The class of transition metal carbodiimides provide a class of materials with potential for new lithium or sodium battery systems [33]. The complex synthesis needs the control of the structure in-situ by neutron diffraction.

Quick access to neutron beam time in order to characterize newly synthesised compounds allows a feed-back of structural information into the synthesis process. Laboratory facilities close to neutron scattering instruments are often essential if sensitive samples have to be prepared just ahead of a neutron measurement. Such requirements for studies in the field of chemistry can be realized at an HBS type facility due to its intrinsic flexibility.

IV.2 Geoscience

Neutron scattering and neutron activation analysis are important methods for the study of geological materials. This is to a great extent due to the possibility of localizing hydrogen, an important and common element in minerals. Diffraction experiments yield a larger quantity and more exact information than X-ray scattering when analysing complex low-symmetric crystal structures of many minerals. Prompt Gamma Neutron Activation Analysis (PGNAA) provides information on the composition of the sample including light elements as well. Applications of PGNAA are diverse and include the investigation of samples in geology and petrology to probe e.g. the composition (major, minor and trace elements) of minerals or sediments, in situ monitoring of chemical reactions, determination of nuclear data and much more.

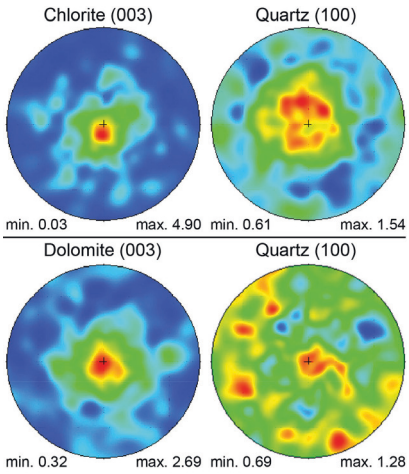

Figure IV.3: *Basal pole figures of chlorite, dolomite and quartz [34]*

Texture is defined as preferred crystallographic orientation in a polycrystalline aggregate. The main mechanisms of geological texture formation are crystallization, sedimentation, plastic deformation, recrystallization and metamorphism. Textures of geomaterials are fingerprints of the earth's history.

Quantitative texture analysis, i.e., the calculation of a three-dimensional orientation distribution function of crystallites, is based on experimental pole figures which represent the orientation distributions of certain crystallographic directions and which

can be obtained from neutron diffraction techniques. Examples illustrate the use of those neutron methods in the field:

- (Fe, Mn)-phosphates play an essential geochemical role in the evolution of pegmatic rocks. The exact crystal-chemical formula is investigated with neutron diffraction to understand the formation process [35].
- For the genesis of the formation of bentonite cation exchange and amount of ions have been investigated using PGNAA to allow better classification of found minerals [36]
- Texture and microstructure of granulites are investigated using neutron diffraction to obtain plastic deformation relevant to help interpret seismic data [37].

IV.3 Environment

The increasing world population density, together with global urbanisation and industrialisation are putting a real strain on the planet and the environment. To keep on growing and prospering, or simply maintain living standards, countries need to minimise this strain and protect their environment. Neutron scattering is helping scientists to fight pollution and develop environmentally friendly processes that generate and release fewer contaminants into the environment. This is also important with respect to protect climate and reduce the release of harmful ingredients triggering climate relevant chemical processes. Prompt and delayed gamma neutron activation analysis can provide information about rare elements and serve as a way to detect contaminants. Neutron diffraction can help to identify the structure of particles and modifications due to interactions with contaminants.

- A combination of cold neutron prompt gamma-ray activation analysis (CNPGAA) and thermal neutron (TN) PGAA was used to determine sulfur in fuel oils for the environmental friendly handling of oil products [38].
- For the optimization of the manufacturing process of multicrystalline silicon (mc-Si) for solar cells in order to reduce energy consumption and costs PGAA was used to determine the boron and hydrogen contents [39].
- The detection of heavy elements in sediments was demonstrated using PGAA to control the concentration of harmful contaminants as cadmium or mercury [40].
- Formation of metastable nitric acid in ice clouds affecting the formation of high altitude clouds in the polar stratosphere was found using neutron diffraction on ice particles.
- Storage of anthropogenic CO2 in geological formations relies on a caprock as the primary seal preventing buoyant super-critical CO2 escaping. Although natural CO2 reservoirs demonstrate that CO2 may be stored safely for millions of years, uncertainty remained in predicting how caprocks will react with CO2-bearing brines. Small angle neutron scattering was used to determine the porosity and prove the viability of geological carbon storage.

IV.4 Engineering

Complex engineering devices can be studied by neutron imaging techniques thanks to the high penetration depth of neutrons in matter. Working systems in real operation conditions can be visualized. Hydrogen containing materials as plastics, oils or soft tissues can be distinguished easily due to the high contrast of hydrogen material in the neutron image as demonstrated on the distribution of oil and lubricants in motor engines improving efficiency and stability of combustion engines.

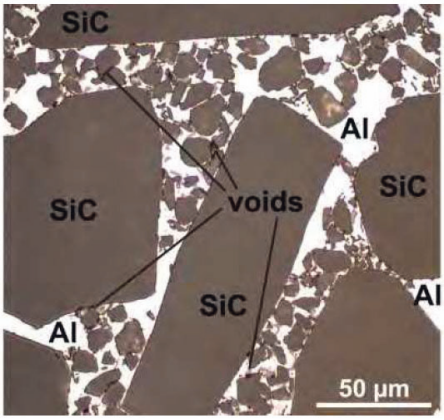

Figure IV.4: *Micrograph of an aluminum magnesium SiC metal matrix composite [41]*

- Steel construction in bridges, lightweight aluminum components in airplanes or cars, rails and axes in trucks or rails have to withstand various kinds of external and internal stress and strain. To monitor such stress and understand the underlying processes and process parameters neutron diffraction is applied providing high spatial resolution and high penetration depth.

- The analysis of microstructures and phase distribution in composite materials and alloys is important to develop new materials to improve sustainability, save energy and protect environment. Experiments with neutrons will help to verify model predictions and improve material simulation efforts.

- In probing material stability texture, stress and strain measurements by neutron diffraction are an indispensable and complementary tool in engineering and material science. In particular in-situ measurements close to operating conditions or applied forces help to improve the materials and provide important bench mark values for simulation and theory.

- Metal matrix composites (MMCs) are widely used in advanced industries because of their outstanding properties. However, the poor weldability of MMCs is one of the major factors that limit the widespread application of MMCs. Friction stir welding (FSW) is considered to be a promising technique for joining MMCs. Using neutron diffraction, the multiscale residual stresses in welds were characterized and used to calculate thermal and plastic misfits

- Studies for components can be accompanied by experimental tests e.g. by imaging of welding structures and textures, cracks, pores and domain structures in engineering materials.

- The characterisation of early stage precipitation in Ni-based superalloys is an important issue as it strongly supports the development of new high temperature alloys. The formation of fine precipitates and their initial growth in an alloy system of a tungsten-rich Ni-based superalloy has been revealed by SANS due to the fact that this method makes it possible to characterize inhomogeneities of the order of 1-300 nm even in-situ at high temperatures, making it the perfect match to receive a size and volume fraction of these precipitates

- Intermolecular forces in liquids and glasses using high pressure, temperature or magnetic fields will be studied to understand and improve materials and systems. The dynamic behavior of liquid metals and alloys as present in many metallurgical processes requires the investigation of diffusion and transport processes down to the atomic level and time scales.

- In many industrial processes as well as in environmental applications such as water cleaning or energy conversion using fuel cells, porous materials or membranes are needed with dedicated performances. Structure and interaction with gases or fluids can be investigated using small angle neutron scattering, neutron reflectometry or neutron imaging.

An HBS type of source is well adapted to the requirements of engineering materials science. The time-of-flight techniques is highly efficient in determining textures as one rotation necessary for monochromatic measurements can be omitted. Spatially resolved stress-strain measurements require fine and highly collimated beams, exactly the beam quality which a high brilliant source delivers.

IV.5 Information and quantum technologies

Due to their magnetic moment, neutrons are very prone to study magnetic phenomena ranging from unconventional superconductors and magnetic nanoparticles to magnetic hetero-structures. The magnetic behaviour and structure of novel materials for multiferroics or magneto-calorics can be investigated. Materials for new permanent magnets and applied magnetics materials, of which a high demand in energy, electronics and automotive industry exists, can be developed and tested having easy access to neutrons. Current topics addressed with neutrons here include the following.

Figure IV.5: *Different skyrmion spin textures [42]*

- New materials create new phenomena as found in spintronics materials. One pathway towards energy-saving "Green IT" is to employ antiferromagnets in thin film heterostructures, so-called antiferromagnetic spintronics. Neutrons have revealed layer-resolved magnetization reversal in novel all-oxide–based synthetic antiferromagnets. On superconductivity new intermetallic materials exhibit unexpected superconductivity as e.g. of $FeTe_{1-x}Se_x$. The search for such new materials is open and can be guided by ab-initio calculations for materials with IC fluctuations as CrAs which have to be tested by neutron scattering.

- The appearance of a magnetic excitation spectrum with an hour-glass shape in energy-momentum space is a characteristic property of high-temperature superconducting cuprates. Despite numerous studies, the origin of this peculiar excitation spectrum is not well understood. Using three-axis neutron spectroscopy, an isostructural but insulating cobaltate that also exhibits an hour-glass magnetic spectrum was studied. A fractal microstructure with a nanoscopic distribution of undoped and hole-doped regions within the cobalt oxygen planes was observed which unravelled the microscopically split origin of the hour-glass spectra on a nano scale.

- In the case of magnetic monopoles in magnetic vortices, called skyrmions, information can be written and erased, which could provide a decisive step toward the realization of novel,

highly efficient data storage devices. The magnetic vortex structures were discovered through neutron scattering experiments on manganese-silicon.

- Highly entangled quantum states are the basis of the quantum technologies of the second quantum revolution, from quantum sensors, via quantum communication, to quantum computing. Such states are often stable only at low temperature, high magnetic field of high pressure. Neutrons with their ability to penetrate the required sample environment and with their sensitivity to the electronic spin degree of freedom are ideally suited to discover or study and understand novel quantum states. This has been proven e.g. by the observation of the Higgs transition in a magnetic Coulomb liquid, the discovery of spiral spin liquids and Weyl fermions or by portraying entanglement between molecular qubits with four-dimensional inelastic neutron scattering.

- Skyrmion lattices – regular crystalline arrangements of skyrmion lines found in chiral magnets provide an excellent showcase for the investigation of topological stability and phase conversion. Small-angle neutron scattering is used to investigate the topological stability and decay of skyrmions to prove the essential features of the topological unwinding of skyrmions.

- Multilayers of rare earth such as gadolinium, dysprosium or terbium and ferromagnetic elements are known to show exchange bias effects. In these kinds of multilayer systems, a hard and a soft magnetic layer are combined and magnetically coupled at the interface. Polarized neutron reflectivity is an effective tool to probe such challenging ferrimagnetic systems and can explain the magnetic behaviour of the system.

The HBS is ideally suited for the study of nanomagnetism in the form of magnetic heterostructures or magnetic nanoparticles. As an example, the study of the magnetic structure of an ordered ensemble of magnetic nanoparticles, a so called mesocrystal, is a challenge for present-day neutron instruments. The samples available are tiny and high brilliance is needed for a successful experiment to deliver highest flux with low divergence in a small beam diameter.

IV.6 Nanotechnology

As tools for nanoscience and nanotechnology, neutron scattering with intense neutron beams helps to characterize and assist in fabricating nanostructured materials, nanoscale devices, and nanosystems. As subatomic probes of dynamics, neutron scattering centers and specialized instruments allow literally to visualize nanostructures and nanomaterials - either human-engineered or biological - at the nanoscale.

An understanding of novel properties at the nanoscale and their relation to function stimulates new research and development activities across diverse application areas such as catalysis, photovoltaics, fuel cells, membranes, adsorbents, coatings, displays, ceramics, thermo-electrics, adhesives, sensors, batteries, pharmaceuticals, and magnetic and semiconducting devices.

Self-assembly driven by thermodynamics and directed self-assembly guided by external fields are important mechanisms for forming heterogeneous nanoscale structures. The benefits of self-assembled nanostructured materials are being explored for a broad range of applications, including drug and gene delivery agents, nanoporous membranes, and miniaturized biosensor arrays. Neutrons have an important role in determining the nanoscale structure of self-assembled systems and measuring the interactions among particles. This is a necessary first step towards achieving full control of the self-assembly process, which would have far-reaching scientific and technological implications.

- By using neutron reflectivity experiments the density distribution profiles of adsorbed diblock polymers with detail at the molecular level were obtained. When combined with state-of-the-art techniques for polymerization and selective deuteration, and applied to controlled model architectures, neutron reflectivity measurements helps to elucidate the structure of complex systems at interfaces under confinement and applied shear stress.
- The interaction between surfaces displaying end-grafted hydrophilic polymer brushes plays important roles in biology and in many wet-technological applications. Neutron reflectometry yields distance-dependent structures of nanometric polymer brushes interacting across water [43].

Again, for studies in the field of nanotechnology, highly brilliant beams combined with low background are required, a true realm of an HBS type of source.

IV.7 Energy technology

The development of new and improved structural materials is a continuous challenge necessary to tackle a broad range of questions and disciplines ranging from energy production, conversion and storage, mobility, and climate. New materials are the driving force in innovation and the creation of welfare and better life. More efficient and energy saving processes for material production and handling in an environmental friendly way are required.

Material sciences benefit of neutron scattering due to the access to samples at relevant conditions combined with in-situ and operando studies. This allows monitoring of processes and the accurate measurement of process parameters which is the basis to understand the process mechanism. Some topics in material science are found in the following fields.

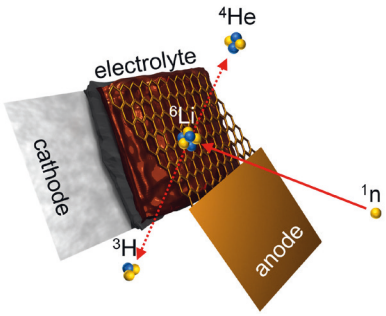

Figure IV.6: *Using neutron depth profiling location of lithium in the battery material can be determined. (Figure: M. Trunk, FRM II / TUM) [44]*

- The analysis of light elements as hydrogen in materials is of great importance in many areas as catalysis, high and low temperature materials, energy storage materials or multilayer chemistry. Neutron diffraction is a versatile method to locate hydrogen in the structure of such materials.
- Conventional Li-ion batteries (LIB) inevitably suffer from capacity losses during operation. The degradation mechanism of all-solid state, thin film batteries can be studied using operando neutron depth profiling to elucidate aspects of the long-term degradation mechanisms.
- For the understanding of chemical reactivity, reaction kinetics and structure dynamics in energy and functional materials complementary studies using neutrons are required. The microstructure and phase distribution in metall composites and alloys on solidification needs accurate liquid diffusion data which can be provided by neutron spectroscopy.
- New or more efficient processes for materials production and energy handling could be developed and improved. Neutrons help to develop improved structural materials, new light weight materials, fuel cells and batteries for mobility, energy production, conversion and storage.

IV.8 Cultural heritage

Being a non-destructive probe, neutrons can penetrate deeply into cultural artefacts or beneath the surface of paintings to reveal structures at the microscopic scale, chemical composition, or provide 3D images of the inner parts of the artefacts. For heritage science purposes, whole artefacts can be placed in the neutron beam and analysed at ambient conditions without tedious sample preparation.

Typical tasks in archaeometry are provenance studies to identify the sources and workshops where material was fabricated and used, to determine the manufacturing processes and conditions, to identify fakes and imitations, to explore conditions of conservation and restoration, to reveal ancient technologies and to date artefacts correctly. In all these tasks the non-destructive methods using neutrons can be applied.

Measurements at neutron imaging stations are made in real time, which can be useful for testing conservation materials and methods. Prompt gamma neutron activation analysis (PGNAA) can be applied for the nondestructive chemical analysis of artefacts.

Figure IV.7: *Non-destructive analysis of north door relief of Florence baptistery [45]*

- Restorers employed two different cleaning methods on the 15th century head of the prophet bronze surface, blackened over the years, at the Baptistery of San Giovanni in Florence: they cleaned a part of it, with a laser, another part chemically using salts and a third portion of the head remained uncleaned. Neutron analysis did show nondestructively which cleaning method was optimal.

- Iron has become one of the most important materials in the study of prehistoric and historic cultures. Therefore, the preservation of iron artefacts and the prevention of corrosion, in particular, plays a predominant role in the work of archaeological museums. PGNAA is ideally suited for determining the chlorine content of artefact pieces without destroying the valuable objects. With sensitivity in the ppm range, PGNAA allows systematic, non-destructive tests of the efficiency of leaching procedures in the preservation of artefacts.

- Phase analysis, structure determination and texture and stress analysis were applied to study medieval high carbon steels to understand medieval processing techniques.

IV.9 Soft Matter, biomaterials and health

Nanocomposites, nanoparticles and nano-materials for medical and life science are developed and used in an increasing number of applications in daily life, engineering, health care and medicine. Scattering methods to study structure and dynamics of such materials to characterise different formulations and behaviour over time are of general importance. Aspects of safety on health and environment of such new materials have to be studied, which needs reliable structural information. Here, neutron scattering methods can provide important and complementary information. As an

example, small angle neutron scattering has been applied to study nanoparticles as drug delivery systems to understand their aggregation and interaction behaviour.

New biopolymers and bio-degradable materials are strongly requested for ecologically friendly and energy saving materials and products. Structure and interaction need to be investigated to develop and modify synthesising processes and adapt to environmental requirements. Deuterated molecules highlight polymer interactions or interaction of drugs and peptides with bio-membranes. Some examples using neutron scattering in this fields of research are the following.

- Tight packing leads to coordinated movements of larger groups of atoms within polymer melts. Neutron spectroscopy makes it possible to detect how long-chain molecules in their liquid melt move. The results contribute to a better understanding of mass transport in liquids, which plays a crucial part in many technologically relevant processes, for example in charging and discharging batteries, electrolysis, and chemical reactions such as catalysis in the liquid phase.

- A currently active field of research is focused on the special class of soft colloids, i.e. elastic and deformable colloidal particles, which display a dual character associated with polymers and hard spheres. Due to their hybrid nature, soft colloids macroscopically show interesting structural and dynamic properties resulting from their unique microscopic structure. Small angle neutron scattering revealed experimental structure factors S(Q) which, in combination with liquid state theory and simulations, lay the basis for understanding soft colloids.

- Polymer drug carriers based on N-(2-hydroxypropyl)methacrylamide (HPMA) co-polymers have been developed for the treatment of tumors, with special focus on site-specific delivery and controlled release of anti-cancer agents into tumor tissues or cells. Time-dependent SANS measurements following sharply changing pH levels has been applied to characterize the drug release and changes in the particle size and shape of HPMA.

- Hydrogen and hydration water is essential for the function of enzymes, e.g. when during a reaction process the hydrogen bonds are reconfigured. Neutrons with their ability to see the relevant hydrogen atoms can reveal reaction pathways and thus provide necessary information for the design of agents. In this way a new approach to combat helicobacter pylori, thought to be responsible for gastric cancer, has been found.

- Theranostics are materials which combine diagnostic and therapeutic capabilities. Promising candidates for theranostics are aggregates containing gadolinium complexes. They have been proposed as contrast agents for magnetic resonance imaging (MRI) and could also be used as anti-cancer drugs. The structure and aggregation of the potential drug has been studied using small angle neutron scattering to clarify if, and how much of the anti-cancer drug doxorubicin could be loaded via these nanostructures.

IV.10 Radiation safety

Radiation effects in electronics is a very important field of scientific and technological research. Radiation tolerance is strategic for many applications of electronics: Space Applications, High Energy Physics (HEP), Nuclear Reactors, Nuclear Medicine. Understanding and quantifying the impact of various types of radiation effects on electronic systems enables the construction of reliable instruments for radiation hostile environments, such as HEP experimental halls, Outer Space.

Radiation damage in electronic semiconductor device occurs when there is a deposition of energy in the form of atomic displacement and/or ionization. Displacement damage dose (DDD) effects in the semiconductor bulk or total ionization dose (TID) effects in the insulators layers and interfaces are cumulative: the damage, measured as shifts in device parameters (leakage currents, thresholds...),

progresses as the device is exposed to increasing amounts of radiation. On the other hand, a Single Event Effect (SEE) occurs when a single ionizing particle generates enough unwanted charge to cause an instantaneous anomalous device or system behaviour. Hence, the need to test commercial industrial products against neutrons is a growing issue that goes far beyond applications in extreme environments. It is true for Avionics as well as for commercial electronics used in mundane applications as our terrestrial environment is by far not radiation free.

- Neutrons produced in high-energy cosmic ray air showers are invasive, ubiquitous, and may induce SEE. The study of neutron-induced SEE in commercial electronics with appropriate irradiation facilities is of strategic importance, in particular for digital electronics industries that flood the market with memory and logic components. High-profile product failures would bring significant loss of market share and revenue.

Radiobiological effects are of utmost important for determining radiation effects on living organisms and for radiation protection, providing the conversion from absorbed dose (Gy) in Equivalent dose (Sv). The data from which these values are determined [47] are derived either directly by dedicated measurements with neutron irradiation of biological samples and from the effects of the bombs at Hiroshima and Nagasaki or indirectly by an estimation of the Linear Energy Transfer (LET) of the secondary particles produced by them in tissue. In both cases, the uncertainties beyond 10 MeV are too high as to make accurate prediction. The spallation source at LANSCE/WNR neutron beam line has been used, not only for the irradiation of chips and electronic circuits, but also for the irradiation of cells and embryo for determining the Relative Biological Effectiveness (RBE) of high energy neutrons [48].

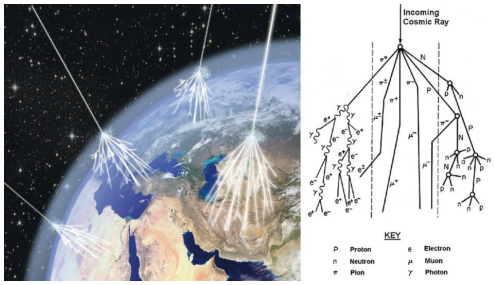

Figure IV.8: *Cosmic ray air showers in the upper atmosphere by energetic primary cosmic rays [46] (Graphic: Asimmetrie/INFN)*

The RBE factor for neutrons is strongly energy-dependent. Although there is abundant literature on the neutron RBE for thermal and fast neutrons up to a few MeV, little is known about the effect of very high energy neutrons, as those that can be produced by cosmic rays. Nevertheless about 80% of atmospheric neutrons have energy below 100 MeV. SEE cross section has a threshold located around few MeV with a plateau above this energy: the definition of the threshold is of utmost importance and can be experimentally measured by means of quasi-monochromatic neutron beam at energy below 100 MeV.

- The response to high-energy neutrons can be a useful source of information about the mechanism of DNA mutations [49]. Recently advanced techniques have been developed for the observation of DNA damage and repair mechanisms [50]. The application of these techniques to culture cells after neutron irradiation would provide important data for assessing the risk of neutron radiation exposure.

- Another problem of recent interest is the behaviour of bacteria exposed to high energy neutrons, a concern when transferring bacteria in/out of earth. Bacteria are very resistant to radiation, requiring doses of the order of 1000 Gy for direct radiation effects, but most of the

studies have been done with radiation beams of energies up to the MeV scale. Little is known about their behaviour at higher neutron energies.

In space missions, the issue of radiation effects is in particular important not only for electronics and critical instrumentation. The direct effects of radiation in human beings is clearly critical. In general, radiation effects originate from either the killing of large number of cells (deterministic effects). With the current shielding technology, it is difficult to protect astronauts from the adverse effects of heavy-ion radiation. The problem of shielding against Galactic protons is compounded by the production of secondary neutrons in the shielding itself. Recently, the strong improvement in magnet construction triggered the possibility of performing active shielding on spacecraft; the secondary neutron production remains the most challenging open issue and research on the mitigation of radiation effects on humans in space is crucial.

- In the International Space Station (ISS), there are two basic components of neutron radiation: the albedo neutrons emanating from the Earth's atmosphere and the secondary neutrons from the interaction of high energy GCRs with spacecraft materials. The neutron energy range of interest for radiation risk assessment is 0.1 to at least 200 MeV. Based on both modelling and measurements covering a portion of the energy range of interest, it was found that secondary neutrons contribute a minimum of additional 30 percent and up to 60 percent of the dose equivalent rates of charged particles [51].

At an HBS type source one could envisage a dedicated target station for studies in this field. Such a dedicated target station has been realized already at CANS, for example at the LENS facility in Bloomington, Indiana. In Leganaro it has been shown that with the proper choice of target material combinations, the spectrum of high energy neutrons from cosmic ray air showers can be closely approximated.

IV.11 Neutron methods

IV.11.1 Elastic scattering

Elastic neutron scattering provides information about structural properties of condensed matter. The deviation of the neutron's direction from the direction of incidence on the sample is higher, the longer the neutron's wavelength is and the smaller the correlation length between comparable structures is. In that sense, neutron scattering is a reciprocal space method and is sensitive to structural (or magnetic) correlations in the range of the neutron's wavelength up to some hundred multiples of the wavelength, if the instrument delivers a sufficiently high angular resolution. Different neutron scattering instruments are used, optimized to different requests on resolution in wavelength and scattering angle(s), together with well adapted detector systems to be able to offer ideal experimental conditions to address the user's questions to his specific sample.

At a pulsed neutron source, the wavelength is typically measured by time-of-flight, i.e. it is determined by the time the neutron needs to travel the distance between the source and the detector. In most cases the length of the source pulse or the opening time of the chopper window immediately after the source defines the wavelength resolution. At the HBS source, different target stations with different pulse lengths are available. This enables one to choose a pulse structure optimal for the experiments to be performed at a certain instrument.

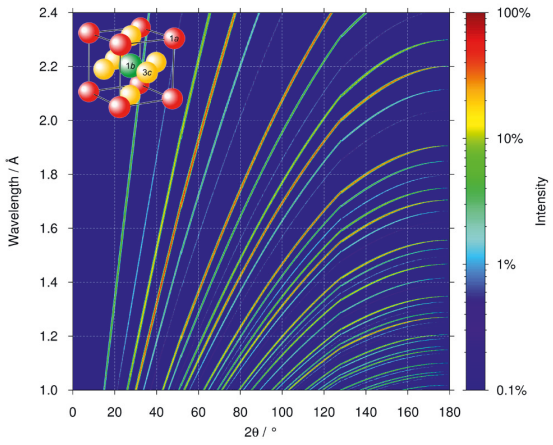

Figure IV.9: *Angle and wavelength dispersive time-of-flight powder diffraction measurement [52]*

As the pulsed source only operates for a short fraction of the time frame, but the detector operates continuously, a large range of wavelengths can be used in every pulse frame to measure elastic scattering. If the scattered neutrons are detected with large solid angle coverage, elastic scattering experiments are typically 10-20 times more efficient compared to a continuous neutron source, where usually monochromatic neutron diffraction instruments with lower detector coverage are employed.

As the wavelength of thermal neutrons matches very well the inter-atomic distances, powder diffraction and single crystal diffraction are methods used to investigate the arrangement of atoms on the scale of atomic distances. Neutron diffraction is complementary to X-ray diffraction. In contrast to X-ray diffraction, the neutron's interaction potential is not increasing monotonously with the atomic number so that light elements, e.g. lithium, nitrogen, oxygen, and most importantly hydrogen, can be investigated in an environment of much heavier atoms. Especially hydrogen atoms are basically invisible for x-rays, so that the structural investigation of organic compounds, hydrides or other hydrogen containing structures is strongly dependent on the opportunity to use neutrons as a probe.

The directionality of the interaction between the neutron and a sample can be used to determine anisotropies in a sample. Texture diffraction is a method using the anisotropy of powder diffraction from a sample to investigate ordering phenomena in polycrystalline objects. This method is used as well to get knowledge about the production process of historical artefacts as about what has happened with geological samples that underwent multiple transformation and transport processes during the evolution of our earth including plate tectonics and vulcanism. Also effects of the production process of engineering materials can be investigated by texture analysis, e.g. the ordering of the crystalline structure in steel grains due to industrial rolling processes. Diffratometers with a high resolution in space as well as in lattice constants can be used to determine the distribution of mechanical stress in mechanically or thermally deformed samples.

Elastic scattering of cold neutrons is used to investigate objects larger than inter-atomic distances due to the longer wavelengths of cold neutrons compared to thermal neutrons. The workhorse instrument for soft-matter science is the Small-Angle Neutrons Scattering (SANS) diffractometer. This instrument is used to determine structure and formation of every kind of macromolecular matter from synthetic rubber via water-oil-emulsions to biological matter as protein solutions. SANS diffractometers are capable to investigate matter on length scales between 5 Å and 2 μm. The longer wavelength of cold neutrons is better suited to determine the shape of proteins which is in many cases sufficient to understand the working principle of enzymes (biological catalysts).

In the case of layered structures, no matter if they are artificially prepared magnetic sensor structures or biological membranes, specular reflectometry is the method of choice to reveal layer composition, density, and thickness as well as the interfacial roughness. Additional structural information parallel to the plane of the layers can be obtained from measuring off-specular scattering during the reflectivity measurement.

Last, but not least, the sensitivity of the neutron's spin to the magnetic environment is the most efficient tool to determine magnetic order phenomena on atomic length scales. Magnetic superstructures of e.g. antiferromagnetically ordered compounds are readily observed by powder diffraction. Single crystal diffraction, SANS, or reflectometry reveal further information about the direction of the magnetization orientation within the sample structure. Together with the used of polarized neutrons and polarization analysis, detailed information about size, direction, and periodicity of the magnetic structure inside the sample under investigation is available.

IV.11.2 Inelastic scattering

Inelastic neutron scattering provides unique information about dynamic properties of condensed matter. Computer modeling of the inelastic neutron scattering cross sections allows one to obtain parameters of model Hamiltonians, such as inter-atomic forces or exchange constants, which enable the prediction of the macroscopic response of a material and thus lead to a microscopic understanding of the relation between structure and function. Neutron spectroscopy gives direct access in absolute units to self-, pair-, and spin-correlation functions, which are the fundamental quantities derived by modern ab-initio theories. Thus, the simplicity of the neutron cross sections and the fact that they can be measured on an absolute scale allows benchmarking of ab-initio theories and computer modeling with huge impact in many different scientific fields. In this important aspect, neutrons are unrivalled, as no other method can provide such a stringent test of microscopic theories. It is true that particular problems can nowadays be addressed with modern synchrotron radiation techniques: steep phonon branches can be determined with high resolution ($\approx$ 1 meV) inelastic x-ray spectroscopy; element specific partial phonon density of states can be measured for certain elements by nuclear resonance scattering; slow dynamics in colloids can be followed by coherent x-ray correlation spectroscopy; and high energy magnon dispersions by resonant inelastic x-ray scattering (RIXS). All these x-ray techniques are largely complementary to inelastic neutron scattering, but none of them gives the same direct and universal access to absolute scattering functions

as does neutron spectroscopy. To give an example: due to the restricted resolution, RIXS can only be used to determine relatively high energy magnetic excitations. But due to the resonance process involved, with its unknown transition matrix elements, RIXS cannot provide a model-free access to the eigenvectors, which neutrons naturally do. For these quite general arguments, neutron spectroscopy will remain essential and unrivalled for many decades to come.

At pulsed sources the neutron time-of-flight is typically used to encode the neutron energy. One distinguishes direct and indirect geometry spectrometers. In direct geometry spectrometers, the sample is illuminated with neutrons of well defined energy prepared by an energy filter during a short period controlled by a neutron chopper. The energy filter can be realised as a crystal monochromator or a series of choppers and pulsed neutron sources. The final energy after interaction with the atoms in the sample is determined by the time-of-flight from the sample to detector. In indirect geometry spectrometers, the sample is illuminated continuously by the white beam from the moderator. The final neutron energy is given by an energy filter placed between sample and detector. The arrival time at the detector yields the information about the initial neutron energy before interaction with the sample.

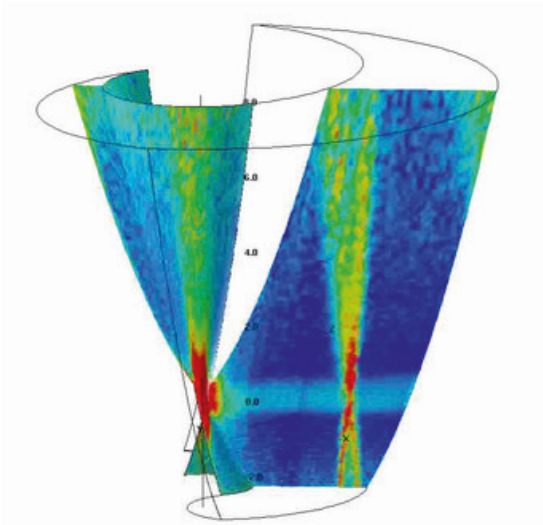

Figure IV.10: *Magnetic excitations in a layered Manganite*

On the modern pulsed sources, both types of time-of-flight spectrometers are operated providing excellent energy resolution in a wide energy range. Equipped with position sensitive detectors, direct geometry chopper spectrometers are also used to investigate coherent excitations in condensed matter - such as phonons or magnons - to cover the scientific case that is served by three axis spectrometers at reactor sources. Recently, new proposals have been presented to achieve good momentum transfer resolution and coverage also on indirect geometry instruments [53, 54, 55]. Typical sample fluxes vary between $10^5, 10^6$ neutrons per cm^{2}s for the direct geometry instruments, and $10^7 - 10^9$ neutrons per cm^{2}s for the indirect geometry instruments, respectively.

On the other hand there is also a large number of very successful ToF spectrometers on continuous neutron sources. They benefit from the fact that the repetition rate can be adjusted to match the dynamic range of the excitation spectrum under study. For spallation sources with the low repetition rates ≤ 60 Hz, typically less than 10 % of the time between the pulses contains usable data, if ones does not make use of techniques such as RRM or Multi E_i mode. In other words, the duty cycle of the secondary spectrometer is only 10 %. At a continuous source, the duty cycle of the primary spectrometer amounts typically to a few percent, but as the repetition rate can be freely adjusted to the requested dynamic range, the duty cycle at the detector approaches 1. Therefore IN4C and IN5 at the ILL still provide a monochromatic flux as high as the instruments at the MW spallation sources. The continuous illumination of the monochromator enables also the use of time focusing, which optimizes the energy resolution in a energy region of interest on the cost of relaxing the resolution for the remainder of the dynamical range. At spallation sources this trick can not (hardly) be applied, as the rather large distances and short pulse lengths define typically a very narrow λ resolution.

Thanks to the low energy nuclear reactions involved in the neutron release, the shielding around the target at the compact sources can be much lighter as compared to spallation sources. This allows a very compact design of the instruments, which can also profit from the proton pulse length matched to the neutron moderation time to increase the flexibility of the instruments and reduce the cost. Furthermore, the HBS features repetition rates matching the requirements in particular of direct geometry time-of-flight spectrometers and narrow band indirect spectrometers, which are typically one order of magnitude larger than the repetition rate of spallation sources.

IV.11.3 Analytics

Neutron based analytical techniques such as Neutron Activation Analysis (NAA), Neutron Depth Profiling (NDP) and Neutron Imaging (NI) (see Section IV.11.4) are non-destructive key techniques for the characterization of materials or items of various origins (geological, environmental, biological, pharmaceutical, cultural, archaeological, palaeontological, cosmological and industrial).

Neutron Activation Analysis is a well established analytical technique at research reactors for the determination of the elemental composition of solid, liquid or gaseous samples. NAA is based on the measurement of isotope specific gamma radiation induced by the interaction of neutrons with atomic nuclei. Depending on when the gamma radiation is measured, NAA falls into two types: (a) Prompt Gamma Neutron Activation Analysis (PGNAA), where the measurement of prompt gamma radiation emitted from nuclei in an excited state is performed during sample irradiation [56] or (b) Delayed Gamma Neutron Activation Analysis (DGNAA), where the measurement of delayed gamma radiation emitted during the radioactive decay of activation products takes place after sample irradiation [57]. In both cases, the detection of gamma rays is achieved with high purity germanium detectors (HPGe-detectors) which are cooled electro-mechanically or with liquid nitrogen and surrounded with an appropriated passive or active shielding.

PGNAA is performed with guided cold neutron beams from research reactors like, for example, FRM II (Forschungs-Neutronenquelle Heinz Maier-Leibnitz) or BRR (Budapest Research Reactor).The equivalent thermal neutron flux at sample position are 2 10^{9} - 5 10^{10} cm^{-2} s^{-1} at FRM II [58] and 7 10^{7} - 1.2 10^{8} cm^{-2} s^{-1} at BRR [59]. The masses of the analyzed samples are typically between 10 mg and 1 g.

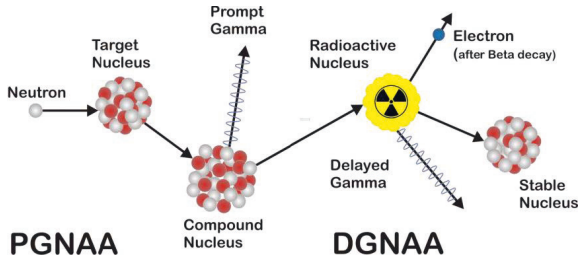

Figure IV.11: *PGAA and NAA mechanism*

PGNAA allows a panoramic analysis of samples, since all elements, excepted helium, emit prompt gamma rays. It is particularly useful for the accurate detection of light elements for which not many non-destructive analytical techniques are available. PGNAA is an unique method to determine the hydrogen in any kind of samples with a detection limit at ppm level or below and at the same time to provides the elemental content (for example, pollutants) of the investigated sample. It is highly sensitive for certain elements such as boron, cadmium, mercury and rare earth elements which can be detected at ppb level. Furthermore, PGNAA may be used for in-situ investigation of chemical processes like catalytic reactions [60]. Large objects may be investigated to some extents by PGNAA using cold or thermal neutron beam [61].

However, neutrons of higher energy are of a better choice for the analysis of large and thick items due to their higher penetration depth. For this reason, a new PGNAA method using fission neutrons delivered by the SR10 beam guide of FRM II with a flux of 1.0 10^{8} cm^{-2} s^{-1} is in development to perform sensitive and accurate analysis of large and thick items [62]. This method is based on the measurement of isotope specific prompt gamma rays induced by fast neutron inelastic scattering reactions.

In the case of DGNAA, the sample is exposed first to a high thermal neutron flux in a research reactor or in an intense neutron beam. For example, FRM II offers thermal neutron fluxes between 5 10^{12} and 1 10^{14} cm^{-2} s^{-1} depending on the irradiation position. At BRR, thermal neutron fluxes are 2 10^{13} and 5.7 10^{13} cm^{-2} s^{-1}. The TRIGA reactor of the Johannes Gutenberg Universität Mainz delivers thermal neutron fluxes between 7 10^{11} and 4 10^{12} cm^{-2} s^{-1}. The masses of samples are usually between 1 and 100 mg. After irradiation and a given waiting time, the sample is transferred to a gamma-ray spectrometer for determination of the activity of activation products. The determination of light elements is difficult since they cannot be well activated. DGNAA is highly sensitive for the determination of sodium and manganese also for scandium, cobalt, and gold, as well as for the rare earth elements. For many elements the detection limits are in the range of ppb. The sensitivity can be further improved when combined with radiochemical separation.

PGNAA and DGNAA are complementary in the analysis of typical major and trace elements. Both methods may be apply for the characterisation of large amount of materials ($>$ 100 kg) using fast neutron pulse sources like neutron generators, where the delayed gamma rays of short-lived activation products induced by fast neutrons are additionally measured [63].

The HBS pulsed neutron source will allow one to perform time resolved prompt and delayed gamma neutron activation analysis with the neutron time of flight technique (TOF-P&DGNAA) to determine the elemental composition, in particularly of heterogeneous samples. This method will provide sample depth resolved information by measuring prompt gamma rays induced by neutrons with various energies (10 eV to 2 meV) having different sample penetration depths and therefore interrogating different sample volumes. The depth resolution depends on the total macroscopic neutron cross section of the sample and on the neutron energy resolution. Furthermore, by performing PGNAA with resonance neutrons (10 eV to 10 keV), the sensitivity for the detection of a specific element may be enhanced or gamma-rays of interfering elements may be suppressed as demonstrated in [64].

Neutron Depth Profiling (NDP) is a non-destructive analytical technique to determine the concentration of some isotopes as a function of the depth in the near-surface region (some micrometres) of a sample [65]. NDP is based on the detection of prompt energetic charged particles emitted during the absorption of cold or thermal neutrons by isotopes such as ^{3}He, ^{6}Li or ^{10}B. Sample neutron irradiation and particle detection take place in a vacuum chamber at a pressure less than 10^{-2} Pa. The number and residual energy of the particles that escape the sample surface are determined using surface barrier detectors, PIN photodiodes or microchannel plates. The recorded charged particle energy spectrum reflects the entire depth profile bounded by the range of the charged particles. The depth corresponding to the energy loss for the emitted particle is estimated from the characteristic stopping power of the material using the SRIM (Stopping and Range of Ions in Matter) [66] software package. The depth resolution varies from a few nanometres to a few hundred nanometres. Depending on the isotope the limit of detection ranges between 10^{11} to 10^{16} atoms cm^{-2} for a neutron intensity of about 10^{9} s^{-1}.

Application fields of NDP are alloys, ceramics, semiconductors, thin films, electronics devices, energy storage systems and brain research. Most recent, NDP has gained a lot of interest due to its sensitivity to the isotope ^{6}Li, as Li is a key element of currently widely spread lithium-ion batteries. NDP provides insight on new developments in the field, i.e. rechargeable lithium-ion batteries with solid electrolytes. Because of the sensitivity to ^{2}2Na isotope, NDP could be also applied to studies of the most promising candidate to replace commercial lithium-ion batteries – all-solid-state sodium-

ion battery. For example, NDP is carried out at FRM II using the PGNAA cold neutron beam line in particularly to investigate and optimize the performance of lithium batteries [44].

IV.11.4 Imaging

Neutron imaging is a technique used for non-destructive investigation or quality control of complex devices on a scale from 100 μm up to some 10 cm. A divergent neutron beam originating from a small source point impinges on the sample and the undisturbed, transmitted beam is recorded by a 2D position sensitive detector. The contrasts in the "photo" recorded show all structures inside the sample that have attenuated the neutron beam.

Neutron imaging is a real-space technique. It resolves structures on length scales above the pixel size of the detector system in use which can go down to some μm. The attenuation of the neutrons can happen either by absorption or by scattering. The absorption contrast is important for elements like B, Li, or Cd, while scattering is a very important process for H containing materials and for every crystalline matter especially for wavelengths slightly below a Bragg edge. For this reason, neutron imaging is technologically relevant to check organic materials embedded in a metallic environment, e.g. lubricants inside a motor or water induced corrosion inside a steel construction. However, science cases include a vast range of areas like in particular geology, construction materials, porous materials, engineering materials, liquid metals, plant sciences, magnetism and cultural heritage.

Depending on the size of the structure under investigation the energy of the neutron beam can be chosen to have a penetration depth appropriate to the attenuation power of the entire sample. Fast neutrons (energy $>$ 100 keV) are used to image entire machines up to 1 m in size, while cold neutrons (energy $<$ 1 eV) are used to image materials and devices with dimensions of centimeters.

A series of neutron images together with a rotation of the specimen inside the beam gives the opportunity to reconstruct the 3-dimensional structure. This method is called neutron tomography.

Resolution of the neutron wavelength in the cold neutron regime around the Bragg edges of the material under investigation allows one to image regions with different crystalline structures. This is of interest e.g. in the steel production, where the mixture and order of martensitic and austenitic phases determines important mechanical properties of the material.

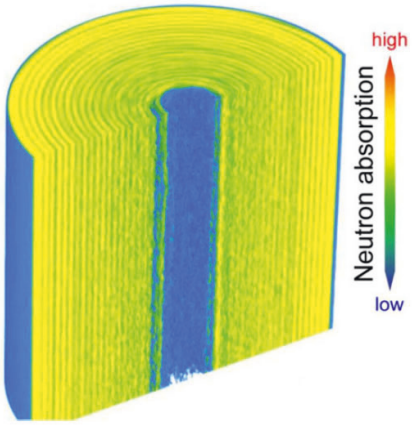

Figure IV.12: *Neutron tomography reconstruction of the interior of cylinder-type Li-ion battery. Absorption levels are visualized by assignment to different colours [67, 68].*

Neutron imaging at a high brilliance source has a few important advantages compared to neutron imaging at a continuous source. On the one hand it is possible to use a beamline that allows one to extract fast neutrons as well as thermal and cold neutrons. So all contrasts for thick and thin structures are available with a single exposure. In addition, the time-of-flight technique allows one to resolve the Bragg edges for free, without any loss in intensity, just by using a time-resolving detector system. No additional monochromatization of the beam is necessary. The small source size and the short length of the beam extraction system are perfectly appropriate for an imaging

beamline. A large divergence of the beam originating from a small source point can be used to receive high-resolution images on a large area, only limited by the detector size, but not by any optical devices needed for the beam transport.

IV.11.5 Irradiation

A number of areas including High Energy Physics (HEP), nuclear medicine and space applications claim demand on dedicated irradiation facilities for the purpose of

- radiation protection (shielding-benchmark experiments) such as those required for space missions and the colonization of the Moon and Mars;
- oncology (direct neutron treatments of certain types of tumors; exposure to secondary neutrons; Boron Neutron Capture Therapy, etc.)
- manufacturers/users of radiation instrumentation and dosimeters (energy response and calibration);
- high-energy and nuclear physics (cross-section data for basic science, MC code development and nuclear applications such as accelerator-driven subcritical fission reactors, transmutation of radioactive waste, online quality control and contraband detection).

Atmospheric neutrons in the 1-10 MeV range comprise 41% of the fast atmospheric neutrons (En $>$ 1 MeV). For this reason, specialized neutron irradiation facilities at compact lower energy accelerators may prove to be of considerable use for digital electronic Industry (semiconductor companies and IC users) to study the sensitivity of devices to these lower energy neutrons. Instead, hard errors such as SEL and SEB typically need higher energy neutrons (E $>$ 100 MeV). Nuclear reactors, although an intense source of neutrons, are of limited interest for SEE studies because the continuous energy spectrum of reactor neutrons does not extend to high energies. Of greater interest are i) broad-band, continuous energy spectrum facilities, that use thick targets to produce an energy spectrum as similar as possible to that of the atmospheric neutrons and ii) narrow band, quasi mono-energetic (discrete) neutron sources using thin Li or Be targets.

Normally, measurements at continuous (broad band) energy facilities are insensitive to any energy dependence effects in the accessible neutron energy range. To highlight or disentangle particular aspects of the radiation effects, narrow band tests, if available, are used. An acceleration factor F $= 1 \times 10^9$ corresponds to an integral neutron flux of $\Phi_{<1MeV} \sim 2 \times 10^7$ n cm^{-2}s^{-1} and implies that one hour of irradiation is equivalent to 3000 years of exposure at flight altitudes. Such a neutron field can be achieved with few μA of current for some tenth of MeV proton energy.

Proton beams with E $>$ 20 MeV are sometimes used as substitutes for neutron SEU tests. Protons, to be able to penetrate a nucleus, have to overcome the Coulomb barrier, but altogether the SEE induced by neutrons and protons with the same kinetic energy are expected to become increasingly similar in the region of a few tens of MeV, upwards: the total nuclear reaction cross sections beyond 50 MeV are very similar.

Lower energy CANS facilities have the potential to be of great use for irradiation test facilities for Industry. Non-standard specialized, accessible, and user-friendly facilities, would be very useful for small/medium electronics industries to check their innovative products for any unexpected sensitivity to lower energy neutrons, especially in the development and engineering phases that lead up to the final standard and expensive validation (certification) phase at the higher energy facilities.

From the perspective of academia, the field of radiation effects, in particular neutron (proton) induced SEE, is a multidisciplinary activity as it involves nuclear, solid state, and device physics. In

addition, when testing physics models and simulations (academic research) it is preferable to check the predicted rates of simple test structures.

Irradiation facilities based on CANS offer versatile options to overcome the lost of regional neutron facilities at affordable cost. Because of their versatility, they are a complement to large scale facilities. CANS can provide continuous beam for irradiation and, having the neutron spectra well characterized. It can be used for irradiation material tests (being it electronics or shielding materials) and to perform accurate integral cross section measurements. Integral cross section measurements are strongly requested by the main international agencies such as IAEA and NEA (www.oecd-nea.org) for nuclear medicine and reactor physics applications, and from KADoNIS (www.kadonis.org) for fundamental physics applications.

IV.11.6 Isotope production

Radioisotopes are used worldwide for various purposes in medicine, industry and science [69]. Application fields of radioisotopes in medicine are nuclear diagnostic imaging (gamma imaging with ^{99m}Tc, ^{131}I, ^{133}Xe ^{67}Ga, ^{81m}Kr, ^{111}In, ^{123}I and ^{202}Tl, positron emission tomography with ^{18}F ^{11}C, ^{13}N, ^{15}O, ^{68}Ga, ^{57}Co, ^{133}Ba and ^{137}Cs , bone density measurement with ^{125}I, ^{153}Gd and ^{241}Am and gastric ulcer detection with ^{14}C), radioimmunoassay with ^{125}I, ^{3}H and ^{57}Co, therapeutic techniques (radiopharmaceutical applications with ^{131}I, ^{32}P, ^{90}Y, ^{188}Re and ^{169}Er and palliative care with ^{90}Y, ^{177}Lu, ^{131}I, ^{153}Sm and ^{213}Bi), radio-therapy with sealed sources (remote-controlled cobalt therapy with ^{60}Co, brachytherapy with ^{137}Cs, ^{192}Ir, ^{103}Pd, ^{125}I, ^{106}Ru and ^{198}Au) and irradiation of blood for transfusion with ^{137}Cs and ^{60}Co.

Industrial use of radioisotopes covers following applications: nucleonic systems (physical measurement gauges with ^{60}Co, ^{137}Cs, ^{241}Am, ^{85}Kr, ^{90}Sr/^{90}Y, ^{147}Pm, ^{14}C and ^{204}Tl, on-line analytic with ^{241}Am, ^{252}Cf and ^{63}Ni, pollution measurement with ^{14}C and ^{147}Pm, home-land security with ^{252}Cf, smoke detectors with ^{241}Am, laboratory or portable analytic systems with ^{55}Fe, ^{57}Co, ^{109}Cd, ^{241}Am, ^{137}Cs, ^{252}Cf, irradiation and radiation processing with ^{60}Co (sterilisation of medical supplies, of pharmaceuticals or food packages, food irradiation, plastic curing), radioactive tracers (chemical reactions efficiency, mass transfer in industrial plants, behaviour of pollutants) and non destructive testing (gamma radiography with ^{192}I, ^{60}Co, ^{75}Se and ^{169}Yb, and neutron radiography with ^{252}Cf).

Research and development in the fields of medicine, industrial processes, environmental protection and biotechnology involves a wide range of radioisotopes such as ^{103}Pd ^{125}I, ^{18}F, ^{32}P, ^{90}Y, ^{188}Re, ^{166}Ho, ^{192}Ir, ^{57}Co, ^{119m}Sn, ^{125m}Te, ^{151}Sm, ^{22}Na, ^{46}Sc, ^{51}Cr, ^{113}In, ^{147}Nd, ^{182}Ta, ^{192}Ir, ^{198}Au, ^{33}P and ^{35}S. Due to the emergence of new technologies and processes some radioisotopes may become obsolete and new ones introduced.

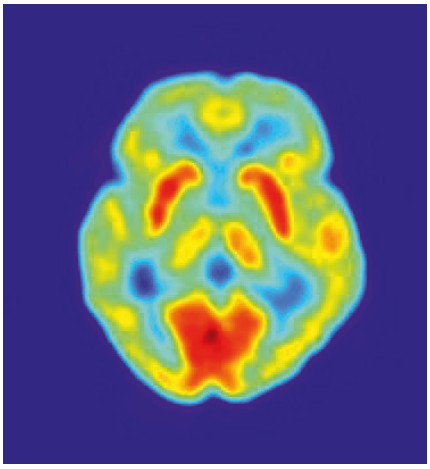

Figure IV.13: *Positron emission tomography (PET) scan of human brain [70] (Picture: Jens Langner)*

The radioisotopes are produced in dedicated reactors or accelerators, in multi-purpose research reactors or in nuclear power plants (for ^{60}C and ^{3}H mainly) [71, 72]. Neutron rich isotopes are

produced in reactors by thermal neutron irradiation and neutron-deficient isotopes by using proton, deuteron or alpha accelerators. The production of radioisotopes may be achieved also using a compact accelerator neutron source with a dedicated target station furnished with sample irradiation positions [73]. The radioisotopes ^{166}Ho and ^{188}Re were produced with neutron activation yields suitable for medical imaging and brachiterapy studies by using a 40 MeV cyclotron and a beryllium target embedded in a lead buffer/graphite reflector assembly for neutron production [74]. Accelerator based neutron sources represent an alternative to reactor in particularly for the production of ^{99m}Tc via its precursor ^{99}Mo. Various accelerator-based methods were already proposed to generate ^{99}Mo with thermal neutrons ^{98}Mo(n,γ)^{99}Mo) [75], fast neutrons ^{100}Mo(n,2n)^{99}Mo) [76] or by fission of low enriched uranium in a water-based solution (https://shinemed.com/demonstrated-technology). Nevertheless the production of radioisotopes with a high activity requires high current accelerators.

IV.11.7 Particle physics

Slow neutrons play an important role as a tool and an object of investigation, addressing key questions of particle physics and cosmology at the low-energy, high-precision frontier, complementary to the high-energy frontier probed at particle accelerators [77]. The current science program is mainly pursued at high-flux neutron sources. It covers a wide range of topics and has the general goals to improve the knowledge of important parameters of the Standard Model (SM) of particle physics, and to search for new physics beyond. The latter include searches for new fundamental forces, dark matter, dark energy and extra dimensions, as well as symmetry violations needed to explain the matter-antimatter asymmetry of the Universe. To achieve these goals requires accurate measurements of key observables in neutron beta decay, neutron gravity, as well as studies of electromagnetic properties of the neutron, for which the search for a non-vanishing electric dipole moment is a prominent example.

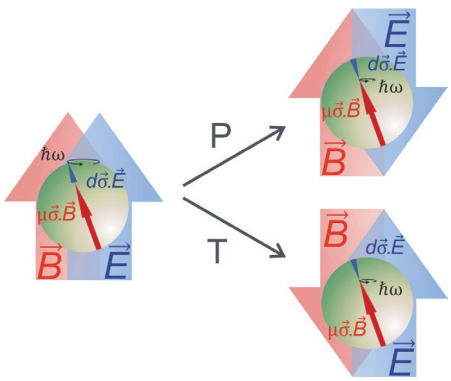

Figure IV.14: Pictogram illustrating the P and T-violation of a nEDM in the presence of an electric and magnetic field [78].

Studies of neutron interactions with the atomic nucleus complement this research, for instance in investigations of the purely hadronic weak interactions and in alternative searches for time reversal invariance violation beyond the SM mechanism. Ultra-cold neutrons (UCNs) have become increasingly popular in such investigations. Moving at only a few m/s, they can be trapped by neutron optical, magnetic and gravitational potentials. With this property they are particularly well suited for accurate experiments that exploit long times for UCN storage and exposure to external fields. Among several methods to produce them, down-conversion of cold neutrons in superfluid helium is pursued at various accelerator based neutron sources laboratories as a promising route to enhance currently available UCN production rates and densities [79, 80, 81]. To this end, the conversion vessel surrounded by suitable pre-moderators is implemented close to the target, where the primary cold flux is typically by three orders of magnitude larger than at an external beam. For the beam power of the HBS, heat loads on the converter due to radiation are still manageable, so that operation at temperatures below 0.7 K becomes feasible, where the saturated UCN density reaches its maximum. It has been shown [81] that at the LENS facility in Indiana, i.e., a source with considerably weaker beam power than planned for the HBS, UCN densities exceeding 1000 UCNs per ccm

can be achieved, which exceed currently available densities by two orders of magnitude and are competitive with projected in-beam UCN sources at high-flux facilities. Obviously, the HBS has the potential to deliver conditions to pursue an ambitious research program with UCNs. Noteworthy is also that large benefit can be expected from development of pre-moderators able to shift the spectrum towards 8.9 Å wavelength, where UCN production in superfluid helium becomes most efficient via the single-phonon process. Due to the limited heat load, at the HBS cooling of the pre-moderator to liquid-helium temperatures is not an issue.

Cold neutron fluxes at a beam facility for fundamental physics at the HBS on the other hand will stay below performances available at an intense beam of a high-flux facility. To attain the necessary counting-statistical sensitivity, high-precision experiments with cold neutrons are therefore also in future to be performed there. Note that the instrument PF1B at ILL currently provides the only beam for this application in Europe. The HBS can nonetheless offer important benefits to this field of research. Large experiments are usually prepared by university groups in their home laboratories and can often not been tested and optimized with neutrons prior to a beam time at highest flux. The availability of a dedicated beam at the HBS would enable tests of new experimental concepts and developments of technologies, including neutron guiding, collimation, polarization, detection of neutrons and decay particles, shielding of backgrounds etc. A neutron beam for this purpose will be an invaluable asset to reach the ultimate performance of experiments and hence optimize the duty cycle and the scientific output of large neutron facilities.

IV.11.8 Nuclear spectroscopy

The use of high-purity germanium (HPGe) detectors assembled in efficient arrays and covering a large solid angle has become a common tool in nuclear spectroscopy since the 1980s [82]. Due to the high resolution and the possibility to exploit coincidences, it is possible to understand even complex level schemes, or to obtain high isotopic selectivity. Information on angular correlations [83] and/or polarization [84] of γ-ray transitions can be obtained, providing the possibility to assign spin and parities to nuclear states. Using additional fast LaBr3:Ce-scintillators it is possible to measure nuclear state lifetimes in the range of a few pico- up to microseconds [85]. Mainly two types of neutron-induced reactions are of interest: (i) Nuclear structure studies using the (n,γ) reaction close to the valley of stability. High-precision experiments profit from clean spectra and high statistical sensitivity allowing to carry out angular correlation and polarization measurements. (ii) Neutron-induced fission is a very efficient way to produce neutron-rich nuclei in the mass range of $85 < A < 160$ and represents a complementary approach to other fission reactions. Spectroscopy carried out directly at a neutron beam allows investigation of prompt γ rays, which can be associated to particular isotopes by multiple coincidences (of γ rays from the isotope and/or the complementary fission product) or by using additional fission product spectroscopy. Examples of the high scientific impact and interest in neutron-induced nuclear physics is demonstrated by the recently carried out EXILL campaign at ILL [86], campaigns at the LICORNE neutron source of the IPN Orsay [87], and the installation of the FIPPS instrument at ILL [88] In the future, this instrument will be combined with a gas-filled magnet for studying fission and performing fission product spectroscopy [89]. An efficient large detector array is also used at the Accurate Neutron-Nucleus Reaction Measurement Instrument (ANNRI) of J-PARC, looking for angular correlation and time reversal violation studies [90].

The neutron beam necessary for this kind of studies needs to be well collimated to low divergence, at the order of 15 mm diameter over a meter of flight length. This is achieved at the ILL by collimating a thermal or cold beam by a sequence of apertures to a pencil beam with a capture equivalent flux of 10^8 n cm^{-2} s^{-1}. Nuclear spectroscopy experiments are limited by the total count rate, for which Germanium detectors still provide good resolution. In most cases, maximum count rates of $5 - 10$ kHz per channel are chosen by adapting the target mass to the available neutron flux, for which signal pile-ups that degrade the spectroscopic resolution are still on an acceptable level. These signal

rates can thus also be achieved at significantly weaker neutron beams. The HBS offers additional features interesting for nuclear spectroscopy studies:

- The timing of the pulse structure of the source can be combined with the event-mode data acquisition of the detectors. This allows distinguishing prompt from delayed events due to β-activity. This is in particular interesting in fission experiments, where a large fraction of the β-activity is due to the excited fission fragments. The pulse structure also helps to suppress other types of backgrounds and thus to enhance the signal-to-noise ratio.

- A second specific feature would be the possibility to tune the neutron spectrum via a dedicated moderator. This would enable to populate nuclear resonances, which offer additional spectroscopic information. Certainly, it is of high interest for neutron-induced fission studies to have a neutron beam with variable energy.

IV.11.9 Neutron interferometry

A quite unique application of neutrons is interferometry [91] based on Mach-Zehnder devices made of single crystals. Typically, three crystal blades of a few mm thickness are needed to achieve interference of diffracted beams. More complex interferometers, including several interference loops, exist too. Between splitting and re-combination, two components of the wave functions of each individual neutron are separated by several centimeters. This system provides a unique test bench for quantum mechanics test and searches for new physics. Another important application is accurate measurements of neutron scattering lengths.

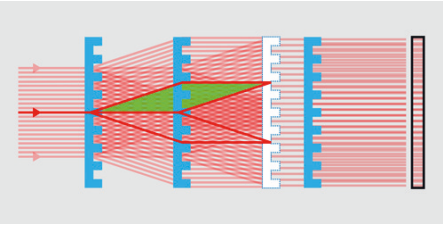

Figure IV.15: *Newly developed moiré neutron interferometer with three silicon phase gratings (G1, G2, G3) [92] (Graphic: APS/Alan Stonebraker)*

To maintain spatial and time coherence of the wave function puts stringent conditions on the location and stability of the crystal blades. They are currently achieved by cutting all three blades out of a single crystal ingot. This limits the size of available interferometers and therefore also the sensitivity of most experiments which is proportional to the area enclosed by the two beam paths. Also the scope of applications depends on the size of objects which can be inserted in a partial beam. Another limitation is due to an interplay of count rate and systematic drifts of the interferometer. The size limitation could be overcome by changing to an interferometer scheme consisting of independent crystals, provided that they are held with nowadays feasible sub-nanometer/sub-nanoradian precision. This requires a dedicated low-noise experimental environment which seems compatible with a HBS facility.

At the HBS, a substantial statistical gain could also be achieved by installing the interferometer at an end-position of a neutron guide equipped with a monochromizing deflector. This would eliminate the need for a separate crystal monochromator, since the first blade of the interferometer would fulfill this function, giving two major benefits. It will improve i) the interferometer crystal acceptance so that a higher diffraction throughput could be achieved and ii) the time stability since a monolithic setup of diffracting objects ensures best possible conditions with respect to temperature gradients and angular misalignments. In combination with the time structure of the source, allowing an additional wave length discrimination by TOF, the scope of application of neutron interferometry is expected to be enhanced along with an improved signal-to-noise ratio. Other applications of the same setup

are neutron polarimetry or ultra-small angle scattering (USANS) which extends SANS techniques to larger structures in the micrometer range.

Again, the flexibility of an HBS type source allows to accommodate a community of scientists working in particle physics, nuclear spectroscopy or neutron interferometry by offering a dedicated source with moderators optimised to the specific requirements of this experimental technique.

V.
CONCEPTUAL DESIGN

The HBS neutron source is designed to be a user facility that offers a variable suite of neutron instruments (see Chapter VI) for all scientific applications of neutron scattering, imaging and analysis. Compared to present-day facilities, excluding the MW spallation sources, it will offer leading capabilities at all of its instruments. In contrast, the flagship MW spallation sources offer unique capabilities for specific experiments, but cannot provide the full breadth needed by a very diverse community.

HBS is a pulsed accelerator-based neutron source where the neutrons are produced by a pulsed proton beam impinging on a metal target. The instruments are grouped around several target stations operating at different frequencies and pulse length to offer optimized neutron pulse structures for the various instrument classes. Dedicated thermal and, where necessary, cold moderators are used to adjust the neutron spectrum supplied to each instrument.

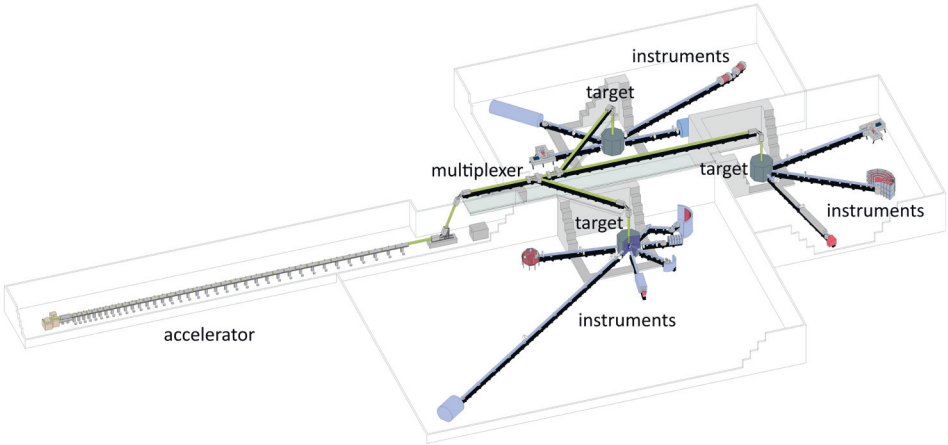

Figure V.1: *General layout of the accelerator-based high brilliance neutron source facility*

Thus, the main components of the HBS facility are:

- a dedicated proton accelerator with optimised energy (up to 70 MeV) and current (100 mA). The proton current is multiplexed to feed several target stations which are operated at different frequencies and pulse structures,

- target–moderator-reflector combinations that offer pulsed neutron beams at optimal frequency and pulse duration to fulfil the needs of the instruments,
- optimised moderators according to the spectral needs of every individual instrument, and
- a number of instruments at each target station, initially up to 6, in order not to dilute the thermal neutron flux density at the point of beam extraction.

The asset of the HBS design comes from a fundamental change of paradigm by:

- a consequent maximization of brilliance instead of source strength, leading to outstanding performance while keeping cost of construction and operation low: "produce less neutrons, but use them more efficiently",
- making the neutron source an integral part of every single instrument. A target station with optimal pulse structure and a dedicated moderator is chosen for every beamline instead of compromising pulse structure and moderator to serve all instruments: "fit the neutron source to every single instrument, not the instrument to the source in the present-day concept of "one has to fit all"" ,

A particular technical novelty of the HBS concept is an equal proton beam power at each target station. This is achieved by an appropriate proton beam multi-pulse structure within the accelerator allowing variable duty cycles at each station. This variability permits further upgrades at individual target stations and instrumentation. While the reference design foresees three target stations, further target stations, e.g. for exclusive industrial use or specific applications such as ultra-high field, can be added later on. The relative simplicity of the target and the compactness of the moderators allow for later increase of proton current and relative simple exchange of moderators and beam extraction systems, as their technologies advances.

The technical outlines and parameters of all of these components are described in the corresponding sections.

V.1 Neutron production

In a Compact Accelerator-driven Neutron Source (CANS), the production of neutrons is based on the interaction of light ions such as protons or deuterons with the atomic nuclei of a dedicated target material. However, a maximisation of the neutron yield may be achieved by selecting the target material to fit the type and energy of the ion under consideration. The results of this optimization are published in [93].

For that, we analytically calculate first the neutron yield for each element of the periodic table from lithium to lead and for primary ion energies ranging from 1 to 100 MeV by using the corresponding cross sections for proton and deuteron reactions given in the database TENDL2017 [94]. The required thickness of the element for the full stopping of the ions is calculated with the software SRIM (Stopping and Range of Ions in Mater) [66]. The method to analytically calculate the neutron yield, the tritium production and the total induced activity owing the interaction of protons and deuterons with a given element, is presented in Appendix A.1.

The dependence of the neutron yield on the atomic number Z of the element and the primary ion energy is shown for protons in Figure V.2. It indicates that a competitive high neutron yield may be achieved for primary ion energies greater than 70 MeV up to 100 MeV and high-Z elements ($70 \leq Z \leq 82$). Within this range the neutron yield varies between 9 and $22 \cdot 10^{14}$ s^{-1} mA^{-1} for protons and 10 and $27 \cdot 10^{14}$ s^{-1} mA^{-1} for deuterons, respectively. These values are 2 to 3 times higher than

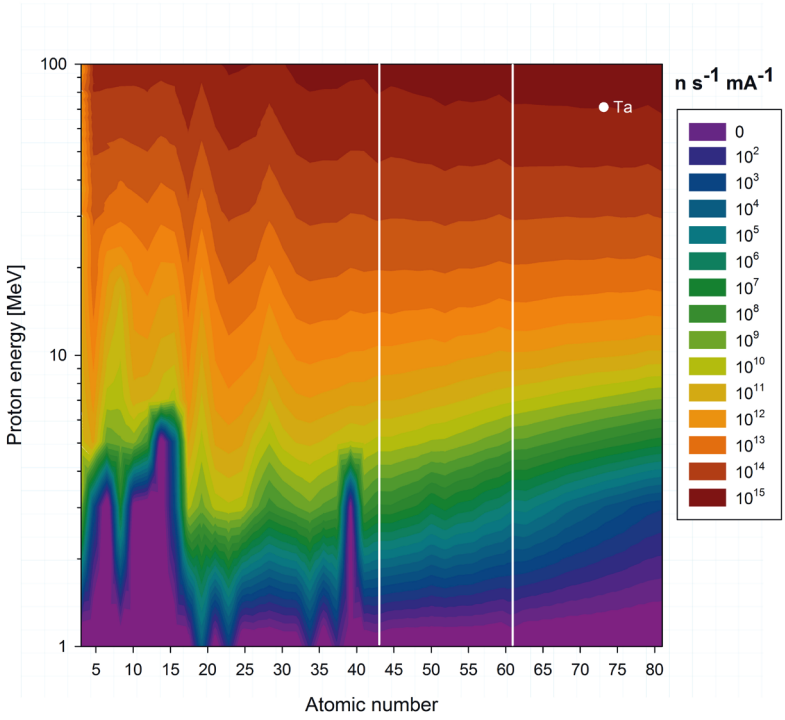

Figure V.2: *Dependence of the neutron yield for protons on the atomic number Z and the primary ion energy. White lines: Tc and Pm, white dot: Ta at 70 MeV*

the neutron yield achieved for the same ion energy range with beryllium, an element commonly proposed as a target. For high Z-elements, the neutron production yield from deuterons is 10% to 20% higher than the neutron production yield from protons. Additionally, deuterons have a larger stopping power than protons, which allows thinner targets to be employed and thus reduces the temperature difference inside the material [95]. However, for the HBS reference design, we decided that the increased neutron yield and the reduced target temperature difference do not justify the operation of a high current deuteron accelerator, which requires a much higher level of complexity in accelerator design and increased measures of radio protection, in comparison to a high current proton accelerator.

The choice of the target material within the 70 - 82 Z-range, where neutron yields for different elements are very similar, will be done based on the requirements of the mechanical properties as described in Section V.5.1.

V.2 Accelerator

V.2.1 Top level requirements

The High Brilliance Neutron Source belongs to the Compact Accelerator Based Neutron Sources (CANS) class. The term "compact" must be seen here in comparison with spallation sources, which typically require an order of magnitude higher beam energy. The driver accelerator for HBS must

be able to reliably accelerate a 100 mA proton beam to an energy of 70 MeV. The beam is sent pulse-by-pulse to three different targets by means of a multiplexer in the High Energy Beam Transfer (HEBT) section. Each individual proton beam behind the multiplexer has a specific time structure in order to optimally serve the different instruments grouped around one target station. The macro pulse lengths result from experimental requirements and are fixed at 52 μs, 208 μs and 833 μs.

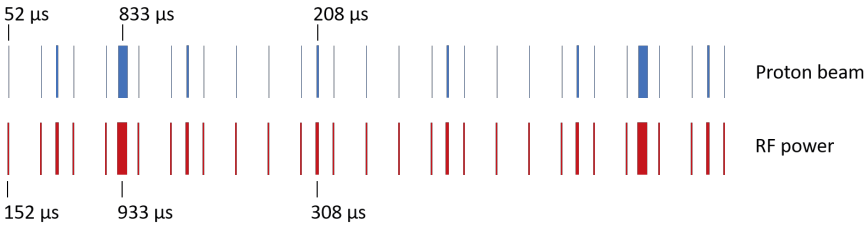

Figure V.3: *Pulse scheme of the HBS linac showing pulses of the three different frequencies of 24 Hz (pulse length 833 μs), 96 Hz (pulse length 208 μs) and 384 Hz (pulse length 52 μs) to be delivered. The spacing in time between the short proton beam pulses is 2.548 ms (384 Hz). The longer pulses are centered between these short pulses. The pulses of the RF power supply always begin 100 µs earlier than the proton pulses.*

The minimum power requirement per target is 100 kW average power. The repetition rates were adapted to the pulse lengths in order to obtain the same average power. With the fixed values of 384 Hz (t_1=52 μs), 96 Hz (t_2=208 μs) and 24 Hz (t_3=833 μs), a maximum average beam power of 140 kW per target and 420 kW total beam power, respectively, is obtained as in (Figure V.3). For all pulses, the beam peak power is identical to 7 MW.

The beam duty factor is 6% and the RF duty factor is 11% because of the high loaded quality factor (2000-10000) of the cavities; a 100 μs RF pulse length must be added to the macro pulse length in order to be able to build up the nominal fields in the cavities. Table V.1 summarizes the top level performance requirements and Figure V.4 shows the conceptual layout of the HBS linac.

Required	Specifications	Unit	Detail/Comment
Particle type	Protons	N/A	User requirement
Accelerator type	RF Linac	N/A	
Beam current	100	mA	Output current
Final energy	70	MeV	User requirement
Beam duty factor	6	%	User requirement
RF duty factor	11	%	Required for cavity filling
Pulse length	52/208/833	μs	User requirement
Repetition rate	384/96/24	Hz	User requirement
Average beam power	420	kW	
Peak beam power	7	MW	
Availability	>95	%	During scheduled operation
Maintainability	Hand-on	N/A	
Life time	>25	Years	

Table V.1: *Top level performance requirements of the HBS linac.*

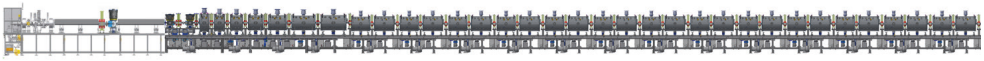

Figure V.4: Conceptual layout of the HBS linac. It consists of an ECR-source, LEBT, RFQ, MEBT and the CH-DTL.

V.2.2 Choice of technology

Worldwide there is an increasing interest in a new generation of high power proton and ion linacs. The term "high power" refers to the product of beam energy and beam current which is the beam power. With a peak beam power of 7 MW and an average power of 420 kW, HBS is clearly a high power linac (Figure V.5 and V.6).

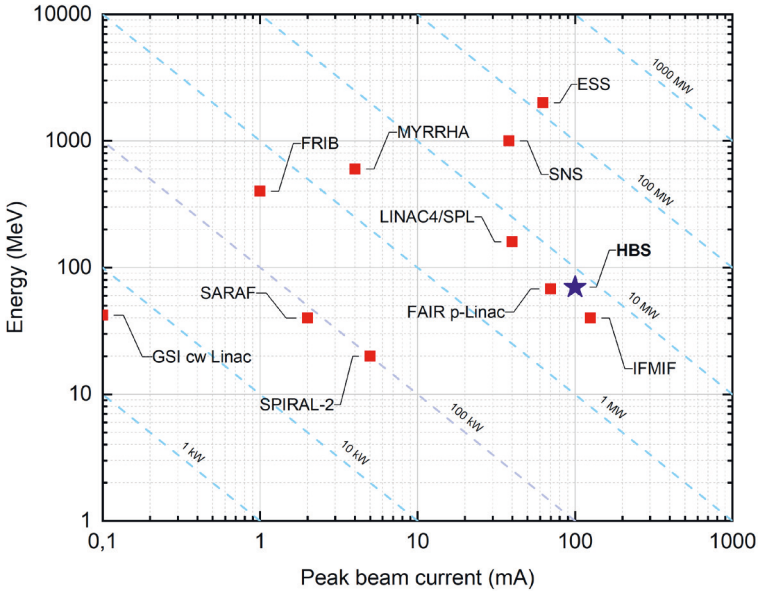

Figure V.5: Peak beam power of modern hadron linacs.

The typical modern hadron linac consists of three major parts (Figure V.7):

- front end (low energy part, E = 0.1-5 AMeV)
- drift tube linac (intermediate energy part, E = 3-200 AMeV
- superconducting section (high energy part, E > 100 AMeV)

One of the most important issues of high-power hadron linacs is the choice of technology with respect to superconducting or room-temperature operation. The advantage of a certain technology depends on various parameters. These include the RF duty cycle η, the peak beam current I and the final energy [96].

The front-end consists of an ion source, a Low Energy Beam Transport (LEBT) and a radio frequency quadrupole (RFQ). The vast majority of all RFQ structures have been realized using normal conducting

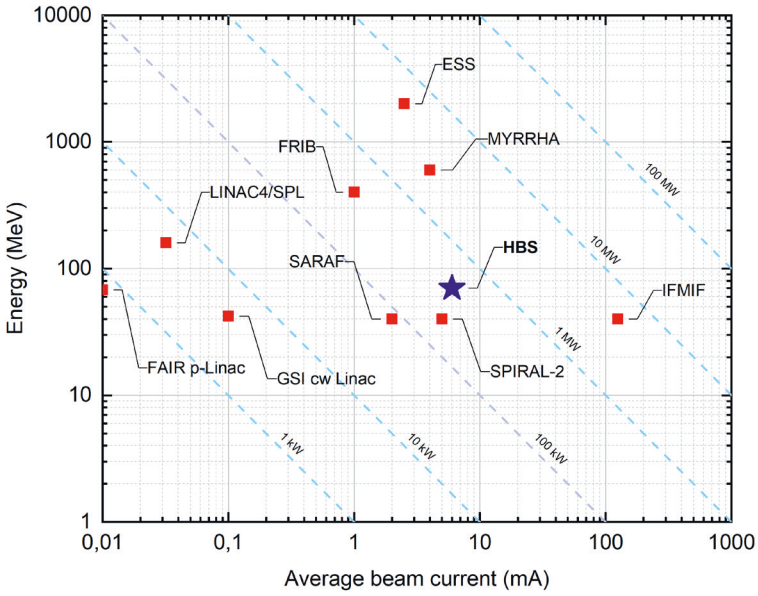

Figure V.6: *Average beam power of modern hadron linacs.*

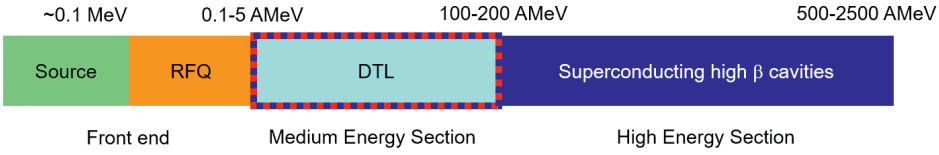

Figure V.7: *Scheme of modern High Power Hadron linacs.*

technology because of particles losses in the RF structure which would likely lead to thermal quench in case of high power superconducting linacs.

The high-energy section starts typically between 100 AMeV and 200 AMeV and mostly uses superconducting elliptical multi-cell cavities and more recently superconducting double-Spoke cavities (ESS, MYRRHA). Even for lower duty factors, superconducting cavities are a good choice with respect to the overall required radio-frequency (RF) and plug power.

In the case of the intermediate energy part, which is completely covered by the HBS linac the situation is not as clear. An important parameter is the transition energy between the room temperature and the possible superconducting section. In general, the higher the duty factor and the lower the beam current, the smaller the transition energy will be (Figure V.8 and V.9).

Each project has to decide on the technology best suited for the specific application. The main issues are capital costs, operating costs (power), technical risk, reliability and availability. During the last few decades, the transition energy between normal conducting and superconducting technology decreased significantly. The main reasons for this are lower operation costs for high duty factor machines and in particularly the availability of suitable superconducting RF structures in the low- and medium-energy range such as quarter-wave resonators, half-wave resonators and CH cavities.

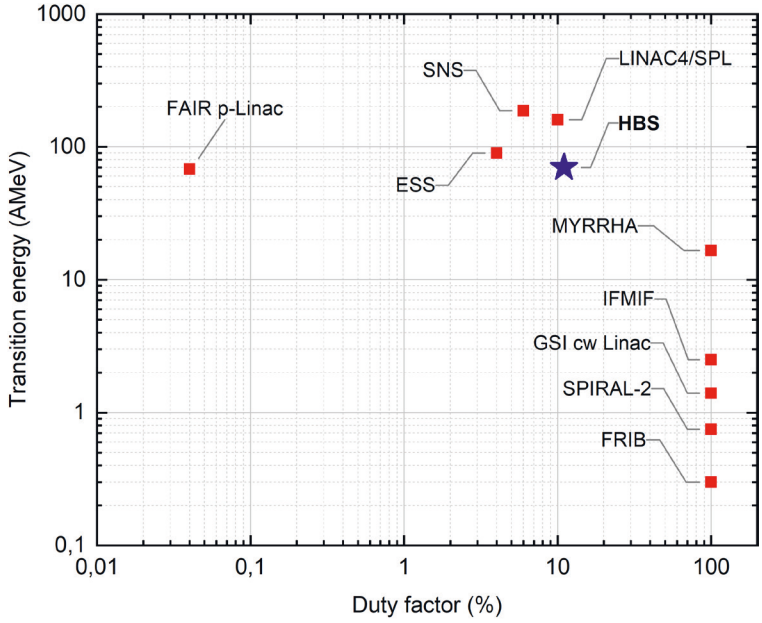

Figure V.8: *Transition energy as function of the duty factor of modern Hadron linacs. For fully room temperature linacs the transition energy is the final energy.*

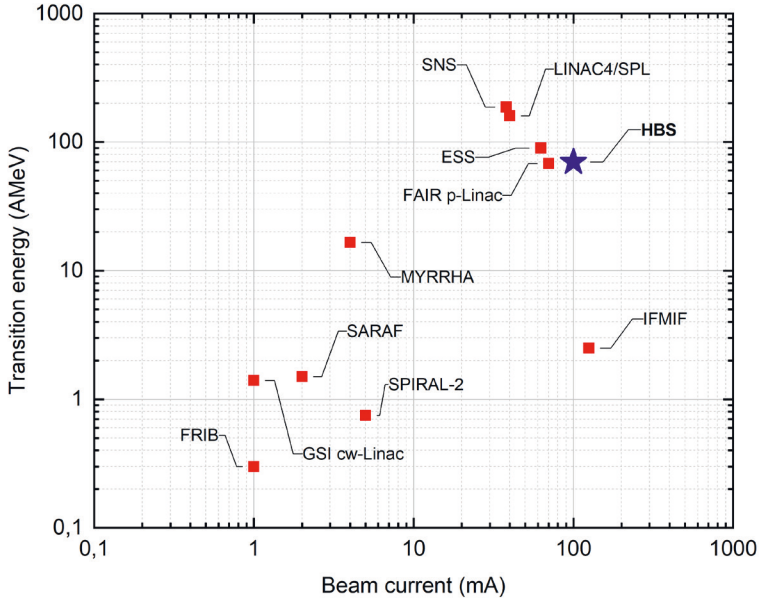

Figure V.9: *Transition energy as function of the peak beam current. For fully room temperature linacs the transition energy is the final energy.*

In general, the shunt impedance is higher at low energies. There are some very efficient low-energy drift tube structures such as H-mode cavities available. Above 100 MeV superconducting cavities are the best choice in most cases even for machines with lower duty cycle because there are no real efficient normal conducting structures available. On the other hand, superconducting high energy cavities can reach high gradients (E_a >10 MV/m) resulting in a much shorter linac.

In general, normal conducting cavities are more favourable at lower energies with high beam current and low duty cycle. For superconducting cavities the opposite is valid (Figure V.10) [96]. Both technologies have their advantages and disadvantages. Superconducting technology requires a cryogenic plant with associated helium distribution. The development of superconducting cavities and cryo-modules requires a large R&D effort with respect to simulations and prototyping. For each cavity type, specific high power couplers have to be developed. In addition, these cavities are very sensitive to contaminations, pressure variations, multi-pacting and vibrations and under certain circumstances they need complex fast frequency tuning systems [96].

Because of the high beam current the required RF power is dominated by the beam power even for room temperature cavities. In case of HBS, superconducting cavities providing 2.5 MeV will need 250 kW RF power plus an appropriate margin. For comparison, an equivalent room temperature structure requires about 100 kW more RF power. Due to the much simpler technology which avoids a cryogenic plant, the development of cryo-modules and suitable power couplers, a room temperature solution is preferred.

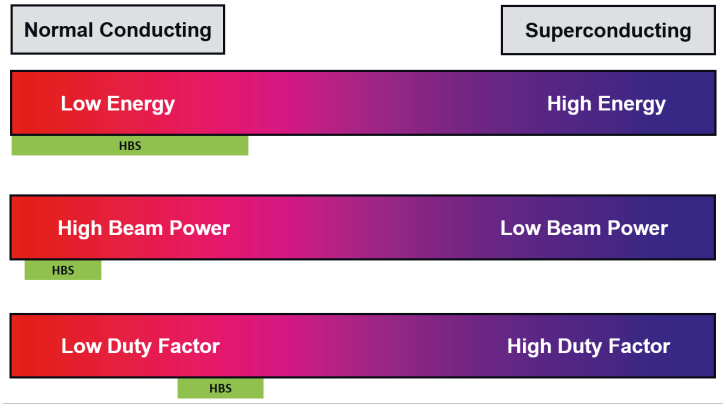

Figure V.10: The preference for room temperature or superconducting technology depends mainly on the energy, beam current and duty factor.

V.2.3 Design philosophy

The realization of high power proton accelerators is usually associated with a large R&D effort with corresponding resources regarding man power, prototyping and testing infrastructure. In the case of HBS, this development effort should be minimized by using technology already been developed. This lowers the cost and the time frame of the development and minimizes risks regarding construction cost, technological difficulties and time schedule. The HBS linac should be as efficient as possible (length, RF power) and as reliable as possible in its role as a user facility. High availability can be achieved by implementing a modular design that allows easy access to all components for repair and maintenance. Furthermore, all components should be operated well below their technical and physical limitations. Redundancies in critical components can significantly increase reliability and availability.

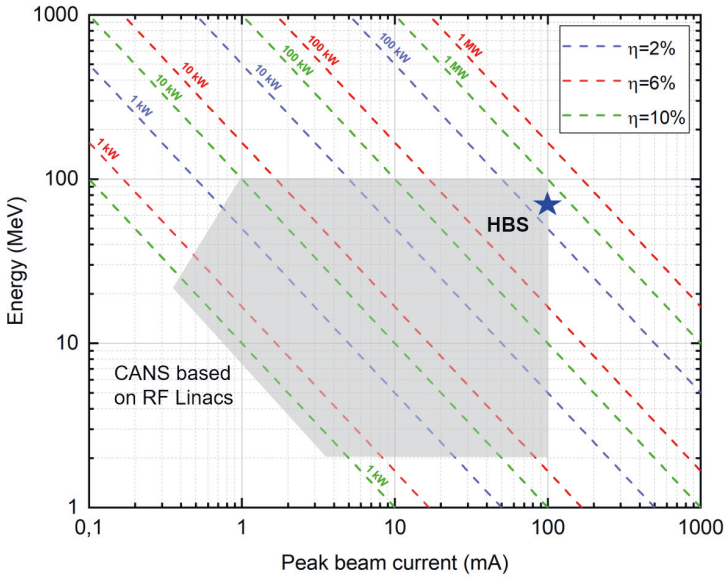

Figure V.11: *The shaded area shows the combinations of peak beam current and energy for compact accelerator based neutron sources (CANS). Depending on the beam duty factor, different average power levels are obtained (coloured lines for η=2%, 6% and 10%). The HBS design concept can cover the whole area only by adapting the front-end and the number of cavities.*

Since further accelerator-based neutron sources will be needed in the future, it is advisable to design HBS in a modular and scalable way. Duty cycle, beam current, pulse lengths and energy can then be varied over a wide range without fundamentally changing the design (Figure V.11). If necessary, only the front end can be adapted for smaller beam currents. The drift tube linac can consist of exactly the same lattice and is only adapted in length to the required energy.

The RF duty factor of 11% already leads to significant thermal loads in the cavities. For the 17 MeV injector of the MYRRHA project, cw capable CH-cavities and the corresponding RFQ were developed [97]. The thermal loads for this project added up to 35 kW/m. The technology for the MYRRHA linac has been successfully tested and is now also available for future neutron sources. Just like MYRRHA, the frequency of HBS should be 176.1 MHz. Thus, the RFQ RF structure can be adopted without any changes [98]. The CH cavities must only be adapted to the beam dynamics of HBS with regard to cell number and cell length. The basic geometry and the cooling system can be adopted. Due to the RF duty factor of 11%, higher gradients can be used compared to cw operation to keep the linac length as short as possible. The exact gradient results from the maximum RF power available per cavity and the beam dynamics. The subsystems of the cavities such as power couplers and frequency tuners can also be used.

The CH linac is realized by a quasi-periodic lattice. Up to an energy level of about 20 MeV there is a magnetic quadrupole doublet between the cavities for transverse focusing. For energies above this, two identical cavities are combined to form a cavity doublet. The lack of internal lenses makes fabrication much easier. The quasi-periodicity leads to a smooth course of the phase advance and thus to low emittance growth. Up to 20 MeV, a conservative beam dynamic with a constant negative synchronous phase is applied. EQUUS beam dynamics is used for cavity doublets, where the cell length is constant. The modular design with short CH-cavities can limit the amplifier power to

500 kW. This allows the use of Solid State Amplifiers (SSA). This modern technology offers significant advantages over classic tube amplifiers. Apart from a significantly smaller foot print, no high voltage is required. Due to the modular design of these amplifiers, individual amplifier modules can fail without interrupting operation.

V.2.4 Proton source

The proton beam will be extracted from a hydrogen plasma, which will be ignited in the plasma generator of the proton source. An Electron Cyclotron Resonance (ECR) ion source is the most favorable type of all source developments, using an RF (Radio Frequency)-driven gas discharge. Due to the ECR condition, a high power coupling leads to high plasma densities and high electron temperatures. Therefore this source type is well suited for high intensity beam production, for example in ESS or IPHI project. The advantages in comparison to other proton source types are:

- High reliability and availability
- Easy handling and maintenance
- High proton fraction, fewer molecule ions such as H^{2+} or H^{3+}
- High proton beam intensities in DC-mode operation

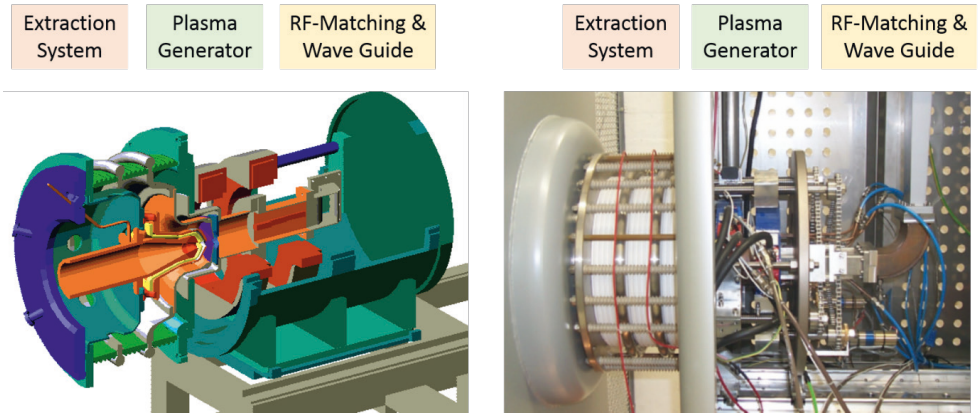

Figure V.12: *Cross sectional view of SILHI-Source (left) and image of TRIPS-Source (right), both sources are divided in the extraction system, plasma generator and RF-matching section.*

On the other hand, disadvantages of ECR-proton sources are a higher beam emittance due to high plasma temperature and beam current fluctuations. These fluctuations are in a range of a few percent and lead to a space charge driven fluctuation of the focal plan right after the particle optics. The resulting emittance growth and high intrinsic beam emittance of an ECR-source have to be taken into account.

A pentode extraction system will provide the extraction and post acceleration of the proton beam. The electric field strength between plasma electrode and puller electrode is adjusted to form a planar plasma sheath. This prevents an additional emittance growth in the extraction system and resulting beam losses. The latter would lead to secondary particle production and hence a reduced life time of the extractor. The field strength of the post acceleration electrodes can be adjusted for

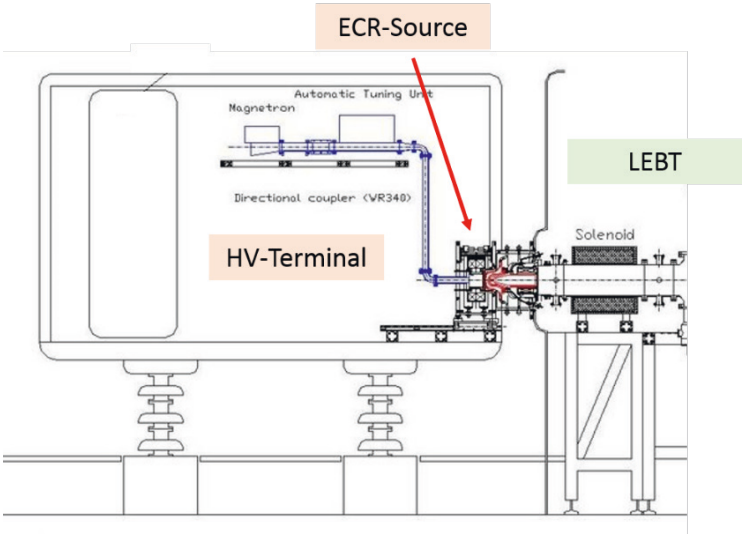

Figure V.13: *Scheme of a high-voltage terminal with ECR-source connected with the following LEBT-section.*

best longitudinal beam matching into the first accelerator stage, the RFQ. It is also equipped with a screening electrode to provide space charge compensation in the following Low Energy Beam Transport section (LEBT).

Two different ECR-proton sources offer a possible solution for HBS. The first one is SILHI-Source from CEA-Saclay [99] and second one is TRIPS-Source from INF-LNS [100]. Both proton sources are able to deliver a proton beam with an energy of 100 keV and a beam current of 110 mA. It seems that there is the possibility for both of the ECR-Sources to increase the beam intensity slightly to compensate the estimated beam losses along the whole accelerator.

The proton source is mounted on a High-Voltage (HV) platform surrounded by a Faraday cage. All power supplies and the RF-generator are installed on this platform to provide the source operation. Downstream of the extraction system the source is connected to the following LEBT by the use of an insulator. Because of the beam intensity and the resulting space charge force, the distance between extractor and first beam optical element, in the case of HBS a solenoid, should be as short as possible to catch the beam.

V.2.5 Low energy beam transport and chopper

The LEBT is a transport section of the front-end of an accelerator between the proton source and the first accelerator stage e.g. an RFQ. Compared with all other sections of the linear accelerator, it is the region with the highest proton density and therefore with the highest space charge forces acting on the beam as a repulsive force. This is the reason why a LEBT should be as short as possible to prevent a decrease of compactness in the phase space of the beam, expressed by emittance growth. On the other hand, the LEBT-section is designed for the following purposes:

- Reduction of gas flow out of the proton source to prevent XUHV vacuum conditions in the RFQ
- Catching the beam after the extraction system and matching into the acceptance of the RFQ

- Creation of a time structure by the use of a chopper

The hydrogen gas needed for the beam production streams out of the proton source and increases the vacuum pressure in the LEBT. Collisions of the proton beam with residual gas lead to charge exchange and momentum spread and bears the risk for the following RFQ. For the HBS-LEBT, two pumping and diagnostic tanks (Figure V.14 and V.15) are foreseen to provide enough pumping power in addition to a poor vacuum resistance of the beam line. This combination acts like a differential pumping system as it is fully integrated in the LEBT-section.

The LEBT is divided into two sections with an E×B-chopper in between. Beam focusing is planned to be provided by four solenoids. This lens type allows space charge compensation by secondary electrons captured in the beam potential [101]. The advantage of space charge compensation is a reduction of the electric field of the proton beam and therefore a reduced risk for emittance growth. An other important point, especially for ECR-sources, is that current fluctuations can be damped slightly. The first solenoid catches the beam right after the extraction system, while the second matches the beam into the chopper device. After the chopper, the third solenoid catches the beam again and the fourth solenoid focuses the beam into the acceptance of the RFQ.

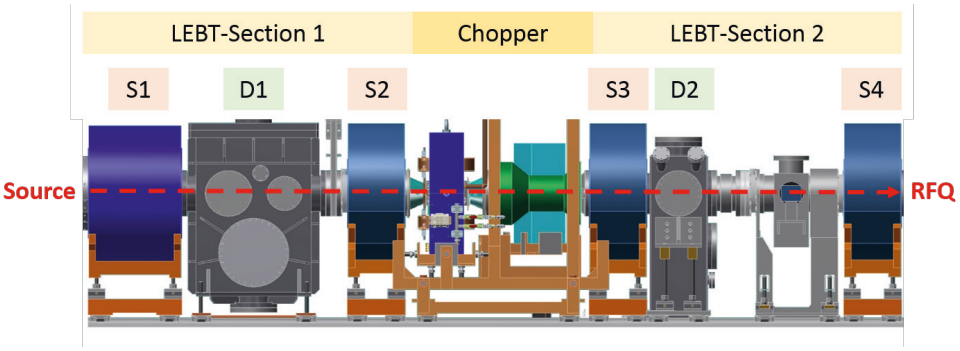

Figure V.14: *Scheme of the low energy beam transport for HBS. It consists of two sections with an E×B-chopper in between.*

To prevent aberrations, the radius of the first solenoid is quite large with a radius of 75 mm while all the other solenoids have a radius of 50 mm. For a chosen aspect ratio of S=0.2, the length of the first solenoid is 400 mm and for the others 250 mm.

For the production of the time structure of the beam (Figure V.3) a chopper is required, because the repetition rate and the shortest pulse length do not correspond with the plasma rise time in a pulsed ECR-source. In conventional LEBT-systems the chopper is located at the entrance of the RFQ. In the case of a beam current of 100 mA and a peak beam power of about 10 kW, the unwanted beam portion has to be dumped carefully with respect to power deposition and secondary particle production. Therefore, a chopper system is foreseen for the HBS-accelerator front end. It consists of an E×B-chopper followed by a septum magnet to ensure the safe deflection of the unwanted beam portion into a dedicated beam dump [102].

The E×B chopper is driven by a high-voltage switch providing the electric field to fulfill the Wien condition with respect to the required pulse lengths and repetition rates. The advantage of an E×B-chopper is the low power consumption compared to a magnetic chopper and the control of secondary particles (and therefore the risk of sparking) compared to electric choppers.

At the end of the LEBT, the beam is injected in the following RFQ. High space charge forces act on the beam due to the small beam spot size demanded by the acceptance of the RFQ. Additionally, the

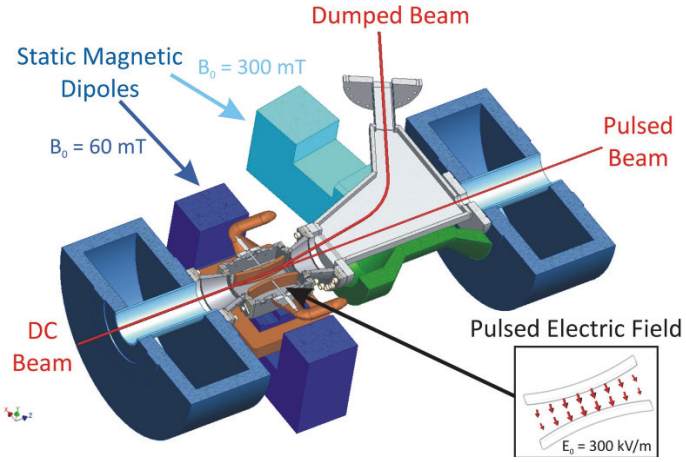

Figure V.15: *Cross-sectional view of the chopper system consisting of an E×B chopper, a static magnetic septum and a beam dump.*

proton beam at the entrance of the RFQ is partly de-compensated. A careful investigation of beam dynamics is necessary to prevent unwanted emittance growth and halo formation which leads to beam losses in the accelerator. A collimation aperture right before the second solenoid removes a small fraction of H^{2+} molecules from the beam and halo particles created by non-linear fields within the extractor.

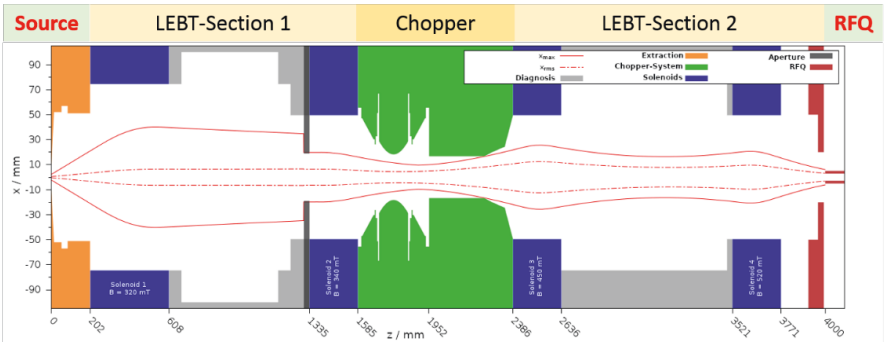

Figure V.16: *Beam dynamic simulation from the exit of the proton source extractor to the entrance of the RFQ show an optimized filling degree of solenoid aperture.*

For proton beam densities larger than $7 \cdot 10^{11}$ m^{-3} the proton ensemble tends towards collective behaviour. Beam dynamic studies show good results with respect to intrinsic emittance growth, if the transit time of the proton beam is shorter than the period of plasma oscillations of the proton beam density. The interface between LEBT and RFQ should be as short as possible to preserve space charge compensation of the pulsed proton beam against the high voltage of the RFQ electrodes.

V.2.6 Radio frequency quadrupoles

Radio frequency quadrupoles (RFQ) are today the standard structures for focusing, bunching and accelerating a DC beam delivered by an ion source. Regardless of the RF structure used, 4 electrodes

(rods, vanes) are periodically charged by RF fields and generate a time-varying electric quadrupole field. As the particles pass through the RFQ, a chain of alternating electric quadrupoles acts as a strong electric focusing device in both transverse planes. Subsequent drift tube cavities require a bunched beam with a small phase and energy width to ensure high transmission and good beam quality. In addition, the energy must be increased in the RFQ so that the length of the acceleration cells in the drift tube cavities becomes sufficiently large at a given frequency. Bunching and acceleration are achieved by longitudinal fields generated by a characteristic mechanical modulation of the electrodes. The electrode geometry is determined by the modulation m, the minimum aperture a, and the cell length $l_c = \beta\lambda/2$. The course of these parameters essentially determines the beam dynamics properties of the RFQ.

Since most of the field energy is used for transversal focusing, RFQ accelerators are relatively inefficient with respect to the required RF power and length. Therefore, the transition to more efficient drift tube cavities should be made as early as possible. For beam dynamic reasons, the higher the beam current, the higher the final energy. The lighter the particles or the smaller the mass-to-charge ratio, the higher the frequency usually chosen. For beam currents that are not too high, typical frequencies are between 300 and 400 MHz. For higher beam currents (100 mA) or high duty cycles, a lower frequency of about 200 MHz is often used to reduce the required electrode voltage.

Parameter	MYRRHA	HBS	Unit
RF Structure	4-Rod	4-Rod	NA
Frequency	176.1	176.1	MHz
Particles	Protons	Protons	NA
Beam current	5	100	mA
RF Duty factor	100	11	%
E_{in}	30	100	keV
E_{out}	1.5	2-3	MeV
R_p	72	72	kΩm
RF losses	108	<2x300	kW
Specific power loss	27	100	kW/m
Thermal load	27	11	kW/m
Beam power	7.5	2x100-150	kW
Total peak power	116	2x350-450	kW
Amplifier	192	2x450-550	kW
Electrode voltage	44	85	kV
Length	4	<2x3	m
$\epsilon_{in,n,rms}$	0.2	0.4	πmm mrad
Transmission (sim)	99.8	>95	%

Table V.2: *Comparison of the MYRRHA RFQ and HBS RFQ parameter*

The two most frequently used RF structures are the 4-Vane RFQ and the 4-Rod RFQ. The 4-Vane RFQ is a cavity that operates in TE_{211}-mode. The advantages are a high shunt impedance and a fairly homogeneous distribution of the power dissipation. Due to the extreme sensitivity to field deviations, the required tolerances are very narrow over large areas and involve a high risk in manufacturing with regard to the functionality of the RFQ.

The 4-Rod RFQ is a transmission line resonator, i.e. the frequency does not depend on the tank dimensions, but only on the geometry of the internal resonance structure. Due to the excellent

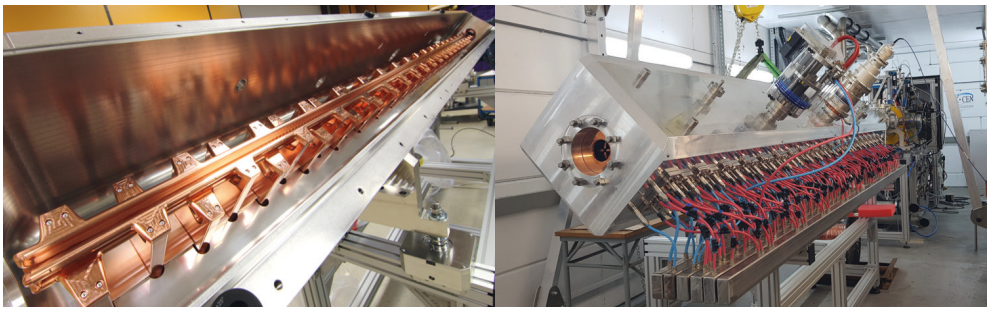

Figure V.17: *The MYRRHA RFQ very similar to the HBS RFQ uses the same technology.*

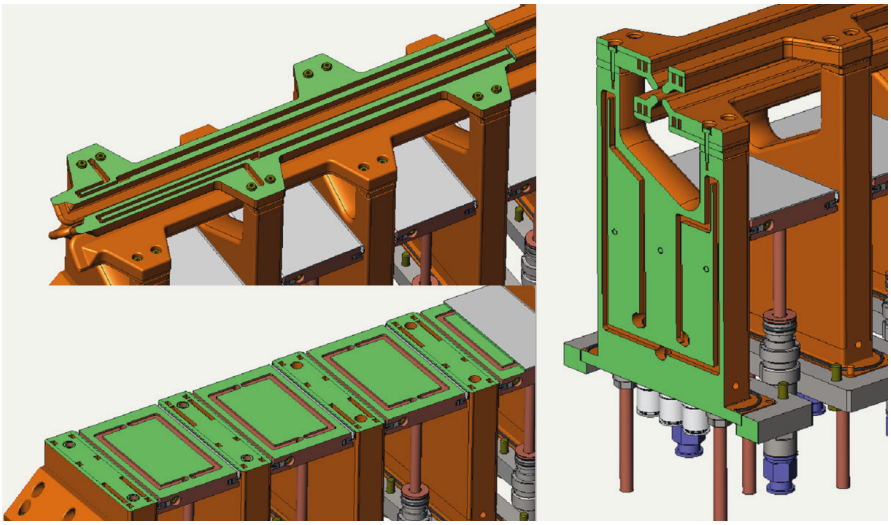

Figure V.18: *Cooling system of the resonance structure of the HBS-RFQ.*

possibility of frequency and field tuning, the modular design and the possibilities for maintenance and repair, clear advantages are seen for this RFQ type and therefore proposed as the RF structure for HBS. In recent years, the 4-Rod RFQ has been further developed in terms of high current acceleration at high duty cycle up to cw operation [98]. These developments were driven by various projects such as MYRRHA, FRANZ or GSI-HLI. Novel cooling methods and technologies have been developed and experimentally validated to handle high thermal loads up to 100 kW/m. The HBS-RFQ will have exactly the same RF structure as MYRRHA (Figure V.17 and V.18). Essential differences are in the electrode modulation due to changed beam parameters as well as in the length of the structure. However, this has no significant influence on efficiency and frequency.

An important aspect is the final energy. This should be high enough to enable a good beam transport along the subsequent Medium Energy Beam Transfer (MEBT). For a current of 100 mA, values between 2 and 3 MeV are a good choice. The exact value must be determined using beam dynamics simulations. For energies well above 2 MeV, the length of the RFQ reaches a value that makes production and tuning considerably more difficult. In addition, the required power is then very high. Therefore it is planned to divide the RFQ into two shorter structures in case a higher final energy is required. In addition, a short MEBT is then used between the individual RFQ accelerators to match the beam from one RFQ to the other. First simulations showed that an electrode voltage of 85 kV is

required. With the expected shunt impedance of 72 kΩm, this corresponds to a specific RF power of 100 kW/m. The thermal load is 11 kW/m with the RF duty cycle of 11%.

V.2.7 Medium energy beam transport

The beam delivered by the RFQ must be adapted to the acceptance of the following drift tube linac. The drift tube linac requires a convergent beam in both transverse planes, while the RFQ provides a beam convergent in one plane and divergent in the other. The transverse matching is done by means of magnetic quadrupoles. In addition, the beam must be longitudinally matched to reduce the phase width, otherwise nonlinear effects in the subsequent drift tube cavities lead to emittance growth and possibly uncontrolled particle losses. To minimize the phase width, re-bunchers are used, which are operated at a synchronous phase of -90°. For HBS, the MYRRHA MEBT will be used with small adjustments regarding the beam energy. The MEBT consists of a quadrupole dublet, two Quarter Wave re-bunchers and a quadrupole triplet (Figure V.19). The MEBT was designed in such a way that there is sufficient space for different beam diagnostic elements (BPM, ACCT). Behind the RFQ there are two additional steerer pairs to compensate for a possible transverse offset of the RFQ beam.

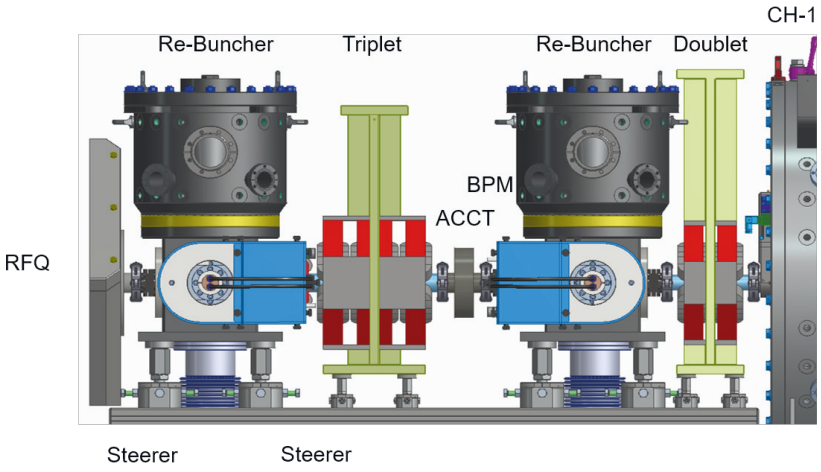

Figure V.19: *Medium Energy Beam Transport (MEBT) between RFQ and CH-DTL.*

V.2.8 Drift tube linac

Various RF structures are available for a normal conducting HBS linac. Basically, the linac should be as efficient as possible in terms of power consumption. Furthermore, beam dynamic aspects, modularity, maintenance, repair, R&D effort, availability of suitable amplifiers and investment costs also play a role. The classic accelerator is the Alvarez DTL. Due to the significant development effort, low efficiency, and the necessity of large tube amplifiers, H-mode structures are proposed. H-mode accelerators use the H_{n11} (TE_{n11}) mode of the empty cylindrical cavity. The term H-mode is based on the longitudinal magnetic field along the structure. Currently, H-mode accelerators up to n=2 are realized [103]. At n=1 we speak of IH-structures (interdigital H-mode structure) and at n=2 of CH-structures (crossbar H-mode structure). H-mode structures have a high shunt impedance, since the current flows transversally only over half (IH) or quarter (CH) of the tank circumference.

Since H-mode structures are real cavities, the frequency is essentially determined by the transverse tank dimensions. CH structures have a slightly lower shunt impedance at the same frequency as IH structures. At higher duty cycles with corresponding thermal load, CH structures offer better cooling possibilities. Due to the CH cavities (176.1 MHz, duty factor 100%) developed for the MYRRHA project, this solution is also proposed for the HBS linac (Figure V.20).

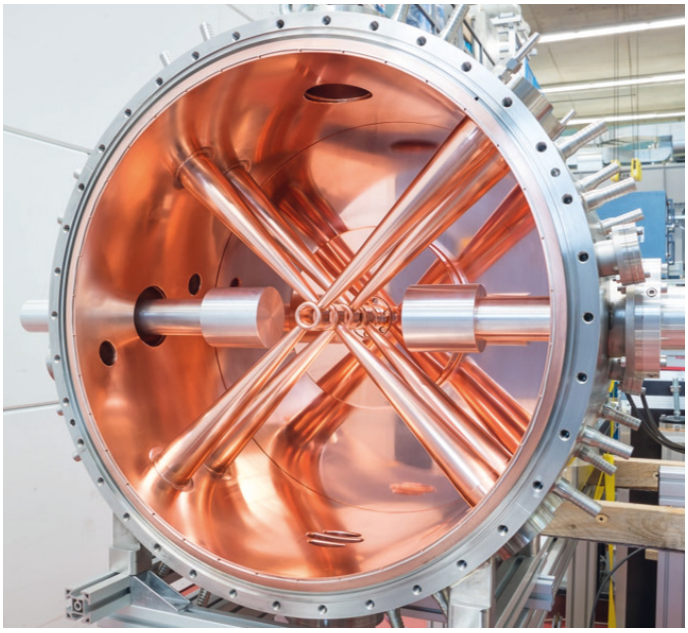

Figure V.20: *CH-Cavity operated with 100% duty factor.*

The technology has been successfully tested and requires a manageable development effort. The frequency tuner, power couplers and the cooling system of the cavities can be taken over (Figure V.21). Only the RF structures have to be designed according to the field distribution and the frequency. The design of the CH cavities is essentially influenced by two factors: the beam dynamics and the available RF power. As already mentioned, the longitudinal phase advance should be as constant as possible in order to minimize emittance growth. This gives boundary conditions for the length of the longitudinal periods and the gradients in the cavities. On the other hand, the length of the cavities should not exceed 1.5 to 2 m in order to keep production simple and to limit the amplifier power to a maximum of 500 kW. Therefore, cavity doublets should be used above a certain energy. Furthermore, it must be considered that the shunt impedance decreases with $1/\beta$. In the first part of the linac a constant synchronous phase with variable cell length is used. In the second part, the cell length is kept constant. Together with the use of magnetic quadrupole doublets between the cavities, an extremely modular structure is achieved (Figure V.22). This provides space for sufficient diagnostics and ensures good access to all elements for maintenance and repair. Furthermore, scalability with regard to energy and beam power is achieved. The design allows a wide range of beam currents from a few mA to 100 mA. Due to the provided cooling, duty factors of practically 0 to 20% are possible. Depending on the number of cavities, energies in the range from 2.5 to 100 MeV are possible. Thus the entire range for compact accelerator-based neutron sources can be covered by small adaptations.

In the case of HBS, about 35 CH cavities are required. The exact value must be determined by simulations. The estimated total length of the HBS linac with the front-end is about 90 m. The

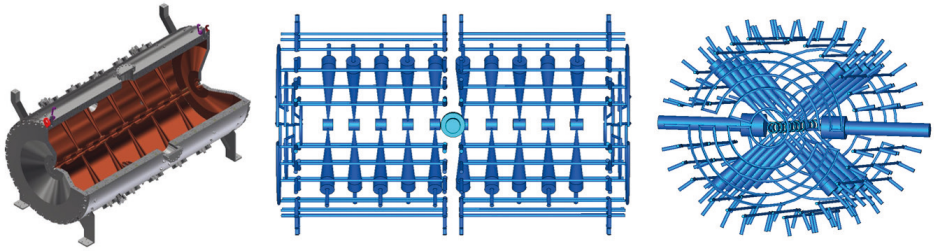

Figure V.21: Cooling system for the CH-cavities. It has been designed for average power levels of 50 kW/m

cavities are made of stainless steel. After the necessary intermediate measurements to check the frequency, the field distribution and the tuning range of the tuners, the cavities are copper-plated with a layer of about 50 μm.

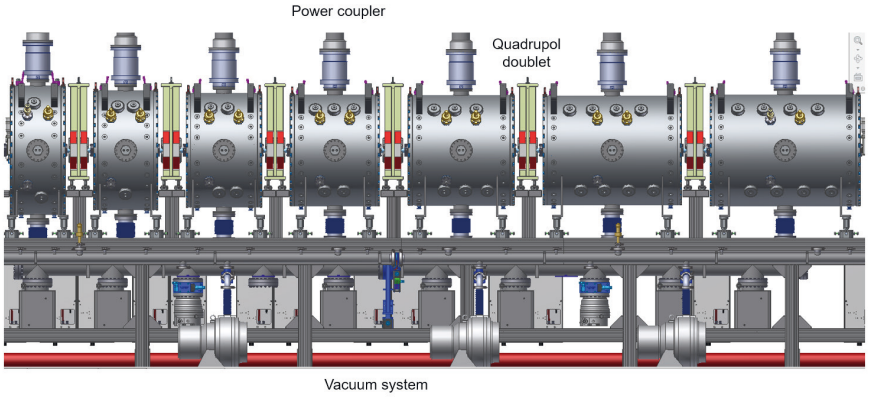

Figure V.22: The modular design of the HBS CH-DTL provides good access for maintenance and repair.

V.2.9 RF system

The RF system of the HBS linac must reliably provide the RF power for the cavities within certain parameters. The total power per cavity consists of the ohmic losses, the beam load, line losses and reserves. The reserves should be at least 30% of the maximum nominal power in order to have sufficient margin for control and redundancy. The different cavities will have different power requirements. Therefore, amplifiers between 200 and 500 kW are required. Possible technologies for the amplifiers are classical tube amplifiers or solid-state amplifiers.

Solid state amplifiers offer some advantages. Several transistors, each delivering about 1 kW RF power, are combined into a so-called pallet amplifier. The required total power is finally obtained via several combiner stages. In contrast to tube amplifiers, solid-state amplifiers can be designed redundantly. In the event of the failure of one or more pallet amplifiers, the entire system is still ready for operation. Solid state amplifiers do not require high voltage and the foot-print is much smaller.

Parameter	Value	Unit
RF structure	CH-DTL	NA
Frequency	176.1	MHz
No of cavities	$\approx$ 35	NA
RF Duty factor	11	%
E_{in}	2-3	MeV
E_{out}	70	MeV
Z_{eff}	30-60	MΩ/m
Specific power loss	100	kW/m
Thermal load	11	kW/m
Aperture diameter	30-40	mm
Gradient	1.5-2	MV/m
Voltage	0.5-2.5	MV
Total power per cavity	50-350	kW
Amplifier power	100-500	kW

Table V.3: *Preliminary parameters of the CH-linac*

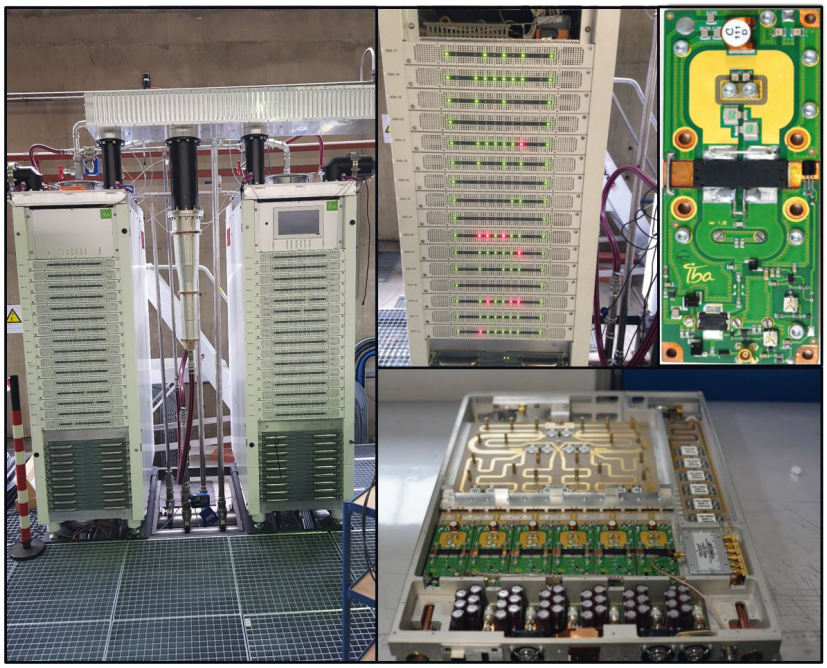

Figure V.23: *200 kW, 176.1 MHz Solid State Amplifier (SSA) developed for the MYRRHA project.*

Furthermore, the market for these amplifiers is strongly determined by competition. Extremely reliable RF systems can be realized with solid state amplifiers. It is therefore recommended to use solid state amplifiers for HBS. Figure V.23 shows a 192 kW solid state amplifier for the MYRRHA project. It

Parameter	Value	Unit
Frequency	176.1	MHz
RF power	200, 300, 400, 500	kW
RF duty factor	11	%
No of amplifier	37	NA
Bandwidth@1 dB	$> \pm 1$	MHz
Input impedance	50	Ω
Output impedance	50	Ω
Input connector type	SMA female	NA
Nominal input level	<+10	dBm
Rise time (10-90%)	<2	μs
Pulse length	152, 308, 933	μs
Repetition rate	384, 96, 24	Hz
Pulse over/undershoot	$< \pm 0.3$	dB
Phase linearity	<10	deg
Pulse droop	< 0.2	dB
Amplitude stability	$< \pm 0.2$	dB
Phase stability	$< \pm 0.2$	deg
Circulator	no	NA
Harmonics at nominal power	<-40	dBc
Overall efficiency	>50	%
	IEC 610000-6-2	
EMC compliance	IEC 610000-6-2	NA
	IEC 60204-1	
Input connector position	front	NA
Output connector position	top	NA
Amplifier technology	Solid state	NA

Table V.4: *Preliminary parameters of the RF amplifiers*

is operated at 176.1 MHz with cw operation. Table V.4 describes the preliminary parameters of the amplifiers.

V.3 Multiplexer

In order to efficiently operate multiple instruments with different requirements for the neutron pulse structure at the HBS facility simultaneously, three different pulse sequences have to be multiplexed into the primary proton beam. For neutron generation at the appropriate target station with a designated suite of instruments, these pulses then have to be distributed spatially by a proton beam deflector system, which will be referred to as the *multiplexer*. This section presents a multiplexer system conceptually designed to meet HBS requirements. Here, we pursue an approach which employs twofold subsequent spatial distribution of the pulses. This section starts with a summary of HBS requirements on the multiplexer's design philosophy and specifications. After this, a general layout of the multiplexer setup is presented including geometric dimensions and required field strengths

of the corresponding magnets. Then the beam dynamics of this setup will be discussed by means of tracking simulations in each beam line and finally the conceptual design of the three different magnets employed in the multiplexer will be presented.

V.3.1 Requirements

As introduced in Chapter V, the HBS features three target stations, each supplying neutrons to a different group of instruments. The corresponding proton pulse sequences on each target have to be set to obtain an optimal balance between relative neutron wavelength uncertainty and bandwidth at a fixed duty cycle of ≈2 %. This results in three different pulse sequences with different frequency and pulse length as listed in Table V.5.

Frequency [Hz]	Time period [ms]	Pulse length [µs]	Neutrons	Instruments
384	2.6	52	Fast	High energy
96	10.4	208	Thermal	High resolution
24	41.7	833	Cold	Long wavelenghts

Table V.5: *Primary proton pulse parameters for three different target stations, i.e. instrument groups, operated at HBS.*

Timing

These three pulse sequences are multiplexed into the proton beam by temporally centring the two lower frequency pulse sequences, i.e. 96 Hz and 24 Hz between two subsequent 384 Hz pulses as shown in V.24.

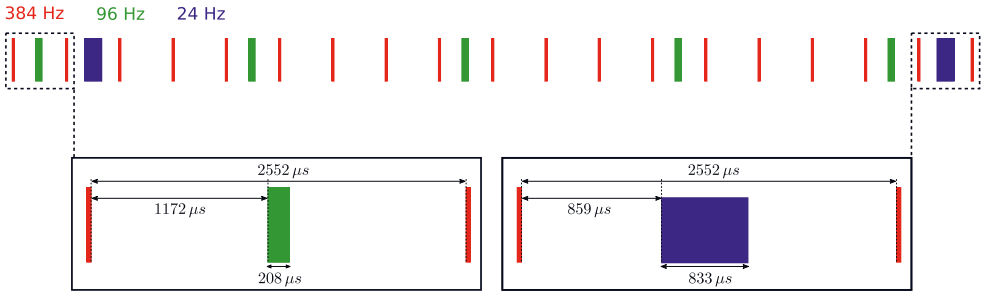

Figure V.24: *Pulse sequences as multiplexed into the primary proton beam. The* 96 Hz *and* 24 Hz *pulses are centred with respect to one period of the* 384 Hz *pulses which results in an interval of* 1172 µs *and* 859 µs *between two subsequent pulses, respectively. Parameters are taken from Table V.5.*

With a period length of 2604 µs at 384 Hz and a corresponding pulse length of 52 µs, the time difference between two subsequent 384 Hz pulses is 2552 µs. Thus, centring pulses with 208 µs and 833 µs pulse length in this interval results in 1172 µs and 859 µs time intervals between adjacent pulses of different frequency, i.e. the time intervals during which the ion beam optical parameters need to be changed in order to separate the 96 Hz and 24 Hz pulses from the 384 Hz pulse, respectively. Consequently, the upper threshold for the settling time of a beam deflection device is 859 µs.

Beam line

In Chapter V, it was shown that the HBS facility will be operated over two floors with the multiplexer situated on the first floor while the accelerator and the target stations will be located on the ground floor. Furthermore, the three target stations need to be arranged such that one obtains a sufficiently large separation between them in order to have enough spatial flexibility for a number of neutron guides and multiple instruments. This requires beam transport from the accelerator to the multiplexer and from the multiplexer to the target in the order of 5 m - 10 m each and therefore calls for beam focusing elements within the total distance from accelerator to target. In addition, the beam power needs to be uniformly distributed over the target disk by fast scanning of a small beam spot over the target disk area. These demands on the beam quality make it beneficial to integrate beam focusing devices into the multiplexer layout. The beam transport from accelerator to target is thus the shortest possible and the number of necessary quadrupole magnets is minimized.

Reliability

As mentioned in Table V.1, the HBS facility will be operated with an availability of >95 % during scheduled operation and a beam intensity of 100 mA which poses certain demands on the multiplexer design. Due to the high beam intensity, it is preferred to ramp up the beam deflection device with no beam in the aperture, thus reducing the radiation induced damage of subsequent components, e.g. beam tubes or further magnets, and the overall radiation exposure by secondary particles. This is ensured by an appropriate synchronisation of the beam deflection to the beam pulsing, i.e. chopping in the LEBT of the accelerator facility as shown in V.15. After the beam is annihilated in the chopper system, e.g. after a 384 Hz pulse in V.24, the beam deflection is settling within less than 859 µs such that the beam is guided onto a well-defined trajectory before the chopper is set off for 833 µs.

The high demand for availability during the scheduled operation of HBS makes it desirable to reduce the duty cycle of highly stressed equipment, as for example the power supplies of the beam deflection devices. This, together with the less challenging requirements of unipolar power supplies (two quadrant chopper) in terms of maintenance makes it advantageous to successively distribute the three pulses as shown schematically in V.25.

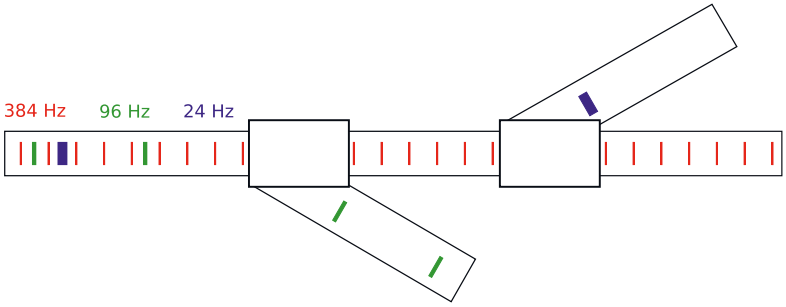

Figure V.25: *Successive separation of* 96 Hz *and* 24 Hz *pulse sequences from the unperturbed* 384 Hz *pulse sequence.*

V.3.2 Layout

In order to meet the requirements derived in the previous subsection a multiplexer layout as shown in Figure V.26 is proposed.

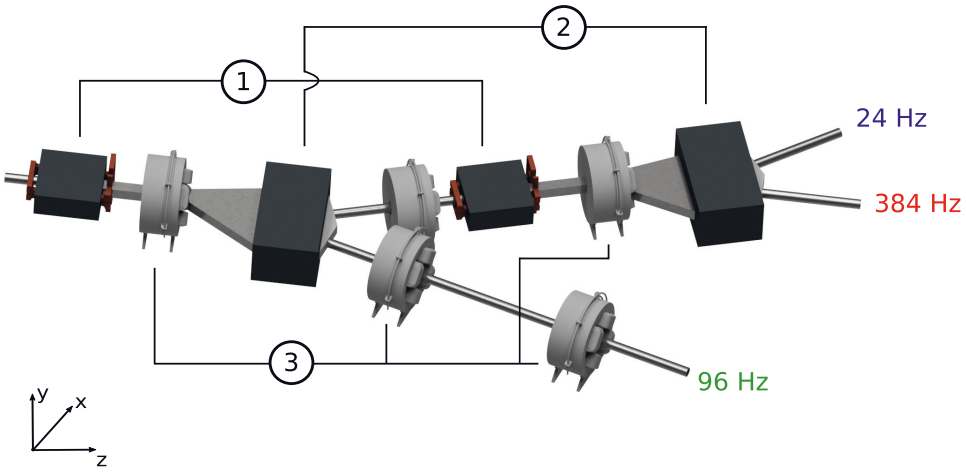

Figure V.26: *Conceptual design of the HBS multiplexer. The design comprises two kicker magnets (1), two opposite field septum magnets (2) and five quadrupole magnets (3) for beam focusing in all outgoing beam lines.*

In Figure V.26, two fast ferrite kicker magnets successively separate the 96 Hz and 24 Hz pulse sequences from the 384 Hz pulse sequence. In both steps of beam separation, two septum magnets deflect the perturbed and unperturbed beam for further horizontal separation. Additionally, five quadrupole magnets form two quadrupole triplet configurations which are powered to perform a point-to-point imaging of the beam.

To define the positions and strengths of the magnets shown in Figure V.26, one has to estimate the horizontal (x-direction in Figure V.26) beam size which can be derived from the approximate transversal emittance of the HBS linac, i.e. $\epsilon_{x(y)}^{\mathrm{norm,rms}} = 1\,\mathrm{mm\,mrad}$. Therefore one starts to look at the longitudinal evolution of the beam envelope in the multiplexer which is dominated by the quadrupole magnets being set to perform a point-to-point imaging. First of all the distances between the quadrupole magnets need to be fixed. In order to have enough space between the quadrupole magnets for kicker and septum magnets, the spacing is iteratively set to be 1.2 m. This gives us the corresponding quadrupole strengths and beam transport matrices for point-to-point imaging. After the minimization of the overall transversal beam size in the multiplexer with fixed transversal emittance and tuneable TWISS parameters[1], one ends up at a RMS beam size of $\sigma_x \approx 5\,\mathrm{mm}$, $\sigma_y \approx 1\,\mathrm{mm}$ at the position of the septum magnet.

With the requirement of a horizontal separation[2] of the two beams deflected in opposite directions to each other at the beginning of the septum magnets of at least $4\sigma_x + \Delta x_{\mathrm{septum}} \approx 20\,\mathrm{mm} + 5\,\mathrm{mm} = 25\,\mathrm{mm}$ and a sufficiently large horizontal separation of the beam tubes at the position of the second quadrupole magnets[3] of at least one quadrupole magnet's width and some additional spacing, i.e. in total $\approx 0.6\,\mathrm{m}$, one can deduce a suitable combination of deflection angles and thus magnetic field strengths and lengths for the kicker and septum magnet.

Figure V.27 shows the Multiplexer as a composition of two 26 mT kicker magnets, two 740 mT opposite field septum magnets and five quadrupole magnets with gradients of $\approx \pm 3 \cdot 1/\mathrm{m}^2$.

[1] For the sake of simplicity we assume $\alpha = 0$, i.e. we map the waist of the beam.
[2] x_{septum} denotes the additional separation that is required in order to maintain two opposite magnetic field regions.
[3] Counting along the direction of beam propagation, i.e. from left to right in Figure V.26

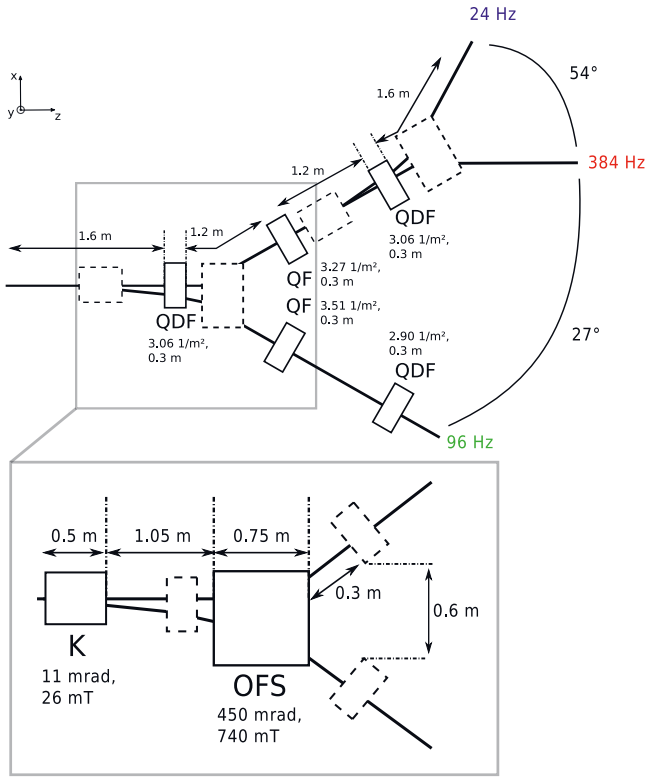

Figure V.27: *Schematic top view of the multiplexer in Fig. V.26 with the quadrupole magnets (top) as well as the kicker and septum magnets (bottom) highlighted individually. QDF, QF, K, OFS denote horizontally defocusing quadrupole magnets, horizontally focusing quadrupole magnets, kicker magnets and opposite field septum magnets, respectively. Note that the distances are not to scale.*

V.3.3 Beam dynamics

In Figure V.27 the geometric layout of the multiplexer is presented as it was derived from the horizontal beam size and additional constraints whereby the beam size itself was deduced from a glimpse into the beam dynamics introduced primarily by the quadrupole triplet configuration. However, strong dipole magnets, as for example the septum magnets, additionally result in beam focusing and defocusing strengths (i.e. edge focusing/defocusing) which are no longer negligible at such large magnetic fields. Therefore a proper beam dynamics simulation in terms of particle tracking was performed for each of the three individual beam lines in Figure V.27. The corresponding results for the beamlines which output the 384 Hz, 24 Hz, 96 Hz pulse sequences are displayed in Figure V.28, V.29 and V.30, respectively.

The figures show the longitudinal evolution of the total envelope (6σ beam diameter) as well as the RMS beam size during propagation through the multiplexer. Furthermore, the horizontal and vertical sub phase spaces are plotted (top and bottom plot on the right side, respectively) at the beginning (red) as well as at the end (blue) of the multiplexer. The initial phase space distribution takes into account the emittance as derived in the previous subsection. All three tracking calculations prove that the composition of quadrupole strengths for the five quadrupoles was chosen such that the

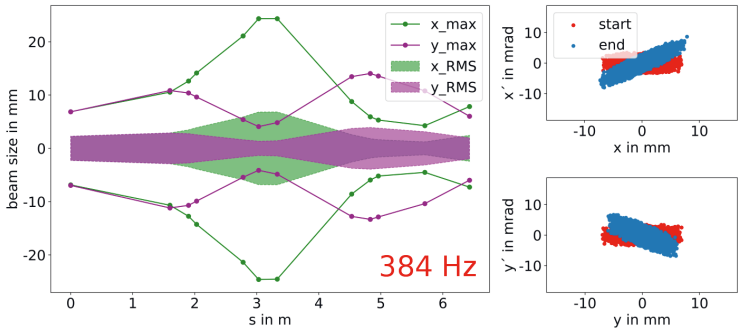

Figure V.28: *Left plot: Envelope ($6\sigma_{x,y}$ and $\sigma_{x,y}$) versus longitudinal position in the* 384 Hz *beamline shown in Figure V.26. Right plot: Phase space distribution at the beginning and at the end of the beamline for the horizontal (top) and vertical plane (bottom).*

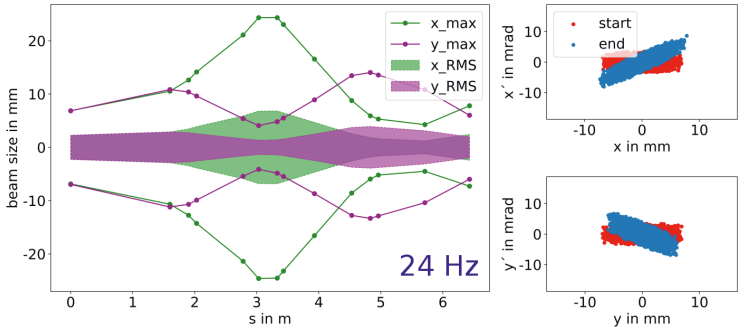

Figure V.29: *Left plot: Envelope ($6\sigma_{x,y}$ and $\sigma_{x,y}$) versus longitudinal position in the* 24 Hz *beamline shown in Figure V.26. Right plot: Phase space distribution at the beginning and at the end of the beamline for the horizontal (top) and vertical plane (bottom).*

horizontal beam size is identical at the beginning of the multiplexer compared to at its end. However, the shape and tilt of the phase space distribution in both transversal subspaces varies throughout propagation. From an ion optics point of view, i.e. the arrangement of beam manipulating magnets in Figure V.27, the beam lines that output the 384 Hz and 24 Hz pulse sequences are identical regarding the transversal beam size as confirmed in Figure V.28 and V.29. However, the 96 Hz pulse sequence carrying beam line differs by the lack of a second deflecting septum, i.e. dipole magnet, and thus requests slightly different quadrupole settings (given in Figure V.27) for point-to-point imaging. This results in minor differences in the beam dynamics as can be seen by direct comparison of Figure V.28 (or V.29) with V.30.

Note that the presented simulations do not take into account space charge induced defocusing effects on the beam by the self-interaction of the particles as well as by the indirect interaction of the particles with the conducting chamber wall. The insertion of these effects into the tracking calculations is relying on currently ongoing developments of a non-relativistic space charge tracking module of the

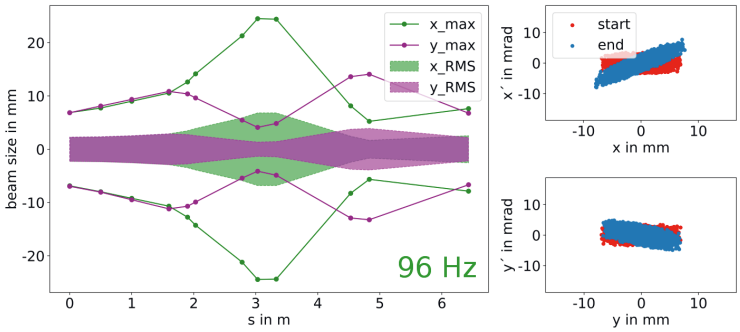

Figure V.30: *Left plot: Envelope ($6\sigma_{x,y}$ and $\sigma_{x,y}$) versus longitudinal position in the* 96 Hz *beamline shown in Figure V.26. Right plot: Phase space distribution at the beginning and at the end of the beamline for the horizontal (top) and vertical plane (bottom).*

used *Bmad* library [4]. However analytical approximations of the direct self-induced space charge and the indirect space charge for a 70 MeV, 100 mA and non-uniform Gaussian distributed proton beam with an RMS beam size of $\sigma \approx 3$ mm in a beam tube with 60 mm inner diameter suggest a relatively small defocusing strength of roughly $K_{\mathrm{SC,direct}} \approx 6 \times 10^{-3}\,/\mathrm{m}^2$ and $K_{\mathrm{SC,indirect}} \approx 6 \times 10^{-5}\,/\mathrm{m}^2$, respectively [104].

V.3.4 Magnet design

The conceptual layout of the multiplexer as derived in the previous subsections calls for a suitable design of three individual magnets as summarized in Table V.6.

Magnet	Magnetic field / Gradient	Length [m]	Duty cycle [%]
Fast kicker	31 mT	0.5	2
Septum	740 mT	0.75	100
Quadrupole	<4 T/m	0.3	100

Table V.6: *Magnet design parameters*

Since the design of the required quadrupole magnets as listed in Table V.6 is covered by standard options, this subsection focuses on the description of the required fast kicker magnets and opposite field septum magnets.

Kicker magnet

The multiplexer design requires a kicker strength of 31 mT. We plan to use a beam tube with inner diameter of 60 mm. The concept of the kicker magnet is based on a window frame design with bedstead coils as shown in Figure V.31. The dimensions of this design take into account the beam tube diameter plus additional spacing for mounting the vacuum tube. With a gap height of 90 mm and a maximal field strength of 40 mT, taking into account a 10 mT safety margin, we end up at

[4] `https://www.classe.cornell.edu/bmad/`

$NI = 3000$ A for the ampere turns. With 20 turns in total, we result in $I = 150$ A and an inductivity of $L = 300$ µH.

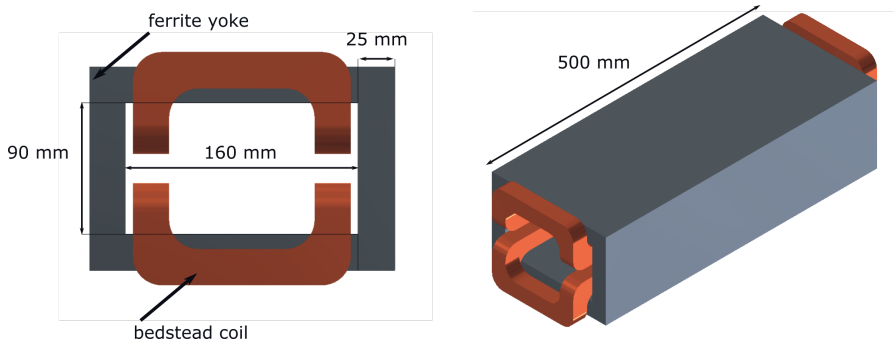

Figure V.31: *Conceptual design of fast kicker magnet of window frame design with ferrite yoke and bedstead coils. Left figure shows the front view, the right part the 3D extrusion.*

For the kicker magnet, a high performance power supply will be required to provide short rise times in order to distribute the pulses. Therefore, one needs to know precisely the specifications of such a power supply governed by the rise time of the current pulse delivered to the magnet. For this purpose, a simulation of eddy-current induced effects in the conducting walls of the beam pipe which predominantly limit the achievable rise times of the magnetic field seen by the beam was necessary.

Studies on the effect of eddy current-induced delays from the stainless steel beam tube during current ramping are displayed in Figure V.32. From Section V.3.1, we know that the required rise time of the magnetic field seen by the beam must be less than 800 µs. By taking into account a safety margin of roughly 50 µs, the rise time of the kicker magnet itself must be below 600 µs according to Figure V.32 in order to properly distribute the pulses to the target stations.

Septum magnet

For the septum magnet, we plan to employ a permanent magnet based system due to the fixed beam parameters of the HBS facility concerning particle energy (70 MeV) and particle species and thus a fixed magnetic rigidity of 1.23 T m. Lowering the integrated field of the septum magnet in order to operate the HBS at lower proton energies will be made possible by successively shortening individual permanent magnet based parts of the septum magnet with iron sheets.

The front face of the septum magnet is shown in Figure V.33. In this figure, the beam is going into the image plane. The septum magnet will be designed such that it offers two different field regions with reversed polarity, thus deflecting the beam entering into the left part of the septum further to the left and vice versa on the right side. The front face of the septum will be designed such that it takes up a beam with a beam size of 20 mm. The beam spots will be separated by 5 mm.

As shown in Figure V.34, the septum design generates a magnetic flux density of 750 mT. The cross section in Figure V.33 will be extruded to 0.75 m whilst also being extended in the horizontal plane in order to account for the trajectories of the protons in this magnetic field.

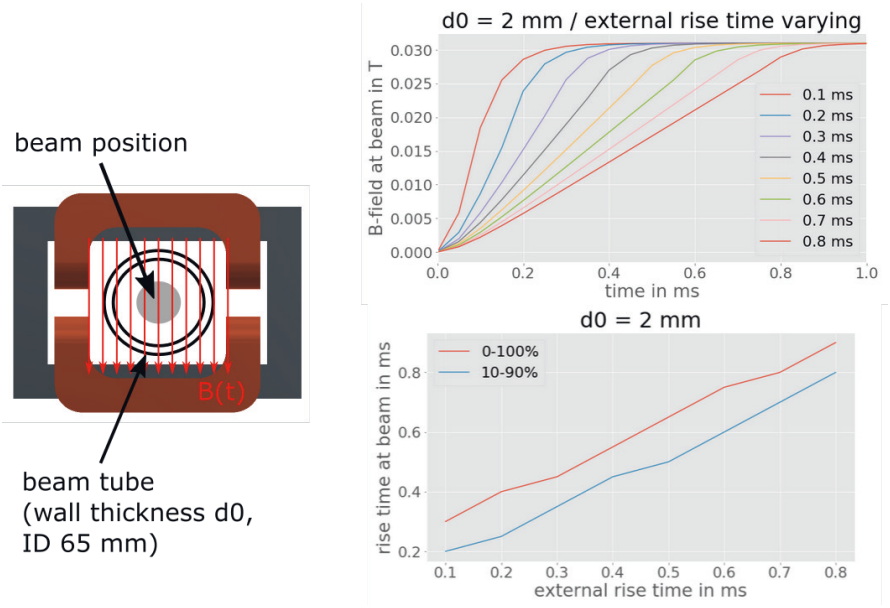

Figure V.32: *The left figure shows a cross-sectional view of the fast kicker magnet as presented in Figure V.31 including a stainless steel beam tube with an inner diameter ID of* 65 mm *and a wall thickness d0 of* 2 mm *as well as the position of the proton beam in the centre of the beam tube. The right figures show a study of the rise time of magnetic dipole field at the beam position in the left figure with respect to external rise time i.e. rise time of the magnetic dipole field outside of the beam tube. The study shows the effect of eddy current-induced delay of rise times from the stainless steel beam tube in the magnet by presenting the temporal evolution of the magnetic dipole field at the beam position for different external magnetic dipole field rise times (top right) as well as the rise time at the beam position versus external rise time (bottom right).*

V.4 Proton beam transport

The beam transport concept will be predefined by dividing the beam transport line of the HBS facility from the accelerator to the targets into three separate segments as shown in Figure V.35.

The HBS facility is based on a proton linac with a normalized rms emittance of approximately $\epsilon_{x(y)}^{\mathrm{norm,rms}} = 1$ mm mrad, a momentum uncertainty $\Delta p/p = 1\%$ and TWISS parameters $\beta_{x(y)} = 1$ m, $\alpha_{x(y)} = 0$ at the matching point to the beam transport line. In the following, one refers to three RMS widths of a gaussian beam profile, i.e. $6\sigma_{x(y)}$, when proton beam size is mentioned which includes approximately 99.5 % of the beam intensity[5]. The proton beam is transported to the top floor at roughly 10 m height by the first segment which will feature two double-bend achromat units as shown in Figure V.36, deflecting into the x-y plane and into the x-z plane successively. The corresponding beam dynamics of these units, each consisting of two quadrupole doublets at the beginning and the end in order to control the TWISS parameters, and a vertically focusing quadrupole to compensate the dispersion and two 45° sector bending magnets, are shown in Figure V.37. Since we bend the

[5]Note that in Subsection 3.2, one has a more relaxed definition of the beam size of $4\sigma_{x(y)}$ in the multiplexer section due to the special demands of two neighbouring opposite magnetic field regions in the septum magnet

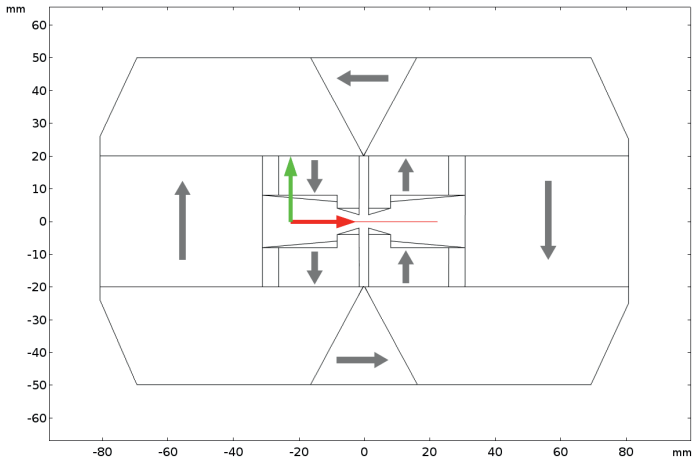

Figure V.33: *The graph shows the 2D geometry of the opposite field septum magnet. The beam is normal to the image plane. The areas comprising grey arrows indicate the permanent magnets and their orientation of magnetization. All other enclosed areas which are mounted on the permanent magnets represent the iron yoke, i.e. carbon steel. The centred area shows unoccupied space for the vacuum chamber including the two beam spots. The beam size at this position is approximated by* $4\sigma_x$ *to be* 20 mm*. The magnetic field gradient during which the dipole field is inverted when going from the left side to the right side of the septum magnet occurs on* 5 mm *horizontal length resulting in* 25 mm *centre-to-centre separation between the two beam spots. The red line shows the cut-line which was used in Figure V.34.*

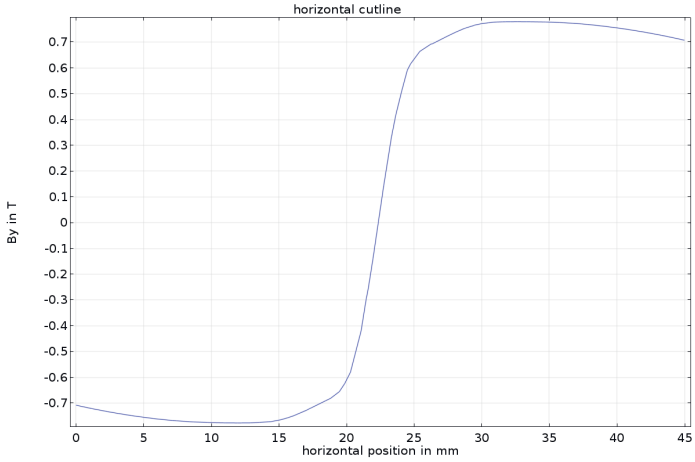

Figure V.34: *This plot shows the magnetic flux density y-component versus* x *coordinate. The* x*-coordinate follows the cutline in Figure V.33.*

beam in both horizontal and vertical degrees of freedom over the whole beam transport line, we aim for dispersion-free optics in the beam transport line to the top floor and from the top floor to the target.

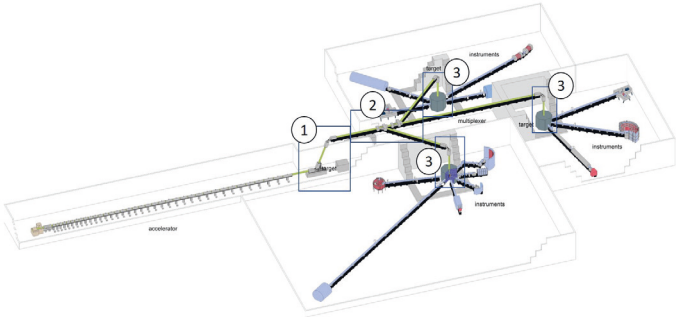

Figure V.35: *Layout of the HBS facility with three target stations. The target stations are classified according to proton pulse structures as indicated. The beam transport from the accelerator to the target station can be subdivided into three segments as shown in the figure. Segment 1 represents an achromatic system to transport the beam to the top floor. Segment 2 comprises the multiplexer unit and segment 3 uses units from segment 1 in order to bend the beam towards the target station without dispersion.*

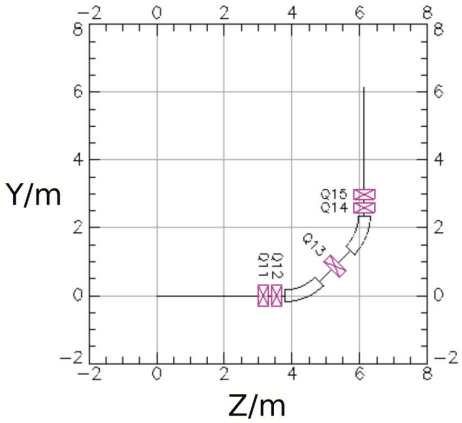

Figure V.36: *Double-bend achromat systems as used in the first and third segment according to Figure V.35. This system will be used in three different orientations: one for bending up into the vertical plane and another one for bending back into the horizontal plane in segment 1. Another one is used for bending down into the vertical plane and towards the target station in segment 3.*

This works for the first segment according to Figure V.37 in combination with a point-to-point imaging of the beam size. Note that in general it was important to keep the betatron amplitude $\beta_{x(y)}$ smaller than 40 m in order to utilize an inner beam tube diameter of 60 mm.

After beam transport to the top floor, segment 2 takes over which comprises the multiplexer device. Hence, this segment separates into three beam lines during propagation. As shown in Figure V.27, this segment comprises a quadrupole triplet. The matching point of this segment is 3 m distant from the last quadrupole of the first segment and 1.6 m prior to the first quadrupole of the multiplexer segment.

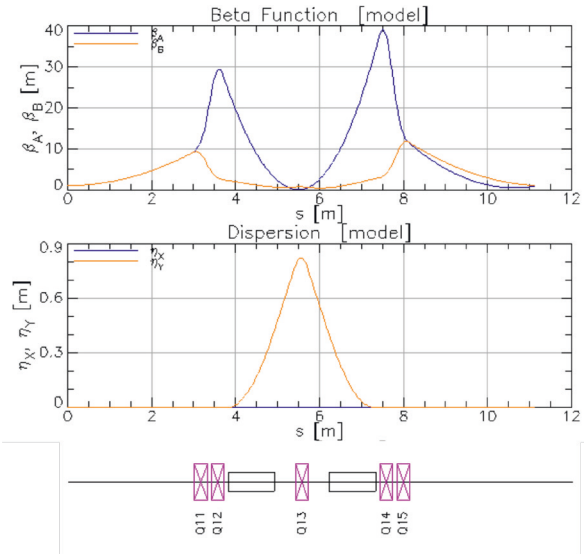

Figure V.37: *Beam dynamics of double-bend achromat systems as used in the first and third segment according to Figure V.35.*

Finally, after segment 2, the 24 Hz and 96 Hz beamlines introduced by the multiplexer, as shown in Figure V.26, will obtain an angular separation of roughly 80° from each other. The 384 Hz beamline is straight with roughly 2 m horizontal offset. The spacing between the target stations is controlled by the length of the beamline from segment 2 to segment 3 (after each meter, one gains approximately 1.4 m additional horizontal separation between the 24 Hz and 96 Hz beamline), which can be realized by further quadrupole triplet configurations as used already in the Multiplexer. Each of these systems extends the beam transport to the target by 5.5 m.

At last, segment 3 reuses the double-bend achromat configuration utilized in segment 1 in all of its three beamlines to bend the beam vertically into the x-y plane in order to irradiate the targets from the top. By using quadrupole triplet configurations in the beamline prior to segment three, one obtains a beam spot on the target with a diameter of 10 mm (as extracted from the linac) which can then be scanned by a kicker system within one pulse of minimum 52 µs over a target area of 100 cm^2. The sector dipoles operate below 0.9 T on 1 m effective length. All dipoles can be connected in series.

V.4.1 Proton beam dump

The beam dump is positioned behind the first dipole magnet of segment 1 on the accelerator level as displayed in Figure V.35. The design of the beam dump is adapted to a possible energy, and thus power, upgrade of the accelerator to 100 MeV and an increased duty cycle resulting in 7.5 mA average current. With a 16 % safety margin, the design goal of the beam dump is to withstand 1 MW average beam power. The expected operating time of the beam dump as a safety device is very low, i.e. it will be used in case of emergency to dump the beam prior to RF shutdown of the accelerator. However, the beam dump is also required for beam adjustment and maintenance. In this case, continuous operation of the beam dump of up to 2 weeks per year needs to be guaranteed. During this scenario the ion optics will be adjusted such that the beam is defocused before impinging on the beam dump, thus lowering the power density.

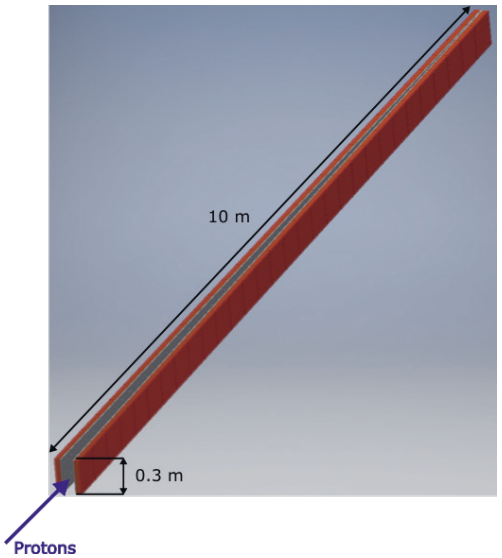

Figure V.38: *Beam dump design for* 1 MW *beam power. The total length of the system will be about* 10 m. *The height will be about* 0.3 m. *Two symmetrical elements will be inclined by about* 0.5° *in order to gradually distribute the beam power over* 10 m.

The beam dump will be made up of several small units. Each unit consists of 30 graphite tiles, each 1 cm thick and 5 cm by 5 cm wide. These graphite plates are bonded onto a 5 cm thick, 30 cm by 30 cm wide copper layer. The protons are stopped in the graphite which has a high resistance to blistering and which shows only minor activity. The copper serves as heat conductor, and a cooling structure for water is applied to the underside. As shown in Figure V.38, bricks of graphite, copper and a cooling structure will be stacked next to each other such that the total beam power is distributed over 10 m within the beam dump. Two stacks are then inclined so that the beam power is gradually deposited in the beam dump.

V.5 Target

The basic function of the target is to produce neutrons by way of a nuclear reaction. Thereby 100 kW beam power is deposited inside the target and converted to heat which needs to be removed efficiently. During the operation, the target is subject to strong loads which could endanger the target integrity. Previous investigations show that there are two main risks concerning the target integrity, i) the hydrogen embrittlement and ii) the mechanical stress due to temperature gradients.

Hydrogen embrittlement is caused by proton accumulation and the creation of hydrogen bubbles due to the high current proton beam. The protons lose energy as they pass through the target material and are stopped inside the target which might lead to a target failure. A careful material selection is thus made in order to maximize the neutron outcome and reduce the risk of hydrogen embrittlement. The basic design of the target is chosen to reduce the risk of hydrogen embrittlement, to remove heat efficiently and handle mechanical stress.

V.5.1 Material selection

In a compact accelerator-driven neutron source, the production of neutrons is based on the interaction of light ions such as protons or deuterons with the atomic nuclei of a dedicated target material as described in Chapter V.1. Additionally to the considerations regarding the neutron yield, the chosen target material should exhibit, besides a high melting point, a suitable combination of thermo-mechanical properties such as high thermal conductivity, low thermal expansion coefficient to reduce thermal and particularly fatigue stress, good elasticity and ductility and high yield strength to act as a solid target. These properties are very important since the target has to withstand a range of temperature differences and stress. Furthermore, high hydrogen solubility i.e. a high blistering threshold, low chemical reactivity and low radiation damageability are required for physico-chemical stability. From materials studies in the field of target development for spallation sources [105, 106] we identify within the material range of $70 < Z < 82$, tantalum and tungsten as the most promising materials for the design of a high performance HBS-target. Neutron yields calculated from the irradiation of the two materials with 70 Mev protons or deuterons are summarized in Table V.7. Relevant properties of tantalum and tungsten for target development are given in Table V.8.

Tungsten is a high density (19.293 g cm^{-3} at 20 ^{o}C [107]) material with a high melting point (3414 ^{o}C [107]) and has excellent corrosion resistance. It has a high thermal conductivity (174 W m^{-1} K^{-1} at 20 ^{o}C) and a low thermal expansion coefficient ($4.50 \cdot 10^{-6}$ m m^{-1} K^{-1} at 20 ^{o}C) [107]. When soft, its elastic modulus is 415 GPa and its yield strength 550 MPa at 20^{o}C [107]. These properties make tungsten attractive for a solid target. However, the manufacturability of tungsten is limited due to its hardness and brittleness at room temperature. Under proton or fast neutron irradiation tungsten becomes much harder and more brittle and losses in ductility [108, 109, 110]. Irradiated tungsten fails at stresses far below the yield stress of unirradiated material [108, 109]. Additionally, due to its extremely low hydrogen solubility ($1.3 \cdot 10^{-19}$ H/W at 100 ^{o}C and 1 atm [111]), tungsten shows pronounced blistering behaviour [112]; its blistering threshold (proton fluence), 2-4 $\cdot$ $10^{22}m^{-2}$ [113], being low, though radiation damage could suppress to some extent the formation of blisters [114]. Furthermore, tungsten is subject to serious corrosion when in contact with water under irradiation [108, 115].

Tantalum is a hard and ductile high density (16.656 g cm^{-3} at 20 ^{o}C [107]) material with a very good workability. It has high corrosion resistance and is inert to practically all organic and inorganic substances. The melting point of tantalum is high (2996 ^{o}C [107]). Its thermal conductivity (57.55 W m^{-1} K^{-1} at 20 ^{o}C [107]) is three times lower than that of tungsten. The thermal expansion coefficient of tantalum ($6.5 \cdot 10^{-6}$ m m^{-1} K^{-1} at 20 ^{o}C [107]) is somewhat higher than that of tungsten. When soft and recrystallized, its elastic modulus is 179 GPa and its yield strength is 310 - 380 MPa at 20^{o}C [107]. In the presence of protons or fast neutron irradiation, tantalum shows hardening with reduced ductility [108, 109, 116]. Pure tantalum exhibits excellent ductility even after irradiation [116]. Furthermore, tantalum has a very high hydrogen solubility (0.76 H/W at 100 ^{o}C and 1 atm [117]) and its blistering threshold ($> 230 \cdot 10^{22}$ m^{-2} [113]) is higher than that of tungsten. Moreover, no corrosion occurs when in contact with water under irradiation [108].

	Protons		Deuterons	
Element	Thickness [mm]	Neutron yield $10^{14}s^{-1}mA^{-1}$	Thickness [mm]	Neutron yield $10^{14}s^{-1}mA^{-1}$
Ta	5.07	9.0	3.14	10.2
W	4.38	9.8	2.72	10.3

Table V.7: *Neutron yield analytically calculated for the irradiation of tantalum and tungsten with protons and deuterons with energy of 70 MeV. The thickness of the material is set to fully stop the ions.*

Element	Melting point	Thermal conductivity	Yield strength	Blistering threshold
	°C	$Wm^{-1}K^{-1}$	MPa	$10^{22}m^{-2}$
Ta (soft, recrystallized)	2996	57.55	310 - 380	$\geq$ 230 [113]
W (soft)	3414	174	550	2 - 4 [113]

Table V.8: *Relevant properties of tantalum and tungsten for target development. The blistering threshold describes the proton fluence.*

Hence, tantalum exhibits clearly better characteristics under irradiation than tungsten to withstand a high intensity proton beam. In particular, its capacity to store large amounts of hydrogen to suppress blistering should be a benefit for the target lifetime. Despite the lower thermal conductivity and yield strength, tantalum (soft, recrystallized) is the material of choice for the design of a target with adapted cooling to reduce induced thermal and mechanical stress.

V.5.2 Neutron spectrum

The neutronic properties (total neutron yield, neutron energy spectrum and angular distribution) of a 5.07 mm thick tantalum target irradiated with 70 MeV protons were studied by numerical simulation using the MCNP toolkit and the cross sections for proton reactions recorded in the TENDL 2017 database. These properties are important for the design and optimization of the moderator/reflector assembly as well as for safety aspects related to radiation protection. The total neutron yield estimated with MCNP is, $9.1 \cdot 10^{14}$ $s^{-1}mA^{-1}$, a value which agrees well with the analytically calculated one (see Table V.7). The angular distribution and the neutron energy spectrum for the primary neutrons created by the Ta(p, xn) reaction for 70 MeV protons is presented in Figure V.39. The simulation indicates that the neutrons are slightly forward directed with 55% of the neutrons emitted in moderator direction and 45% backwards in accelerator direction. The peak energy of the neutrons is 0.45 MeV and the neutron spectrum goes up to 70 MeV.

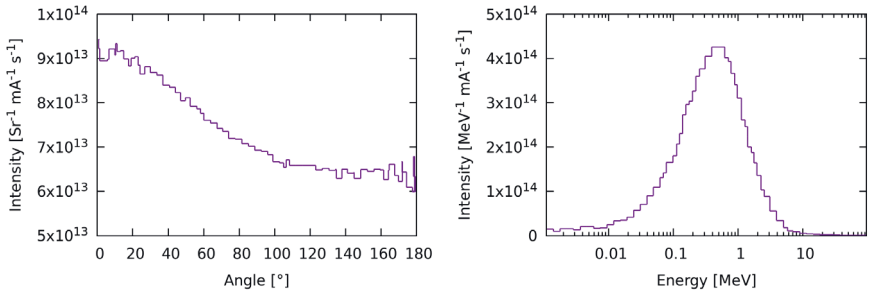

Figure V.39: *Angular distribution (left) and neutron energy spectrum (right) for the primary created neutrons by the Ta(p, xn) reaction for 70 MeV protons. The angular distribution is integrated over the whole energy range and the energy spectrum is integrated over 4 π.*

V.5.3 Basic target design

The design of the target must ensure safe and reliable operation at 100 kW. Two target designs are proposed to achieve this goal (see Fig. V.40): an internally-cooled target design and a externally-

cooled target design. The internally-cooled design follows the concept of high brilliance in a consistent manner. For this purpose a target is required which is as compact as possible, considering the thermal load generated by the proton beam. The externally-cooled reduces the mechanical stress inside the target by decoupling the heat sink and the target via a liquid, thermally conductive layer. Each target design follows its own philosophy, however both are based on the same guiding principles regarding stability.

As mentioned before, the main risks concerning target integrity are hydrogen embrittlement and mechanical stresses. In addition to the presented material selection, the risk of hydrogen embrittlement is further reduced by the adjustment of the target thickness to proton energy in order to avoid hydrogen implantation at the Bragg peak [6]. Instead, the protons are stopped inside a dedicated layer at the distance of the Bragg peak behind the target. By the combination of the two measures, the adjustment of the target thickness and the use of tantalum, no critical hydrogen accumulation is expected.

Most of the mechanical stress is caused by thermal loads. The small dimension of the target in combination with the high power induced by the proton beam generates strong temperature gradients within the target and thus appropriate cooling designs, mountings and material selections are required. Within the few last years, previous developments for CANS have tried to manage these thermal-induced stresses by using a rotating target or liquid targets or a combination of different materials. HBS has developed a stationary solid target in order to decrease the complexity and enhance the target's reliability. The basic target consists of a mounting system and a tantalum device which is either internally or externally cooled by water.

		Heat transfer coefficient	Achievable power density
Method	**Coolant**	$W\ m^{-2}\ K^{-1}$	$kW\ cm^{-2}$
External	Water	4,000 - 16,000 [118]	0.13
forced cooling	Liquid metals		0.26
External	Water	4,000 - 4,700 [119]	0.2 - 0.4
heat sink	Liquid metals		0.4 - 0.8
Microchannels	Water (1-phase)	10,000 [120]	0.2 - 3.0 [121]
	Water (2-phase)	100,000 [120]	3 - 380 [122]
	Liquid metal		1 - 3.5 [12]

Table V.9: *Cooling capabilities of various cooling concepts*

It has been recognized that heat dissipation and mechanical stability are the two main limitation factors during the development of a high density power target. Although heat dissipation capacity strongly depends on the exact conditions of the respective situation including factors such as pressure, velocity and the geometry, the order of magnitude of cooling power for different cooling methods can be found in the literature. A brief summary is shown in Table V.9. It can therefore be concluded that conventional water cooling with or without a heat sink is not sufficient to reach the desired heat removal capacity in the order of $1\ kW/cm^2$. The use of liquid metals (e.g. gallium, galliastan) could enhance the heat removals capacity compared to water coolants, but this still does not achieve the desired value. By contrast, the use of micro channels indicates that sufficient cooling power can be achieved. Micro channels minimize the viscous boundary layer which is the main cause for thermal resistance at the interface between the coolant and the walls. Several published experiments achieved heat fluxes which are significantly above the desired $1\ kW/cm^2$.

[6] The energy loss per penetration depth is a function of the proton energy. This means that for a mono-energetic proton beam the protons are stopped inside a small interval at the position of the so called Bragg peak

Figure V.40: Comparison of internally-cooled (left) and externally-cooled (right) target: 1: target material, 2: beam stop, 3: cooling channels, 4: heat sink, 5: structural material

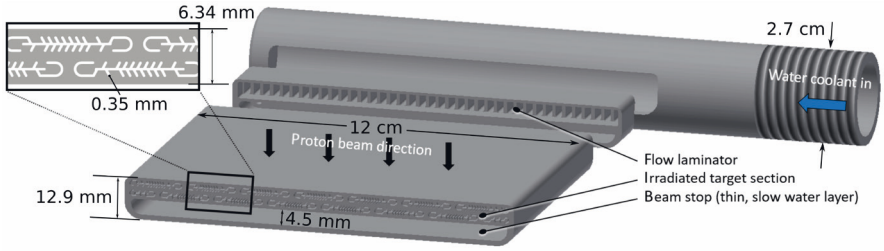

Figure V.41: Basic structure of the internally cooled target

Internally cooled target

The guiding principle of the internally cooled target is for it to be as compact as possible on the one hand and extremely reliable on the other. Brilliance is a property of the neutron beam which, among others, depends strongly on the target-moderator assembly dimension. Thus reducing the target size leads to an increase of the brilliance of the neutron beams. Miniaturization is limited by the thermal stresses and heat removal capacity. Thermal stresses arise as a result of temperature gradients inside a component or inside an assembly, whereas the heat removal capacity is correlated to the size of the cooled area.

The basic structure of the internally cooled target is shown in Figure V.41. The figure shows a coolant feed water line, the flow laminator and one half of the irradiated target section. Each component of the target consist of tantalum and the single components are welded together into a solid unit. The irradiated centre of the target consists of a rectangular plate with a length of approximately 12 cm, penetrated by micro channels. Both open sides of this plate are connected to one feed water line and one discharge pipe, respectively. The flow laminators are interconnected between the supply lines and the tantalum plate in order to reduce the force acting on the micro channel openings which are caused by the momentum of the water. The thickness of the irradiated tantalum plate is adjusted to the lower stopping power of water compared to tantalum and thus the thickness is increased from 5 mm to 6.34 mm. After passing this plate, the protons are halted by a dedicated beam stop layer made of water. This water layer is covered by a thin tantalum wall. A comprehensive view of the target is presented in Figure V.42.

The inner micro channel cooling has two main advantages compared to a conventional one-sided cooling. On the one hand, the boundary surface between the water coolant and the target material is increased significantly, or rather by a factor of 8.5 for the present geometry. The heat transfer at this surface is the dominant heat transfer resistance and thus the increase in surface area also enhances the heat flux. On the other hand, heat is removed inside the target and thus the temperature gradients

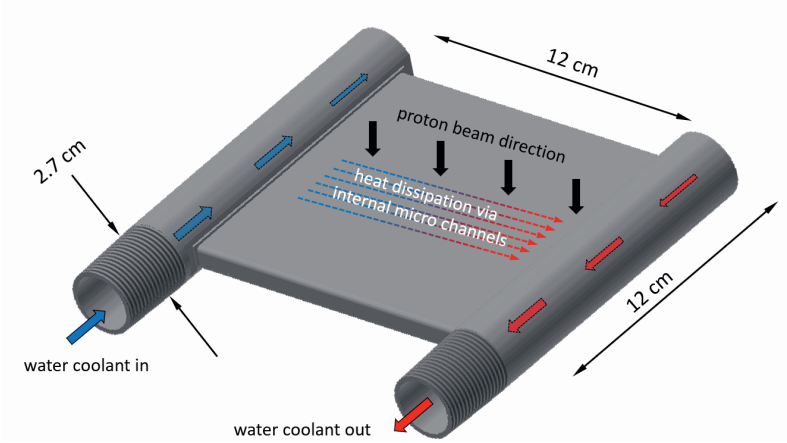

Figure V.42: *Basic functionality of the internally-cooled target*

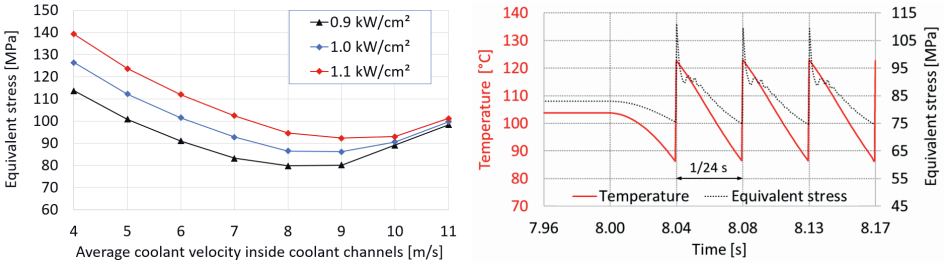

Figure V.43: *Left: Equivalent stress inside the target caused by temperature induced stress (time averaged beam power) and coolant pressure. Right: Time dependent maximum of temperature and stress inside internally cooled target caused by 100 mA pulsed proton beam at 24 Hz at 8 m/s coolant flow*

within the target are smaller compared to conventional one-side cooling due to the reduced thickness of the tantalum that requires cooling.

Beside the heat dissipation capacity, the mechanical stresses are the second limiting factor in terms of achievable power density. Temperature gradients inside the target cause stress as well as pressure gradients and forces created by the mounting or impinging coolant. Thus, the reduction of the temperature gradients reduces the stress inside the target which is achieved by the internally-cooled target geometry.

The actual cooling capacity of a micro channel system depends on the flow velocity and the channel geometry. In general, a higher flow velocity or smaller micro channel width increases the heat transfer capacity and thus reduces mechanical stresses. However, both parameters have an impact on the pressure loss inside the channels, which contributes to mechanical stress, making an optimization process necessary. Figure V.43 shows simulation results of the maximum equivalent stress inside the target caused by temperature-induced stress and the coolant pressure over the average flow velocity inside the target. The simulations were performed with ANSYS CFD and ANSYS FEM and based on micro channels with a width of 0.35 mm. Preliminary studies have shown that this width is a good compromise between pressure loss, heat removal capacity and the available manufacturing technology. The graph at Figure V.43 indicates that the lowest stress values can be expected at flow

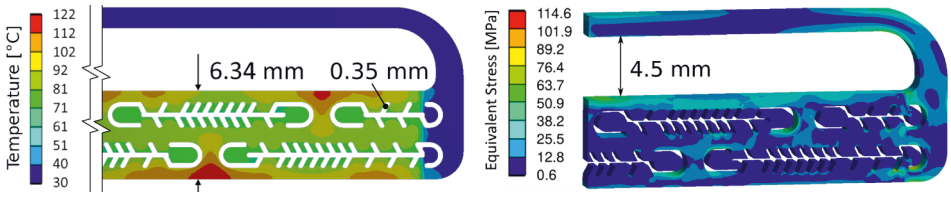

Figure V.44: *Left: Temperature distribution (left) and stress distribution (right) in a section of the internally cooled target directly after one proton pulse irradiation of a 24 Hz cycle.*

velocities between 8 m/s and 9 m/s. Lower velocities reduce the pressure-induced stress but increase temperature-induced stress. For higher velocities the pressure loss becomes dominant in relation to the temperature-induced stress and hence the total stress rises. In the later investigations, a flow velocity of 8 m/s was chosen, which causes a pressure drop of $1.8 \cdot 10^5$ Pa within the channel length of 10 cm and results in a strong heat transfer coefficient inside the micro channels of $4.3 \cdot 10^4$ W/m^2/K.

The highest loads on the target occur during the lowest proton beam repetition rate due to the longest irradiation time within one pulse. The time-averaged thermal load and the thermal peak load are constant at all repetition rates. For this reason, a transient thermal and structural FEM simulation was performed for the 24 Hz thermal load case. The result of the time-dependent behaviour of temperature and stress are shown in Figure V.43. The first 8 seconds of the simulation are performed with a constant heat load in order to save computation time. After 8 seconds, a pulsed heat load simulates the pulsed proton beam. The average temperature of the target is in the range of 100 °C. The highest temperature inside the internally-cooled target does not exceed 124 °C at the chosen design. The maximum stress is below 120 MPa, which is well below the yield strength of the tantalum material of 310 MPa. However an optimization of the arrangement of the micro channels will further decrease the tension.

The temperature distribution at a section through the target at the end of one proton pulse is shown in Figure V.44. The non irradiated side of the target as well as the beam stop cover plate both show almost no sign of being heated. Within the irradiated section, the temperature distribution is quite homogeneous due to the arrangement of the coolant channels. The stress distribution at a section through the target at the end of one proton pulse is shown in Figure V.44 at the left side. Since the stress inside the target is caused by temperature gradients and water pressure, there is no uniform stress curve within the target, however there are two regions with stress peaks. The first region ins which stress peaks occur is the boundary of the tantalum beam stop cover. The stress peaks occur at this position because the beam stop cover act like a lever arm. The second region in which stress peaks occur are the ends of the micro channel fins, which have some kind of a notch effect. A reduction of the local stress peaks through geometric optimization is currently being performed although all local stress peaks are already below the acceptable stress limits ind of notch effect due to the internal water pressure.

Externally cooled target

In contrast to the internally cooled target presented in Section 5.3 which was optimised for the highest brilliance with a compact design utilising innovative cooling techniques, the externally cooled target is optimised for a good filling of many neutron guides. The dimensions are therefore relaxed in order to allow a larger space for the neutron guide placement in the target-moderator assembly. The requirements for the heat density removal capacity are thus not as strict as for the internally cooled target and rather conventional cooling techniques can be utilised.

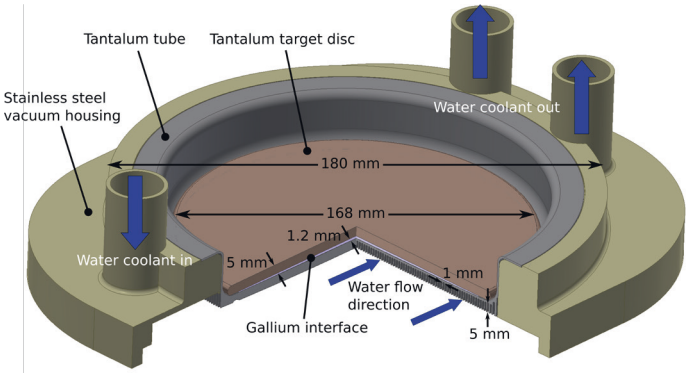

Figure V.45: *Basic structure of the externally cooled target with the tantalum target disc lying on a gallium interface layer embedded in a tantalum tube*

The basic design as presented in Figure V.45 consists of a 168 mm diameter and 5 mm thick tantalum disc "floating" on a 1.2 mm thick liquid gallium layer placed inside a 180 mm diameter and 1 mm thick tantalum tub acting as a heat sink. These compounds are mounted by a structure material like cobalt free stainless steel also acting as a vacuum barrier. The tantalum disc acts as the neutron production material, the liquid gallium interlayer servers as a thermal interface material as well as a proton beam stop between the tantalum disc and heat sink.

The advantage of a liquid metal interlayer is the possibility to keep thermal contact between target and heat sink, which allows slight deformation of the target and the heat sink. The risk of thermal delamination especially under thermal cycling is thereby avoided as well as the generation of tension peaks at the interface, like it could occur with rigid bonding. The gallium also acts as a beam dump, preventing the target material, as well as the heat sink, to be embrittled by entrapment of hydrogen isotopes too quickly. This can be realised by choosing a slightly thinner target disc than the range of the ions in the material, i.e. by positioning the Bragg peak inside the Ga layer.

The material for the tub needs to withstand the aggressive gallium layer and it needs to act as a structure material. Liquid metals attack solid metals by a mechanism called liquid metal corrosion or liquid metal embrittlement. Refractory metals such as tantalum, tungsten, molybdenum show little or almost no reaction to liquid metals [123]. Tantalum was therefore chosen for this target concept, besides the properties described in Chapter V.5.1 . Other materials might show improved thermo-mechanical properties like the molybdenum alloy TZM (Mo99/Ti0.5/Zr0.1) and thus further improvement of the concept might be possible within the TDR. The thermal conductivity is 126 W m^{-1} K^{-1} [124] and the constituents Mo and Ti are resistant to gallium [125, 126].

An array of cooling channels of 1 mm with and 5 mm height are machined in the tantalum block with a spacing of 0.5 mm to each other. The effective cross section area of the total of 206 micro channels is 515 mm^2. The cooling fluid is fed trough two feed-water pipes with a inner diameter of 25 mm each and its velocity is reduced in the D-shaped cavity volume. From there it flows trough the array of channels and is afterwards collected in a second D-shaped cavity. With a cooling medium velocity of 6 m/s causing a pressure drop of 10.000 Pa across the channels, the performed ANSYS CFD simulations show a heat transfer coefficient of 3.5×10^4 W m^{-2} K^{-1} which was afterwards used for the ANSYS FEM simulations.

In Figure V.46 the temperatures inside the target simulated with ANSYS FEM are presented for an average power deposition of 100 kW with a homogeneous power density profile throughout the target thickness. On the left hand side, the temperatures inside the target are presented for the static case. The temperature rises throughout target layer from around 200 °C at the gallium interlayer

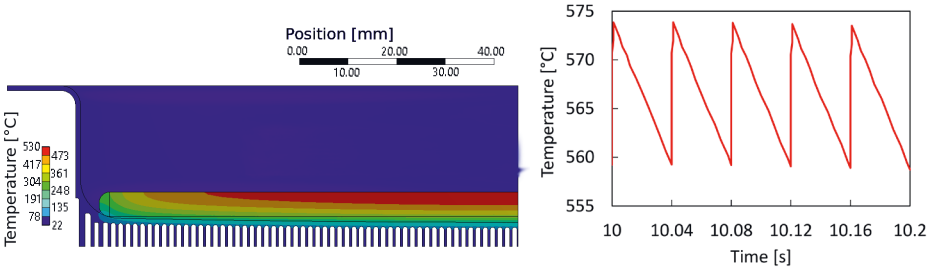

Figure V.46: *Left: Temperature in the target disc for a steady state operation. Right: Temperature in the target in pulsed mode with 24 Hz after reaching steady state*

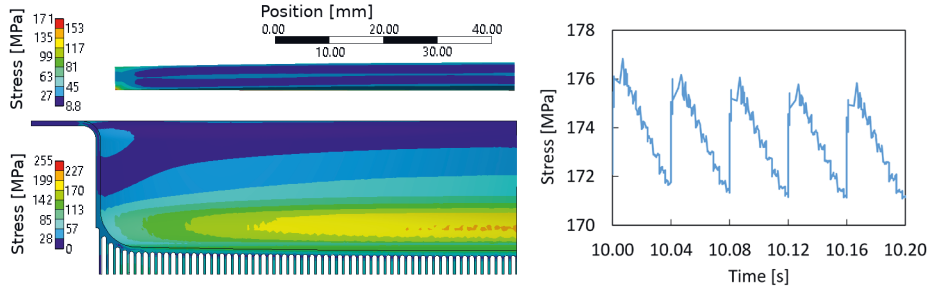

Figure V.47: *Left: Stress in the target disc (top) and the tantalum tub (bottom) for the steady state at an average power of 100 kW. Right: Stress in the target in pulsed mode with 24 Hz proton beam frequency.*

up to 520 °C at the target surface as the heat is just removed from one side. This temperature rise is depending on the thickness of the target and therefore on the proton energy [95] and might be reduced with a lower proton energy. On the right-hand side, the time dependent maximum temperature inside the target for a 24 Hz proton beam is presented, which would result in the highest temperature difference of around 15 °C. For the higher frequencies, the temperature difference would be smaller as the proton pulse width scales with the frequency.

As the temperature in the gallium interlayer rises up to 200 °C and inside the tantalum target up to 520 °C, an evaporation of the materials might be happening. But with a vapor pressure (presented in Figure V.48) at these temperatures of approximately 10^{-19} Pa and 10^{-39} Pa for gallium and tantalum [127], respectively, an evaporation of the individual materials can be neglected.

As the gallium liquid interlayer decouples the target and the tub mechanically, each was simulated with ANSYS FEM for the mechanical stress separately and is presented in Figure V.47. On the left hand side, the mechanical and temperature induced stress for the static case is presented. Inside the target disc, the stress is below 100 MPa but rises up to 170 MPa at the corners. The stress inside the tub is larger and rises up to 250 MPa at the centre of the tub but well below the yield strength of tantalum. A further optimisation or a different material might further reduce the stress. On the right hand side, the stress inside the target disc for a 24 Hz proton beam is shown. The difference is around 4 MPa which is a region where no fatigue problems are expected.

Due to the conventional design of the heat sink, the pressure drop is not very large and the size of the target structure can be scaled quite well. Additionally, the tantalum disc does not act as a structure material and thus the thickness can be reduced as by the proton energy required. This concept can therefore be scaled down to lower proton energies.

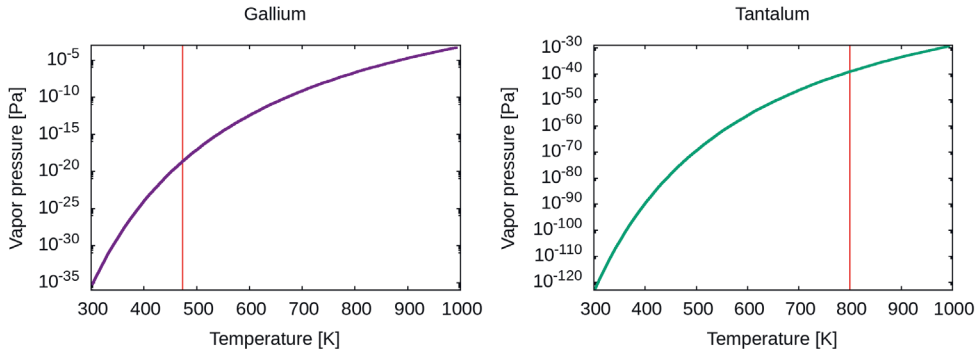

Figure V.48: *The graph shows the vapor pressure for gallium on the left-hand side and for tantalum on the right-hand side [127]. The red line indicates the highest temperature present in the target assembly for the different materials.*

V.6 Moderator-reflector assembly

The primary neutrons emitted from the nuclear reaction of the protons with the target are typically released with some MeV kinetic energy (see Chapter V.5.2). This corresponds to equivalent temperatures well above 10^{10} K. The spectrum demanded by the instruments covers the range between 1 meV (e.g. for a SANS diffractometer, a reflectometer, or a backscattering spectrometer) up to around keV (e.g. for neutron imaging or PGNAA analysis), corresponding to temperatures between 15 K and 10^{7} K. Moderator materials are used to reduce the energy of the neutrons towards the temperature of the moderator material via collisions with the atomic nuclei of the moderator material and thus enable the adjustment of the neutron energy to the experimental needs.

For a high brilliance neutron source, it is mandatory that the neutron cloud originating from the very compact target volume is enlarged as little as possible to achieve a high density of thermalized neutrons that can efficiently be extracted and directed towards the instruments. This is achieved by an onion-shell assembly with a high-density hydrogen-based thermal moderator surrounded by reflector material that sends back the neutrons escaping from the moderator region with a high probability. The target is inserted into the thermal moderator, so that the primary neutrons are emitted preferentially towards the centre of the thermal moderator. Additional one-dimensional cryogenic moderators are inserted in the extraction channels to supply neutron spectra below room temperature to the individual instruments as needed. The complete HBS target and thermal moderator ensemble is surrounded by a suitable reflector system inside a radiation-shielding cage (see Figure V.49).

The velocity of a neutron is proportional to the square root of its energy and inversely proportional to its wavelength. The classification of the neutron spectra within this CDR is shown in Table V.10 and follows the proposal according to [128]. The energy spectra demanded by the instruments vary over several orders of magnitude and include cold, thermal, and fast neutron spectra. The energy is transferred via inelastic collisions from the neutrons to the molecules of the moderator. Typically, the lighter the nuclei of the scattering material are, the higher is the amount of energy transferred in every collision. For that reason, materials with a high portion of hydrogen, beryllium, or carbon are preferable for neutron moderation.

Different types of moderators are necessary to provide these spectra. The thermal moderator surrounds the entire target including the end of the proton beamline, so that almost all high-energy neutrons emitted from the target can be used. Thermal beams can be extracted from the flux maximum inside the thermal moderator through extraction channels. Additionally, suitable cold moderators can

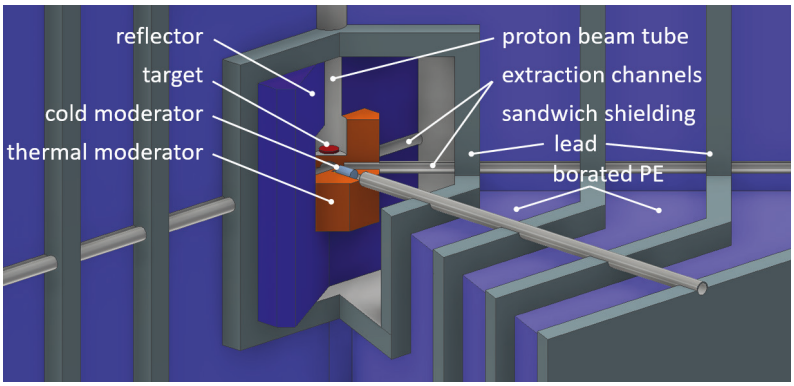

Figure V.49: *A peek into the Target-Moderator-Reflector (TMR) unit*

	Wavelength	Energy range
Fast neutrons		$E > 10$ keV
Resonance neutrons		2 eV $< E < 10$ keV
Epithermal neutrons		500 meV $< E < 2$ eV
Thermal neutrons	0.4 Å - 3 Å	10 meV $< E < 500$ meV
Cold neutrons	3 Å – 9 Å	1 meV $< E < 10$ meV
Very cold neutrons	> 9 Å	$E < 1$ meV

Table V.10: *Wavelength and energy ranges of moderated neutrons. In addition, the term "Hot neutrons" can be applied for the wavelength range 0.1 Å – 0.8 Å.*

be placed into individual extraction channels inside the thermal moderator. The reflector surrounds the entire thermal moderator and is penetrated by the extraction channels. The moderators are intrinsic parts of the instruments. The thermal moderator is shared between all instruments built at a single target station, while secondary one-dimensional moderators, e.g. cold sources, are individual for a single instrument. The exchange of the one-dimensional moderators can be performed at short notice during a source shutdown; the thermal moderator can be exchanged whenever the target is changed.

Within this CDR, we present the design of a high-density polyethylene thermal moderator and one-dimensional cold moderators based on liquid para H_2 or solid CH_4 together with simulation results of the neutron spectra emitted. Transient resonance or epithermal neutrons are available during the incomplete moderation process in the thermal or cold moderators. Many ideas for other secondary moderators are available. Some of them exceed the potential of the simulations presently available because of a lack of nuclear databases. Experimental work is ongoing to characterize the neutron spectra emitted from some of the most promising candidates. Other ideas, e.g. hot sources or ultra-cold neutron moderators, need to be designed and evaluated in the context of a specific instrument, which is beyond the scope of this CDR.

V.6.1 Thermal moderator

According to the current concept, the thermal moderator in every target station will be made of polyethylene with a diameter of about 20 cm. The thermal moderator encloses the end of the proton beam line including the target and is surrounded by the neutron reflector.

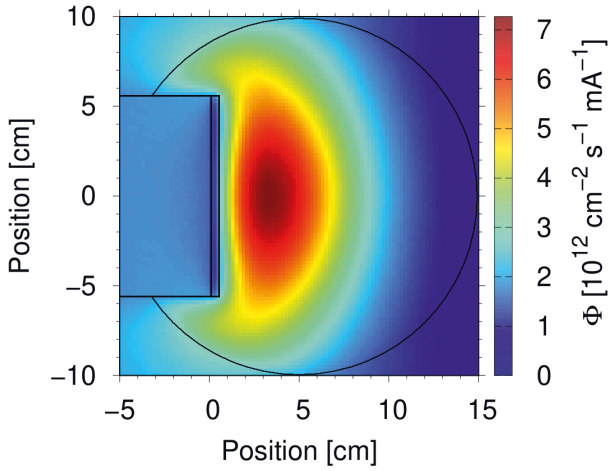

Figure V.50: *Map (horizontal cut) of thermal neutron flux (10 meV $\leq E \leq$ 500 meV) inside the thermal moderator and reflector. Proton beamline enters on the left, the left face of the target is at the origin of the coordinate system.*

Figure V.50 shows the time-averaged thermal neutron flux inside the moderator-reflector assembly. The thermal flux maximum is located about 3 cm downstream the target, well surrounded by thermal moderator material. An intense, directed thermal neutron beam can be extracted from the thermal flux maximum by the use of an extraction channel (see Figure V.55 without cryogenic insert) [129].

It is clearly visible that the thermal moderator according to this concept is too big to be illuminated homogenously and too dense to place a reasonable number of extraction channels into the flux maximum. We currently follow several ideas to optimize the distribution and extraction of thermal neutrons, but the results are not yet available for the presentation in this document and will be published independently.

The extraction channel is placed into the maximum of thermal flux and allows one to extract a neutron beam directed to the instrument, while the neutrons outside the divergence range towards the instrument re-enter the moderator volume to keep the density of the thermal neutron cloud. For this reason, the flux depression due to the extraction is negligible.

Figure V.51 shows the peak brilliance of a neutron beam extracted from the thermal moderator. As expected for a 1-dimensional extraction system, the highest brilliance is achieved for the smallest diameter of the channel. In the case of larger extraction channels it is observed that they need to be placed at a higher distance from the thermal maximum, because otherwise the amount of thermal moderator material between target and extraction channel is not sufficient due to the void inside the extraction channel. In contrast, if the extraction of epithermal or resonance neutrons is requested, it is of advantage to place the extraction channel closer to the target to benefit from a more incomplete moderation process.

Figure V.52 (left) shows the neutron emission inside a divergence cone with 5^o opening with respect to the extraction channel axis. This diagram has been produced by convolution of a neutron emission simulation with the finite proton pulse length. This explains the artefacts at t $> 1000\mu$s showing statistical noise with the length of the proton pulse. Figure V.52 (right) shows the spectrum of the neutrons emitted from a thermal extraction channel. The spectrum peaks at 60 meV, equivalent to a wavelength of about 1.2 Å.

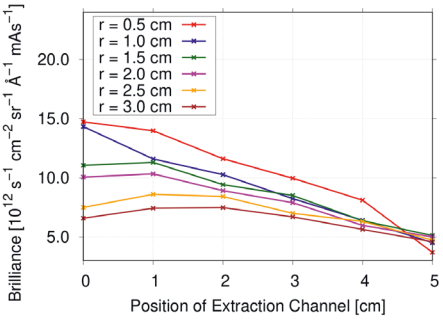

Figure V.51: *Neutron brilliance for different extraction channel positions and radii. The position is measured relative to the position of the thermal flux maximum without extraction channel.*

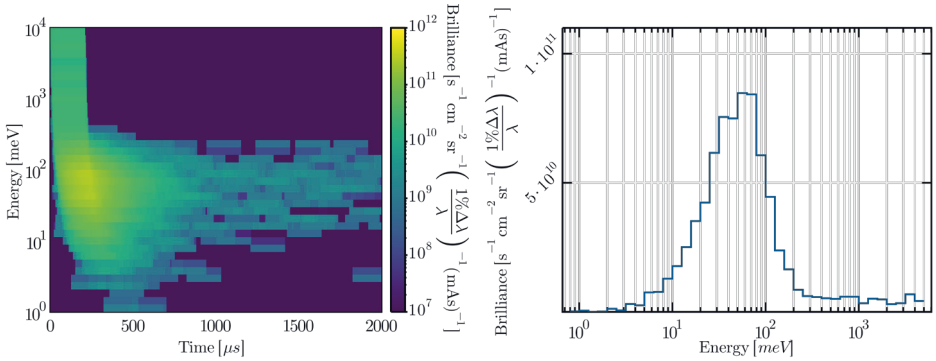

Figure V.52: *Left: Energy and time dependence of the neutron brilliance at the thermal extraction channel for a proton pulse length of 208 μs. Right: Spectrum of neutrons emitted through the thermal extraction channel.*

In the energy regime above 300 meV transient neutrons are observed during the moderation process. As the moderation process in polyethylene is fast [130], the delay of the emission of these neutrons from their generation in the MeV enery range is not resolved. Figure V.53 (right) shows that these epithermal and resonance neutrons are emitted with a useful brilliance and the time structure of the epithermal neutron pulse is equal to the time structure of the proton pulse within an accuracy of 10 μs. The intensity of epithermal and resonance neutrons can be increased by reducing the distance between the target and the respective extraction channel to accomplish a more incomplete moderation of the extracted neutrons.

In the energy regime below 300 meV one observes a storage of the neutrons in thermal equilibrium within the polyethylene moderator block. During the proton pulse the moderator volume is filled with freshly moderated neutrons. The thermal neutron storage is drained by neutron extraction or diffusion out of the moderator volume as well as by absorption of thermal neutrons by the moderator material itself, mainly by the hydrogen nuclei in the polyethylene. The analysis shows that in our geometry absorption is the dominating neutron-loss process in the thermal moderator. Figure V.53 (left) shows the pulse shape of the thermal neutron pulse emitted from the thermal extraction channel. The increasing and the decreasing slope of the pulse can be described by the same exponential function with a time scale of 150 μs, as can be seen in the orange curves fitted to figure V.53 (left).

In contrast to that, the shape of the epithermal neutron pulse shown in figure V.53 (right) follows the shape of the proton pulse.

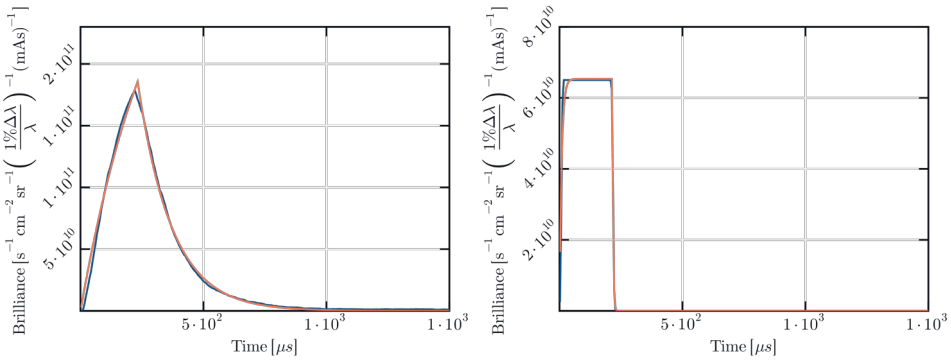

Figure V.53: *Left: Thermal neutron pulse, obtained from energy spectrum integrated between 10 and 500 meV. Right: Epithermal neutron pulse, obtained from energy spectrum integrated between 500 meV and 2 eV. The length of the proton pulse is 208 μs in both cases.*

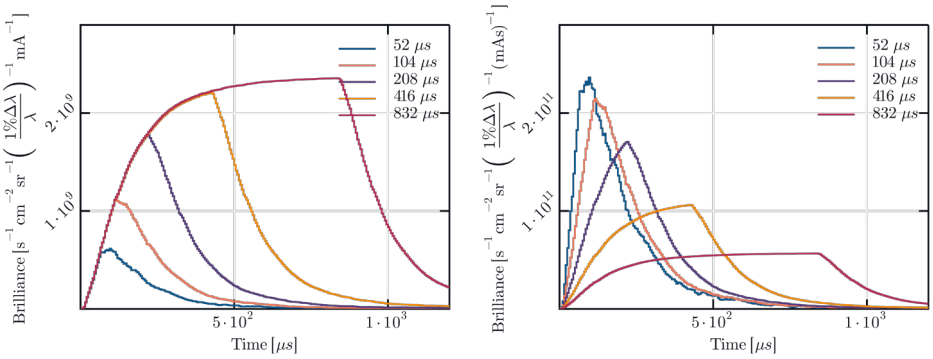

Figure V.54: *Left: Thermal neutron brilliance of a single pulse for different proton pulse lengths. Right: Thermal neutron brilliance for different proton pulse lengths multiplied with the respective proton pulse frequencies.*

Depending on the length of the proton pulse, different neutron pulse shapes can be produced, as can be seen in figure V.54 (left), all with the same decay function. As the duty cycle is the same at all target stations, there is a fixed anti-proportional relationship between pulse length and repetition rate, i.e. shorter pulses are emitted more often. In the case of the neutron instrument, it means that the signal arising from a short neutron pulse is measured at a higher frequency, and therefore can be added up stroboscopically in an efficient way.

This fact is shown in figure V.54 (right), where the pulse shape is multiplied by the respective pulse frequency, indicating the useful neutron intensity from the respective pulses. All curves in this plot have exactly the same integral, because the time-averaged number of primary neutrons emitted from the target and all processes in the moderator and in the extraction system are exactly identical, as we did not yet take into account a variation of the thermal moderator / reflector system between the individual target stations within this report. The shape and the peak height differ strongly. The longest pulses are closest to a rectangular shape, while the shorter pulses have a higher peak

saturating below about 100 μs. The most symmetrical pulse shape is produced with a proton pulse length matching the decay time, i.e. about 150 μs.

V.6.2 Cold moderator

Cold moderators decrease the neutron energy spectrum below the thermal spectrum by moderating the neutrons in a suitable moderator material at cryogenic temperatures. Present day neutron sources typically operate one single cold moderator which is designed to provide one specific neutron spectrum but feeds several instruments that may have different spectral requests. The HBS changes that "one-size-fits-all" standard and instead supplies every instrument with cold neutrons from their own adapted cold neutron source. In this sense, the cold moderator is no longer part of the neutron source, but an intrinsic part of the instrument and can be optimized individually during the process of the design of every instrument.

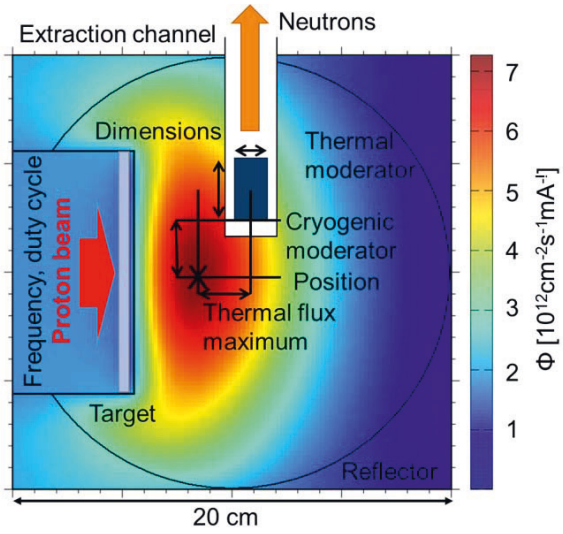

Figure V.55: *Extraction channel with 1-dimensional cold neutron source insert*

In addition, the usage of individual moderators for every instrument allows the optimization of the extraction of the cold neutrons in the direction of the instrument. A compact one-dimensional cold moderator can be placed inside the thermal moderator at a position where it is fed with thermal neutrons in an optimized way from all sides while the cold neutrons are extracted only in one direction (one-dimensional) through an extraction channel towards the instrument. As sketched in Figure V.55, the dimensions and positioning of the cold moderator have been optimized in a parameter variation study.

For a compact, one-dimensional cold source, a moderator material is needed that interacts strongly with thermal neutrons to provide a high density of cold neutrons within a small volume. Only for materials containing a high density of light hydrogen can this be achieved. Suitable materials are e.g. liquid hydrogen H_2, solid methane CH_4 or solid mesitylene C_9H_{12}. In the case of deuterated cryogenic materials, the moderation cross section is typically too low, so that the cold neutron beam would be too dilute.

Particularly well suited for a one-dimensional cold moderator is para-hydrogen [131]. The lower curve in Figure V.56 shows the scattering cross section for pure para-hydrogen as a function of the

neutron energy. For neutron energies below 20 meV (i.e. wavelengths above 2 Å), the scattering cross section is more than one order of magnitude lower than for thermal neutrons. This results in a mean free path for thermal neutrons of about 1 cm compared to a mean free path for cold neutrons of some 10 cm. A drawback of the reduced scattering cross section at low neutron energies is the reduced probability of the multiple scattering of cold neutrons, so that the neutron temperature typically remains well above the thermal equilibrium corresponding to the temperature of the cold moderator.

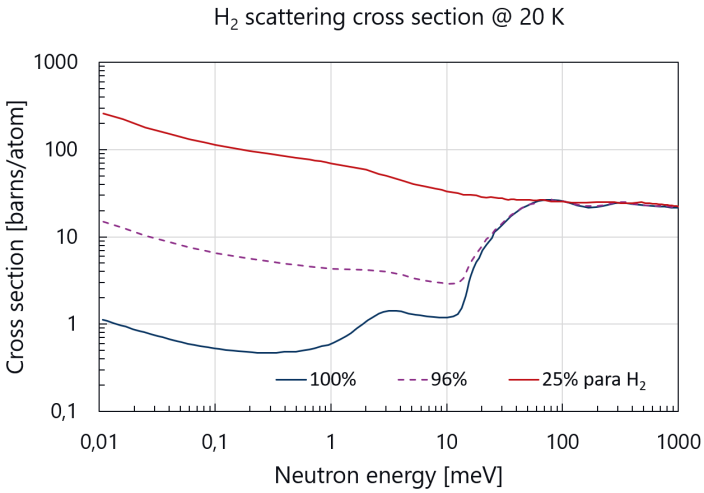

Figure V.56: *Neutron scattering cross section for pure para-hydrogen (100%), high-temperature equilibrium hydrogen (25% para, 75% ortho), and a mixture of 96% para- and 4% ortho-hydrogen at 20 K. The cross sections have been calculated on the basis of the ENDF-VII database following Ref. [131].*

Based on these specific properties, a one-dimensional cold finger moderator has been developed. The name refers to a design which consists of a long vacuum tube with a small cryogenic moderator vessel (e.g. cylindrical with 10 cm in length and 2 cm in diameter) at one end and with vacuum space surrounding it, which is necessary for thermal isolation. This design enables the installation of the cold moderator inside the thermal moderator through a single extraction channel without the need for dismantling the shielding or reflector. Full flexibility towards future developments in the field of cold moderators is achieved with this approach. By positioning the cryogenic moderator inside the thermal flux maximum, it is fed optimally with thermal neutrons through the entire side surface without depletion in the centre. The cold neutrons can be emitted freely towards the instrument through the extraction channel with a view onto the entire volume of the cylinder, as the length of the cylinder does not exceed the mean free path for cold neutrons.

Figure V.57 shows the neutron spectra of two different cold finger moderators emitted from an extraction channel containing parahydrogen . In the two cases described here, a cylindrical para-hydrogen moderator 10 cm in length with a radius of 1 cm or 2 cm, respectively, has been simulated by MCNP. The vacuum space around the cryogenic moderator is 1.2 cm to all sides, where the view onto the thermal moderator surface is free. In the case of the thicker cylinder, one observes a cold spectrum peaked at 10 meV neutron energy, or 3 Å wavelength, together with a reduced thermal spectrum as described in Chapter V.6.1. In the case of the narrow cylinder, the brillance of the cold neutrons is higher, but the brilliance of thermal neutrons is comparable to the brilliance of cold neutrons. This

setup is well suited to instruments preferring a bi-spectral neutron beam. Whether or not focusing neutron optics can efficiently extract the cold neutrons from the centre of the extraction channel is currently under investigation.

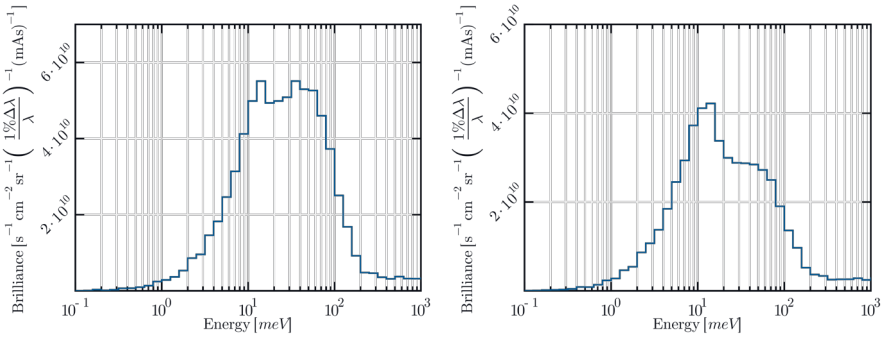

Figure V.57: *MCNP simulations of the neutron spectrum emitted from an extraction channel with a para-hydrogen cold source. Left: length 10 cm, radius 1 cm. Right: length 10 cm, radius 2 cm.*

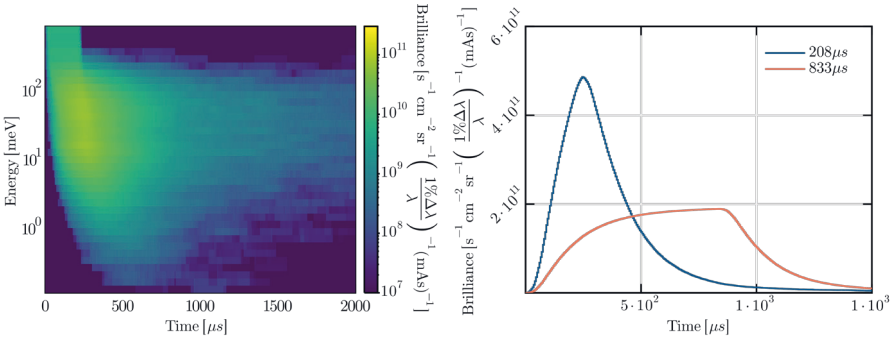

Figure V.58: *Left: Energy and time dependence of the neutron brilliance at a cold extraction channel (para H_2, length 10 cm, radius 1 cm) in forward direction for a proton pulse length of 208 μs. Right: Time structure of the neutron pulses at a 96 Hz (blue) and a 24 Hz target station (orange), respectively. The brilliance is averaged over the energy range E = 1 – 100 meV and multiplied with the repetition rate of the beam.*

Figure V.58 (left) shows the time structure of the neutron beams extracted from a one-dimensional para-hydrogen cold finger moderator. The cold neutrons follow the same time dependence as the thermal neutrons, i.e. the time structure is dominated by the feeding of the cold moderator with thermal neutrons. The time the neutrons stay inside the cold source can be neglected since for para-hydrogen multiple scattering events are improbable. As the intrinsic time scale of the cold neutron source is convoluted by the length of the proton pulse delivering fast neutrons, either a mainly symmetrical peak shape can be produced at the 96 Hz target station, or a more rectangular peak shape at the 24 Hz target station, as can be seen in Figure V.58 (right). The area of the curves, i.e. the total number of neutrons delivered, is identical.

Preliminary studies indicate that a compact para-hydrogen moderator doped with ortho-hydrogen can combine the advantages of both hydrogen states: an improved thermalization even with de-

creasing neutron energies due to the orthohydrogen content but still with a low self-absorption at cold energies due to the parahydrogen as the main contribution. The curve in the middle of Figure V.56 show the cross section for a para-hydrogen moderator doped with 4% of orthohydrogen. As the simulation of the neutronic properties of an ortho/para-hydrogen mixture moderator suffers from difficulties in the databases, a prototype with a dedicated mixing cryostat was developed for the experimental validation, which can create variable liquid ortho-parahydrogen mixtures at 20 K.

The prototype design of the cold finger moderator is shown in Figure V.59. All supply lines (e.g. cryogenic supply) and wires (e.g. measurement and control) are located inside the vacuum tube but outside of the cold neutron flight path at the centre of the tube. In this way, the cold moderator can be placed and operated inside the thermal moderator while the coolant, vacuum and moderator supply are located outside the neutron shielding. As a design option, the use of a secondary vacuum tube is possible which would cover the feed lines and wires and would be placed in parallel to the first vacuum tube.

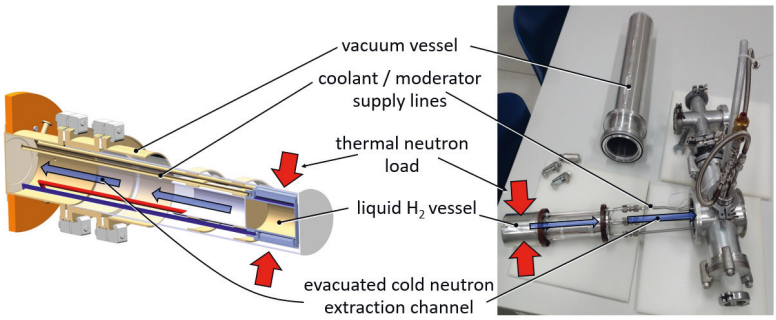

Figure V.59: *Pilot installation of the ortho-parahydrogen mixture cold moderator*

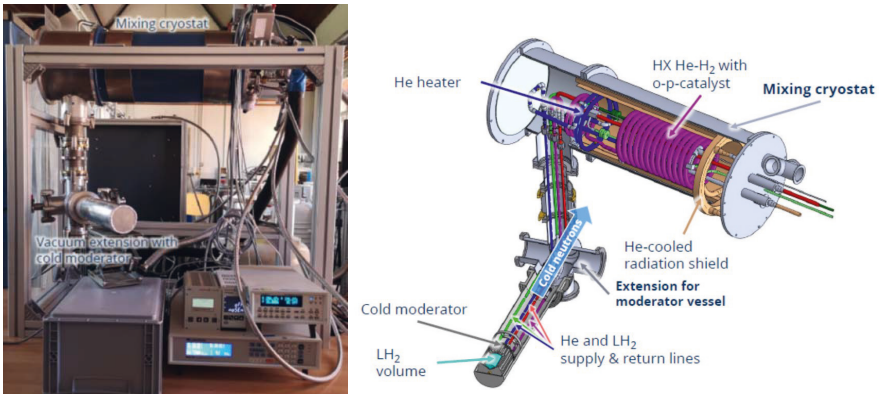

Figure V.60: *Mixing cryostat for the supply of variable ortho/para-hydrogen mixtures. More details can be found in [132]*

The prototype design of the mixing cryostat (upper large vacuum cylinder) and the cold finger (lower small vacuum cylinder) which contains the moderator vessel with a volume of approximately 200 ml liquid hydrogen is shown in Figure V.60. The mixing cryostat has two hydrogen feed lines at ambient temperature. Both lines are cooled within a helium countercurrent heat exchanger towards 17 K. The helium coolant is designed as an open circuit, fed from a helium Dewar and recycled into a helium

recovery line in the case of the prototype. During that process, one hydrogen line passes a catalyst which transforms the natural hydrogen ratio into almost pure para hydrogen. Behind the exchanger, both hydrogen streams are combined and guided to the moderator vessel inside the cold finger. By adjusting both hydrogen mass flow rates separately, the ortho-para ratio inside the moderator vessel is set. The spatial separation of the moderator vessel and the cryogenic supply enables the quick installation of the moderator inside an appropriate neutron extraction channel.

The basic concept of the ortho/para-hydrogen moderator prototype with a mixing cryostat can be adapted to different moderator materials and moderator geometries. The small moderator vessel is placed inside the thermal moderator at the end of a neutron extraction channel. The vessel is spatially separated from the cryogenic support but both are thermally connected (e.g. via a cooling circuit, heat bridge or heat pipe). As each supply line of the moderator vessel is guided parallel to the neutron extraction path but outside the flight path itself the moderator supply installations can be stored outside the shielding, but the moderator can be installed or removed easily without the need for dismantling the shielding or reflector. Cooling capacity can be provided by an open circuit or a cold head depending on the cooling capacity required.

In the case of the actual HBS setup, the hydrogen cold moderator will be realized as a cryogenic closed-cycle system. This means that hydrogen is continuously circulated through the cold moderator vessel in subcooled liquid state, so that it can simultaneously act as a cold moderator and "self"-coolant. After leaving the moderator vessel, the hydrogen is transported towards a cryostat outside the shielding, in which it is again subcooled by passing the cold head of a single-stage cryocooler. Its cooling capacity is approximately 25 W at 17 K, which is sufficient for a heat load of 20 W onto the cryogenic system, which was estimated to be the upper limit from the gamma and neutron induced head load as well as the thermal radiation and conduction from the structural components of the system. Additionally, the cooling system is expandable by installing another cryocooler in series in case a higher cooling capacity is needed.

For solid cryogenic moderators cooling can either be realized by using a circulating cold He-flow with a similar operating principle as the one mentioned above or by using a thermal bridge between a cryocooler and the cold moderator vessel. This choice depends strongly on the lowest desired operating temperature of the cold moderator.

V.7 Reflector

The reflector surrounds the entire thermal moderator and sends back some of the neutrons that leave the thermal moderator thus increasing the neutron flux in the moderator. This increases the efficiency of the neutron extraction at the cost of an increase of the decay time of the population of the thermal moderator, i.e. at the cost of an increased pulse length.

A neutron reflector is made of a material that does not absorb neutrons, but has a high scattering cross section. Typical candidates are Be or Pb. Be as a light element is also an efficient moderator material, i.e. fast neutrons reaching a Be reflector will be moderated before being returned into the thermal moderator. Pb as a heavy element is not a thermal moderator, but has relevant (n,2n) cross section for fast neutrons. This process reduces the energy of fast neutrons so that the neutrons reflected can be processed more efficiently by the thermal moderator.

The influence of various reflector materials on the intensity and pulse structure of the neutron emission from a thermal extraction channel was simulated for (i) a beryllium reflector, (ii) a lead reflector, and (iii) an absorber of borated polyethylene. The latter acts as an absorber instead of a reflector and thus is expected to lead to short neutron pulse lengths. Figure V.61 shows the influence of the different reflector materials on the thermal neutron pulse structure at a 96 Hz target station with the thermal moderator as described in Chapter V.6.1. The comparison between the beryllium and the

lead reflector shows that the emitted intensity is only slightly higher in the case of Be. The main decay time of the neutron pulse is the same for beryllium and lead reflectors, but in the case of beryllium, a second, longer, decay time is observed for t > 700 μs. This second decay time is attributed to neutrons that have been thermalized inside the Be volume and reach the extraction channel only after a longer diffusion time inside the (only weakly absorbing) beryllium. This increased decay time is a disadvantage of the beryllium reflector compared to only a tiny advantage in intensity. In addition, a lead reflector acts as a first shielding against the gamma radiation emitted from the target region.

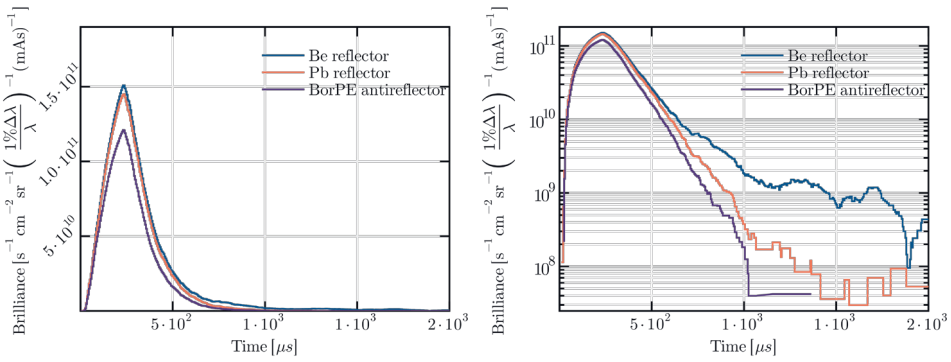

Figure V.61: Pulse structure of the thermal neutron emission from the PE thermal moderator surrounded by different reflector materials. Left: linear intensity scale, right: logarithmic intensity scale

In addition, beryllium is a material that is associated with strong restrictions due to its toxicity, and the waste treatment of beryllium with activated traces is very difficult to undertake, while the waste management for lead is well established, even for nuclear installations. Last but not least, a lead reflector is significantly cheaper than a beryllium reflector of same size. For this reason, a lead reflector is the preferred choice.

The analysis of the borated polyethylene absorber instead of the reflector shows an intensity drop of only 15% and no change in the pulse shape compared to the lead reflector. This is due to the fact that the thermal neutron cloud is strongly confined and localized in the over-sized polyethylene thermal moderator, as described in Chapter V.6.1. For this reason, the influence of the reflector thickness is weak, too. For the pulse structure and intensity simulations shown in this report, we chose a 30 cm thick reflector shell surrounding the thermal moderator.

It is expected that the reflector configuration for a high frequency target station that is intended to deliver short pulses will be different from the reflector configuration at the slower target stations. Together with corresponding parameter studies to develop an optimized thermal moderator the reflector will be modified to be able to offer the best configuration for the pulses required by the instrument at a certain target station.

V.8 Shielding

The goal of the shielding is to maintain the gamma and neutron dose rates as low as is reasonably achievable (ALARA principle) to avoid the unnecessary radiation exposure of those working in adjacent rooms (in the instrument halls and the technical hall) during neutron source operation. Furthermore, the shielding should allow various maintenance works in a neutron source area to be performed after the shut-down of the associated proton beam-line. On the other hand, the dimen-

sions of the shielding should be optimised to position the different instruments as close as possible to the neutron source in order to take maximum advantage of the neutrons produced. The shielding is made of seven layers of two different materials: four layers of lead and three layers of borated polyethylene (16.1 wt.% B_2O_3), surrounding the reflector as shown in Figure V.62. The reflector is also part of the shielding. Borated polyethylene acts as a fast neutron moderator and a slow neutron absorber. Lead reduces prompt and delayed gamma radiation issuing from the proton and neutron activation of the target and from the neutron activation of the shielding and other components embedded in the target station. Lead also acts as a fast neutron moderator due to the (n,xn) reaction. For optimization, the thickness of the lead layers is fixed to 10 cm, while the thickness of each layer of borated polyethylene varies from 10 to 40 cm in 10 cm step. The neutron and gamma dose rates generated during accelerator operation with 70 MeV protons and an average current of 1.43 mA are calculated with the transport code MCNP6.1 (ENDF/B-VII.1 database) using a simplified geometry of the target station (sphere) shown in Figure V.62. Average neutron and gamma dose rates at the surface of the various shielding configurations and for the different reflectors are given in Table V.11 and V.12, respectively, and represented graphically in Figure V.63.

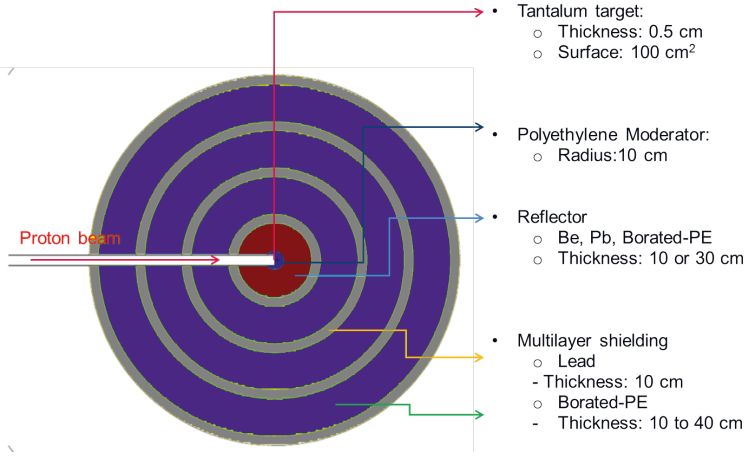

Figure V.62: *Spherical model of the target station for calculation of the neutron and gamma dose rates with transport code MCNP6.1*

	Reflector					
Shielding configuration	BPE 10 cm	Be 10 cm	Pb 10 cm	BPE 30 cm	Be 30 cm	Pb 30 cm
30 cm BPE + 40 cm Pb	38(2)	34.5(5)	34.2(5)	9.7(2)	7.4(2)	7.4(2)
60 cm BBPE + 40 cm Pb	4.9(1)	4.6(1)	4.4(1)	1.62(7)	1.39(7)	1.52(7)
90 cm BPE + 40 cm Pb	1.03(6)	1.03(6)	1.06(6)	0.47(4)	0.45(3)	0.46(3)
120 cm BPE + 40 cm Pb	0.35(3)	0.35(3)	0.37(3)	0.17(2)	0.17(2)	0.19(2)

Table V.11: *Average neutron dose rate in Sv/h at the surface of shielding during accelerator operation (70 MeV protons, average current of 1.43 mA) for various reflectors*

Depending on the shielding configuration and the type and thickness of the reflector, the surface dose rate ranges from 38 to 0.2 Sv/h for neutrons and from 43 to 0.2 mSv/h for gamma rays. In accordance with the shielding thickness, the neutron dose rate as well as the gamma dose rate

Shielding configuration	Reflector					
	BPE 10 cm	Be 10 cm	Pb 10 cm	BPE 30 cm	Be 30 cm	Pb 30 cm
30 cm BPE + 40 cm Pb	43(2)	40(2)	38(2)	10.9(9)	10.9(9)	8.5(9)
60 cm BPE + 40 cm Pb	6.6(6)	6.6(6)	5.0(5)	1.9(2)	2.1(3)	1.7(2)
90 cm BPE + 40 cm Pb	1.1(2)	1.6(2)	1.5(2)	0.5(1)	0.7(1)	0.5(1)
120 cm BPE + 40 cm Pb	0.5(1)	0.5(1)	0.5(1)	0.28(6)	0.18(5)	0.18(5)

Table V.12: *Average gamma dose rate in mSv/h at the surface of shielding during accelerator operation (70 MeV protons, average current of 1.43 mA) for various reflectors*

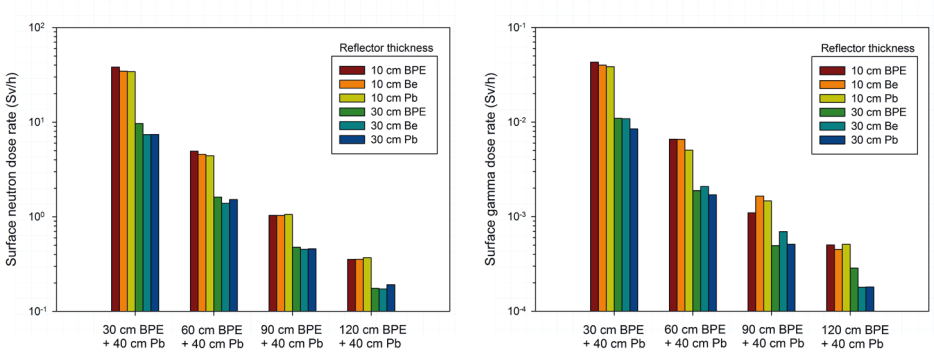

Figure V.63: *Left: Average surface neutron dose rate. Right: Average surface gamma dose rate*

decreases by a factor of somewhere between four and two when the thickness of a given reflector increases by a factor of three. When the thickness of the layers of borated polyethylene are increased from 10 to 40 cm, the neutron dose rate decreases by a factor of between 90 and 110 and the gamma dose rate by a factor of between 75 and 90 for 10 cm thick reflectors. For 30 cm-thick reflectors, the neutron and gamma dose rate decreases by a factor of between 40 and 60. For layer thicknesses upwards of about 30 cm, the neutron dose rate is independent of the type of reflector involved.

The dose rate after the shut-down of the proton beam line is calculated using the software for radiation protection SISy (version 2.5.2) based on the activity of ^{182}Ta, which is the major source of radiation to be shielded (see Chapter VIII.3). The dose rate is estimated conservatively for 360 days of uninterrupted irradiation of the tantalum target leading to a ^{182}Ta activity of 46 PBq. The values are given in Table V.13 and shown graphically in Figure V.64. Depending on the shielding and reflector thickness, the dose rate ranges from 23 to 0.9 μSv/h.

In order to select the shielding configuration, an upper dose rate limit of 10 mSv/a for maintenance in the neutron source area after the shut-down of the proton beam line is considered here by way of an example. This value is only half the yearly dose rate limit for a person expose to radiation (20 mSv/a) according to the German radiation protection ordinances (StrSchV) and hence provides an additional safety margin (conservative approach). Calculating with 2000 working hours per year, it leads to a dose rate limit of 5 μSv/h. Based on this value and in view of a minimisation of the neutron and gamma dose rate outside the neutron source area during the operation of the proton beam-line, the shielding configuration with 120 cm of borated polyethylene is chosen for further

Shielding configuration	Reflector					
	BPE 10 cm	Be 10 cm	Pb 10 cm	BPE 30 cm	Be 30 cm	Pb 30 cm
30 cm BPE + 40 cm Pb	23	21	20	9.8	9.7	9.3
60 cm BPE + 40 cm Pb	7.7	7.4	5.9	4.4	4.1	3.3
90 cm BPE + 40 cm Pb	3.5	3.4	2.6	2.4	2.1	1.5
120 cm BPE + 40 cm Pb	1.9	1.9	1.5	1.3	1.3	0.9

Table V.13: *Dose rate in μSv/h at the surface of shielding after shutdown of the proton beam-line. The tantalum target was irradiated for 360 days leading to a ^{182}Ta activity of 46 PBq; ^{182}Ta being the major source of radiation in the system.*

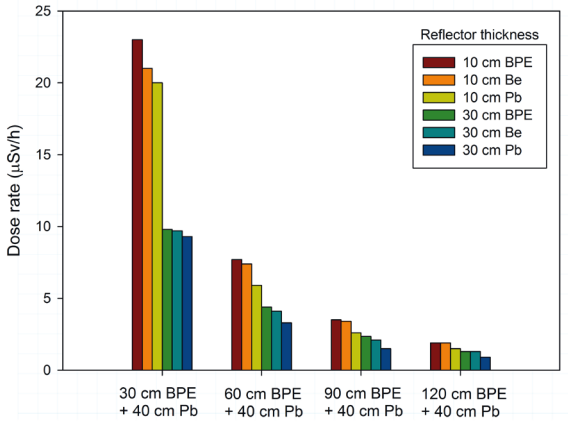

Figure V.64: *Dose rate at surface of shielding after shut-down of the proton beamline and 360 days of irradiation of the tantalum target without interruption.*

dose rate calculations. The average energy of neutrons escaping the shielding is 1 MeV and the neutron flux averaged over the shielding surface is $2.2 \cdot 10^5$ cm^{-2}s^{-1}. The neutron source with the selected shielding including a 30 cm-thick beryllium reflector, is positioned in the middle of a room with an area of 10×10 m^2. The distance between the outer surface of the shielding and the inner surface of the room wall is 4 m, providing space for the instruments choppers, the storage of spent targets and the remote handling system for target exchange. According to [133], the room wall is composed of two layers of different materials and has a thickness of 140 cm. The inner layer with a thickness of 70 cm is made of ordinary concrete with 50 wt.% polyethylene aggregate to moderate fast neutrons escaping from the shielding. The outer layer is made of ordinary concrete with 2 wt.% boron carbide for absorption of slow neutrons, and has also a thickness of 70 cm. The neutron and gamma dose rate maps are shown in Figure V.65. The dose rate during operation at the outer surface of the wall is lower than 0.02 μSv/h. The results above show that efficient radiation shielding may be achieved by using conventional materials such as lead, borated polyethylene and ordinary concrete doped with polyethylene and boron carbide. Additional shielding at the side of the proton beamline and at the target exchange system will be considered during the technical design of the target station.

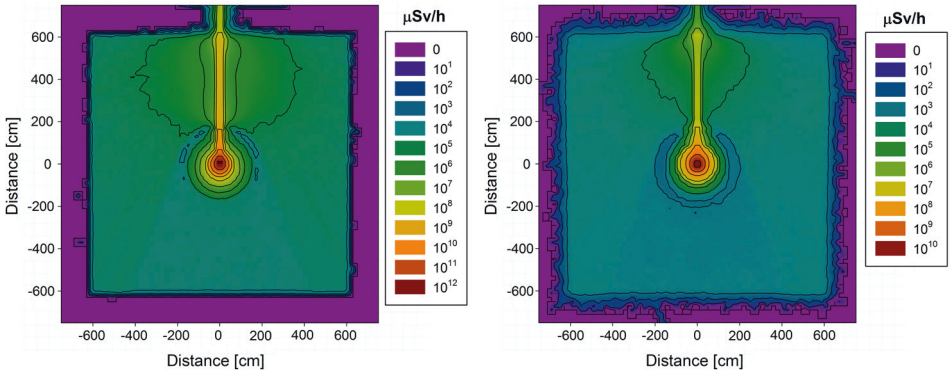

Figure V.65: *Left: Neutron dose rate distribution during operation of the proton beam line (70 MeV protons and 1.43 mA average current) in the neutron source area including the walls of the room (cut in the plane of the proton beam line). Right: Gamma dose rate distribution during operation of the proton beam line (70 MeV protons and 1.43 mA current) in the neutron source area including the walls of the room (cut in the plane of the proton beam line).*

V.9 Target station design

The engineering design of the target station is a compromise between perfect geometry from the neutronic point of view, consisting of a spherical moderator and reflector assembly surrounded by spherical shielding, and practical geometry from the construction point of view. The design has to consider all relevant requirements, for example, it must make it possible to easily replace the target, the thermal moderator and the cold moderators, withstand the mechanical loads of the entire shielding, guarantee sufficient accuracy in the alignment of components and facilitate the removal of all heat from the system. The draft of a possible design is shown in Figure V.66.

The entire design is based on a modular approach. It means that both the sandwich shielding and the reflector are composed of single elements which allow the partial disassembly of the target station, for example in order to replace the thermal moderator or to prepare a simple decommissioning of activated components at the end of the facility's life time. These single elements are surrounded by an aluminium mounting frame which acts as a support structure. The edges of the elements will be arranged offset from each other in order to prevent neutron leakage.

For reasons of clearity, the current design will be divided into three layers in subsequent sections, the bottom layer, the centre and the upper layer. The bottom layer is located below the neutron production and extraction level at a height of approximately 100 cm. This layer primarily consists of a massive shielding structure of alternate layers made of borated polyethylene and lead along with a support structure. There are no further installations such as support lines, electrical supply or moving parts inside the bottom layer. The lower part of the lead reflector completes this lower layer. The modular design of this layer has to ensure the mechanical stability of the entire target station.

The centre layer includes the entire neutron production and extraction installations and it contains the major part of the supply lines. The neutron target is located at the centre of this layer covered by the thermal polyethylene moderator with a diameter of about 20 cm, the lead reflector and the shielding. The proton beam arrives vertically from the top through the proton guide. A beam window at the end of the proton guide separates the accelerator vacuum from the neutron target inside the thermal moderator. For the Technical Design Report we will study the possibility to work with a window free proton beam line, which is the clearly preferred option. The neutron extraction channels run

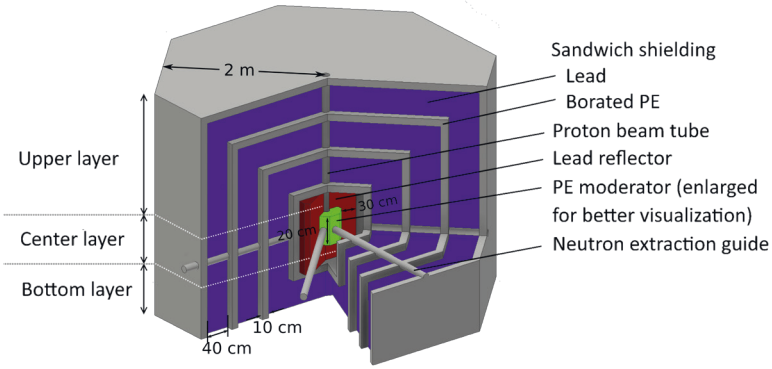

Figure V.66: *Schematic drawing of target station with shielding with a total radius of 2 m.*

horizontally from the thermal moderator to the outer shielding. These extraction channels follow a modular approach which means they are designed as a plug which can be inserted into channels inside the shielding. The plug contains the neutron guide and complements the reflector and the sandwich shielding. The plug and the extraction channels are described in detail in the neutron beam extraction chapter (Chapter V.9.2). The target itself can be inserted or removed from the target station as a kind of cassette together with a firmly attached small part of the thermal moderator. For that purpose, an additional horizontal opening with a dedicated plug has been designed. The plug contains all target supply lines such as the coolant supply and control and measurement lines. The entire target exchange is fully remote controlled including the lock on the coolant supply and the opening of the shielding via the removal of the plug. The exchange of the outer part of the thermal moderator is only possible after the removal of the target cassette; this exchange requires the dismantling of certain parts of the modular shielding.

The upper layer is located above the neutron production and extraction level at a height of approximately 200 cm. This layer consists of the massive upper shielding structure and contains the last section of the proton beamline. A mechanical device allows the separation of the vacuum via the shutter and the removal of this section of the proton beam line, for example, to inspect and change the beam window if necessary. The remaining parts of the thermal moderator can also be exchanged after dismantling of the target, the proton beam line and the cold moderators.

V.9.1 Cooling

The components which require cooling inside the target station are the neutron target, the thermal moderator and the cold moderators.

The neutron target requires a water coolant supply. The heat released by the proton beam and the prompt and delayed radiations have to be removed by the water. The heat deposited in the target by prompt radiation during operation and by gamma radiation after an operation time of 360 days is recorded in Table V.14. Prompt radiation is emitted with a constant rate during operation while the emission of decay radiation increases over time. Assuming a one-year uninterrupted operation, about 103 kW heat are released inside the target during operation (100 kW beam power and 3 kW prompt and decay radiation) which requires a water mass flow of approximately 1.35 kg/s for the efficient cooling of the internally cooled target. This volume of mass flow causes a pressure loss of 2.2 bar within the target station and will warm it up by 15 to 20 °C. After operation, the target is still heated with around 3 kW due to delayed radiation created by proton and neutron induced activation

products presented in Figure V.67 and explained in more detail in chapter 3 which requires ongoing cooling. The target water supply has to be designed as a closed circuit to prevent the release of tritium or activation products outside the target bunker. For this purpose, a heat exchanger will be installed inside the target bunker. A secondary water circuit will remove the heat from the target. Due to the delayed radiation, a possible pump failure has to be caught. A water reservoir will therefore be placed above the TMR which can cool the target up to two days until the proton induced heat deposition inside the target has decayed. The failure analysis is still ongoing and a reduction in operation days might be an option to reduce the heat deposition after operation as the neutron induced activity and therefore its heat deposition scales with the operation days.

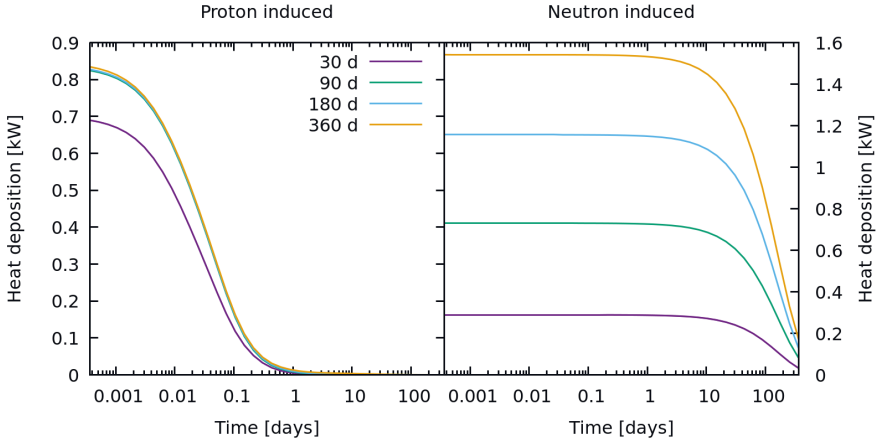

Figure V.67: *Calculated heat deposition inside the Ta target for proton and neutron induced radiation. It is assumed that the heat deposition is caused by the light particles (decay energies obtained from https://nucleonica.com).*

The cold moderators require cryogenic coolant supply. The cryogenic coolant supply can be designed as a closed cycle with a cryocooler system consisting of a cryogenic head and a compressor unit or as an open cycle with a cryogenic gas supply. In both cases, the cryogenic supply is placed outside the shielding of the target station but inside the target bunker. The electric power consumption is in the order of 10 kW in the case of an efficient cryocooler system. There are several solutions for the technical design of the heat exchanger between the cold moderator vessel and the cryogenic coolant supply such as helium circuits, thermal bridges or heat pipes. However, the actual realisation will be adapted to the modular concept of the cold finger design.

The heat release by prompt and delayed radiations (mainly gamma radiation) in different zones of the polyethylene moderator and reflector is given in Table V.14.

Close to the end of an operation cycle, a total of 928 W are deposited inside the thermal polyethylene moderator caused by prompt and delayed radiation and approximately 3.9 kW are deposited inside the reflector. The thermal moderator is a poor heat conductor and hence acts as a thermal insulator. In addition, the lead reflector which surrounds the polyethylene moderator is in turn surrounded by a sandwich shielding made of several layers of lead and polyethylene which also acts as a thermal insulator. However, the entire target station is penetrated by numerous thermal bridges which have the potential to dissipate the deposited radiation heat. The proton beam line and the major parts of the cold moderator and its cryogenic support lines are made of aluminium and hence act as a thermal conductor connecting the inner polyethylene moderator with the environment. In addition, the entire shielding and reflector system is composed of single elements. These single elements will be surrounded by an aluminium mounting frame which further increase the heat transfer ability.

	Radius [cm]	Prompt radiation [W]	Prompt radiation [W cm^{-3}]	Delayed radiation [W]	Delayed radiation [W cm^{-3}]
Tantalum target					
Target	-	53	0.40	2620	20
Polyethylene moderator					
First layer	0 - 4	41	0.15	88	0.33
Second layer	4 - 7	113	0.11	290	0.28
Third layer	7 - 10	104	0.04	266	0.10
Lead reflector					
First layer	10 - 20	239	0.008	3243	0.11
Second layer	20 - 30	93	0.001	150	0.002
Third layer	30 - 40	46	0.0003	42	0.0003

Table V.14: *Heat deposited inside the tantalum target, the thermal moderator and the reflector by prompt radiation during operation and by delayed radiation after an operation time of 360 days. Heat deposition is calculated with MCNP6.*

Simulations were performed using ANSYS with simplified geometries in order to estimate the resulting temperature distribution caused by the deposited radiation heat. These simulations have shown that the major part of the heat can be dissipated passively via the structure described above. However, an additional improvement of the effective thermal conductivity within the thermal moderator may be necessary to achieve the desired temperature within the material. The simulations also indicates that this may be achieved, for example, by inserting a thin grid made of aluminium into the polyethylene.

V.9.2 Neutron beam extraction

Up to six instruments can be supplied with neutrons from one target station. The neutrons are extracted horizontally at the level of the target via extraction channels. The extraction channels begin inside the thermal moderator close to the position of the highest thermal neutron flux. Every extraction channel is adapted in geometry and position to extract the neutron phase space that is best suited to the requirements of the instrument attached there.

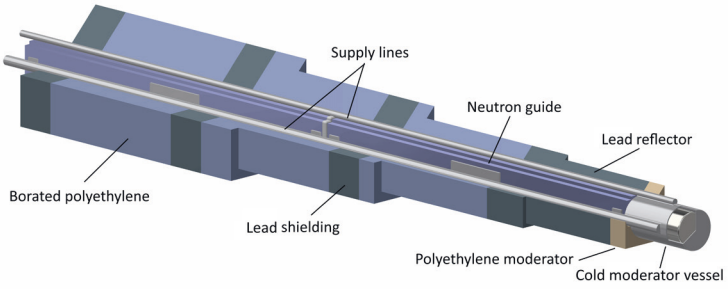

Figure V.68: *Schematic drawing and cut-off of an extraction channel plug with cold moderator attached*

The technical design of the extraction channels follows a flexible modular approach: the target station is equipped with six openings which are supplied with plugs. The openings lead from the outer surface of the thermal moderator through the reflector and the shielding layers in a straight line to the exterior. The cross-section of the openings is approximately 20 by 20 centimetres. Towards the outside, the opening is enlarged in several steps. The gradual enlargement prevents neutron or radiation leakage through the gap between the extraction channel and the plug. The schematic view of this type of extraction plug is shown in Figure V.68. Each plug contains a neutron guide and complements the reflector and the sandwich shielding. Furthermore, each plug can be designed individually for its corresponding application. For example, the plug can be equipped with cryogenic supply lines and measuring lines parallel to the neutron guide in the case of a cold neutron extraction channel. In this case, the cold moderator vessel itself will be attached firmly at the front of the plug.

The plug together with the cold source and neutron guide can be exchanged in a straightforward way during the shutdown period of the neutron source without extensive work at the target-moderator-reflector unit. The flexible plugging of extraction channels allows the customization of the neutron extraction to take place, in order to optimize the instrument's performance by the application of individual cryogenic moderators, the adaptation of the shape of the thermal extraction port, and the use of dedicated neutron optics starting close to the moderator surface.

V.9.3 Target handling

At the end of each operation cycle, the neutron target must be changed and inspected. For radiation safety reasons this target handling has to be fully automatic. After a certain cool-down period has elapsed, the water cooling of the target will be stopped, the water blown out of the target and the last section of the accelerator vacuum will be separated out. After that, a mechanism opens a small section of the shielding and the water supply lines of the target will be cut. A section of the thermal moderator including the target will be automatically pulled out of the TMR-unit on rails and stored inside a bunker. A new moderator - target section can be placed inside the TMR-unit and automatically connected to the supply lines. It must be ensured that no-one is inside the target bunker during the target handling operation. The reliability of the target handling system will be demonstrated at the TMR-pilot unit at Forschungszentrum Jülich within the next few years.

VI.
INSTRUMENTATION

The instruments built at a pulsed CANS are intrinsically operated in time-of-flight (TOF) mode. They can be distinguished mainly by the bandwidth they can use and the resolution needed. Bandwidth and resolution are defined by choppers, which in most cases results in a loss of neutron flux at the sample position. At HBS, a more efficient approach is applied matching the repetition rate of the neutron beam to the instrument length such that the maximal useful phase space volume is filled at the instrument. For the HBS reference design three different repetition rates have been selected: low frequency (24 Hz), medium frequency (96 Hz) and high frequency (384 Hz). Instruments using the same repetition rate are grouped together and located at the corresponding target station (Figure VI.1).

The low particle energy of 70 MeV allows a compact target-moderator–reflector assembly, bringing a larger fraction of the produced neutrons to thermal or cold energies. The low particle energy compared to spallation sources also results in expected less background due to the prompt pulse of fast neutrons, while the TOF mode already guarantees a low background level as in general the neutron detection takes place while there is no proton beam on target. The moderator geometry can also be optimized to emit preferentially into a narrow solid angle, thus increasing the brightness along these directions. The low nuclear energies involved require significantly less bulky shielding, not only saving cost, but also allowing optical components such as guides or choppers to be located closer to the moderator so that larger phase space volumes can be extracted.

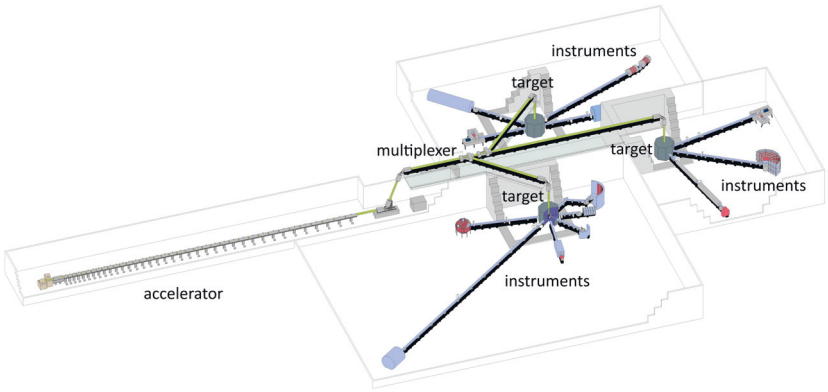

Figure VI.1: *Possible arrangement of instruments at HBS*

	Length [m]	Resolution	Bandwidth	Flux [cm^{-2} s^{-1}]	Frequency [Hz]
SANS	20.0	5% $\Delta\lambda/\lambda$	2.0-9.0 Å	9.4×10^7	24
Reflectometer	22.0	4% $\Delta\lambda/\lambda$	1.3-8.0 Å	1.7×10^7	24
SELENE reflectometer	22.3	1.5-5.1%	3.0-10.4 Å	4.0×10^7	24
NSE	35.0		6.0-16.0 Å	5.0×10^7	24
PDGNAA-1	12.5	10.0-40.0%	1 meV-80 eV	3.4×10^9	24
NDP	15.0	10.0% $\Delta\lambda/\lambda$	2.0-15.0 Å	2.0×10^8	24
Thermal powder diffr.	100.8	0.0061-0.014 $\Delta\, d/d$	0.75-2.4 Å	1.5×10^8	24
Cold neutron imaging I	6.0	2.0-10.0%	1.0-15.0 Å	3.0×10^8	96
Cold neutron Imaging II	12.0	1.0-5.0%	1.0-15.0 Å	3.0×10^7	96
Thermal neutron imaging I	6.0			3.0×10^8	96
Thermal neutron imaging II	12.0			3.0×10^7	96
Diffractive neutron imaging	22.0	0.5-2.0%	1.0-15.0 Å	2.0×10^7	96
Disordered material diffr.	61.0	0.016-0.028 $\Delta\, d/d$	0.5-1.2 Å	1.9×10^7	96
Powder magnetism diffr.	21.0		2.0-4.0 Å		96
Macromolecular diffr.	12.5		2.0-4.0 Å	4.0×10^7	96
Engineering diffr.	20.0	>0.27%	0.97-3.03 Å		96
GiSANS	5.1		2.0-8.0 Å	1.3×10^7	96
Cold chopper spectr.	18.5		1.6-10.0 Å	3.4×10^5	96
XTOF spectr.	12.8		10-200 meV		96
Vibrational spectr.			50 meV-1 eV		
Backscattering spectr.	102.5	3.0-20.0 μeV	6.05-6.0 Å	7.0×10^6	96
Epithermal neutron imaging	37.0		25-80 meV	5.0×10^9	384
High energy chopper spectr.	28.5	4% ΔE/E	0.5-2.5 Å	9.0×10^4	384
PDGNAA-2	21.0	50%	0.6 eV - 10 MeV	2.7×10^7	384

Table VI.1: *Basic parameters of instruments at the target stations of HBS*

Depending on the instrument, a cryogenic moderator shifting the neutron spectrum to energies between 1 meV and 10 meV is needed. For this purpose a one-dimensional finger moderator can be inserted into the extraction channel positioned at the thermal maximum in the thermal moderator.

The cryogenic moderator is filled with a suitable material such as solid methane, mesitylene or liquid hydrogen with a specific ortho/para ratio at cryogenic temperatures. The dimensions and the moderator material of the cryogenic one-dimensional moderator are optimized to the requirements of the instrument. MCNP6 simulations were used to determine and optimize the neutron phase space volume leaving the extraction channel (Figure V.55). The neutron bandwidth, the pulse width and the divergence are all matched to the requirements of the instruments. With this approach, each instrument has its own source. Table VI.1 gives an overview over a possible suite of instruments at the HBS with some basic parameters. It is evident that instruments at the HBS are very competitive to instruments at present day research reactor or medium size spallation sources. In what follows, the instrument design and layout is described in some detail.

VI.1 Imaging

Neutron imaging beamlines serve a very wide range of science cases. Correspondingly, measurement conditions are adapted to different resolution needs and sample sizes from study to study, and beamlines need to be designed for high flexibility. The detectors utilized are movable devices which can be exchanged within minutes and a suite of different detectors is required to cover a good range of use cases from decimeter sized samples down to millimeter sized samples, from some 100 micrometers to just a few micrometers of resolution in space and from hours down to microseconds in time. Transmission and contrast strongly depend on neutron wavelengths and spectrum, which is a feature fixed by the initial moderator choice. Therefore, several beamlines at two different moderators must be considered, namely one at a cold and one at a thermal moderator (potentially removable for fast neutron imaging). The thermal beamline will excel in industrial investigations but also for cultural heritage and R&D applications for full devices (such as fuel cells, batteries, particulate filters etc.), while the cold neutron beamlines will provide the highest resolution and contrast as well as novel contrast modalities enabled by the time structure and sensitivity to crystalline and microscopic structures relevant in basic material science.

The facility offers another interesting aspect, that could potentially be exploited for imaging applications. Two beamlines from different targets could be crossed at a sample position. While this is currently just an idea, crossed beams could enable stereoscopic observations of processes, or the combination of different spectra/energies for specific investigations.

VI.1.1 Cold neutron imaging

The cold neutron imaging beamline will perform high resolution, high sensitivity measurements utilizing in many cases particularly the time structure of the source for quantitative wavelength dispersive imaging. For this the instrument will be operated at a 96 Hz target station with a cold moderator. In order to be able to tailor experimental parameters such as beam size and resolution (including wavelength resolution) to the needs of a measurement the instrument will feature two measurement positions at about 4 m, and 10 m from the moderator. The moderator shall have a diameter of 4 cm and shall act as the “point”-source, which will render an additional pinhole - as conventionally used for neutron imaging – obsolete for most measurements.

Correspondingly, the first measurement position will feature a beam size of about 15 x 15 cm^2 due to the beam channel extracting the neutrons. The wavelength resolution for the core wavelengths around 3 Å will be around 5% and the bandwidth about 10 Å. These conditions will allow for high flux measurements enabling in particular high sensitivity, and fast or very high resolution studies. This position is ideally suited for studies of hydrogen in metals, energy conversion processes as well as water uptake in different materials or two-phase flows. The position also offers good potential for dual spectrum measurements to probe, for example, the aggregate state of water in devices. In

addition, the moderate wavelength resolution is well suited for spatial resolved SANS studies through dark-field contrast imaging in soft matter or engineering applications.

The second measurement position at 10 m offers improved wavelength resolution and is hence well suited for depicting contrast in crystalline structures such as in phase mapping studies in engineering and applied metals, as well as ceramic materials in 2D and 3D. The collimation ratio of 250 at this position is in the region of the most commonly used moderate resolution on centimeter-to-decimeter sized specimens, but also for Bragg edge studies. The achievable beam size for full spectrum measurements is already at the maximum conventionally required, and will have to be reduced for smaller samples and in particular for the Bragg edge studies (3 x 9 cm^2 field of view (FOV)). This optional reduction will also enable a chopper to be placed upstream to avoid pulse overlap for the most useful 4.5 Å bandwidth. Two optional choppers for bandwidth definition are envisaged at about 2.2 m and 5 m from the moderator, which can be removed from the beam when no wavelength resolution is required and hence no advantage is taken of the pulsed nature of the source.

Instrument parameters	
Target	96 Hz
Moderator	cold
Moderator to sample distance	4 m
Collimation ratio L/D	100
Wavelength range / bandwidth	$1 - 15$ Å$/10$ Å
Beamsize up to	15 cm
Potential wave length resolution	5% (2-10 %)
Spatial / temporal resolution up to	5 μm / 10 ms
Flux (up to)	3×10^8
Moderator to sample distance	10 m
Collimation ratio L/D	250
Wavelength range / bandwidth	$1 - 15$ Å$/4.5$ Å
Beamsize up to	35 cm
Potential wave length resolution	3% (1-5 %)
Spatial / temporal resolution up to	10 μm / 100 ms
Flux (up to)	3×10^7

Table VI.2: *Instrument parameters for cold imaging beamlines*

VI.1.2 Thermal neutron imaging beamline

A thermal beamline again utilizes a 96 Hz target but views a thermal moderator (potentially removable in order to perform imaging with fast neutrons) with a 4 cm diameter. An aperture wheel at the exit of the target shielding at about 2 m enables it to trade spatial resolution capability for flux again for 2 measurement positions at about 4 m and 10 m from the moderator. The thermal beam enables investigations of dense objects and devices such as statues, ancient weapons, engines and other industrial devices, wood and metals etc.

The first position at 4 m provides a 15 x 15 cm^2 FoV at a low collimation ratio of 100 but at a very high flux for kinetic studies of massive samples and devices. Running engines, motor blocks and the like can be penetrated and stroboscopic approaches enabling time resolutions in the 10 msec range.

At measurement position 2, the FOV has increased and the moderate collimation of 250 can further be increased by choosing smaller or asymmetric pinholes at the 2m position aperture wheel. This provides ample flexibility to tune the resolution for investigations of dense large and medium sized objects, the observation of corrosion in, for instance, steel reinforced concrete, investigations of liquid metals as well as components from automotive and aerospace applications. Spatial resolutions from 20 – 400 μm can be considered, with FOV sizes up to 35 x 35 cm^2, depending on the requirements of a study.

The instrument might also be well suited for imaging with fast neutrons, but specific installations, including in particular a removal or partial removal of thermal moderation have still to be considered in detail. In case such a solution is not possible a dedicated beamline and the corresponding scientific case for imaging with fast neutrons has to be considered carefully, as fast neutrons enable the penetration of massive samples and can be valuable in applications involving batteries or active waste storage research amongst many others. Currently a lot of effort is being spent in improving the spatial resolution capabilities in this range.

Instrument parameters	
Target	96 Hz
Moderator	thermal
Moderator to sample distance	4 m
Collimation ratio L/D	100
Beamsize up to	15 cm
Spatial / temporal resolution up to	10 μm / 10 ms
Flux (up to)	3×10^8
Moderator to sample distance	10 m
Collimation ratio L/D	250/330/500/asym
Beamsize up to	35 cm
Spatial / temporal resolution up to	20 μm / 100 ms
Flux (up to)	3×10^7

Table VI.3: *Instrument parameters for thermal imaging beamlines*

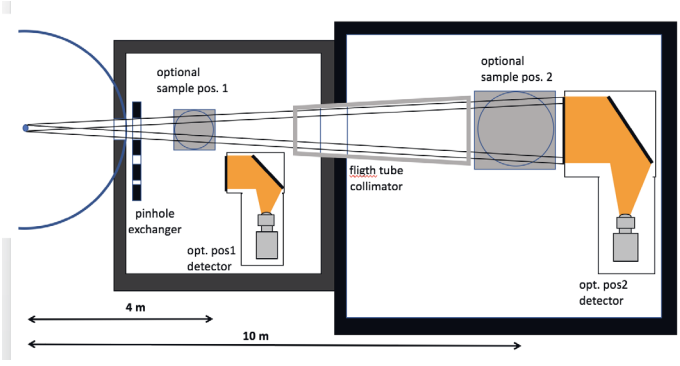

Figure VI.2: *Schematic layout thermal neutron imaging beam line.*

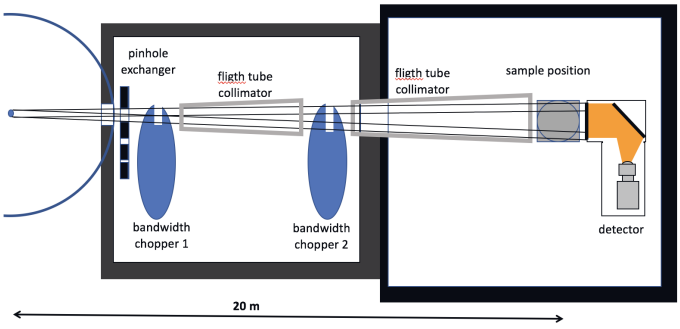

Figure VI.3: Schematic layout diffractive neutron imaging beam line.

VI.1.3 Diffractive neutron imaging beamline

A dedicated beamline for high wavelength resolution diffractive imaging, potentially combined with diffraction capabilities is considered due to the excellent flux and time-structure capabilities of HBS. At a cold moderator at 96 Hz and with a 4 cm diameter a measurement position at about 20 m can enable wavelength resolutions suitable for all kinds of Bragg edge imaging applications with a specific focus on strain mapping, which gains significant importance with the advent of additive manufacturing technologies.

The limited wavelength band of about 2.2 Å at a repetition rate of 96 Hz indicates the high efficiency required for such sophisticated applications. While the implementation of such a technique could be considered at the cold neutron imaging beamline, the addition of a neutron guide from close to the moderator to 5 – 7 m upstream from the 20 m sample position could further boost the performance of this method at a dedicated beamline. The beam size could be limited to around 5 – 7 cm across and the collimation ration to about 200. This will imply relatively relaxed requirements on the guide and high flux for diffractive imaging. The beamline would in addition feature two choppers to define the wavelength band required.

Such a set-up could in addition feature diffraction detector banks enabling combined diffraction/imaging characterizations of complex systems such as in-operando batteries and phase transitions in various sample environments.

Instrument parameters	
Target	96 Hz
Moderator	cold
Moderator to sample distance	20 m
Wavelength range / bandwidth	1-15 Å, 2.2 Å
Collimation ratio L/D	500
Beamsize up to	10 cm
Potential wavelength resolution	1% (0.5 - 2%)
Spatial / temporal resolution up to	100 μm / 600 ms
Flux (up to)	2×10^7

Table VI.4: Instrument parameters for thermal imaging beamlines

VI.1.4 Epithermal and high energy neutron imaging beamline

A dedicated beamline for higher energy neutrons is to be considered in order to optimize performance through dedicated instrumentation for maximizing efficiency, enabling, for example, isotope and element mapping through resonance absorption in the epithermal range. Moreover, higher energy neutrons provide potential for transmitting denser and thicker samples. This is of importance in a number of cases of technological interest, such as for large batteries. A dedicated beamline should feature two positions, one for conventional high energy neutron imaging and one for resonance absorption investigations, the first being relatively close to the source in order to maximize the available flux. The source can nevertheless be of a few cm in diameter, ideally about 5 cm for a 10 m sample/detector position to still match the achievable resolution. For the resonance absorption, imaging pulses should be very short, ideally below 1 μs in order to easily resolve resonance peaks in the epithermal range. For the same reason the beamline should be relatively long, which however impacts the available flux. A length of about 50-100 m should be considered. The epithermal range-to-probe is relatively narrow in time so a high source frequency can be chosen, for a 60 m position, the highest proposed frequency of 384 Hz with a period of 2.6 ms appears suitable. A T0 chopper might be useful to cut the spectrum at certain high energies and allow also for a complementary thermal neutron imaging capability on such instrument.

Instrument parameters	
Target	384 Hz
Moderator	epithermal
Pulse width	0.5 μs
Moderator to sample distance	10 m
Viewed source size	5 cm
Energy range	25 meV to 80 meV
Collimation ratio L/D	200 (1200 at 60 m)
Beamsize up to	20 cm
Spatial / temporal resolution up to	500 μm / 100 μm
Flux (up to)	5×10^9 / 10^7

Table VI.5: *Instrument parameters for epithermal and high energy neutron imaging beamline*

VI.2 Diffraction

Neutron diffraction instruments are well-suited to solve structural properties on the atomic scale in materials, and are particularly useful in revealing magnetic structures and clarifying the positions of light elements on a background of heavier ones, *i.e.* in a case where x-rays lack contrast or suffer from background.

Powder diffractometers are the work-horses used for structure determination due to the ease of sample preparation and the straightforward protocol of quantitative data analysis. Instruments may specialize in performing certain tasks, for example choosing peak fluxes from either thermal or cold moderators; high spatial resolution requires a very short wavelength and conversely, for studying large unit cell materials (e.g. metal-organic framework structures), longer wavelengths are needed. Recent developments also show the possibility of performing simultaneous bi-spectral extraction from both thermal and cold moderators. A further specialization of neutron instruments is typically made by trading resolution for intensity, choosing either high flux and low resolution or vice versa. While

at short pulsed sources such instrument characteristics are fixed, more flexibility can be gained with pulse-shaping choppers as applied on instruments at the long pulse source ESS. Here, the example for thermal powder diffraction shows the very flexible capabilities available, which include high resolution studies at the HBS. A similar approach is taken by the engineering diffractometer, with more complexity of so-called "wavelength frame multiplication" to increase the wavelength bandwidth.

The original pulse width at the HBS is relatively broad compared to short pulse spallation sources, however, it is still sufficient for powder diffraction studies of disordered materials or when using larger wavelengths for magnetic structures. For single crystal diffraction, emphasis can be given to focusing onto small samples rather than high spectral resolution. For applications in macromolecular crystallography, the pulsed HBS time structure provides additional information compared to standard Laue diffraction by separating the different diffraction orders by the neutron time-of-flight. Finally, it seems worthwhile to benchmark the concept for classical reactor instruments for operation at the HBS, *e.g.* a monochromatic D20-like instrument, with the advantage that higher orders from the monochromator can be used, as they are easily separated in time.

The following considerations apply to all proposed instruments listed below. Source time structure and instrument length determine bandwidth and spectral resolution. The natural bandwidth Λ is simply given by the instrument length L and the source frequency $f = 1/T$,

$$\Lambda/\text{Å} = \frac{3956\ \text{m/s}}{L/T}. \tag{VI.1}$$

Instead of using the natural pulse width $T0$, a shorter pulse Δt can be obtained by pulse-shaping choppers. One should note, however, that for using a pulse-shaping chopper, the original pulse needs to be sufficiently long and/or the chopper must be placed close enough to the source. The position D of the pulse-shaping chopper determines the filling of the time frame T for an instrument length of L with bandwidth Λ and should be

$$\frac{T0}{T} \geq \frac{D}{L-D}, \tag{VI.2}$$

which yields the neutron speed of $\bar{v} = (L-D)/T$ related to bandwidth

$$\Lambda/\text{Å} = \frac{v(1\ \text{Å})}{\bar{v}} = \frac{3956\ \text{m/s}}{\bar{v}}. \tag{VI.3}$$

The spectral resolution is determined by the ratio of pulse width to time-of-flight t from source to detector,

$$\frac{\Delta\lambda}{\lambda} = \frac{\Delta t}{t}. \tag{VI.4}$$

In order to obtain the final d-spacing resolution, divergence and path uncertainties need to be included

$$(\frac{\Delta\, d}{d}) = \sqrt{(\Delta\lambda/\lambda)^2 + (\Delta\theta\cot\theta)^2 + (\Delta l/l)^2}, \tag{VI.5}$$

where the divergence in the Bragg angle θ results from the incident divergence, the ratio of sample size to sample-to-detector distance and the spatial resolution of the detector. The length (and time) variation due to Δl is usually negligible and only matters in cases where very high resolution is required.

VI.2.1 Thermal powder diffractometer with flexible and high resolution

The diffractometer is placed at the long pulse target station (f=24 Hz, T=41.67 ms, T0=0.833 ms pulse length) using a cold and a thermal moderator, similar to the DREAM instrument currently being

built at ESS. The spectral resolution can be improved in a flexible way by 2 orders of magnitude using pulse-shaping choppers. As a result of this flexibility, the instrument covers most needs for powder diffraction, from high-resolution measurements (down to 0.0004 in backscattering geometry), e.g. for subtle peak splitting due to change of symmetry, to high-intensity measurements, e.g. for small samples.

The instrument is optimized for a resolution of 100 μs pulse length giving a resolution of $\Delta d/d$ = 0.39% at $2\Theta = 90^\circ$, $\lambda = 1.6$ Å (see Table VI.6). If the pulse choppers are placed just outside the shielding block (D = 2 m), the total instrument length is L = 102 m giving a bandwidth of 1.65 Å (see Equations VI.2 and VI.1). Alternatively, one could build a more compact instrument of larger bandwidth and reduced resolution by putting the choppers inside the shielding block.

The detector should extend over a wide range of scattering angles and cover a large solid angle, probably in horizontal cylinder geometry. The guide system will be elliptical with a high m coating close to source and sample to enable high guide transmission and high divergence at the sample. Assuming a brilliance transfer of 75% in the guide system and 10% transmission of the pulse chopper, we can expect a flux of 5 $\cdot$ 10^5 n cm^{-2} s^{-1} for the high-resolution setting of 100 μs pulse length; using the whole pulse and full divergence results in a 300 times higher flux (see Table VI.6).

Instrument parameters	
Target	24 Hz
Moderator	PE+H_2
Moderator to sample distance	100.8 m
Detector to sample distance	1.2 m
Wavelength band	0.75 - 2.4 Å
Detector range	$7^\circ < 2\theta < 175^\circ$
d-range (Q-range)	0.4-20 Å (0.3-16.7 Å^{-1})
High-resolution setting	
Pulse length	100 μs
Incoming divergence	0.25°
Resolution (Δd/d)	0.0061 - 0.0017 (0.0004) for $90^\circ < 2\theta < 175^\circ$
	0.044 for 2θ = 7°
Flux at sample	5×10^5 n cm^{-2} s^{-1}
High-intensity setting (full pulse)	
Pulse length	833 μs
Incoming divergence	2°
Resolution (Δd/d)	0.0047 - 0.014 for $90^\circ < 2\theta < 175^\circ$
Flux at sample	1.5×10^8 n cm^{-2} s^{-1}

Table VI.6: *Instrument parameters for the thermal powder diffractometers*

VI.2.2 Diffractometer for nanoscaled and disordered materials

This thermal powder diffractometer is dedicated to the measurements of small samples ($<$ 1 cm) with a high neutron flux at the expense of reduced resolution (Δd/d). The instrument will be capable of the pair-distribution function (PDF) measurements with an atomic resolution of 0.13 Å.

The instrument is very well-suited for diffraction studies of crystalline, amorphous and nanoscaled materials. The combination of PDF technique, small sample size and high neutron flux is a powerful

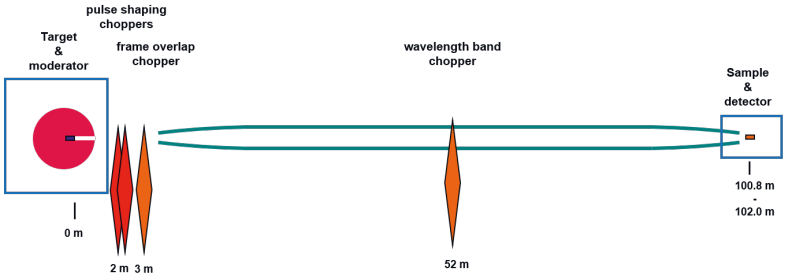

Figure VI.4: *Schematic layout of thermal powder diffractometer*

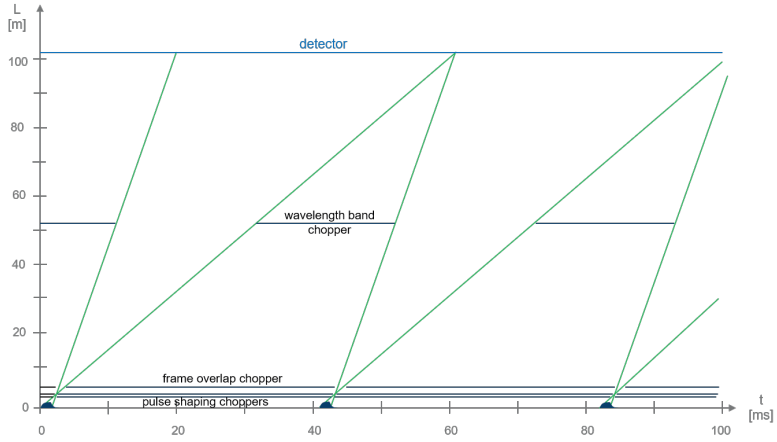

Figure VI.5: *Space-time diagram of thermal powder diffractometer*

tool that can be used by a large variety of user communities including soft matter, biology, environmental science, condensed matter physics and many others. We note that only few PDF dedicated instruments currently exist at reactor and spallation sources in Europe and therefore, the proposed instrument would be a welcome addition to the suite of neutron diffractometers at HBS.

The science case of the instrument is broad, but in what follows, we will highlight research topics that would particularly benefit from thermal powder diffraction measurements.

Nanoscaled materials: the PDF measurements can help us to understand the effect of surface modification, thermal treatment, lithiation and pressure on the local crystalline structure of nanoscaled materials, which is key to improving their performance as drug-delivery agents, sensors and cathodes in battery materials.

Liquid and glasses: isotope substitution plays a vital role in neutron diffraction studies of liquid and glassy materials, especially for understanding the hydrogen bonding mechanisms. Other examples include studies of the solid-liquid interface in energy storage materials, phase transitions in the bulk-metallic glasses at elevated temperatures and pressure-induced structural changes in glasses.

Confined materials: magnetic properties of the materials, as well as phase behaviour of liquids can be drastically changed in confinement. It is relevant for hydrogen storage and composite magnetic materials. Studies of local structure of nano-confined water are important to understand its adsorption properties, transport mechanism in shale formation and electric field induced phase transitions.

Nucleation and crystallization: the mechanisms of the nucleation and growth of nanoparticles, liquid crystals and glass crystallization are of high interest. The growth mechanisms are often complex and they include multi-phase and order/disorder transitions. Studying the growth dynamics with neutron scattering can shed light on the specific macroscopic properties of solid and amorphous materials.

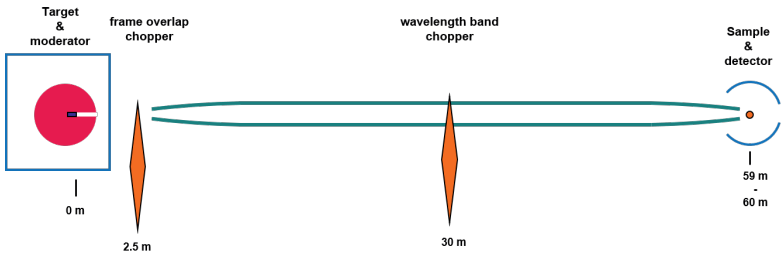

Figure VI.6: *Schematic layout of diffractometer for nanoscaled and disordered materials*

Instrument parameters	
Target	96 Hz
Moderator	PE
Moderator to sample distance	60 m
Detector to sample distance	1 m
Wavelength band	0.69 Å, 0.5 Å $< \lambda <$ 1.2 Å
Resolution	$0.016 < \Delta d/d < 0.028$
Detector range	$10^\circ < 2\theta < 140^\circ$
Flux	1.9×10^7 n cm^{-2} s^{-1} for 1.1° divergence

Table VI.7: *Instrument parameters for diffractometer for disordered materials*

In order to address such a broad scientific scope, we propose an instrument with L = 60 m and Δt = 0.24 ms (f = 96 Hz), with a usable bandwidth of 0.69 Å. Considering a 1 cm sample size, a sample-to-detector distance of 1 m and a detector pixel size of 5 mm, the resolution $\Delta d/d$ will vary from 0.016 to 0.028 and is approximately constant over a wide range of scattering angles. A highest real space resolution of 0.27 Å will be achievable at $Q_{max} = 24$ Å^{-1}.

We propose ^{10}B-based position sensitive detectors covering the range of scattering angles from 10 to 140° with a vertical cylinder geometry, similar to monochromatic reactor diffractometers such as D20 at ILL.

The position sensitivity of the detectors will provide an additional capability for the TOF Laue single-crystal diffraction.

VI.2.3 Single crystal and powder magnetism diffractometer

Magnetism is a prevailing domain of neutron scattering, attracting a relatively large user community. Typical demands are mediate/low rather than high resolution in Q or d-space, low-T, magnetic fields, pressure, low background and eventually polarized neutrons. Bragg signals as well as (mediate/low resolution) powder signals can certainly be measured efficiently at the HBS. With such a choice of resolution the instrument will be efficient also for diffuse scattering. Particular needs at high Q-

resolutions for larger unit cells can be fulfilled by phase shifting the chopper system towards longer wavelengths.

The combination of single crystal and powder measurements is a natural option for the position sensitivity of detectors favourably covering a large solid angle. A wavelength band 2-4 Å, taken from the peak flux of a cold source provides the Q-range of interest and can be polarized to a high degree by the neutron optics. Time resolution will be fixed by the choice of the target station 96 Hz with $\approx$200 μs pulse length. Focusing optics (Selene or Kirkpatrick-Baez) are considered for measuring small samples in a massive sample environment, for example in high pressure studies, and can adopt the incoming divergence. For polarized neutrons, there are new developments for powders to explore out-of-plane scattering and 3D information for the anisotropy of magnetic scattering, offering very precise moment determination from nuclear magnetic interference.

Detector position (volume) sensitivity is easy to fulfill with state-of-the-art B-10 detectors. In particular, these allow for a very high dynamic range for measuring intense Bragg and weak diffuse signals simultaneously.

Polarization analysis (PA) is a very attractive option, either with He-3 filters or by polarizing super-mirrors, for studying complex frustrated magnetism. PA may not need to cover a very large solid angle, specifically probing a smaller section of interest may well serve many needs.

Typical science cases in magnetism are related to low temperature physics. A possible exploration of its dynamics in neutron energy loss can typically be fulfilled with a rather compact geometry and the given sample-to-detector distance. Hence, the optional use of a monochromating chopper in front of the sample can perfectly transform the diffractometer to a suitable spectrometer.

Instrument parameters	
Target	96 Hz
Moderator	cold, methane, (PE)
Pulse width	240 μs
Moderator to detector distance	22 m
Wavelength band	2 Å $< \lambda <$ 4 Å
Detector-to-sample distance	1 m
Detector range (B-10, He-3)	$3^\circ < 2\theta < 170^\circ$
	0.8 m height, $<$ 5 mm spatial resolution
Neutron optics	m $<$ 3
Flux at sample	8.4×10^6 n cm^{-2} s^{-1}
Flux on small samples	6×10^5 n s^{-1} in 10 mm^2
Collimation	$30' \times 30'$ (h $\times$ v)

Table VI.8: *Instrument parameters for the single crystal diffractometer*

VI.2.4 Macromolecular diffractometer

The field of macromolecular crystallography consists mainly of protein crystallography, DNA and RNA. Some zeolithe or large organic molecules also form crystals, which may be investigated with this method. Typical samples come in two different conditions: for room temperature measurements they are typically enclosed in a glass capillary with an outer diameter of less than 2 mm. At cryo-conditions, the samples are kept at 100 K in a loop on a stainless steel pin with a 0.6 mm outer diameter. They are usually kept at cryo-temperatures by a gas stream of nitrogen from an

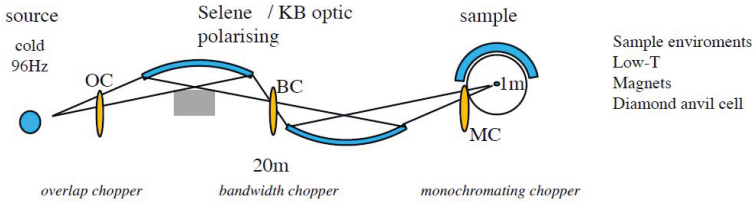

Figure VI.7: *Schematic layout of single crystal diffractometer*

cryostream set up. About 50% of the proposals at the BIODIFF diffractometer at MLZ are measured with this sample environment in place. In principle, the sample is stable at these cryo-temperatures and the data acquisition time is not so critical.

The instrument parameters of a TOF macromolecular diffractometer at the HBS borrow from the MANDI concept (see [134]). The wavelength band should be around $\Lambda = 3.3$ Å or less with a tunable wavelength centred between 2-5 Å. The divergence of the beam should be relatively small ($< 0.7°$) and adjustable in order to accommodate large unit cell sizes of up to 300 Å. If high resolution is required, as in this case, one should also be able to cut down on the pulse duration reducing the wavelength error. The sample itself does not contribute considerably to the error budget since its length is usually small, in the order of 1 mm. This translates into an error of the time of arrival of less than 1 μs for the relevant neutron wavelengths.

One may also note that the NMX concept (at ESS) uses a cold moderator with a standard wavelength range of around 2 Å $< \lambda <$ 3.8 Å. Pulse shaping is not required even at the long pulse source ESS to separate different reflection orders in a Laue spot by time-of-flight measurements. Scaling the NMX parameters and its spectral resolution, given by $l = 150$ m, $\Lambda = 1.8$ Å and $T0 = 3$ ms, suggest a possible instrument length of $l = 12.5$ m and $\Lambda = 3.3$ Å placing the instrument at the 96 Hz target.

The detector coverage should be as large as possible. Moreover, a very reliable detector concept should be chosen, since data acquisition times are expected to be quite long. Since the cross section of the samples is typically 1 mm by 1 mm or less, a high brilliance source may be a very suitable choice for this type of instrument, if the neutron transport to the sample is performed carefully.

Instrument parameters	
Target	96 Hz
Moderator	cold, methane, (PE)
Moderator-to-detector distance	12.5 m
Wavelength band	1.0 Å $< \lambda <$ 4.3 Å
Sample-to-detector distance	1 m
Flux at sample	4.0×10^7 n cm^{-2} s^{-1}
(on small samples)	$\sim 10^5$ n s^{-1} in 1 mm^2
collimation	$30' \times 30'$ (h $\times$ v)

Table VI.9: *Instrument parameters for the macromolecular diffractometer*

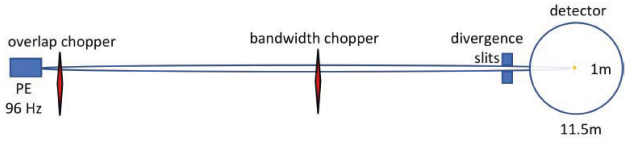

Figure VI.8: *Schematic layout of the macromolecular diffractometer*

VI.2.5 Engineering diffractometer

Typical tasks for a neutron diffraction instrument dedicated to the investigation of engineering materials are the analysis of textures, phases and stresses in materials.

The range of engineering materials which may be studied, is broad. It includes for example lightweight materials such as magnesium or aluminium used in the transport sector as well as high-temperature materials such as TiAl used in turbo chargers. However, it also includes smart materials, e.g. shape memory alloys. The analysis of residual stresses within a material shall be mentioned here in terms of its application using an engineering diffractometer. Knowledge about residual stresses helps in understanding the mechanical properties of a material. They play, for example, an important role in the load carrying capacity of a material.

The stress analysis, however, sets high demands on the d-resolution of the instrument. Besides divergence and path uncertainties, time resolution plays an important role to achieve a high d-resolution (see equation VI.5). Engineering diffractometers such as the BEER instrument at the ESS reach time resolutions of up to 0.1%. A high time resolution can be achieved either by a long instrument using the given pulse length of the source or by shaping of the pulse length using choppers.

We concentrate, here, on the latter case and choose therefore the medium HBS pulse length of 0.208 ms with a frequency of 96 Hz and a pulse repetition time of 10.4 ms. We focus, furthermore, on a compact instrument design with only 20 m from the source to the detector. The rather short instrument can achieve cost reductions due to savings in neutron guide and shielding costs. For the 20 m long diffractometer, the natural bandwidth of the instrument without choppers is about 2.06 Å. A chopper cascade consisting of four choppers using the wavelength frame multiplication method does the shaping of the 0.208 ms long source pulse. The first chopper of the cascade is placed about 1.2 m from the source, i.e. within the shielding of the source. The engineering feasibility of the chopper position has still to be proven. The first chopper allows the shaping of the bandwidth Λ depending on the first chopper position D, for example 1.2 m leads to a bandwidth of about 0.686 Å. Making use of the full natural bandwidth of 2.06 Å requires the creation of three subframes from the first chopper. A second wave frame multiplication (*wfm*) chopper is placed in a distance between 0.02 and 0.12 m relative to the previous chopper. The movable choppers, which are operated in optical blind mode, allows the tuning of the wavelength resolution independent of the wavelength. The wavelength resolution is given in the optical blind mode by

$$\frac{\Delta\lambda}{\lambda} = \frac{\Delta t}{t} = \frac{z_0}{L_{wfm}} \tag{VI.6}$$

where z_0 is the distance between the two *wfm* Choppers and L_{wfm} the distance of the middle position between the two disks and the detector. The movable set-up thus provides a tunable wavelength resolution between 0.11 to 0.64 %. Two additional choppers complete the *wfm* chopper cascade. They are needed to avoid cross talk between the subframes created by the first two *wfm* choppers. A frame definition chopper defines the wavelength band used and allows it to switch to pulse suppression mode. In pulse suppression mode, the usable wavelength band is doubled. For the effective use

of the pulse suppression mode, the *wfm* chopper disks are designed to allow for the creation of 6 subframes out of the HBS source pulse.

Besides a broad wavelength band, a wide angular coverage of the detector is needed for a broad d-range. Two 1 m^2 detectors, therefore, are placed at $\pm 90^\circ$ at a distance of about 1.5 m from the sample, covering an angular range of about $\pm 18.43^\circ$. For a wavelength band centered at 2 Å, this set up results in a d-spacing of about 0.60 to 2.59 Å which covers the relevant diffraction peaks for most engineering materials. Another advantage of the two detectors positioned at $\pm 90^\circ$ is that two strain components are measured at once. The distance of about 1 m to the sample position allows enough space for bulky samples as well as the use of a sample environment dedicated to engineering science such as stress rigs. The gauge volume of the sample is defined by different sets of diaphragms and radial collimators. Further extension of the detector area, e.g. in the off-plane region above the sample is possible, for example to increase the coverage of a pole figure during texture measurements.

Instrument parameters	
Target	96 Hz
Moderator	PE
Moderator-to-detector distance	18.5 m
Detector-to-sample distance	1.5 m
Wavelength band	2.06 Å, 4.12 Å (pulse suppression mode)
Resolution $\frac{\Delta d}{d}$	$>$0.27 %
Detector range	+71.57° $< 2\theta <$ ± 108.43°

Table VI.10: *Instrument parameters for the engineering diffractometer*

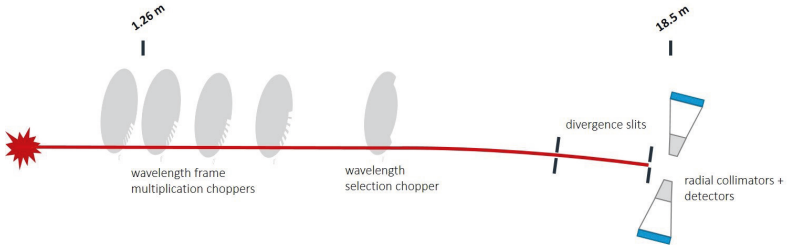

Figure VI.9: *Schematic layout of engineering diffractometer*

VI.3 SANS

VI.3.1 High resolution SANS

The SANS diffractometer is the workhorse instrument to investigate materials structurally on length scales above the atomic structure from the nm to the μm range in transmission geometry. The transmission geometry permits the efficient investigation of polycrystalline matter as well as ordering phenomena or anisotropy perpendicular to the beam direction without the necessity of a fine alignment of the sample. The optional use of polarized neutrons and polarization analysis yields additional sensitivity for magnetic order and allows the suppression of background from nuclear spin-incoherent scattering, originating e.g. from hydrogen atoms in the sample.

The wide range of length scales under investigation requires a variable collimation and angular resolution of the detector system. In particular, resolving μm length scales needs a high angular resolution together with long wavelengths cold neutrons, ideally with a wavelength $\lambda > 7$ Å. The high angular resolution of the neutron beam impinging on the sample is classically realized with a pinhole geometry. The transmission of a pinhole collimation is proportional to the 4th power of the length of the collimation, unless the size of the pinholes become larger than the sample or the neutron source. Shorter collimation lengths can be realized by moving neutron guide segments into the collimation flight path. The angular resolution of the 2D position sensitive detector system is defined by the intrinsic spatial resolution of the detector and the distance between sample and detector. At smaller distances, the angular range covered by the detector is increased at the cost of angular resolution. The increased length of the instrument, which is good for the performance of the optical elements as well as for the detector system, confines the available bandwidth without frame overlap. Therefore, the instrument is designed to operate at the target station with the lowest frequency, i.e. 24 Hz, and the instrument length is limited to 20 m between the moderator and the most distant detector position. Within this distance, a bandwidth of 7 Å, e.g. 2 - 9 Å, can be used.

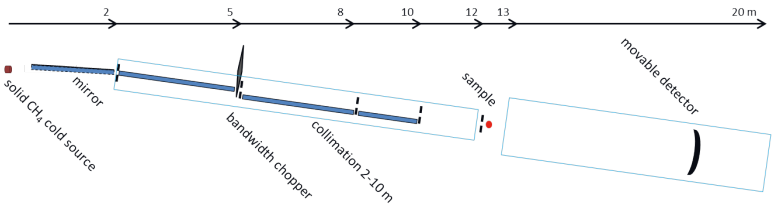

Figure VI.10: *Schematic layout of the high resolution SANS instrument*

Figure VI.10 shows a schematic layout of the proposed instrument. For reasons of background reduction, the instrument starts with a mirror immediately after the cold source, within the primary shielding of the TMR unit. This mirror (m=4, 1.5 m long) brings the detector out of the sight of the primary beam to reduce the fast neutron background of the instrument. It can feed a collimation offering 20 x 20 mm wide pinholes at up to 4 places between 10 m and 2 m in front of the sample. Optionally, the last section of the collimation can be used to introduce a cavity-type broadband polarizer into the beam to supply polarized neutrons. A 2D position sensitive detector is movable inside the evacuated detector tube between 1 m and 8 m distance from the sample.

Instrument parameters	
Target	24 Hz
Moderator	10 K, e.g. solid CH_4
Moderator-to-sample distance	12 m
Detector-to-sample distance	1 - 8 m
Wavelength band	7 Å, e.g. 2 - 9 Å
Q-range	10^{-3} Å^{-1} < Q < 1 Å^{-1}
Flux	9.4×10^7 n cm^{-2} s^{-1}

Table VI.11: *Instrument parameters for the high resolution SANS instrument*

The pulse emitted by the 24 Hz source after a 13 m flight path, or longer, is narrow enough to satisfy the wavelength requirements of a SANS experiment: at a 13 m distance, the wavelength resolution is $\Delta\lambda = 0.27$ Å, which is already better than 10% for a 3 Å wavelength. A single chopper is used

to define the wavelength band. With a chopper distance of 5 m from the source, frame overlap will only occur with neutrons of a 33 Å higher wavelength, which can be neglected.

The high-resolution measurements strongly benefit from a cold neutron source efficiently delivering neutrons with wavelengths $\lambda > 5$ Å. The para-H_2 cold source described in Chapter V.6.2 is not optimized for this application. A better choice would be a solid CH_4 or mesithylene moderator at a temperature below 10 K and an optimized geometry to feed the beamline with a low energy phase volume.

VI.3.2 GISANS

GISANS is a surface sensitive scattering technique. Instrumentally it mainly depends on a high degree of control over the collimation and thus divergence of the incoming neutrons as well as the possibility to control the impinging angle of the neutron beam onto the sample. Since both correlations in- and out of the sample plane are investigated, a high spatial resolution of the detector as well as a secondary flight path matched to the collimation distance is also desirable. In order to achieve small momentum-transfer Q, GISANS is usually operated with a cold neutron spectrum of wavelength $\lambda > 2$ Å, and operating in tof-mode is to be preferred in order to achieve high flux conditions. The design of the HBS allows a dedicated moderator with a pre-collimation of the beam. Moreover, the adjustable frequency of the source allows the optimization of the collimation and sample-to-detector distances with respect to the TOF properties of the HBS spectrum.

Instrument parameters	
Target	96 Hz
Moderator	$<$ 60 K, pencil shape
Moderator-to-sample distance	2.505 m
Detector-to-sample distance	0.25 - 2.505 m
Wavelength band	2-8 Å
Q-range	0.01 $Å^{-1} < Q < 2$ $Å^{-1}$
Flux	1.3 $\times$ 10^7 n cm^{-2} s^{-1}

Table VI.12: *Instrument parameters for GISANS instrument*

In order to make the best use of the conditions offered at the HBS, a pencil-shaped cold moderator can be combined with a short collimation distance. A short collimation and hence sample-to-detector distance can allow the use of a very wide pulse. The limited collimation can be offset by a small beam size, which is realized by a small pencil moderator and a high pulse frequency, which allow the sample flux and resolution on an overall shorter instrument. Another option would be the use of a focusing collimation, which however restricts the instrument to the use of larger samples.

Taking those considerations into account and considering the performance of current GISANS setups leads to the favouring of an instrument with a relatively short fixed moderator-to-sample distance and a moveable detector which at most can be moved as far from the sample as the moderator-to-sample distance. The size of the detector, determining the maximum Q has to be correlated with the lowest available wavelength. At 96 Hz source frequency and with a 2-8 Å wavelength band we arrive at a maximum moderator-detector distance of 5.1 m to fill the full tof frame with neutrons. Thus, the maximum sample-to-detector distance and collimation distance amount to 2.505 m in each case. In order to avoid frame overlap between the single pulses, two frame overlap choppers of 96 Hz are needed directly at the moderator slit as well as close to the sample. With a conventional detector size of 50x50 cm^2 this leads to the instrument parameters given in Table VI.12. These calculations assume a minimal pixel and beam size of 3x3 mm^2. A cold moderator would be needed with a flux

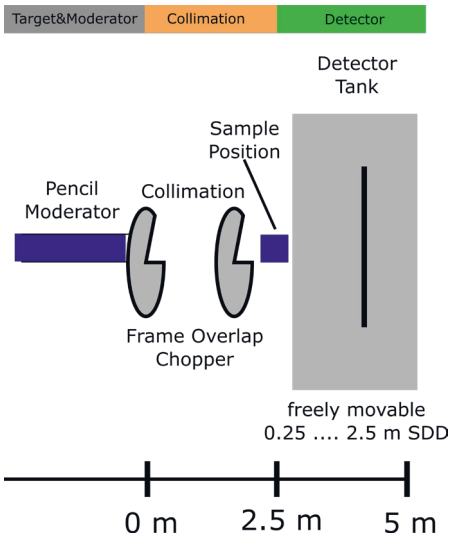

Figure VI.11: *GISANS instrument sketch. Distances for collimation and position for choppers, sample and detector are shown. The sample can be rotated to set the incoming angle. The detector bank is movable inside the detector tank.*

maximum well above a wavelength of 2 Å, at a distance where the majority of the peak is not cut off by the chopper to fulfill all tof conditions. With a suitable flux maximum at 4 Å this renders a temperature of 60 K or less.

Such an instrument, while exploiting the full flux of a HBS target/moderator system should be fairly compact. Optimal use of the tof conditions, a cold and geometrically suitable moderator as well as distances and slit openings will provide a competitive instrument. Still, the compactness of the instrument will amount to less required shielding and flight optics, apart from the choppers. As the first collimation and moderator slit is identical, this may even remove the need for a neutron guide altogether. With only a minimal loss in resolution, a polarizer can be included into the polarization section, either between the collimation slits or between the moderator and the first slit.

Summing up all those properties a GISANS at the HBS can provide a powerful instrument while being moderate in terms of technical requirements and budget. Most current GISANS experiments could be performed at such an instrument, limited only in flux and thus measurement time for an experiment.

VI.4 Reflectometry

VI.4.1 Specular reflectometer with SELENE optics

Reflectometers are used to measure layered structures either artificially prepared like thin films, or biological membranes to determine layer composition, density, layer thickness and interfacial roughness. For this, they measure the reflectivity R as a function of the momentum transfer $q_z = 4\pi sin(\Theta/\lambda)$. Reflectometers without TOF measure the reflectivity by illuminating the sample with a well-collimated beam varying Θ at a fixed λ. For reflectometers operated in TOF as described in Chapter VI.4.2, scanning is relized by varying λ at a fixed angle θ. At a reflectometer utilizing the SELENE optics, the specular reflectivity is measured by varying both θ and λ. By varying both parameters, the acceptable phase-space volume is largely increased in comparison to conventional

reflectometers, also increasing the flux by up to an order of magnitude at the sample position. In this high intensity mode, the off-specular reflectivity cannot be measured.

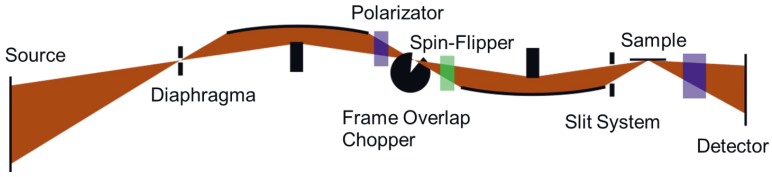

Figure VI.12: *Sketch of a reflectometer with a SELENE optics.*

Instrument parameters	
Target	24 Hz
Moderator	H_2
Moderator-to-focal point distance	0.3 m
Focusing section length	20 m
Sample-to-detector distance	2 m
Divergence	1.5 °
Wavelength band	3 - 10.4 Å
Resolution	5.1 % - 1.5 %
Flux	$4 \times 10^7 s^{-1} cm^{-2}$

Table VI.13: *Instrument parameters for a reflectometer with a SELENE optics.*

Figure VI.12 presents a reflectometer with SELENE optics. It consists of a diaphragma close to the source acting as a virtual source for the reflectometer defining the footprint of the beam at the sample position. By adjusting the footprint to the sample size, the background can be minimized. Two-half elliptical mirrors are aligned such that the virtual source at the diaphragma position is projected to the sample position. The left focal point of the first elliptical mirror is located at the diaphragm, the other focal point is shared by both elliptical mirrors and the right focal point of the second elliptical mirror is placed at the sample position. As it is not necessary to coat the whole of the elliptical mirrors, a large space is present between both mirrors for a polarizer, spin-flipper, frame-overlap chopper and other optical elements when necessary. Absorbers in the middle of both elliptical mirrors prevent a direct view of the sample to the source, reducing the background greatly. A slit system directly placed in front of the sample can be used to define the angular divergence. Closing this slit system to a small divergence, a conventional mode can be realized to screen q_z by varying λ.

As the reflectivity scales with q^{-4} and therefore with λ^4, it is best for a reflectometer, to use long wavelengths. Therefore, such a reflectometer will be operated at an extraction channel with an inserted H_2 moderator optimized for long wavelengths and therefore at the 24 Hz target. As a reflectometer with a SELENE optic can handle a large divergence, the diaphragma should be located close to the moderator surface. For the Target/Moderator/Reflector assembly presented in Chapter V.6, a useful position is the exit of the reflector. For this, the elliptical mirror needs to be close to the TMR unit, placing a limit on the coated surface.

By using the analytical formulas given in reference [135], an initial optimization of the presented boundary conditions can be done and the result is presented in Table VI.13. The optimization results in an instrument length of 22.3 m and a flux at the sample position of $4 \cdot 10^7 s^{-1} cm^{-2}$ for the high intensity mode which is comparable to reflectometers operated at research reactors [136, 137].

VI.4.2 Reflectometer with off-specular scattering

Reflectometry is a method to investigate layered structures. Typically, these samples are laterally not entirely flat and homogeneous due to the preparation process. If these inhomogeneities extend to a length scale of some μm, off-specular scattering, i.e. scattering within the plane of the incoming and specularly reflected beam, is emitted. This off-specular scattering signal is also a background modifying the specular reflection signal, as it contains information about the lateral structure of the sample under investigation.

Reflectometers can be built with either a horizontal or vertical scattering plane and the sample aligned perpendicular to this. This proposal describes an instrument with a horizontal scattering plane, because it can be realized with less mechanical effort. An instrument with a vertical scattering plane is necessary to measure reflectivity and off-specular scattering from liquid layered structures that are of interest mainly for biological applications. Most parameters of the instrument proposed can be transferred to a vertical reflectometer. Additional care must be taken in terms of the supply of the incoming beam, as it is necessary to be able to vary α_i while the sample stays horizontal.

Figure VI.13 shows a top view of the schematic layout of such a reflectometer. The instrument described here is suitable to efficiently measure specular reflectivity as well as off-specular scattering. To discriminate between specular reflectivity and off-specular scattering, the angle of incidence α_i needs to be defined with high precision, while all reflected and scattered beams are registered simultaneously on a position-sensitive detector.

For off-specular scattering experiments, the angle perpendicular to the scattering plane is not resolved. This is only necessary to resolve lateral structures with nm length scales with GISANS using the dedicated instrument (see Section VI.3.2). For this reason, the necessary collimation of the incoming beam is performed by two slits with a vertical opening. In the plane perpendicular to the scattering plane there is no need to resolve the angle of the neutrons impinging on the sample. A focussing of the incoming beam is possible, so that the instrument will be quipped with an ellipsoidal neutron guide in the vertical direction that is continued throughout the collimation section up to the second slit. The first focal point of the ellipse is in the cold source, while the second focal point is at the sample position to deliver an intense beam, small in size, to small samples.

The neutron guide in the scattering plane does not need to transport a high divergence, it can be bent to reduce the background of fast neutrons at the sample and detector positions.

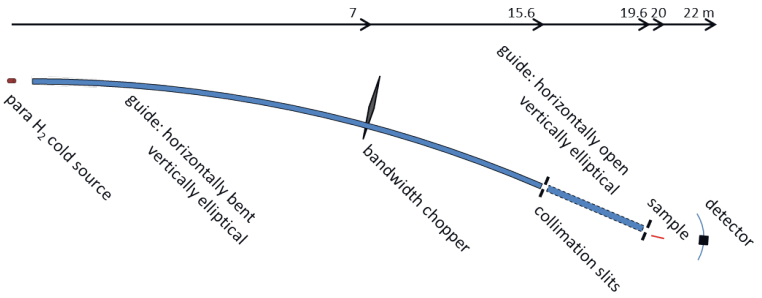

Figure VI.13: *Schematic layout of the reflectometer with off-specular scattering option*

As the reflectivity decreases strongly with Q, the use of the long-wavelength part of the neutron spectrum (corresponding to small Q values) is still efficient, even if the intensity is much lower compared to the short-wavelength part. For this reason, a para-H_2 cold source is a very suitable choice to feed this instrument, because it efficiently delivers neutrons in the wavelength range 1-3 Å, where

the measured reflectivity is small. The largest wavelength band is available using the 24 Hz target station, but a limit is set due to the resolution requirements of the experiment.

Typically, for example for measurements of total reflection edges or superstructure Bragg peaks of multilayer samples, a relative wavelength resolution of 4% or below is required, at least for the small Q region. An instrument length of 22 m between cold source and detector yields 4% wavelength resolution for all wavelengths above 4 Å with a 6.7 Å wide wavelength band, defined by a single chopper well in front of the collimation section. Dependent on the resolution requirements, one may choose to measure a wide Q range with high flux and low resolution, for instance with a 1.3 - 8 Å wavelength band, or shift the band to longer wavelengths, providing higher resolution with a limited Q range and lower flux. An extended Q range can always be reached by performing successive measurements at different α_i.

Instrument parameters	
Target	24 Hz
Moderator	liquid para H_2
Moderator-to-sample distance	20 m
Detector-to-sample distance	2 m
Wavelength band	6.7 Å, e.g. 1.3 - 8 Å
Wavelength resolution	4% at 4 Å wavelength
Q-range	2×10^{-3} Å^{-1} < Q < 0.5 Å^{-1}
Flux	1.7×10^7 s^{-1}cm^{-2} at 2 mrad collimation

Table VI.14: *Instrument parameters for the reflectometer with off-specular scattering*

VI.5 Spectroscopy

VI.5.1 Cold chopper spectrometer

The cold chopper spectrometer is used to study low energy coherent excitations, in particular those of magnetic origin, and relaxational phenomena with an emphasis on soft matter and material science with narrow energy resolution. It is placed at the 96 Hz target station facing the para-hydrogen moderator providing a brilliant initial neutron spectrum $1.5 < \lambda < 9$ Å to cover the full application range of cold neutron spectroscopy. The required secondary time-of-flight resolution dictates a sample-to-detector distance $L_{\mathrm{SD}} \geq 3$ m, providing a secondary bandwidth

$$\Delta\lambda' = \frac{h}{m_n}(L_{\mathrm{SD}} f_{\mathrm{rep}})^{-1} \approx 14\text{Å}, \tag{VI.7}$$

which covers sufficient dynamical range, when the primary spectrometer is tuned to an initial energy as low as $E = 1$ meV. The energy resolution can be varied by means of two counter rotating chopper assemblies with a maximum speed of 18.000 revolutions per minute. The overall instrument length is limited by the most relaxed energy resolution at a long neutron wavelength. As we envision the use of an initial neutron wavelength $\lambda > 6$ Å only for ultimate energy resolution applications, we fix the instrument length from moderator to the final chopper assembly to 14 m, which provides an initial wavelength resolution of 2% for $\lambda = 5$ Å and of 1 % at $\lambda = 10$ Å, if the full moderator pulse is accepted at the sample.

The final chopper assembly $L_{\mathrm{MS}} = 1.5$ m upstream the sample controls the sample illumination between 20 and 50 μs to enable different secondary time-of-flight resolution. The chopper assembly

that controls mainly the initial wavelength resolution is placed half way between the final chopper assembly and the moderator to enable monochromatic operation as well as a modest Repetition Rate Multiplication (RRM) using three chopper pulses out of one moderator pulse, in order to use the 1/100 s time frame more effectively for the short wavelength part of the moderator spectrum. It consists of 2 pairs of counter-rotating choppers run in an optical blind configuration to enable a continuous variation of the wavelength resolution and focus specific regions of the sample excitation spectrum if demanded by the experiment [138].

Polarization analysis can be implemented simply by using supermirror devices for the primary polarizer. The secondary spectrometer can be equipped either with wide angle spin filter cells and coil configurations (as developed by JCNS for the spectrometers TOPAS at the MLZ and TREX at the ESS) or, alternatively with radial supermirror devices (as used on the cold instrument DNS at JCNS) as a maintenance free solution. However, the large solid angle coverage is difficult to achieve for the high resolution spectrometer discussed here, which implies a large sample-to-detector distance. A potential solution could employ a robot placing a reasonable sized analyser at a specific position.

Instrument parameters	
Target	96 Hz
Moderator	liquid para-hydrogen
Moderator-to-sample distance	15.5 m
Detector-to-sample distance	3 m
Initial wavelength range	1.6 Å$< \lambda < 10$ Å
Scattered wavelength range	0 Å$< \lambda < 13$ Å
Detector range	$3^\circ < 2\theta < 150^\circ$
Flux @ $\lambda = 5$ Å, $\delta\hbar\omega = 100\mu$eV	3.4×10^5 n cm^{-2}s^{-1}

Table VI.15: *Instrument parameters for the cold chopper spectrometer*

VI.5.2 High energy chopper spectrometer

Knowledge of the high energy excitation spectrum in condensed matter is crucial for the understanding of the lattice dynamics and hence the thermal behaviour in novel functional materials or the spin dynamics in magnetic materials ordering at applicable temperatures around and above room temperature. In addition, any theory of high temperature superconductivity will be tested, whether it can explain the high energy magnetic excitation spectrum. The 384 Hz target station provides ideal conditions for a high energy chopper spectrometer as its moderators are a brilliant source of neutrons in the neutron energy range 10 meV $< E <$ 300 meV. At the same time, the high repetition range in combination with a sample-to-detector flight path $L_{\mathrm{SD}} = 2$m yields the scattered neutron bandwidth $\Delta\lambda' \approx 5$ Å, so that the dynamic range extends to the full range of interest for thermal neutron energies.

As the high energy chopper spectrometer focuses neutron energy loss scattering, the initial wavelength resolution is matched by the secondary resolution even for the comparably short sample-to-detector distance. The chopper system consists of an illumination control chopper $L_{\mathrm{MS}} = 1.5$ m distance upstream from the sample to provide sufficient space for the sample environment and other equipment. The wavelength resolution chopper assembly is placed outside the target monolith. It consists of four pairwise counter rotating discs in an optical blind configuration, which allow a continuous variation of the initial wavelength resolution [138, 139]. Due to the high repetition rate of the source, the spectrometer can operate in a monochromatic mode, which requires an additional chopper to prevent cross talk from earlier pulses. The chopper system will enable an initial wave-

length resolution of 0.005 Å $\geq \delta\lambda \geq 0.025$ Å. Similar to the energy resolution, the larger initial wave vector puts stronger constraints on the initial collimation. It has been shown, that quasi-elliptic neutron guides with a length > 25 m can efficiently transport neutron beams of 1 cm $\times$ 1°.

Instrument parameters	
Target	384 Hz
Moderator	Liquid para-hydrogen
Moderator-to-sample distance	26.5 m
Detector-to-sample distance	2 m
Initial wavelength range	0.5 Å$< \lambda < 2.5$ Å
Scattered wavelength range	0 Å$< \lambda < 5$ Å
Detector range	$3° < 2\theta < 150°$
Flux @ $E = 45$ meV, $\frac{\delta E}{E} = 4\%$	9×10^4 n cm^{-2}s^{-1}

Table VI.16: *Instrument parameters for the thermal chopper spectrometer*

VI.5.3 XTOF spectrometer with high $\vec{Q}$-resolution

Using focusing Bragg optics, the direction and the size of the initial wave vector of the neutron $\vec{k}$ become correlated. This can be explored to increase the phase space volume by which the sample is illuminated without deteriorating the energy resolution in a specific region of the dynamical range, the so-called time-focusing. In particular for thermal neutrons, for which the angular acceptance of neutron guides is limited, one may employ a much wider divergence range to increase the intensity on the sample and still keep the resolution for the dynamic range in focus of the experiment. The compact design of HBS allows a short distance between the moderator and the sample and therefore the emission time is long enough to apply time-focusing.

A completely new type of instrument can be envisioned to cover the science case of three-axis spectrometers at today's reactor sources. From eq. VI.7 it is clear that any voxel on the detector records a constant $\vec{k}'$. If we now use a focusing monochromator and a rotating crystal as the focal point of the monochromator, a small beam with the collimation falling onto the monochromator illuminates the sample for a short time given by the rotation velocity. Narrowing down two dimensions of phase space, the two remaining increase, i.e. wavelength distribution and the transmission time. However, time focusing matches the resolution for a specific range of k' and so one can scan $\vec{k}$ to record the scattering function $S(\vec{Q}, \omega)$ with high resolution in the energy loss range of the spectrum.

At HBS, with a 96 Hz target station, a large monochromator at $L_{mono} \approx 6$ m distance from the moderator could focus a beam with relaxed spectral width onto a rotating second monochromator crystal in $L_{mc} = 2$ m distance from the static monochromator. The rotation direction is chosen such that the Bragg condition is first fulfilled for the long wavelength part of the band transmitted by the focusing monochromator and later for the short wavelength part. The time-focusing condition for a geometry with 2 m distance from the first to the second monochromator and sample-to-detector distance $L_{\mathrm{SD}} = 2$ m is shown in Figure VI.14.

The appropriate choice of the harmonic and rotation frequency commensurate with the moderator frequency enables versatile instrument configurations to cover a wide dynamic range, while focusing a specific region with optimized flux/resolution conditions. The potential gain can be estimated using the ratio between the wavelength resolution defined by the pulse length and the time the rotating crystal remains in the Bragg condition, and the wavelength resolution of a flat monochromator crystal. This ratio varies between 5 and 15 for the thermal energy range 0.7 Å$< \lambda < 2.5$ Å.

The choice of the 96 Hz target station is guided by the exploration of the above mentioned versatility, the required pulse length needed for the time-focusing and the high peak brightness of the thermal moderator. A compact spectrometer with a movable detector array covering $3^\circ < 2\theta < 90^\circ$ could be implemented (Figure VI.15).

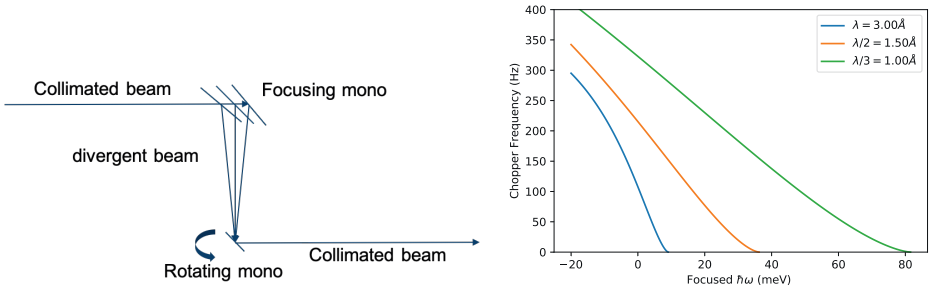

Figure VI.14: *Left: Schematic of the double crystal monochromator for an X-ToF spectrometer with a static focusing and a rotating crystal monochromator. Right: Focusing frequency as a function of the requested focus energy for different harmonics of the (002) reflection from a pyrolitic graphite crystal. The scattering angle is $2\theta = 30^\circ$.*

Instrument parameters	
Target	96 Hz
Moderator	PE
Moderator-to-sample distance	10.8 m
Detector-to-sample distance	2 m
Initial energy range	10 meV$< E < 200$ meV
Energy transfer range	-50 meV$< \hbar\omega < 200$ meV
Detector range (movable)	$3^\circ < 2\theta < 90^\circ$

Table VI.17: *Instrument parameters for the thermal crystal-chopper spectrometer*

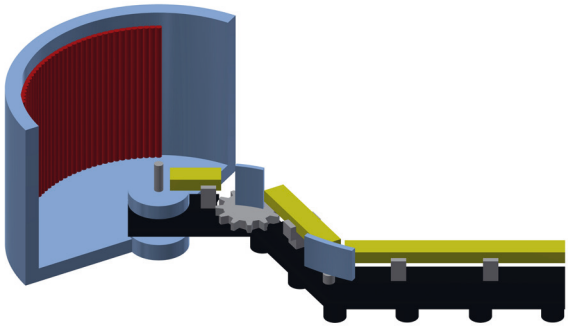

Figure VI.15: *Schematic drawing of HBS X-ToF spectrometer.*

VI.5.4 Vibrational spectrometer

Compact sources enable novel instrument designs also for vibrational spectrometers used to study localized excitations in the energy range of hundreds of meV. Recently it has been realized that direct geometry instruments provide distinct advantages over indirect geometry instruments, namely a superior signal-to-noise ratio, an improved resolution for large energy transfer and access to a significantly larger range of momentum transfer [140]. These advantages come at the price of a broader energy resolution going to low energy transfer, thus requiring a scan of incident neutron energy and correspondingly longer measurement times, if a large dynamic range needs to be covered. For the HBS, we suggest to explore the potential of a compact spectrometer with a crystal monochromator that can focus neutrons from a wide solid angle onto the sample. The use of a Fermi chopper will allow time-focusing to optimize the energy resolution in particular for large energy transfers, which is the scientific region of interest. This type of instrument could also benefit from a dedicated hot moderator, which would provide ideal conditions in the neutron energy range between 50 meV $< E <$ 1000 meV. However, also a conventional thermal moderator is expected to provide a high brightness in the energy region between 10 meV $< E <$ 300 meV.

VI.5.5 Backscattering spectrometer

Backscattering spectrometers are used to study relaxational and diffusional motions on the time scale of ns. The energy resolution $\delta\hbar\omega \approx 1\mu$eV allows also the distinction of hyperfine levels of atoms. For time-of-flight backscattering the intensity becomes extremely low if the primary energy resolution δE is matched to the secondary energy resolution $\delta E'$ for perfect single crystals.

We envision the use of elastically deformed analyzer Si(111) crystals at a slight departure from ideal backscattering condition to enable a secondary energy resolution $\delta E' \geq 2$ μeV [141, 142]. To match the initial energy resolution, one either needs to shorten the moderator pulse by means of the decoupling or the poisoning of the moderator, or one shapes the pulse to control the initial resolution δE. As the former has significant implications on the neutron economy in the moderator, we opt for the latter solution, which adds the constraint that the chopper limits the bandwidth depending on the distance of the chopper from the moderator L_c and the moderator pulse length. For the HBS, the closest position of a chopper is at $L_c = 2$ m, from there, the overall instrument length can be estimated at $L_c/dutycycle \approx 100$ m. These boundary conditions lead us to choose the solid methan moderator at the 96 Hz target station to realize a dynamic range of ± 150 μeV. For this instrument length, a pulse length $\tau_c = 75$ μs yields a primary neutron energy resolution $\delta\hbar\omega = 2$ μeV. Such a pulse length can be realized even for beam cross section of modest size using state of the art chopper technology with counter-rotating discs. Since backscattering spectrometers request only modest wave vector resolution, a quasi-elliptic guide system will be optimized for a wide divergence distribution of $4^\circ \times 4^\circ$ (FWHM) on the sample, also providing a reasonably small pinhole at the position of the pulse shaping chopper assembly.

Polarization analysis has in the recent past been discussed as a means of improving the signal-to-noise ratio by distinguishing the spin-incoherent scattering for elements like H, Li, N, Cl or K, which are relevant for material research in energy and life sciences. In particular, studies of collective relaxation phenomena would become feasible with backscattering resolution by separating the coherent structure factor. By measuring the spin flip scattering cross section, any coherent scattering, either from the sample or from the sample environment, is reduced by the flipping ratio. Thanks to the narrow energy range in a backscattering experiment we consider values above 50 as achievable. The flux penalty due to polarizing the beam and analysing the spin state of the scattered neutron should not exceed a factor of 0.2, finally providing a one order of magnitude improvement in signal-to-noise ratio.

Instrument parameters	
Target	96 Hz
Moderator	Solid methane
Moderator-to-sample distance	100 m
Detector-to-analyser distance	2.5 m
Initial wavelength range	6.05 Å$< \lambda < 6.5$ Å
Scattered wavelength	6.27 Å
Analyser range horizontal	$10^\circ < 2\theta < 150^\circ$
Analyser range vertical	$-22^\circ < 2\theta < 22^\circ$
Energy resolution range	3 μeV $< \delta\hbar\omega <$ 20 μeV
Flux @ $6.05 < \lambda < 6.5$ Å, $\delta\hbar\omega = 3$ μeV	7×10^6 n cm^{-2}s^{-1}

Table VI.18: *Instrument parameters for the backscattering spectrometer*

VI.5.6 Neutron spin echo

Among neutron spectrometers, the neutron spin-echo (NSE) is the one with the highest resolution and the ability to cover a dynamic range difficult to access with other experimental methods. The NSE technique makes use of the direction of the neutron spin as a stopwatch to measure small differences in the neutron velocity before and after scattering. Typically neutron spin-echo is employed to study dynamical properties both of soft and biological matter but it can also extend the ability to tackle a number of hard matter problems. The typical length scale probed by NSE is in the nanometer range while the time-range extends from ps to several hundreds of ns.

Among the known NSE instruments, the generic IN11 type (i.e. IN15 at ILL, J-NSE at MLZ or the SNS-NSE) exploits magnetic precession coils for spin-coding and is the one that achieves the highest resolution. The Wide Angle NSE spectrometer - in the form first demonstrated by the SPAN (HZB), then expanded for the new WASP at ILL - also uses spin-precession coding in a magnetic field, however with a different symmetry which allows for a larger detection solid angle but at lower resolution. The last typology of NSE is the so-called resonance spin-echo that replaces each large magnetic coil with two resonant flippers. In its MIEZE configuration, the resonance spin-echo is particular suitable for magnetic scattering.

Spin-echo spectrometers are well-suited for pulsed source, as already demonstrated by the NSE spectrometer operated by JCNS at the SNS spallation source and by the studies on a possible NSE at the future European Spallation Source (ESS). The maximum time scale (Fourier-time) accessible with NSE is given by

$$\tau = min\left(0.18\left[\frac{ns}{Tm\mathring{A}^3}\right]J_{max}\lambda^3, H\left[\frac{ns}{\mathring{A}^2}\right]\lambda^2\right), \tag{VI.8}$$

where J_{max} is the magnetic field integral proportional to the largest achievable field in the precession region and H is the field integral homogeneity parameter. The spectrometers of last generation can reach $J_{max} > 1.5$ Tm and a H=2.5 ns Å^{-2}. Usually, experiments in soft and biological matter need Fourier-times of the order of 100 ns, which can be obtained with a wavelength of 8 or 9 Å at the existing NSE spectrometers. Hard-matter samples require generally shorter times. Relying on a good flux for cold neutrons at the sample position is essential for successful operation of the instrument. As an example, on average, the measurement of a single Q-curve of a polymer melt at J-NSE requires circa 15 hours for sample, reference and background and with statistics of about 3% (wavelengths of 8 to 10 Å). The measurement time scales almost linearly with the neutron intensity.

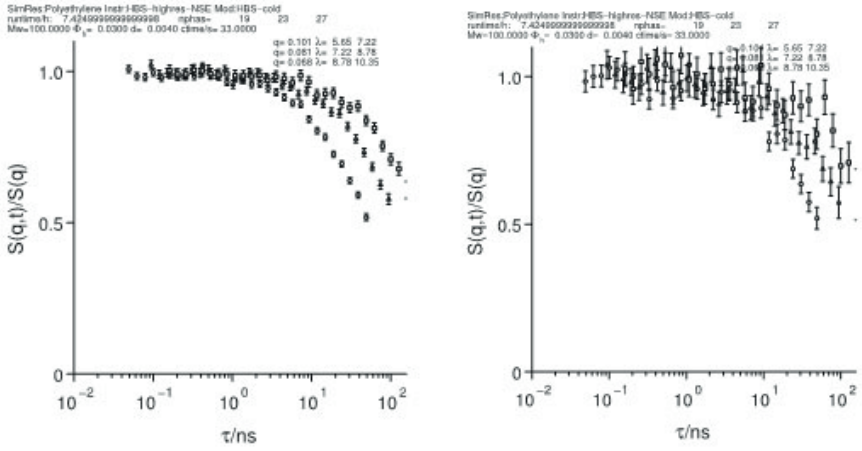

Figure VI.16: *Simulated intermediate scattering function of a typical soft matter sample (partly deuterated polymer melt plus reference sample) for 10% of the ESS intensity (left), and 1% of the ESS intensity (right), with 7.5 hours measurement time. It shows that high resolution data could be recorded in an acceptable time at the flux planned for HBS if its brilliance exceeds several percent of the ESS design brilliance.*

Lastly, the dimension of the moderator also plays a role on the performance of the instrument. Because of the large samples (≈3 x 3 cm^2) and of the precession path length (typically 3 - 4 m long) a carefully designed (still to be investigated) neutron beam optics must be integrated into the neutron guide feeding the instrument. It has to accept a divergence of about 2 x 2 degrees from the source and transform it to an output window at the instrument of 4 x 4 to 6 x 6 cm^2 with a divergence of about 0.6 x 0.6 degrees in a homogeneous fashion. For the envisaged long wavelengths this should be possible. Design and assessment of losses/performance has still to be performed.

Nevertheless, for an eligible spin echo spectrometer at the HBS a large moderator window (radius $>$ 3 cm) is preferable together with a good flux at the sample position for wavelengths between 6 Å and 13 Å (preferably 16 Å). A source frequency of 24 Hz (pulse length circa 50 μs) would allow a wavelength band of circa $\Delta\lambda = 4.7$ Å, for a moderator-detector distance (DMD) of 35 m (as was the case with ESSENSE). A larger band, e.g. $\Delta\lambda = 8$ Å, for DMD = 20.5 m, can also be used but the practical gain will not increase proportionally. Three or four disk choppers (rotating at the source frequency), positioned circa between 6 and 15.5 m could extract the wavelength-frames needed to cover the desired range of wavelengths. The state of the art of the precession coils is that of J-NSE and IN15. Both instruments mount coils with an optimized geometry that maximizes the filed integral homogeneity; the coils are superconducting in the case of J-NSE, and are water-cooled copper magnets at IN15. The increased field homogeneity requires weaker corrections and extends the range of accessible Fourier times by a factor of 2-3 compared to the previous generation of instruments, providing the best energy resolution for the accessible wavelength band.

Three principle types of NSE spectrometers could be considered with slightly different fields of application: a classical J-NSE or IN15 type spectrometer mainly for soft matter applications, a wide angle NSE similar to SPAN and WASP for a large solid angle coverage suitable for investigating glass transitions and proton diffusion, or a resonance NSE such as RESEDA with the MIEZE option for medium resolution measurements of magnetic samples, including sample B-fields.

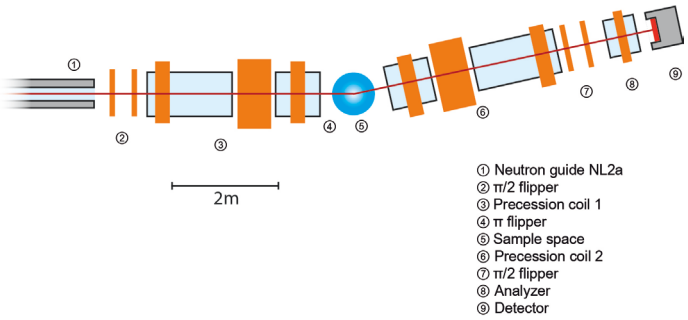

Figure VI.17: *NSE instrument schema as realized for the J-NSE at MLZ. The segmented main coils guarantee an optimized field homogeneity for high resolution, for a pulsed source such as the HBS only the pi/2-flippers and the pi-flipper need to be ramped with the incoming neutron wavelengh during the pulse arrival, as has been realized at the SNS-NSE. All other magnetic fields are static during measurement of a Fourier time.*

Instrument parameters	
Target	24 Hz
Moderator	para H_2 (or other moderator optimized for long wavelengths)
Moderator-to-sample distance	31 m
Detector-to-sample distance	4 m
Wavelength range	6 Å $< \lambda <$ 16 Å
average Flux (up to)	5×10^7 cm^{-2} s^{-1}

Table VI.19: *Instrument parameters for an NSE spectrometer based on the design of the ESSENSE spectrometer proposed at the ESS.*

VI.6 Analytics

VI.6.1 Prompt gamma neutron activation analysis

Prompt gamma neutron activation analysis (PGNAA) is an analytical technique for the nondestructive elemental analysis of samples of diverse origins. PGNAA is routinely applied at continuous neutron sources i.e. research reactors using either a thermal or cold neutron beam without any neutron time-of-flight (TOF) information. The capability to perform time resolved prompt gamma neutron activation analysis (T-PGNAA) with resonance neutrons was demonstrated on the INES beam-line at the pulsed spallation neutron source ISIS [64, 143]. Selecting neutrons in the cold, thermal or resonance energy range provides an elemental selectivity for accurate quantification by eliminating interference or by increasing the signal-to-background ratio. Furthermore, neutrons with various energies have different sample penetration depths and therefore interrogate different sample volumes, providing information on the sample homogeneity. In T-PGNAA neutron energy-dependent gamma-ray spectra are measured with a well-shielded high purity germanium detector (HPGe-detector) using time-of-flight method. The HPGe-detector counts are recorded as a function of the gamma energy (y-axis) and the neutron time-of-flight i.e. the neutron energy (x-axis) to produce a two dimensional matrix

for data analysis. A vertical cut along the y-axis at a chosen neutron energy provides the prompt gamma-ray spectra recorded for this neutron energy. A horizontal cut along the x-axis at a chosen gamma-ray energy delivers neutron capture spectra showing the variations in neutron capture cross sections i.e. isotopic sensitivity as a function of the neutron energy. Isotopic contrast and selectivity is obtained by screening over the detector events in neutron and gamma-ray energy.

Taking advantage of the time structure of the HBS source, we propose two instruments to perform time-resolved prompt, and delayed gamma neutron activation analysis of samples with various sizes, offering great flexibility according to the sample type and information required. The broad energy range that can be used and the medium beam size will also allow for transmission imaging capabilities and the spectral choice can be used to tune contrast and penetration capabilities to the needs of investigation. Care must be taken to ensure a suitable transmission imaging detector is installed close to the sample.

Instrument parameters	
Target	24 Hz
Moderator	liquid para-hydrogen
Moderator-to-sample distance	12 m
Detector-to-sample distance	0.3 to 0.5 m
Beam size	4 cm
Neutron energy range	1 meV to 80 eV
Energy resolution	10 to 40 %
Peak flux 1)	2.3×10^6 $cm^{-2}s^{-1}$ (1 - 80 eV)
	5.1×10^7 $cm^{-2}s^{-1}$(0.1 - 2 eV)
	3.9×10^9 $cm^{-2}s^{-1}$ (10 - 100 meV)
	3.9×10^9 $cm^{-2}s^{-1}$ (3 - 10 meV)
	1.3×10^9 $cm^{-2}s^{-1}$ (1 - 3 meV)
Average thermal-equivalent flux	3.4×10^9 $cm^{-2}s^{-1}$

(1) analytically calculated for a neutron guide equipped with a m=3 supermirror

Table VI.20: *Instrument parameters for time-resolved prompt and delayed gamma neutron activation analysis with slow neutrons (PDGNAA-1)*

The first instrument where parameters are given in Table VI.20 is dedicated to the analysis of small-to-medium size samples. For this, the instrument will be operated at the 24 Hz target station with a cold (bi-spectral) moderator (liquid para-hydrogen, 10 cm length and 1 cm radius) providing an optimal cold, thermal and epithermal neutron flux at the sample position to perform in-depth analysis of thick samples. The distance of 12 m between sample and cold source allows the time-resolved acquisition of prompt gamma-ray spectra at various neutron energies ranging between 1 meV and 80 eV during the first 30 ms from the end of a fast neutron pulse. Afterwards, delayed gamma rays from activation products with a longer half-life than the frame length can be measured during the 10 ms before the start of the next neutron pulse. A bandwidth chopper positioned 2 m upwards from the sample offers the option of increasing the acquisition time for delayed gamma-ray spectra by selective rejection of neutrons with energies lower than 100 meV. A beam size changer allows samples of various size to be investigated. The instrument delivers an average thermal-equivalent neutron flux of $3.4 \cdot 10^9$ $cm^{-2}s^{-1}$ at sample position, which is comparable to the flux achieved for PGNAA instruments at research reactors ($6.5 \cdot 10^9$ $cm^{-2}s^{-1}$ at NIST, $2 \cdot 10^9 cm^{-2}s^{-1}$ at FRM II and $9.6 \cdot 10^7$ $cm^{-2}s^{-1}$ at BRR).

Instrument parameters	
Target	384 Hz
Moderator	-
Moderator-to-sample distance	20 m
Detector-to-sample distance	0.6 to 1 m
Beam size	6 cm
Neutron energy range	0.6 eV to 10 MeV
Energy resolution	50% (1 to 500 eV)
Peak flux	3.8×10^8 cm^{-2}s^{-1} (0.1 - 10 MeV)
	5.0×10^7 cm^{-2}s^{-1}(0.3 - 20 keV)
	4.3×10^7 cm^{-2}s^{-1} (50 - 500 eV)
	2.5×10^7 cm^{-2}s^{-1} (10 - 50 eV)
	2.2×10^7 cm^{-2}s^{-1} (2 - 10 eV)
	2.3×10^7 cm^{-2}s^{-1} (0.6 - 2 eV)
Average fast neutron flux	7.6×10^6 cm^{-2}s^{-1}
Average resonance neutron flux	1.9×10^7 cm^{-2}s^{-1}

Table VI.21: *Instrument parameters for time resolved prompt and delayed gamma neutron activation analysis with fast neutrons (PDGNAA-2)*

The second instrument where parameters are given in Table VI.21 is dedicated in particular to the analysis of large samples with fast and resonance neutrons. The instrument is operated at the 384 Hz target station enabling the extraction of resonance neutrons after fast neutron pulses. Fast and resonance neutrons are extracted from an empty channel with a radius of 3 cm positioned close to the target. The distance of 20 m between sample and source allows the time-resolved acquisition of prompt gamma-ray spectra at various neutron energies ranging between 0.6 eV and 20 keV during the first 1.5 ms from the end of a fast neutron pulse. Afterwards, delayed gamma rays from activation products with a longer half-life than the frame length can be measured during the 1 ms before the start of the next neutron pulse. Optionally, prompt gamma rays induced by fast neutron inelastic scattering can be measured during the fast neutron pulses. In order to avoid irradiation of the sample with thermal neutrons, the beam line is equipped with two Gd-Choppers at distances of 4 m and 7 m, respectively, from the source with open times of 300 μs and 525 μs, respectively, from the end of the fast neutron pulses. The instrument delivers at sample position an average fast neutron flux of $7.6 \cdot 10^6$ cm^{-2}s^{-1} and an average resonance neutron flux of $1.9 \cdot 10^7$ cm^{-2}s^{-1}. For comparison, the fast neutron flux of the SR10 beam line at FRM II is about 10^8 cm^{-2}s^{-1} and the incident neutron flux at the INES beam line (ISIS) is $2.5 \cdot 10^6$ cm^{-2}s^{-1} (energy range 0.07 - 68 eV).

VI.6.2 Neutron depth profiling

Neutron depth profiling (NDP) is a non-destructive analytical tool to study near-surface distributions of some light isotopes (^{3}He, ^{6}Li, ^{10}B, ^{14}N, ^{22}Na and few more) in solids [65]. Absorption of a neutron results in nuclei decay with the emission of a monoenergetic charged particle (alpha-particle, proton or triton) and a recoiling nucleus. Before escaping the sample surface each particle loses a certain amount of energy depending on the stopping power of the host material. The detected energy spectrum depicts the in-depth distribution of a corresponding absorbing isotope. As NDP can be considered non-destructive, batteries can be explored in situ and operando for many cycles of battery charging and discharging, which is in high demand in the battery community.

Being inspired by such demand, new NDP spectrometers have appeared or are under construction at major neutron facilities worldwide. Recently, a new NDP spectrometer has been designed and built for operation on the vertically focused cold neutron beam of the JCNS reflectometer MARIA (MLZ, Garching) [144]. An extremely high thermal equivalent flux of $7 \cdot 10^9$ n/cm^2/sec at the sample on MARIA allows, for example, time resolved characterization of thin-film lithium-ion batteries within 10 seconds or even faster depending on the absorbing isotope (^{6}Li) content.

The NDP technique faces some challenges: the background has to be optimized to allow characterization of the isotopes with low energy products after neutron absorption, particularly ^{3}He and ^{14}N, and the beam size at a sample position should allow effective usage of the beam on smaller samples or scanning of samples (for 3-D depth profiling). Creation of a dedicated facility at the HBS with custom-designed focusing neutron optics, optimized shielding of the charged particle detectors, usage of the appropriate materials (with minimum possible background production) and the feeding of the spectrometer with an appropriate wavelength distribution of neutrons will help to overcome those challenges. The NDP technique will establish a new frontier in sensitivity and effectiveness of neutron flux usage. With minimized background and activation of instrument components, it will provide a healthy working area for the instrument scientists and users.

The neutron absorption cross-section is directly proportional to the mean wavelength of the neutron spectrum delivered to the sample. As the HBS concept provides flexibility in moderator design, one can significantly boost the efficiency by having the neutron spectrum shifted to longer wavelengths (~10 Å). The NDP technique is not restricted by the total beam divergence (contrary to standard scattering methods which require a highly collimated beam), meaning that one can use 2-D neutron beam focusing. To maximize the flux at the sample, we propose utilizing a double focusing neutron guiding system (vertical and horizontal) with an additional neutron focusing lens (supermirror-multichannel or capillary, depending on the desired size of the "focal" spot at the sample position). The instrument should also be equipped with a basic choppers system – involving a bandwith (overlap) chopper and monochromating choppers. Working with a given monochromatic wavelength will allow the precise determination of the absorption cross-section, leading to a more accurate determination of the isotope concentration. The schematic drawing of the optical components is shown in Figure VI.18.

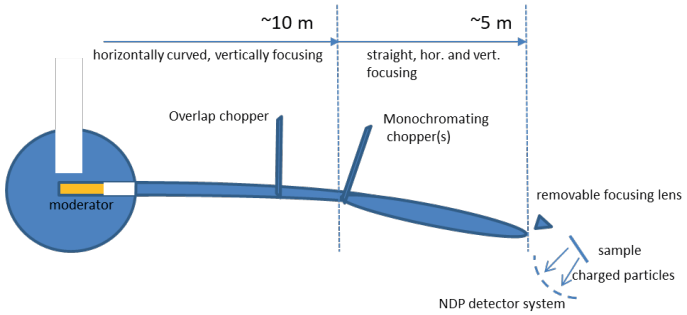

Figure VI.18: *Schematic view of the HBS NDP instrument*

Following the current state-of-the-art, the NDP spectrometer can be equipped with a multidetector system using an array of standard charged particle detectors, e.g. silicon surface barrier technology. In this case, the gain in charged particle collection is proportional to the number of detectors. Alternatively one can consider a new, promising development – a 2-D multichannel detector for charged particles. Here the gain increases with the active area of the detector. Altogether the performance of the NDP spectrometer at the HBS can be estimated as competitive with the world-leading NDP facilities (NIST, JCNS at MLZ) and furthermore it should provide new opportunities for researchers: the characterization of thicker samples with higher resolution, improved sensitivity to ^{3}He and ^{14}N iso-

topes, 3-D depth profiling, and more. Additionally such a facility will provide a very high flux density at a small focal spot (< 1 cm^2), which will be invaluable for developments in neutron instrumentation and detectors.

VII.
OPERATION

VII.1 Regular operation

The HBS facility will offer a full user service based on the operation of the accelerator on a "24 hours a day, 7 days a week" schedule. However, operations will be interrupted for regular maintenance periods of the accelerator system and the exchange of neutron targets. In addition regular longer shut-down periods will occur for the instalment or exchange of larger components necessary for the technical operation of the facility. It is anticipated that the average availability of the facility for user experiments will be approximately 200 days per year.

VII.2 Control systems

The HBS control systems consist of components and tools connecting all HBS equipment to present a homogeneous and ergonomic interface to operators, engineers and physicists enabling the safe and reliable operation of the HBS.

From a control system point of view, the HBS can be subdivided into the HBS machine (ion source, accelerator, target, moderator and conventional facilities), responsible for neutron production, and the instruments using these neutrons for research. For the HBS machine, a central control room is being planned that is permanently manned with operators, whereas instruments are locally controlled by dedicated measurement scripts and programs. The operation of instruments is typically fully automatic, requiring the presence of instrument users or scientists only for measurement definition and to start the experiment, for the development and testing of dedicated scripts or for sample change. From the perspective of the control system, the instruments and source are only loosely coupled via the timing system and the mechanisms to make information about the machine (e.g. proton charge and energy, omitted pulses, etc.) available to the instruments. Due to the loose coupling and the different modes of operation, it is planned to have one control system for the machine and individual control systems for each instrument. Since requirements are different, the control systems of the HBS machine and the HBS instruments can use different control system technologies and implementation approaches.

The HBS machine and instrument control systems will be designed as distributed and object-oriented systems. Despite the different implementation, all will follow the same classical three-tier architecture as indicated in Figure VII.1.

- At the lowest level, the resource tier facilitates the access to the front-end equipment of the HBS machine enabling direct equipment control and data collection. Conceptionally, the resource

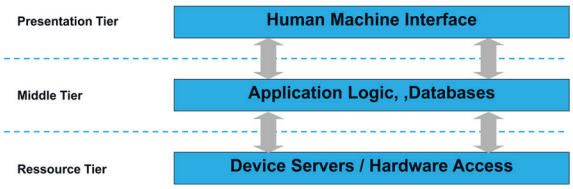

Figure VII.1: *Three-tier architecture of the control system*

tier presents device abstractions of front-end equipment to the middle tier. For the connection of the front-end equipment a wide range of interface standards must be supported.

- The middle tier implements the application logic of the control systems, e.g. procedures for automatic start up, shutdown or auto-tuning. Databases for configuration, archived process values and logging information reside at this tier. A name service implemented at the middle tier provides location transparence for the devices exported by the resource tier.
- The presentation tier is responsible for the HMI (Human Machine Interfaces) that enables machine and instrument operation for operators, engineers and physicists. At the presentation tier a set of graphical and non-graphical tools are running on console computers which implement an abstract, aggregated and homogeneous view of the HBS and hide unwanted details.

VII.2.1 HBS machine control system

Requirements and functionality

The HBS machine control system functions can be grouped horizontally according to the machine subsystems:

- Ion Source and Accelerator: Core function is the RF system responsible for proton acceleration. Equipment to be controlled includes RF cavities, power supplies for magnets and beam instrumentation such as beam position monitors and beam current measurement devices.
- Target, thermal moderator and cold moderator: The control system is mainly responsible for the cooling functions of these subsystems. Equipment to be monitored and controlled includes pumps, valves, leak detectors, pressure gauges and temperature sensors.
- Cryogenic Plant for the Helium cooling of the cold moderator: The cryogenic plant will be delivered by a commercial vendor and is expected to come with its own proprietary control systems, used for its local control. The sending of parameter values and commands as well as the read-back of process values is accomplished via the HBS machine control system resource tier.
- Vacuum System: There will be a common vacuum system for the ion source, the accelerator, the target and the neutron guides. In the vacuum subsystem different types of pumps in differential pumping systems, valves and pressure gauges have to be controlled and monitored.
- Conventional facilities: This subsystem is responsible for the control of pressed air, water and electrical power supply, including the control of compressors, pumps and valves as well as the continuous monitoring of process values such as air pressure, air flow, water pressure, water flow, water temperature and electrical power, voltage, current, and the cos phi of all main circuits.

Orthogonal to this horizontal structure, the HBS control system is structured into the following functional groups which are related to all subsystems:

Timing System: Due to the pulse structure of the neutron beam, neutron instruments and HBS machine components have to be synchronized. This can be achieved with a central clock that is distributed via a timing network together with event data and trigger pulses. Event receivers have to be implemented at individual devices that decode timing and event data and produce pulses for the synchronization of the device hardware. For neutron detectors a timing resolution below 100ns is sufficient, but for the internal operation of the ion source and beam focusing components of the accelerator, a resolution in the order of 1ns is envisaged. A good candidate for the timing network would be White Rabbit developed by CERN as an improvement of the Precision Time Protocol (PTP) according to IEEE 1588, achieving sub-nanosecond accuracy.

Machine Protection System: The Machine Protection System prevents machine damage due to device failures or abnormal events such as beam loss, failure of a cooling system or failure of the vacuum system. In order to accomplish this, all subsystems must have electrical interface signals for the indication of fault situations and for the immediate switch to a safe state.

Personal Protection System: The personal protection system has to ensure the protection of humans against any hazards from the machine, which may lead to injuries. The main focus is the exposure to radiation, but also other hazards such as electrical shock must be prevented. The personal protection system will be implemented as a highly reliable failsafe system that ensures a safety level according to ISO 13849 PL e (roughly corresponding to IEC 61508 SIL 3). With regard to radiation safety, it will manage the entrance and exit from radiation-controlled areas. Additionally, radiation levels will be monitored. Any access violation or any violation of radiation level thresholds will lead to an immediate shutdown of thew ion source and accelerator.

Alarm/Logging System: The alarm and logging system is responsible for the collection, distribution and archiving of alarms (information on abnormal situations) and logging events (diagnostic information). At the presentation tier, a GUI-based console application allows the definition of alarms and logging events, presents these to the operator and supports the retrieval of archived alarms and logging events.

Process Archive: During operation of the HBS machine all relevant process data must be collected and archived for later analysis. A GUI-based-console allows the selection of process data for archiving, definition of archiving intervals and persistence times in the archive as well as later retrieval and presentation in configurable graphs, e.g. as a time series.

Operational Security: Since remote network access to the HBS machine control system shall be allowed, appropriate cyber security mechanisms must be implemented. One of the mechanisms is the strict separation between the technical network and the control devices from the standard office network. In order to reduce operational faults, a role-based access to the control systems must be implemented that gives different levels of control to specific user groups.

HMI (Human Machine Interface): On operator consoles and wall displays in the control room GUIs will be implemented that allow control, optimization and state supervision of the HBS machine. This includes the presentation of real-time summaries of all relevant machine parameters. For standard operation, easy startup, shutdown and auto-tuning buttons will be offered. The role-based access allows the presentation of different granularity levels to individual user groups. An homogeneous appearance and good ergonomic behaviour are key design parameters for all GUIs

Architecture and implementation

For many decades, Forschungszentrum Jülich has demonstrated its competence to build and maintain complex particle accelerator systems, e.g. the synchrotron COSY. As a consequence, all competences to implement the HBS control system from scratch are available in Jülich. In order to reduce implementation efforts, the intention is to base implementation on a control system software tool that is well established in the research community. The most promising and wide spread candidates are EPICS and TANGO. JCNS has long-term experience with TANGO since all JCNS instrument control systems at the MLZ have been implemented with it. Because the control systems of all JCNS instruments planned for the ESS must be based on EPICS, JCNS has started to build up an EPICS competence. So in principle, both systems could be used and the final decision will depend on the degree of support provided by the accelerator vendor. Since EPICS is already used at the synchrotron COSY, it seems to be the more appropriate candidate for the HBS control system. In both systems, Linux will be deployed on all computers as the operating system and for the communication networks only Ethernet will be used with communication protocols based on TCP/IP or UDP/IP.

Front-end electronics for the RF systems and the beam instrumentation should be based on MTCA.4, which is heavily employed in many current accelerator control systems, e.g. at the XFEL.

The front-ends of the different cooling subsystems, of the conventional facility subsystem and of the vacuum subsystem will follow a distributed architecture implemented with industrial grade PLCs and decentral periphery systems connected via field bus systems. Due to JCNS's long-term experience with and the market dominance of Siemens, it is intended to use the Siemens S7-1500 for the PLC systems, ET200SP and ET200MP for the decentral periphery systems and PROFINET, PROFIBUS, AS-i and IO-Link as fieldbus systems. At the HBS control systems resource tier, industrial PCs are used that are connected via PROFINET to these front-ends. The implementation of the machine protection system and the personal protection system will be based on the Siemens distributed safety concept with failsafe S7-1500F CPUs, failsafe F-Modules and PROFIsafe communication, which allows PL e according to ISO 13849 to be achieved.

VII.3 Instrument control system

VII.3.1 Requirements and functionality

Conceptionally, each neutron instrument can be grouped into sections such as beam definition, sample area, beam analysis and neutron detection as shown in Figure VII.2. Beam definition may include choppers, selectors, or monochromators for energy definition, devices for beam polarization or variable collimations. The sample area contains mechanical devices for sample exposure such as sample tables, goniometers and sample-changers, as well as devices for the definition of the sample environment, e.g. pressure, temperature or magnetic field. In the beam analysis section, specific energy ranges or polarization states may be filtered out of the scattered beam. In the detection section, scattered and filtered neutrons are record by a wide range of detector systems. A major task in neutron instrument control is the movement of a large variety of mechanical axes. Also a wide range of sensors, programmable power supplies and controllers for physical parameters such as temperature or pressure must be controlled. Since event rates and event sizes in neutron detection systems are relatively low compared to nuclear or high energy physics, neutron instruments do not have a dedicated data acquisition system. Data acquisition is also part of the control system,: typically detector device servers residing on the resource tier do continuous detector readout during measurement and store the acquired data into data files.

In the HBS neutron instruments, detectors as well as choppers have to be synchronized with the pulse structure of the source via a connection to the timing system. In order to allow later dynamic re-

binning and measurement during mechanical movements, neutron data will not be stored in the form of histograms but as event-mode data, which means that each detected neutron is recorded with a timestamp. Therefore all other process data, e.g. mechanical positions, or sample environment parameters have to be time-stamped, too, and the corresponding devices must have an interface to the HBS timing system. In comparison to the HBS machine, the HBS instruments are much more dynamic. They will experience continuous setup changes, especially in the sample environment. There will be a steady change of measurement scenarios, for which dynamic measurement sequences have to be programmed and executed. As a consequence, a more or less static HMI as required by the HBS machine control system is not appropriate for the instrument control system. Instead, the neutron instruments will be controlled by a dedicated instrument measurement program. The measurement program will have a client server structure. The server part runs on the middle tier of the control system and the client part on the presentation tier. With the client it is possible to define, start and stop dynamic measurement sequences, which will be executed by the server. A GUI tool and a scripting language tool are necessary for the definition of measurement sequences.

Figure VII.2: *Schematic structure of a neutron instrument*

All instruments are equipped with a beam shutter that shuts off the beam for instrument access. The required personal safety subsystem in each instrument control system is responsible for the implementation of an interlock between the beamshutter and instrument access.

VII.3.2 Architecture and implementation

JCNS has been developing neutron instruments for decades and operates 12 instruments at its main outstation at the MLZ in Garching. All these instruments share the same architecture and technologies for the instrument control systems. In order to minimize implementation by relying on existing developments and the support of trained personnel, all HBS instrument control systems shall be implemented with the same architecture and the same technologies.

All instrument control systems will all be based on TANGO which has been developed by the ESRF. TANGO is an open-source software toolkit for the development of control systems according to a three-tier architecture. MySQL will be used for all databases (process archives, alarm/logging archives, configuration databases) at the middle tier. TANGO systems are consistently object-oriented and employ CORBA and zeromq for communication with device servers. All instrument computers running TANGO device servers, middle tier components or clients in the presentation tier will use a Linux operating system. At the resource tier, industrial PCs - predominantly CPCI systems - will be installed.

NICOS, developed at MLZ Garching, will be the measurement program for all HBS instruments. NICOS offers scripting in Python and in a simpler command language as well as a configurable GUI for graphical user operation. Functionalities comprise an electronic logbook, history plots and detector data plots. NICOS follows a multiple-client/single-server model, where the server acts as the execution environment for scripts and any device access. It further refines the TANGO device model and is written in Python using pyQt for the GUI. As an example, Figure VII.3 shows the NICOS client GUI for the time-of-flight instrument DNS at MLZ. Figure VII.4 shows the overall SW structure of the HBS instrument control systems.

Besides detector electronics, the front-end equipment mainly consists of electromechanical devices such as motors, switches, encoders, pumps, valves and different kinds of sensors. Similar to the HBS

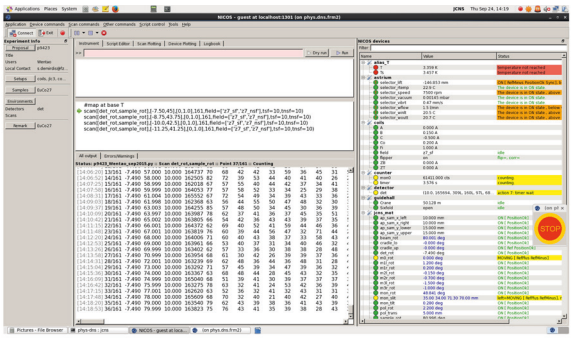

Figure VII.3: NICOS client GUI for the time-of-flight instrument DNS at MLZ.

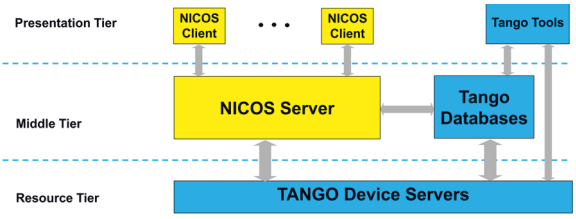

Figure VII.4: Software structure of the HBS instrument control systems

machine control system, all these devices will be controlled by Siemens S7-1500 PLCs with ET200SP and ET200MP decentral periphery systems. For interconnection, the fieldbus systems PROFINET, PROFIBUS, AS-i and IO-Link will be used. As a typical example, Figure VII.5 shows the physical architecture of the instrument control system of the time-of-flight instrument DNS at MLZ, which is still using the S7-300 PLC, the predecessor of the S7-1500.

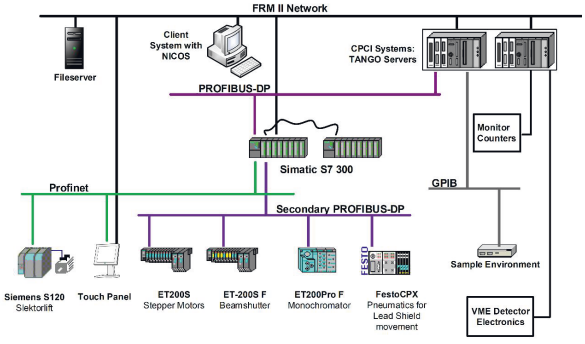

Figure VII.5: Physical architecture of the instrument control system of DNS

VII.4 Risk management and improvement

The main objective of the HBS organization will be to operate the HBS safely, reliably and with maximum availability. To keep an HBS facility running, the organization needs to establish certain processes. As the design of the HBS will follow best engineering practice, a reliable and safe facility will be the result. To manage the left-over operational risks and to stay at the cutting edge of safety and operational performance, a risk management process will be implemented.

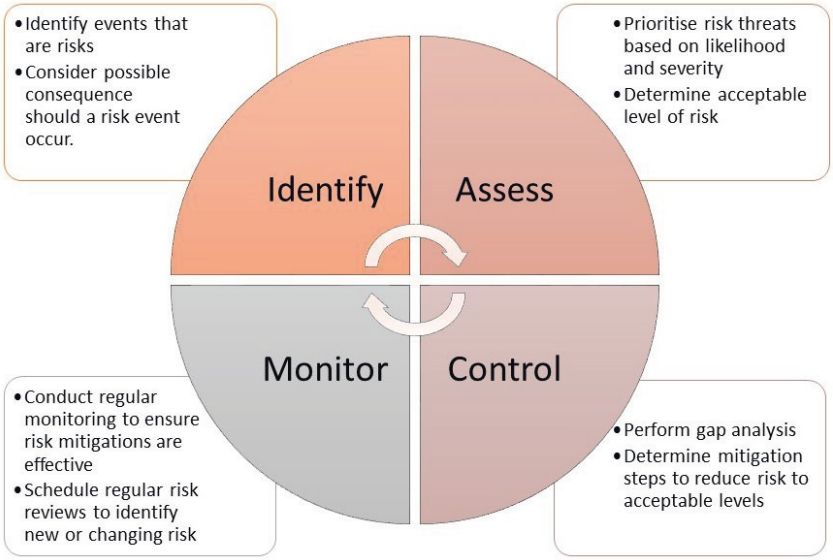

Figure VII.6: *Risk assessment procedures*

A risk is exposure to an event that, if it occurs, has an (negative) effect on at least one objective of the organization. The first objective subject to risk management is safety. Additional objectives are investment protection and the availability of the HBS facility. For a user facility, an availability above 95 percent is aimed for.

Any failure of components within the facility can lead to risks which can affect the operation, handling or use of the facility. Risks associated with the accelerator may include a failure of the ion source, failure in beam transport and beam alignment, or a power failure. Target risks could include severe misalignment of the proton beam, loss of cooling, failure of cryogenic systems, loss of vacuum, loss of activated material etc.. Instruments and user operation can be affected by improper handling or failure of infrastructure systems (power failure, cooling, vacuum, etc.). Overall, the operation and safety of the facility can be affected by power failure or failure in the water-cooling supply and vacuum supply, failure in the computing network or in the handling of activated material, natural disasters or attacks.

The main steps in risk management are: identifying an event as a risk, determining the severity and consequences of that event, assessing the likelihood of the event to take place, comparing the overall risk to the agreed acceptable risk levels, determining mitigation steps to either reduce the likelihood or to mitigate the consequences of the risk, monitoring the effectiveness of the mitigation steps and looking for new risks. For each potential risk identified, plans to minimize and handle the risks are put in place. The process of risk Management is outlined in the international standard ISO 31000. For the safety of machinery, the norm for risk assessment is ISO 12100.

Modern risk management process considers not only negative risks: it also identifies chances and opportunities. In this way, the risk management process will also be a driver for the continuous improvement of the HBS. All processes of the HBS will be collected in an integrated management system. To achieve the highest standards of safety and reliability, certification to meet the standards ISO 4501 and ISO 9001 is being consider as an option for the HBS management system.

VIII.
SAFETY

HBS will be designed and constructed in accordance with regulatory requirements in order to guarantee a high level of safety during the operation, maintenance and handling of radioactive materials, and thus to offer personnel and users a safe, open and friendly working atmosphere. Aspects covering radiological (protection against ionizing radiation) as well as non radiological (fire, non ionizing radiations and fields, high voltage, cryogenics) safety are given below. Based on knowledge and experience gained collectively for the safe operation of accelerators and neutron sources around the world, a general safety concept can be provided for HBS. Nevertheless, the details and realization of the safety procedures, including risk management, must be discussed with the licensing authorities.

VIII.1 Non-radiological safety

Non-radiological safety deals with the safety from all other conventional hazards and non-ionizing radiation which may arise from the operation of various subsystems in the HBS facility. The accelerator will be equipped with state-of-the-art safety systems. However, high-voltages, high magnetic fields and radio frequency (RF) radiations present safety hazards. To minimize these hazards, appropriate warning boards with danger signs and visual indications will be placed near such locations. If necessary, suitable grounded cages with interlocked doors will be installed to isolate devices with high voltages from the working environment. To avoid exposing people to unacceptable levels of RF energy, specifically engineered control measures will be considered. Cryogenic systems will be used for the cold neutron sources. Cryogenic liquids present significant hazards due to their intense cold and substantial gas production. In previous developments, a safety concept was formulated and approved by the GRS (Gesellschaft für Anlagen- und Reaktorsicherheit) for handling cryogenic hydrogen, methane or mesitylene moderator within a nuclear facility operating under German atomic law (AtG). Since accelerator-based neutron sources refer to the German radiation protection ordinance (StrSchV) safety issues are less pronounced and the approved safety concept can be adapted. Persons handling cryogenic liquids will be adequately trained and provided with proper personal equipment. Last but not least, an efficient fire protection system will be installed in the whole facility.

VIII.2 Radiological safety

The aim of radiation protection is to reliably prevent the deterministic effects of radiation and to reduce the risk of stochastic effects to a reasonably achievable level. Therefore, the objectives of radiation safety at HBS are to ensure that during normal operation, the maintenance and handling of radioactive components, the radiation dose to personnel, users and population is kept below the limit values defined by the authorities. Furthermore, it must be ensured that any unnecessary radi-

ation exposure and contamination are avoided and radiation exposure is kept as low as reasonably achievable (ALARA principle). These objectives will be met by maintaining safety features which comprises: appropriate shielding, safety interlocks, access to control systems, switches, and alert and caution systems. The German radiation protection ordinance (StrSchV) forms the legal basis for the construction and operation of a facility producing ionizing radiation. According to Art 1 § 7 StrSchV a licence including all safety requirements is mandatory to operate HBS (accelerator and target stations). Before commissioning, all separate components of the facility must be subject to quality assurance (Art 1 § 115 StrSchV). After commissioning, the facility must be inspected regularly (Art 1 § 116 StrSchV). According to Art 1 § 5 StrSchV, a licence for the handling of radioactive materials is mandatory. Furthermore, according to Art 1 § 45 StrSchV a sufficient number of qualified radiation protection commissioners is required for its safe operation. The facility will be classified into the following zones: areas which are accessible at all times, supervised/controlled/restricted entry areas, areas accessible with appropriate administrative controls and inaccessible areas during accelerator operation and controlled entry during shutdown. All entrances of the latter areas will be interlocked during accelerator operation. The accelerator hall/tunnel, the instrument hall and the neutron source rooms will be equipped with safety interlock switches. Buttons for search and secure procedure will be placed in the accelerator hall and the neutron source rooms to ensure that no person has remained in the interlocked areas before accelerator start up. Moreover, several emergency proton/neutron beam shut-off switches will be installed to shut down the accelerator or close the neutron shutters. A number of optical and acoustic warning systems will be placed in the relevant part of the facility to alert/caution the personnel inside the facility of the operational status. Locations with radiological hazards will be demarcated from other areas by putting appropriated symbols indicating the radiation level in work areas and precautions to be taken by working personnel.

In order to keep radiation exposure as low as possible, radiation shielding will be built in different parts of the facility such as along the whole proton beam line, around the beam dump, the neutron targets (see Chapter V.8), the neutron guides and the instruments. Neutron and gamma dose rate monitoring systems will be placed along the proton beam line, in the neutron source rooms and at the position of the neutron instruments. If necessary, systems for airborne particulate radioactivity monitoring will be installed. Safety procedures including beam safety interlocks, real-time beam diagnostics, and vacuum control will ensure that the average beam power at a target station does not exceed 100 kW. Deviations from the authorized accelerator working range during operation will lead to an accelerator shut down or to a deflection of the proton beam to a 1 MW beam dump. The latter will be used for the commissioning of the accelerator. The neutron channels will be equipped with shutters, the temperature and pressure or mass flow of the target coolant will be monitored continuously, the target temperature and surface from the accelerator side will be monitored continuously be pyrometry and endoscopy.

The accelerator will be operated after ensuring that all shutters of the neutron channels are closed and the parameters of the target cooling system are within the limits and accelerator safety interlock switches are activated. The neutron supply for a given instrument is achieved by opening the shutter of the corresponding neutron beam-line according to the regulations of radiation safety. A deactivation of the safety switch in a neutron source room, a deficiency of the target cooling system as well as an increase in the neutron/gamma local dose rate causes a shutdown of the accelerator. The pyrometry as well as the endoscopy of the target is performed to anticipate a change of the target preventing its fracture and thus a contamination of the proton beam-line and the accelerator. The proton beam tube will in addition be equipped with a fast closing shutter which will prevent accelerator damage due to an unexpected fracture of the target. Target diagnostics will be interlocked with the operation of the accelerator. All systems for radiological safety will be monitored during HBS operation and their functionalities periodically inspected according to a maintenance plan.

VIII.3 Handling of activated material

Radionuclides are produced by proton and neutron activation of the target and by neutron activation of the components of the target monolith such as the moderator, reflector, biological shielding and further structural materials. They are also generated in the accelerator components, beam dump and associated shielding by the proton beam itself and induced secondary particles. The radioactive materials produced will be considered as radioactive waste or released from clearance measurements. Based on German regulations, the handling (storage, discharge, transport and disposal) of radioactive waste is defined in Art 3 § 1-11 and clearance procedures in Art 1 § 31-42 of StrSchV. According to Art 3 § 1 the yearly amount of radioactive waste produced during the operation time must be estimated. The design of the components that could be radioactive should be realized in such a way as to minimize residual activity in order to facilitate their dismantling, handling and storage.

As an example, the proton- and neutron-induced activity of the tantalum target (the major source of radioactivity) is estimated for an incident proton beam of 70 MeV and an average current of 1.43 mA (71 mA peak current, 2% duty cycle, 100 kW average power) and for irradiation times of 30, 90, 180 and 360 days. The activity of proton-induced radionuclides is calculated by considering the penetration depth (obtained with SRIM) of protons in tantalum and using the cross sections database TENDL2017. The average neutron (thermal, epithermal, and fast) fluxes in the target are determined by the transport code MCNP6.1 where the target is embedded in a polyethylene moderator with a radius of 10 cm surrounded by a 30 cm thick beryllium reflector (see Figure V.62). The activity of the neutron-induced radionuclides is calculated using the cross-section database JENDL-4.0 and the Neutron Activation Tables [145]. The radionuclides formed and their activity at the end of the irradiation of a 2.2 kg tantalum target (internally-cooled target, material without impurities) are listed in Table VIII.1.

The total activity, decay heat and dose rate are given in Table VIII.2. The decay heat is calculated from the total energy (Q-value) released by the radioactive decay. The heat deposited in the target is estimated from the mean energy of the electrons emitted during the decay of activation products and then lodged in the material. The dose rate is calculated with the SISy software (version 2.5.2) for radiation protection [146]. Depending on the irradiation time the total activity of the target ranges from 24 to 64 PBq. The proton-induced activity (15 to 18 PBq) is slightly dependent on the irradiation time since the radionuclides formed with the highest activities have short half-lives (see Table VIII.1). The neutron-induced activity (8 to 46 PBq) is mainly related to the radionuclide ^{182}Ta with a medium half-life $T_{1/2}$=114.43 d (see Table VIII.1). The decay heat and the dose rate follow the same trends. The activity of ^{182}Ta yields 70 to 90 % of the total dose rate. Therefore, ^{182}Ta is the major source of radiation to consider for shielding issues, particularly when the neutron source is shut down.

As shown in Table VIII.4, the activity of the tantalum target is an order of magnitude lower than the activity induced by one-year's irradiation of massive targets made of tantalum, tungsten or mercury with 1.33 GeV protons (32.85 Ah) [147] and the activity of the nuclear fuel of a medium flux reactor (BER II) after 291 days operation. The target activity is of the same order of magnitude as that produced in the tungsten target of the ISIS facility irradiated with 800 MeV protons (1.94 Ah, 540 days in fifteen irradiation campaigns each 30-50 days over 4 years) [148]. In the latter, 30 % of the activity is related to ^{182}Ta produced by neutron activation of the target cladding made of tantalum. Proton capture, spallation or fission produce different radionuclide inventories impacting the strategy for storage and final disposal of the radioactive material [149]. In particularly, the fission of uranium generates long-lived actinides which are not produced in proton capture or spallation so long as uranium or thorium are not used as target materials. However, spallation targets contain high activities of long-lived alpha emitters such as ^{145}Pm ($T_{1/2}$=17.7 y), ^{148}Gd ($T_{1/2}$=74.6 y), ^{50}Gd ($T_{1/2}$=1.79 My), ^{154}Dy ($T_{1/2}$=3 My) and ^{146}Sm ($T_{1/2}$= 103 My) [148, 150, 151]. They contain also large amounts of tritium ($T_{1/2}$= 12.3 y) with activities ranging between 10^{13} to 10^{15} Bq at the end of irradiation [148, 152, 153]. In our case, the tritium activity generated in the tantalum target (see Table

Irradiation parameters					
Isotope	Half life	30 d	90 d	180 d	360 d
Proton induced					
^{179}W	37.05 m	3.42E+15	3.42E+15	3.42E+15	3.42E+15
^{177}W	135 m	3.05E+15	3.17E+15	3.17E+15	3.17E+15
^{176}W	2.5 h	2.44E+15	2.60E+15	2.60E+15	2.60E+15
^{175}W	35.2 m	1.88E+15	1.88E+15	1.88E+15	1.88E+15
^{178}Ta	9.31 m	1.75E+15	1.75E+15	1.75E+15	1.75E+15
^{174}W	31 m	1.05E+15	1.05E+15	1.05E+15	1.05E+15
^{180}Ta	8.15 h	7.60E+14	1.22E+15	1.30E+15	1.31E+15
^{176}Ta	8.09 h	3.42E+14	5.43E+14	5.81E+14	5.84E+14
^{174}Ta	1.05 h	1.77E+14	1.77E+15	1.77E+15	1.77E+15
^{175}Ta	10.5 h	1.56E+14	2.75E+14	3.11E+14	3.17E+14
^{177}Ta	56.56 h	1.30E+14	3.44E+14	5.09E+14	8.54E+14
^{173}W	7.6 m	7.76E+14	7.76E+14	7.76E+14	7.76E+14
^{178}W	21.6 d	4.89E+13	1.45E+14	2.85E+14	5.84E+14
^{173}Ta	3.14 h	4.82E+13	4.82E+13	4.82E+13	4.82E+13
^{180m}Hf	5.5 h	2.16E+13	2.16E+13	2.16E+13	2.16E+13
^{173}Hf	23.6 h	8.84E+12	2.03E+13	2.85E+13	3.31E+13
^{171}Hf	12.1 h	6.22E+12	1.16E+13	1.36E+13	1.40E+13
^{169}Hf	3.24 m	3.46E+12	3.46E+12	3.46E+12	3.46E+13
^{170}Hf	16.1 h	2.89E+12	5.94E+12	7.50E+12	8.02E+12
^{172}Ta	36.8 m	2.63E+12	2.63E+12	2.63E+12	2.63E+12
^{181}W	121.2 d	1.11E+12	3.31E+12	6.59E+12	1.31E+13
^{179}Ta	1.82 y	1.04E+12	3.14E+12	6.27E+12	1.25E+13
^{175}Hf	70 d	2.76E+11	8.27E+11	1.66E+12	3.25E+12
^{179}Lu	4.59 h	2.17E+11	2.73E+11	2.76E+11	2.76E+11
^{178}Lu	28.4 m	1.96E+11	1.96E+11	1.96E+11	1.96E+11
^{178m}Lu	23.1 m	1.15E+11	1.15E+11	1.15E+11	1.15E+11
^{172}Hf	1.87 y	1.63E+10	3.52E+10	7.03E+10	1.40E+11
^{3}H	12.33 y	1.54E+10	4.61E+10	9.16E+10	1.80E+11
Neutron induced					
^{182}Ta	114.43 d	8.62E+15	21.8E+15	34.5E+15	46.0E+15
^{182m}Ta	15.84 m	2.20E+13	2.20E+13	2.20E+13	2.20E+13
^{180}Ta	8.15 h	1.31E+12	1.31E+12	1.31E+12	1.31E+12
^{181}Hf	42.39 d	2.28E+08	4.53E+08	5.57E+08	5.87E+08
^{179}Ta	1.82 y	6.56E+07	1.90E+08	3.64E+08	6.67E+08

Table VIII.1: *Activity (Bq) of main radionuclides produced at the end of the irradiation of a 2.2 kg tantalum target. The proton energy is 70 MeV and the average current 1.43 mA. The average neutron fluxes in the target are: $1.72 \cdot 10^{12}$ cm^{-2} s^{-1} for thermal neutrons, $8.83 \cdot 10^{12}$ cm^{-2} s^{-1} for epithermal neutrons and $1.83 \cdot 10^{13}$ cm^{-2} s^{-1} for fast neutrons.*

VIII.1) is three to four orders of magnitude lower depending on the irradiation time. Nevertheless, the management of tritium during HBS operation will be addressed and the environmental impact of tritium release evaluated.

Due to the high activity generated at the end of irradiation, the replacement of the target can be done only by remote control. After the shut-down of the accelerator and the target cooling system, the target unit is uncoupled from the accelerator beam tube. Afterwards, a part of the shielding is removed extracting with it the target unit. Finally, using a robot system, the target unit is disconnected

Irradiation parameters				
	30 d 1.03 Ah	90 d 3.09 Ah	180 d 6.18 Ah	360 d 12.36 Ah
Activity (PBq)	24.0	38.6	51.9	64.0
Proton induced	15.4	16.8	17.4	18.0
Neutron induced	8.6	21.8	34.5	46.0
Decay heat (kW)	6.6	10.8	14.7	18.1
Proton induced	4.1	4.5	4.7	4.7
Neutron induced	2.5	6.3	10.0	13.4
Heat deposition (kW)	0.99	1.57	2.00	2.39
Proton induced	0.70	0.84	0.84	0.85
Neutron induced	0.29	0.73	1.16	1.54
Dose rate (Sv/h)	2422	5116	7626	9917
Proton induced	752	889	936	997
Neutron induced	1670	4227	6690	8920

Table VIII.2: *Activity, decay heat, heat deposition and dose rate obtained at the end of the irradiation of a 2.2 kg tantalum target. The proton energy is 70 MeV and the average current 1.43 mA. The average neutron fluxes in the target are: $1.72 \cdot 10^{12}$ cm^{-2} s^{-1} for thermal neutrons, $8.83 \cdot 10^{12}$ cm^{-2} s^{-1} for epithermal neutrons and $1.83 \cdot 10^{13}$ cm^{-2} s^{-1} for fast neutrons. The dose rate is given for a distance of 1 meter from the unshielded target. 1 PBq corresponds to 10^{15} Bq.*

from the cooling pipe and stored in a dedicated facility with appropriated shielding inside the neutron source area. Depending on the operation cycle of the neutron source and the target life-time, the target will be reused or disposed of. The spent targets remain stored for decay inside the neutron source area.

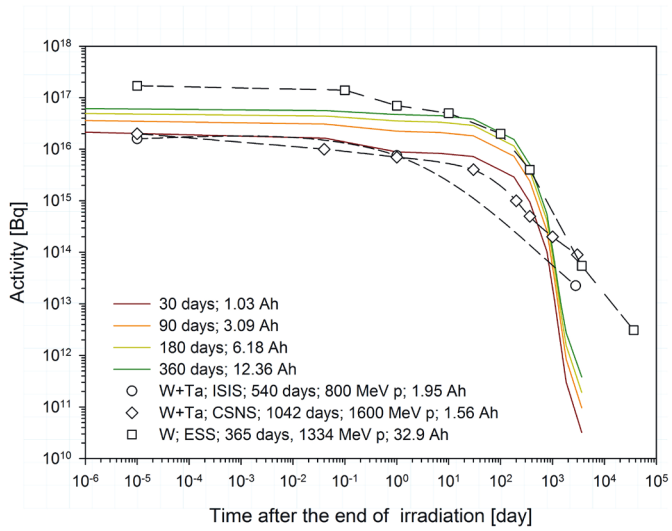

Figure VIII.1: *Decay of the tantalum target activity (coloured lines) compared with the decay of the activity of spallation targets (see Table VIII.4 for various irradiation conditions).*

The decay of the total activity of the tantalum target is shown in Figure VIII.1. The main radionuclides, the total activity, the decay heat and the dose rate after 1, 3, 5 and 10 years decay time from the end of target irradiation are listed in Table VIII.3. Up to a decay time of 3 years ^{182}Ta is still the main radionuclide. Afterwards, the long-lived radionuclides ^{179}Ta ($T_{1/2}$=1.82 y)and ^{3}H ($T_{1/2}$=12.33 y) become predominant. After a decay time of 5 years the activity of the tantalum target becomes much lower than that of a spallation target (Figure VIII.1). Even after a cooling time of 100 years, the activity of a spallation target is still very high (some TBq) [147, 151]. In our case, activity in the GBq range mainly due to tritium is expected after a cooling time of 30 years.

	1 yr	3 yr	5 yr	10 yr
Irradiation 30 d, 1.03 Ah				
Radionuclides	100% ^{182}Ta	97% ^{182}Ta 3% ^{179}Ta	44.7% ^{182}Ta 50.9% ^{179}Ta 3.8% ^{3}H 0.6% ^{172}Hf	71.8% ^{179}Ta 27.3% ^{3}H 0.9% ^{172}Hf
Activity (TBq)	944	12	0.30	0.032
Decay heat (W)	274	3.3	0.04	0.0005
Dose rate (Sv/h)	183	2.2	27*	0.23*
Irradiation 90 d, 3.09 Ah				
Radionuclides	100% ^{182}Ta	97% ^{182}Ta 3% ^{179}Ta	40.5% ^{182}Ta 54.8% ^{179}Ta 4.1% ^{3}H 0.6% ^{172}Hf	71.9% ^{179}Ta 27.2% ^{3}H 0.9% ^{172}Hf
Activity (TBq)	2380	30	0.85	0.097
Decay heat (W)	691	8.6	0.11	0.002
Dose rate (Sv/h)	461	5.6	72*	0.69*
Irradiation 180 d, 6.18 Ah				
Radionuclides	100% ^{182}Ta	96% ^{182}Ta 4% ^{179}Ta	34.9% ^{182}Ta 60% ^{179}Ta 4.1% ^{3}H 0.7% ^{172}Hf	72% ^{179}Ta 27% ^{3}H 1% ^{172}Hf
Activity (TBq)	3780	47	1.6	0.19
Decay heat (W)	1098	13.2	0.42	0.003
Dose rate (Sv/h)	732	8.8	109*	1.38*
Irradiation 360 d, 12.36 Ah				
Radionuclides	99.8% ^{182}Ta 0.2% ^{179}Ta	93.7% ^{182}Ta 6.2% ^{179}Ta	26.3% ^{182}Ta 67.8% ^{179}Ta 4.9% ^{3}H 1% ^{172}Hf	72.4% ^{179}Ta 26.8% ^{3}H 0.8% ^{172}Hf
Activity (TBq)	5050	65	2.8	0.38
Decay heat (W)	1467	17.6	0.57	0.006
Dose rate (Sv/h)	977	12.1	158*	2.7*

* dose rate in mSv/h

Table VIII.3: *Radionuclides, activity, decay heat and dose rate obtained for various decay times after the end of the irradiation of a 2.2 kg tantalum target. The percentage in front of the radionuclide represents the fraction of the activity given bellow. The dose rate is given for a distance of 1 meter from the target unshielded. 1 TBq corresponds to 10^{12} Bq.*

After 5 years cooling time the spent tantalum targets may be transfer into a MOSAIK (MII-15EI with 12 cm lead shielding) cask which can receive about 30 to 40 targets. Depending on the target irradiation

time, the dose rate at the cask surface ranges between 16 μSv/h and 84 μSv/h for one stored spent tantalum target. For the cask transport, a dose rate at the cask surface lower than 500 μSv/h or 2 mSv/h must be ensured.

The activity of the main radionuclides formed by neutron activation of the polyethylene moderator (without neutron extraction channels), the reflector made of beryllium or lead and the shielding composed of four lead layers (each 10 cm thick) and three layers of borated polyethylene (each 40 cm thick) are given for various irradiation times in Table VIII.5. In the following discussion, we consider an irradiation time of 30 years which corresponds to the operation period of the HBS facility. The total activity of the polyethylene moderator due to the long-lived activation products ^{3}H ($T_{1/2}$=12.33 y), ^{14}C ($T_{1/2}$=5370 y) and ^{10}Be ($T_{1/2}$=1.51 My) is in the MBq range. A free release of this material will probably not be possible due to the activity of ^{14}C and therefore it will be disposed as radioactive waste. In the case of the borated polyethylene as part of the shielding, the activity of the above-mentioned radionuclides is lower than 1 MBq. The main part of the activity is located in the first layer of borated polyethylene. The corresponding specific activity of this material layer is lower than 0.5 Bq/g so that a free release of the complete material can be considered after a short waiting time. The beryllium reflector contains a large amount of tritium with an activity in the TBq range. This high activity combined with the toxicity of beryllium makes the safe handling and disposal of such radioactive material (about 500 kg) very expensive. Therefore, beryllium should be avoided as a reflector and replaced by lead. After a decay time of about fifteen years, the total activity of the lead reflector is 160 MBq and is related mainly to the long-lived activation products ^{204}Tl ($T_{1/2}$=3.78 y) and ^{205}Pb ($T_{1/2}$=1.51 My). The specific activity of the two radionuclides becomes 25 Bq/g so that a free release of the lead reflector can be envisaged. After one-year's decay time the specific activity of the lead shielding is 0.04 Bq/g and its free release can be considered. In the technical design of the target-monolith, aluminium will be used as structural material. Interaction of neutrons with aluminium produces short-lived radionuclides such as ^{28}Al ($T_{1/2}$=2.24 m), ^{27}Mg ($T_{1/2}$=9.46 m) and ^{24}Na ($T_{1/2}$=14.96 h) and the long-lived radionuclide ^{26}Al ($T_{1/2}$=0.71 My).

Target	Mass [kg]	Proton energy [MeV]	Charge [Ah]	Activity [PBq]
Proton capture				
Ta	2.2	70	1.03	24.0
			3.09	38.6
			6.18	51.9
			12.36	64.0
Spallation				
W+Ta [148]	46+7	800	1.95	15.9
Ta [147]	639	1334	32.9	460
W [147]	743	1334	32.9	170
Hg [147]	168	1334	32.9	120
W+Ta [152]	58+1.4	1600	1.56	20
Fission				
U (20% ^{235}U) BER II	8.6	111 MWd/kg	291 d	260

Table VIII.4: *Comparison of the activity generated by different modes of neutron production.*

The activation of accelerator components is produced by protons escaping the beam and hitting the vacuum chamber. The proton- and neutron-induced radioactivity in the various accelerator parts as well as in the beam dump including shielding structures is predicted generally using the simulation code FLUKA [154, 155]. For the geometrical modelling, this requires a detailed material composition of each accelerator component which is not yet available for the HBS accelerator. Nevertheless, based

Isotope	Half-life	Irradiation time 1 yr	5 yr	10 yr	30 yr
Polyethylene moderator, 3.5 kg					
^{3}H	12.33 y	1.69E+06	2.44E+07	4.28E+07	8.10E+07
^{14}C	5730 y	2.68E+05	4.32E+06	8.66E+06	2.58E+07
^{10}Be	1.51 My	2.42E+03	3.73E+04	7.80E+04	2.34E+06
Beryllium reflector, 488 kg					
^{3}H	12.33 y	2.24E+12	1.00E+13	1.76E+13	3.33E+13
^{10}Be	1.51 My	9.75E+07	4.88E+08	9.75E+08	2.93E+09
Lead reflector, 3,000 kg					
^{209}Pb	3.25 h	3.15E+12	3.15E+12	3.15E+12	3.15E+12
^{203}Pb	51.8 h	2.12E+10	2.12E+10	2.12E+10	2.12E+10
^{205}Hg	5.2 m	5.66E+09	5.66E+09	5.66E+09	5.66E+09
^{203}Hg	46.6 d	5.45E+09	5.48E+09	5.48E+09	5.48E+09
^{206}Tl	4.20 m	2.21E+08	2.21E+08	2.21E+08	2.21E+08
^{204}Tl	3.78 y	2.14E+08	7.65E+08	1.07E+09	1.27E+09
^{208}Tl	3.05 m	1.53E+07	1.53E+07	1.53E+07	1.53E+07
^{205}Pb	15.3 My	2.53E+06	1.26E+07	2.53E+07	7.58E+07
Borated polyethylene shielding, 43,950 kg					
^{3}H	12.33 y	1.89E+04	2.73E+05	4.78E+05	9.07E+05
^{14}C	5730 y	3.00E+03	4.82E+04	9.66E+04	2.89E+05
^{10}Be	1.51 My	2.73E+02	4.21E+03	8.80E+03	2.64E+05
Lead shielding, 100,000 kg					
^{209}Pb	3.25 h	4.83E+10	4.83E+10	4.83E+10	4.83E+10
^{203}Pb	51.8 h	4.84E+07	4.84E+07	4.84E+07	4.84E+07
^{205}Hg	5.2 m	1.29E+07	1.29E+07	1.29E+07	1.29E+07
^{203}Hg	46.6 d	1.24E+07	1.25E+07	1.25E+07	1.25E+07
^{206}Tl	4.20 m	5.04E+05	5.04E+05	5.04E+05	5.04E+05
^{204}Tl	3.78 y	4.88E+05	1.74E+06	2.44E+06	2.90E+06
^{208}Tl	3.05 m	3.49E+04	3.49E+04	3.49E+04	3.49E+04
^{205}Pb	15.3 My	5.68E+04	2.83E+05	5.68E+05	1.70E+06

Table VIII.5: *Activity (Bq) of main radionuclides produced at the end of various irradiation times of the polyethylene moderator, the reflector (beryllium or lead with a thickness of 30 cm) and the shielding made of lead (four layers with a thickness of 10 cm each) and borated polyethylene (three layers with a thickness of 40 cm each).*

on the simulation results obtained for an intermediate-energy proton linac [154], total specific activity ranging between 10^5 and 10^6 Bq/g is estimated for the accelerator cavities considering an energy loss of 1 W/m. Main contributors to the activity are radionuclides with half-lives between days and 100 years such as ^{51}Cr ($T_{1/2}$=27.7 d), ^{56}Co ($T_{1/2}$=77.3 d), ^{88}Zr ($T_{1/2}$=83.4 d), ^{88}Y ($T_{1/2}$=106.6 d), ^{57}Co ($T_{1/2}$=271.8 d), ^{54}Mn ($T_{1/2}$=312.3 d), ^{49}V ($T_{1/2}$=330 d), ^{22}Na ($T_{1/2}$=2.60 y), ^{55}Fe ($T_{1/2}$=2.73 y), ^{60}Co ($T_{1/2}$=5.27 y), ^{3}H ($T_{1/2}$=12.33 y) and ^{63}Ni ($T_{1/2}$=100 y). The beam dump including cooling circuit and shielding will be designed taking into account a minimization of the residual activity.

Further radioactive materials will be produced by the neutron activation of the samples, parts of the instruments, neutron beam dumps and shielding structures. They will be handled on a case by case basis during HBS operation by staff responsible for radiation protection.

IX.
INFRASTRUCTURE

The operation of the HBS neutron source is based on a three-zone concept where each zone requires specific infrastructure. The first zone is the accelerator hall containing the linear accelerator with the ion source, the proton beam-line and the multiplexing unit for the distribution of the pulsed proton at the different target stations. This zone includes also the high voltage supply and the workshops for accelerator maintenance. For radioprotection, the accelerator hall as a supervised area is equipped with neutron and gamma monitoring systems and the appropriate shielding.

The second zone is the three target bunkers containing the target stations with the closed target cooling circuit, the cryogenic system for the cold moderator (optional) and appropriate devices for the maintenance of target station components as well as for target change, according to StrlSchV. The target station may be considered as an unsealed source and therefore the target bunker will be defined as a controlled area requiring a ventilation system and an air monitoring system. The radioactive components issued from the maintenance of the target station may be stored in an isotope storage room as a part of the target bunker before being released or transferred to a federal state collection facility.

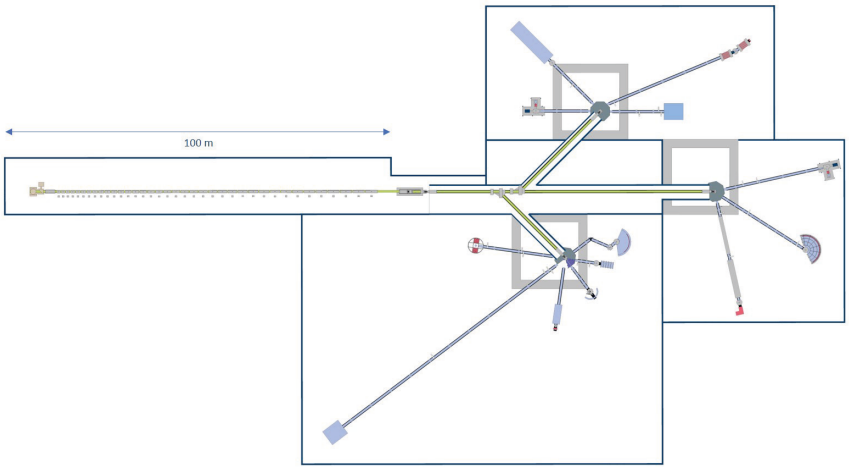

Figure IX.1: *Floor plan of the HBS core facility*

The third zone is the three experimental halls attached to the individual target bunkers containing the neutron guides and the instruments with adapted shielding. For radio-protection, the experimental hall as a supervised area is equipped with neutron and gamma monitoring systems. The area of the individual instruments will be handled as a restricted area during operation with an open beam. The supply of hydrogen, helium or nitrogen for the cryogenic system is installed separate to these buildings.

IX.1 Building requirements

A draft floor plan with the required dimensions of the HBS is shown in Figure IX.1. The experimental halls have the largest space requirements. Each of these halls will have a floor area of approximately 2,400 square meters in order to provide sufficient space for the instruments, including their sample preparation spaces, workshops and control rooms. The size of individual halls may vary depending on the space requirements of individual instruments therein. Each experimental hall requires the appropriate assembly hall cranes with a load bearing capacity of 5 t and a lifting range of 8 m.

The target zones are located inside the experimental halls. Each target zone has a floor area demand of 10 times 10 m with a soil bearing capacity of 5 t/m^2 and will be equipped with a crane with load bearing capacity of 5 t and a lifting range of 6 m. The target zones are surrounded by 2 m thick concrete walls. The operation of each target station requires a closed cooling circuit with 120 kW cooling capacity. The ground will be equipped with a collection tray to catch possible coolant leakage and concrete storage locations to store the activated neutron targets.

All three target zones will be connected at the ground floor to a truck loading bay with a soil bearing capacity of 5 t/m^2. The room will be equipped with a crane with a load bearing capacity of 20 t. At the second floor, on top of the truck loading bay, there is the multiplexer and proton beam transport line area.

The accelerator hall has a floor area demand of approximately 100 times 20 m. The hall requires a connection load of around 12 MW and a coolant capacity in the same order of magnitude. That hall will be equipped with a crane with a load bearing capacity of 5 t.

In addition to the core facility, all the necessary rooms and spaces for the employees and the changing users of the instruments must be provided. For the operation of the facility 20 - 25, employees are needed to operate the accelerator and target stations. For the operation of the instruments, 2 scientists and 1 technician per instrument are needed. For administrative tasks such as radiation safety, management of the user office and other issues 20 employees are planned. The total required space of HBS thus totals about 13000 m^2.

IX.2 Energy supply and cooling

The estimation of the required electrical connected load as well as the estimation of the annual electricity consumption are important for the planning of a large-scale technical facility. Since the total consumption data can only be quantified after an exact specification of all components, all values shown in Table IX.2 and discussed in the following are only estimates based on experience or the scaling of working accelerator facilities. To determine the annual electricity consumption, it is assumed that the plant is operated for 5000 hours per year. This corresponds to slightly more than 200 days of continuous operation.

The largest single electricity consumer is the ion accelerator which alone demands more than half of the electric power load within the HBS facility. The accelerator itself has a total power requirement of 12 MW during operation including the proton source, LEBT, RFQ, MEBT, RF-Structures and the

	Length [m]	Width [m]	Height [m]	Floors	Area [m^2]
Accelerator	100	20	8	1	2000
Beam transport	40	15	12	2	1200
Target station A	12	12	8	1	144
Target station B	12	12	8	1	144
Target station C	12	12	8	1	144
Instrument hall A	60	28	10	1	1680
Instrument hall B	38	38	8	1	1444
Instrument hall C	75	52	8	1	3900
Offices	45	15	10	3	2025
Total	≈180	≈70	8-12	1-3	12681

Table IX.1: *HBS building space*

vacuum supply. Since the largest part of this energy remains as heat in the accelerator structure, an equally powerful water cooling system is necessary. Attached to the accelerator is the beam transport system which transports the beam to the individual target stations. The beam transport system requires additional power of up to 0.5 MW. The connected load can be multiplied by the expected 5000 operating hours to estimate the annual consumption since the accelerator and the beam transport system account for the main energy consumption only during operation. The water cooling capacity is neglected in the estimation of the annual consumption, since this is provided by a heat exchanger (e.g. cooling tower or air cooler) or a cooling water pipe.

Each target station is located inside a target bunker. The power consumption of each bunker including the target station itself is up to 0.5 MW. The largest electric consumer are the air conditioning system and the dedicated safety circuits to avoid any exposure or loss of activated material during operation inside the target bunker. The target station itself consumes only a small portion of the power e.g. for vacuum support, monitoring and coolant support. In addition, each bunker requires a water cooling supply of approximately 0.2 MW for the cooling of the target and moderator system and a cryogenic cooling supply for the optional cold moderators of up to a few tens of kilowatts. The connected load can be multiplied by the annual hours in operation to estimate the annual consumption since the air conditioning system including its safety circuits, the vacuum system and the target monitoring system run throughout the year.

For the various instruments operated in the three instrument halls, each instrument may require a power and cooling supply of up to 0.5 MW depending on cryogenic systems, sample environment, vacuum systems and detector electronics. With up to six 6 instruments in one instrument hall, each hall may require up to 3 MW of power. Combined, the three instrument halls are thus the second largest energy consumer after the accelerator. The required heating of the hall depends strongly on its construction and possible specific requirements of the instruments. For this reason, the given values of 0.3 MW per small instrument hall and 0.8 MW for the large instrument hall are only extremely conservative estimations. The instruments consume the major part of their energy only during operation while the power used for heating is consumed during the cold season. Thus, the connected load can be multiplied by the expected 5000 operating hours and the heating power can be multiplied by six months in order to estimate the annual power consumption.

The office building and workshops, placed within the instrument halls, are expected to require a maximum total power consumption of 0.4 MW in total, depending on installations of equipment in workshops and offices. This requirement will include the operation of computer systems and

networks. The total power consumption can be multiplied by the 5000 annual working hours to estimate the annual consumption since energy is mainly consumed during the working hours. The heating power is multiplied by six months analogue to the instrument halls.

The total required electrical power is estimated at a value of ∼23 MW for the facility in total. The total annual consumption would be about 130 MWh. The plan is to cover this demand by the installation of renewable energy systems for the production of electricity, mainly using windmills and photovoltaic systems. The design and construction of all buildings will also involve state-of-the-art engineering, low carbon emissions and energy saving technologies.

	Electrical connected load	Heating power	Water cooling	Cryogenic cooling	Annual consumption
	[MW]	[MW]	[MW]	[kW]	[kWh$\times 10^3$]
Accelerator	12.0	-	12.0	-	60.000
Beam transport	0.5	-	-	-	2.500
Target station A	0.5	-	0.2	8	4.450
Target station B	0.5	-	0.2	8	4.450
Target station C	0.5	-	0.2	32	4.660
Instrument hall A	3.0	0.3	(included in power)		16.314
Instrument hall B	3.0	0.3	(included in power)		16.314
Instrument hall C	3.0	0.8	(included in power)		18.504
Offices and workshops	0.4	0.1	-	-	2.438
Total	23.4	1.5	12.6	48	129.63

Table IX.2: *Energy supply for HBS buildings*

X.
COMMISSIONING, DECOMMISSIONING

X.1 Commissioning

Following procedures established at accelerator-based large scale facilities, the commissioning of the facility will be a stepwise effort following the timeline of the construction of the different compartments. After the construction of the accelerator, the commissioning of the ion source, LEBT, RFQ, MEBT and DTLs will be established step by step. The accelerator system will start with a low level of proton beam energy and current, and will then be successively ramped up to the final design values of 100 mA and 70 MeV. By the stepwise installation of the DTLs commissioning of the proton beam transport system will also follow step by step in line with commissioning of each individual target station.

By this stepwise procedure the full commissioning of the accelerator up to its final energy and the full proton beam transport system to all three target stations will take about 3.5 years. Each target stations will be commissioned within three months after construction. The instruments will be commissioned step by step following the construction of the individual instruments. This may take up to one year for all instruments at an individual target station. A total commissioning time of 2.5 years for the full operation of the first target station and experimental hall sums up and one additional year of commissioning for each following target station and experimental hall (Figure X.1).

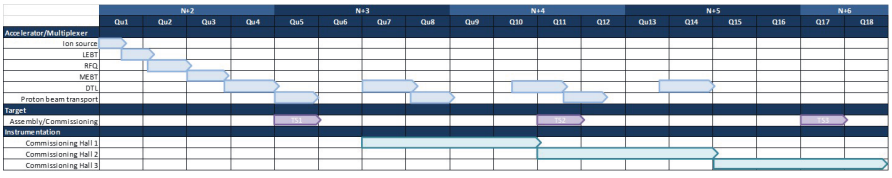

Figure X.1: *Time line commissioning*

X.2 Decommissioning

According to the IAEA (International Atomic Energy Agency), decommissioning refers to the administrative and technical actions taken to remove all or some of the regulatory controls from an authorized facility [156]. Decommissioning includes administrative operations such as the elaboration of decommissioning plans and the application for free-release authorizations as well as technical operations such as decontamination, the dismantling and the management of non-radioactive and radioactive

materials. Planning the decommissioning of the HBS facility will be considered at the earliest stage of its development i.e. at the design and construction stages and will continue during the lifetime of the facility starting at the stages of commissioning and operation and potential upgrades.

In order to ensure safe dismantling, the HBS facility will be designed and constructed to minimize the amount of radioactive and hazardous materials and to facilitate the management of activated materials used by using modular shielding and technical components. As part of the facility's initial authorization, an initial decommissioning plan including risk analysis, will be developed to demonstrate the feasibility of decommissioning, to define a decommissioning strategy and to estimate costs. It will include the collection of relevant information and data as well as the radiological characterization of the different parts of the HBS facility (accelerator hall, target stations and experimental halls) according to their final designs in view of radiation safety issues. Additional information to improve the initial decommissioning plan will be gained during the commissioning and operation of the HBS facility. At the final shutdown of the HBS facility, a final decommissioning plan will be established ensuring the safety and protection of workers and the public from radiation, the safe management of radioactive and non-radioactive waste, as well as environmental protection. In order to meet safety requirements for the decommissioning process, internationally approved safety standards developed by IAEA will be adapted in accordance with national radiation protection regulations.

X.3 Waste management

The management of radioactive waste produced during the commissioning, operation and decommissioning of the HBS facility will be performed in compliance with the German radiation protection ordinance (StrSchV) and in agreement with the regulatory bodies. As far as possible clearance procedures will be applied in order to minimize the amount of radioactive waste. The management of non-radioactive waste will be performed according to the German Closed Cycle Waste Management Act (KrWG).

XI.

INVESTMENTS, COSTING & TIMELINE

Here the cost for a full-fledged HBS facility in the reference design with a basic configuration of three target stations and 13 instruments is estimated under the following assumptions:

1. The facility is being build in the environment of a research centre, where support is granted for administrative services, i.e. through the departments for purchasing, human resources, finances, occupational safety and radio protection and legal services.

2. During the construction phase support from engineering and building departments and workshops is available; here these services are not prized in a full cost calculation.

3. The price for the land, where the facility is being build, is not considered, and it is assumed that the land is fully developed with access roads, media and necessary electricity supply and thus ready for building.

4. For the core team, the cost of one full time equivalent is fixed at a flat rate of 100 kEuro per year.

The actual full cost of the facility depends on the choice of its location and the price of the above mentioned services and can therefore only be calculated after a decision on the site has been reached. Clearly a realization on a green field will be significantly more expensive than a realization at a larger research centre such as Forschungszentrum Jülich.

Under these assumptions the cost of of an HBS reference facility has been estimated in 2019 prices as detailed below. The total investment necessary is in the range of EUR 370 million at 2019 prices. At present contingency of 30% is estimated. A more precise cost estimate will be done with the forthcoming Technical Design Report TDR. Table XI.1 lists the costs estimated for the main components of HBS. The cost of the linear accelerator including the ion source, RFQ, LEBT, MEBT, DTLs, multiplexer and the operating system represents about 30% of the total cost. The estimated costs for the target station include the cryogenic system for the cold neutron source(s), the water cooling system for the individual target assembly and the shielding materials. Altogether this will be in the range of EUR 4-5 million for each target station implemented.

To equip the target stations with a reasonable number of instruments (4-5 at each station), an estimated average cost of about EUR 7 million per instrument is calculated. The total cost for instrumentation depends on the choice of instrument types to be installed to cover the scientific needs of the facility. In addition, the performance of many instruments can be improved by the installation of detector systems covering a larger angular range. Dedicated sample environment, laboratory equipment etc. are added as "Ancillary" costs to the facility.

	n=0	n=1	n=2	n=3	n=4	n=5	n=6	n=7	Total
Accelerator	12.0	15.0	18.0	18.0	18.0	15.0	7.0	4.0	107.0
Target	1.0	1.0	3.0	4.0	2.0	1.0	1.0	1.0	14.0
Instruments	6.0	10.0	12.0	16.0	16.0	12.0	12.0	10.0	94.0
Building	10.0	18.0	20.0	18.0	16.0	16.0	18.0	10.0	126.0
Ancillary	-	2.0	3.0	4.0	5.0	6.0	6.0	3.0	29.0
Sum (M€)	29.0	46.0	56.0	60.0	57.0	50.0	44.0	28.0	370.0

	n=0	n=1	n=2	n=3	n=4	n=5	n=6	n=7
Scientists	12	14	16	18	20	25	25	25
Engineers	20	25	30	33	37	40	40	40
PostDocs	10	12	14	16	18	20	20	20
Support	8	10	12	14	16	20	20	20
Sum (FTE)	50	61	72	81	91	105	105	105
Staff (M€)	5.0	6.1	7.2	8.1	9.1	10.5	10.5	10.5

Table XI.1: *Distribution of investments (Mio EUR; "Ancillary" denotes sample environment, laboratory equipment etc.) and staff in the core team (FTE and total in Mio EUR assuming 100 kEuro/FTE/a) during construction (year 0 to 5) and commissioning (year 6 to 7) of the HBS facility*

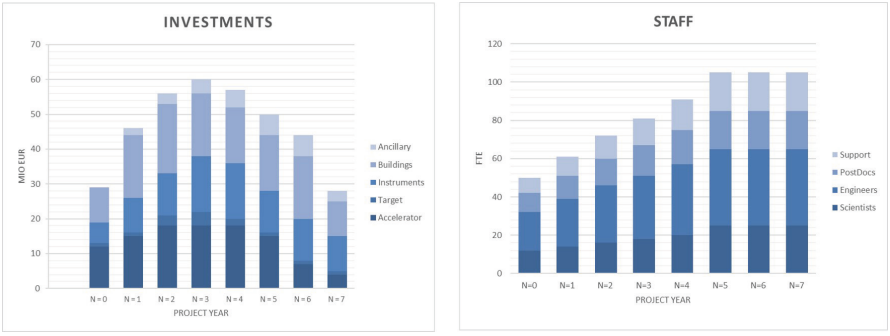

Figure XI.1: *Left: Distribution of investment costs during project time-line. Right: Distribution of staff during project time-line*

The corresponding buildings account for up to 34% of the total cost of the implementation of the facility. Over the construction period of 6 years technical and scientific staff is gradually build up to reach 105 FTE needed for the reliable operation of the HBS as user facility. These numbers refer to the core team of HBS with accelerator, target and instrument operation. Additional expert support is needed during the construction phase as mentioned above.

During the operation phase of HBS additional positions are required to fully exploit the scientific potential of the facility, i.e. a number of PhD and master students (about 15) plus specialists in the various fields of application. At a research centre, such specialists can be recruited from the various scientific institutes, while for a green field realization additional staff is needed not only in terms of scientists using the facility, but also in terms of the above mentioned administrative and technical service departments. The construction phase relates to about 6 years with a follow up of successive commissioning periods of up to 2 years (see Chapter X).

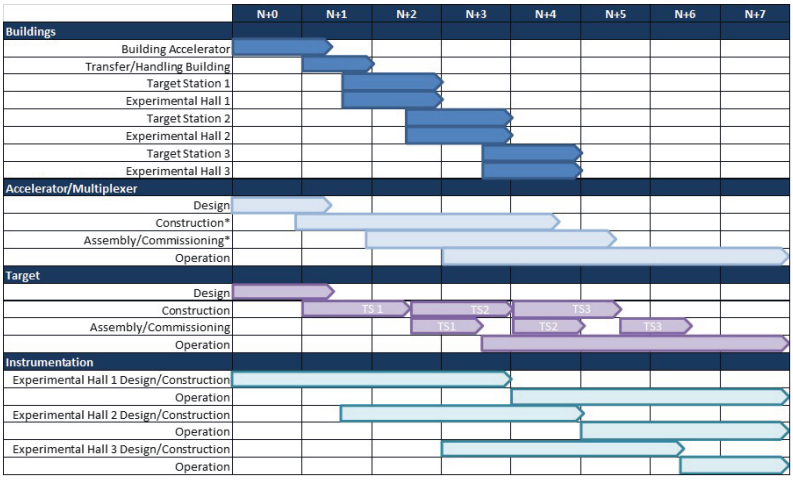

Figure XI.2: *Project time line. *Construction and commissioning of the accelerator will happen step by step so operation will start already before final construction is finished.*

A breakdown of the various costs categories and staff numbers estimated over the project timeline is given in Figure XI.1. In Figure XI.2, the envisioned construction, commissioning and operation times are displayed. The accelerator will be built and commissioned in parts, step by step. By adding more and more DTL's the final particle energy will be increased, as will be the length of the accelerator. At each intermediate step - i.e. particle energy - the accelerator configuration will be optimized and operation of the accelerator to commission the target stations and instruments will already be possible before the final construction of the accelerator is reached.

XII.

COOPERATION AND DELINEATION

Following the recommendations in the "Strategy Paper on Neutron Research in Germany: 2020-2045" [157], a network of national and regional neutron sources is very important in order to provide a co-operating eco-system offering both low flux experiments right up to European top-class sources for neutron science. Within this eco-system, compact accelerator-driven neutron sources have the potential to add value to the network of neutron facilities and provide a basis for the efficient use of the existing and future top tier sources such as ILL, MLZ and ESS.

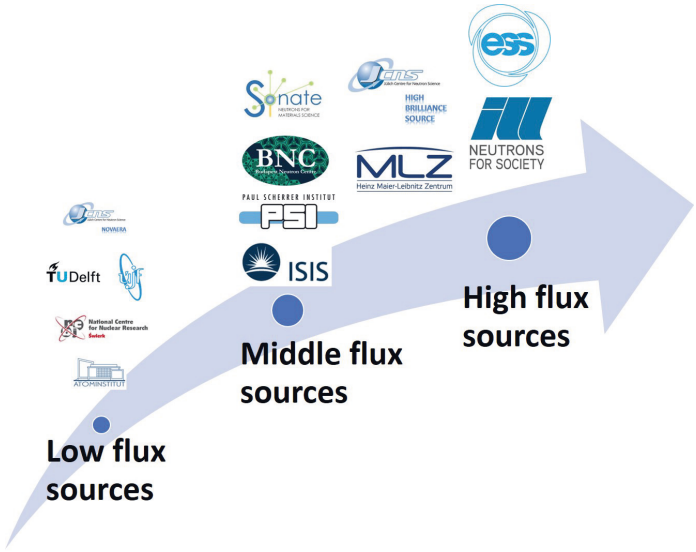

Figure XII.1: *European ecosystem of neutron sources.*

The HBS project aims to provide a full-fledged, medium size facility designed to maximize beam brilliance. Together with other similar European sources, the HBS serves to secure a functional and resilient network of neutron sources in Europe and to fill the anticipated gap in instrument days due to the ongoing closure of older neutron sources [2]. It is a response to the increased demand for experiments on small samples, such as systems of biological macromolecules or nanomagnets.

Required by the various technological challenges for the development and operation of this novel kind of compact accelerator-based neutron source, the project is embedded in an international network

of expertise made up of national and international institutes providing excellence in the different areas of expertise. Based on a Memorandum of Understanding, partners in the project comprise on the national scale the Helmholtz Zentrum Geesthacht, the Helmholtz Institute Mainz, the University of Frankfurt, RWTH Aachen University and the Technische Universität Dresden, and on the international scale, the Laboratoire Léon Brillouin, CEA Saclay, ESS Bilbao, Legnaro National Institute, the Paul Scherrer Institut and RIKEN RAP.

Figure XII.2: *HBS project network*

With the design goal of a 100 kW target station, the HBS will exceed the existing CANS facilities by up to 2 orders of magnitude in neutron flux and will achieve a neutron yield comparable to existing middle flux neutron research reactors or spallation sources. Due to its improved brilliance, instruments at HBS will compete with existing instruments even at modern research reactors such as at the MLZ.

With this unique performance, HBS will bridge the gap between the top-tier neutron sources in the world and small to medium flux facilities. It will neither replace nor to do without existing medium and high flux neutron facilities but foster the resilient network of neutron sources in Europe and abroad. Due to the scalable design of the HBS concept, a variable number of target stations and instruments are possible. This allows HBS to be adapted to the specific needs of certain communities and regions also in terms of the necessary investment and operational costs.

ACKNOWLEDGEMENT

This Conceptual Design Report has been compiled with the kind support of a large number of colleagues at the Jülich Centre for Neutron Science and the Institut für Kernphysik at Forschungszentrum Jülich and other collaborating institutes. The editors would like to thank in particular:

- Pierfrancesco Mastinu, INFN Laboratori Nazionali di Legnaro, Italy (Chapter IV.10 and IV.11.5)
- Markus Strobl, Paul Scherrer Institut, Villigen, Switzerland (Chapter IV.11.4 and VI.1)
- Oliver Zimmer and Michael Jentschel, Institut Laue Langevin, Grenoble, France (Chapter IV.11.7, IV.11.8 and IV.11.9)
- Holger Podlech and Oliver Meusel, Institut für Angewandte Physik, Goethe Universität Frankfurt, Germany (Chapter V.2)
- Jochen Fenske, Helmholtz Zentrum Geesthacht, Geesthacht, Germany (Chapter VI.2.5)
- Artur Glavic, Paul Scherrer Institut, Villigen, Switzerland (Chapter VI.4.1)

Chapter IV.1-9 on the Science Case is largely based on the HBS science workshop which took place in Unkel, Germany, in April 6-7, 2017 [23, 158]. We thank all participants of this workshop for their valuable contributions, in particular the plenary speakers Andreas Meyer (DLR), Eberhard Lehmann (PSI), Laszlo Rosta (BNC), Olwyn Byron (Glasgow), Frank Gabel (IBS), Frank Schreiber (Tübingen), Anne Caroline Genix (Montpellier), Henrik Ronnow (EPFL), Christian Pfleiderer (TUM), Paul Attfield (Edinburgh) and Richard Dronskowski (RWTH Aachen), contributing participants Werner Paulus (Montpellier), Ras-mus Toft-Pedersen (DTU), Jeremy Lakey (Glasgow), Bill David (ISIS), Holger Kohlmann (Leipzig) and Luigi Paduano (Naples), as well as the editors Sebastian Benz (RWTH Aachen), Philipp Jacobs (RWTH Aachen), Margarita Krutyeva (JCNS) and Manual Angst (JCNS).

A.
APPENDICES

A.1 Production of secondary products

In a Compact Accelerator-driven Neutron Source (CANS), the production of neutrons is based on the interaction of light ions such as protons or deuterons with the atomic nuclei of a dedicated target material. However, a maximization of the neutron yield as well as a reduction of the production of by-products like tritium may be achieved by selecting the target material with regards to the type and energy of the ion considered and other required physical properties to ensure mechanical, thermal and chemical stability of the target.

The production of secondary particles like neutrons, tritium and other activation products for a particle beam hitting a target material depends on the involved cross sections, the particle energy and the range of the particles inside the target material. This can be well analyzed using Monte Carlo codes like MCNP6 or Geant4 but this would be very time consuming task for all target materials, particles and involved energies. Therefore, an analytic approach [93] for the calculation of secondary production is a valid approach to get a first estimation.

The general formula for the calculation of the secondary particle yield for a given primary particle energy E and an energy loss of ΔE is given by

$$p(E, \Delta E) = \frac{N_A}{M} \rho \delta(E, \Delta E) \cdot \sigma(E, \Delta E), \tag{A.1}$$

where N_A is the Avogadro constant, ρ is the density of the target material, M is the molar mass of the target material, δ is the range of the primary particles with an energy of E and an energy loss of ΔE and σ is the involved cross section for the production of the secondary particles. The thickness of the target material for a given particle energy and an energy loss can be calculated by using the SRIM toolkit [66].

The neutron yield, the tritium activity and the total induced activity were calculated by mean of Formula A.1 for each element of the periodic table from lithium to lead and for primary ion energies ranging from 1 to 100 MeV by using the corresponding cross sections for protons and deuterons reactions given in the database TENDL2017 [94]. The dependence of the neutron yield on the atomic number Z of the element and the primary ion energy is shown for protons and deuterons in Figure A.1. It shows that at low energies ≤ 30 MeV, low Z-materials, like beryllium or lithium, produce the most neutrons and are therefore used in most low energy accelerator neutron sources. At higher energies ≥ 30 MeV, high Z-materials start to produce more neutrons and should be therefore preferred for a large scale facility. Moreover, it indicates that a competitive high neutron yield may be achieved for primary ion energies greater than 70 MeV up to 100 MeV and high-Z elements ($70 \leq Z \leq 82$). Within this range the neutron yield varies between 9 and $22 \cdot 10^{14}$ s^{-1} mA^{-1} for protons and between 10 and

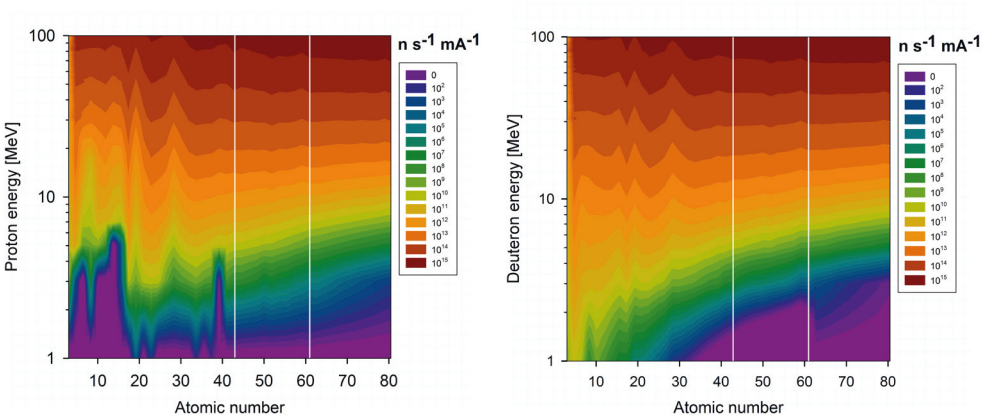

Figure A.1: *Dependence of the neutron yield for protons (left) and deuterons (right) on the atomic number Z and the primary ion energy up to 100 MeV.*

$27 \cdot 10^{14}$ s^{-1} mA^{-1} for deuterons. This values are 2 to 3 times higher than the neutron yield achieved for the same ion energy range with beryllium, an element commonly proposed as target. For high Z-elements, the neutron production yield from deuterons is 10% to 20% higher than the neutron production yield from protons. Additionally, deuterons have a larger stopping power than protons, which allows to employ thinner targets and by consequence reduce the temperature gradient inside the material [95]. Anyhow, for the HBS reference design, we decided that the increased neutron yield and the reduced target temperature gradients do not justify the operation of a high current deuteron accelerator, which requires a much higher level of complexity in accelerator design and increased measures of radio protection, in comparison to a high current proton accelerator.

Tritium is a relevant radionuclide in radiation safety due to its relatively high diffusion in materials. The tritium activity induced by protons and deuterons was determined for an irradiation time of 2000

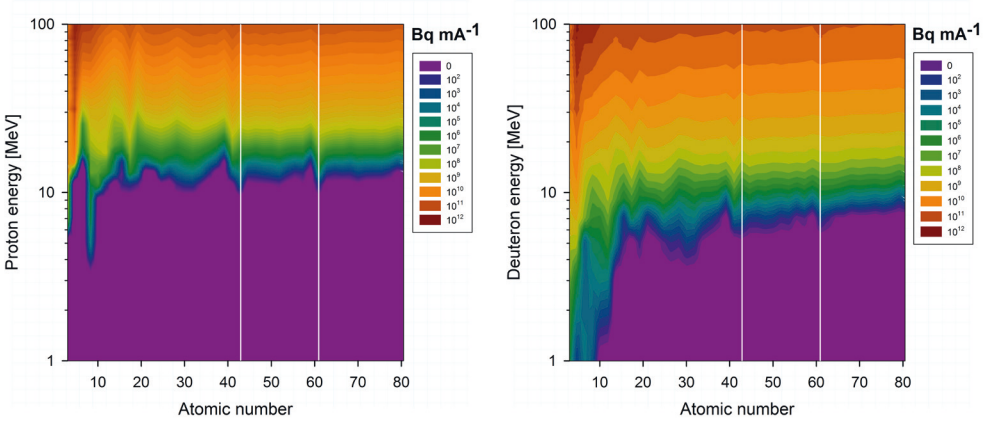

Figure A.2: *Dependence of the tritium activity induced by protons (left) and deuterons (right) on the atomic number Z and the primary ion energy up to 100 MeV. The irradiation time is 2000 h.*

hours. The dependence of the tritium activity on the atomic number Z of the element and the primary ion energy is shown for protons and deuterons in Figure A.2. For a given target element and incident energy, deuterons produce more tritium than protons. The difference in tritium activity between deuterons and protons decreases with increasing atomic number Z. The highest tritium activities are obtained for the light elements ($Z \leq 10$). For example, 2000 hours irradiation of beryllium (Z=4) with 70 MeV protons and deuterons, respectively, induce an tritium activity of 0.83 and 1.85 TBq mA^{-1}, respectively. The tritium activity induced by irradiation of tantalum (Z=73) is 0.029 and 0.045 TBq mA^{-1}, respectively, and is one order of magnitude less than this of beryllium.

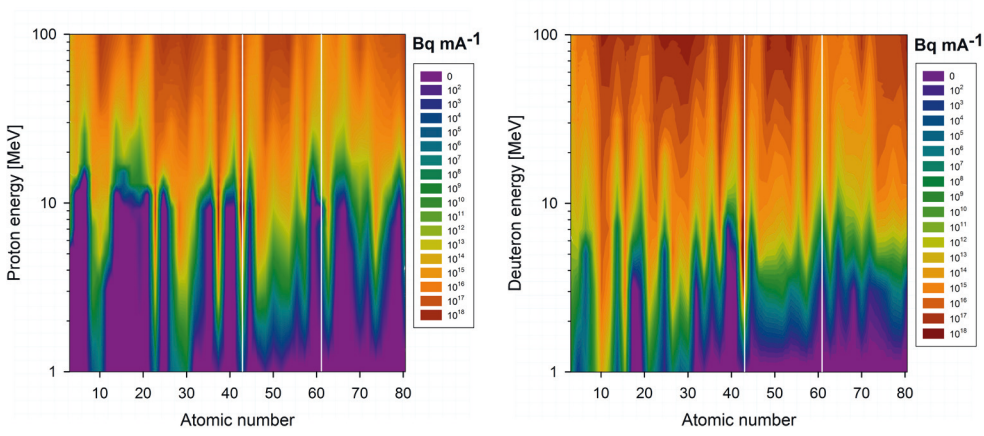

Figure A.3: Dependence of the activity induced by protons (left) and deuterons (right) on the atomic number Z and the primary ion energy up to 100 MeV. The irradiation time is 2000 h.

The activity induced by protons and deuterons was determined for an irradiation time of 2000 hours. The dependence of the activity on the atomic number Z of the element and the primary ion energy is shown for protons and deuterons in Figure A.3. Protons and deuterons produce activities of same order of magnitude, except for some low-Z elements like beryllium, fluorine, chromium and cobalt and incident energies lower than 15 MeV, where deuterons generate much more activity than protons. The activity induced by 2000 hours irradiation of tantalum with 70 MeV protons and deuterons, respectively, is 11.1 and 23.1 PBq mA^{-1}, respectively.

Element	Thickness [mm]	Neutron yield 10^{14} s^{-1} mA^{-1}	Tritium activity GBq mA^{-1}	Total activity PBq mA^{-1}
Protons				
Ta	5.07	9.0	29	11
W	4.38	9.8	28	60
Deuterons				
Ta	3.14	10.2	45	23
W	2.72	10.3	47	64

Table A.1: Neutron yield, tritium activity and total induced activity analytically calculated for the irradiation of tantalum and tungsten with 70 MeV protons and deuterons. The thickness of the material is set for a full stopping of the ions. The activities correspond to the activity of the material after 2.000 hours irradiation time.

As an example, the neutron yield, the tritium production and the total activity for tantalum and tungsten targets irradiated with 70 MeV protons and deuterons is shown in Table A.1.

A.2 Beam brilliance at HBS

To compare the neutron brilliance of HBS with existing neutron facilities, two of the many design options of the HBS target-moderator system that were simulated were analyzed in detail: (1) a thermal water moderator with an extraction channel of 2 cm diameter and (2) a cold hydrogen moderator of 2 cm diameter surrounded by inside the water moderator using an extraction channel of 4.4 cm diameter forming effectively a bispectral source.

- **HBS:** MCNPX data were analyzed at the transition from moderator to reflector in the target system. The resulting spectra were described as a sum of 2 (thermal) or 3 (bispectral) Maxwellian distributions. This allows extending the spectra to longer wavelength where the MCNPX statistics are poor.
  A pulse is simulated for the 96 Hz option in a narrow wavelength range with many time channels using the simulation package VITESS [159]. The peak flux is obtained as the maximal brilliance found in a single time channel.
- **FRM II:** The brilliance for the existing FRM II moderators were obtained in simulations by A. Röhrmoser of the beamlines SR1 (cold), SR5 (thermal) and SR9 (hot). They were found to be in good agreement with measurements [16]. In March 2011, these data were provided in VITESS. They can also be found in the corresponding report describing the facility [17].
- **ILL:** For ILL, the thermal beamline H12 and the horizontal cold source (HCS) were chosen. The HCS shows a somewhat higher brilliance than the second vertical cold source (VCS). H12 serves only one instrument and has the highest thermal brilliance of the beamlines according to the 'Yellow Book' [18]. This shows the potential of the ILL source and therefore matches best the comparison with simulated moderator performance of the other sources.
  While the H12 brilliance (as a function of wavelength) is directly available in a file, the HCS characteristics are described as a sum of 3 Maxwellians. The brilliance as a function of wavelength has therefore been determined by a VITESS simulation.
- **ISIS:** The ISIS facility has 7 moderators on 2 target stations [19]. The only thermal moderator is the water moderator on Target Station 1 (TS1); which was used for the comparison. Target Station 2 (TS2) has gone through a long and thorough optimization and is therefore of superior design compared to TS1. Among its 4 cold moderators - 3 methane and 1 hydrogen; 2 coupled and 2 decoupled - the coupled hydrogen seems most appropriate for a comparison with the HBS bispectral source.
  The ISIS part of the VITESS source module was written by D. Champion and included in the package in August 2005. It uses output data of MCNP simulations of the target/moderator systems (for the proton beam currents foreseen for the operation in full power, $160 + 40\mu$A). The simulations were performed using 40 Hz for TS1 and 10 Hz for TS2.
- **ESS:** The ESS published a detailed description of the performance of the Butterfly 1 moderator (run at 14 Hz) [20], which has been constructed in the meantime. It describes the brilliance of both moderator parts, cold and thermal, as a function time, wavelength and direction and also shows brilliance spectra averaged over all beamports. The direction dependence means that the brilliance varies to some degree from beamport to beamport.

Where the averaged data were not available, the brilliance was simulated using VITESS for one beamport (S3), which shows exactly the same maximal brilliance as the average brilliance for the thermal moderator, while that of the cold moderator is 14% higher.

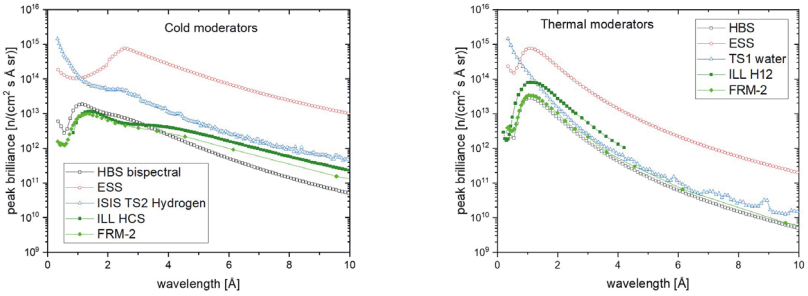

Figure A.4: *Comparison of neutron brilliance of cold (Left) and thermal (Right) neutron yield at various neutron sources*

A.3 Brilliance calculation

In order to calculate the brilliance delivered by a neutron moderator system, which is necessary to evaluate instrument performances, it is inevitable to perform Monte Carlo simulations. As these simulations are computationally complex and therefore time consuming, it is necessary to simplify the model and to reduce the number of parameter variations. This will be discussed in the following together with the geometry used for the MCNP simulations, the input parameters and the data treatment afterwards.

MCNP geometry, input and output parameters

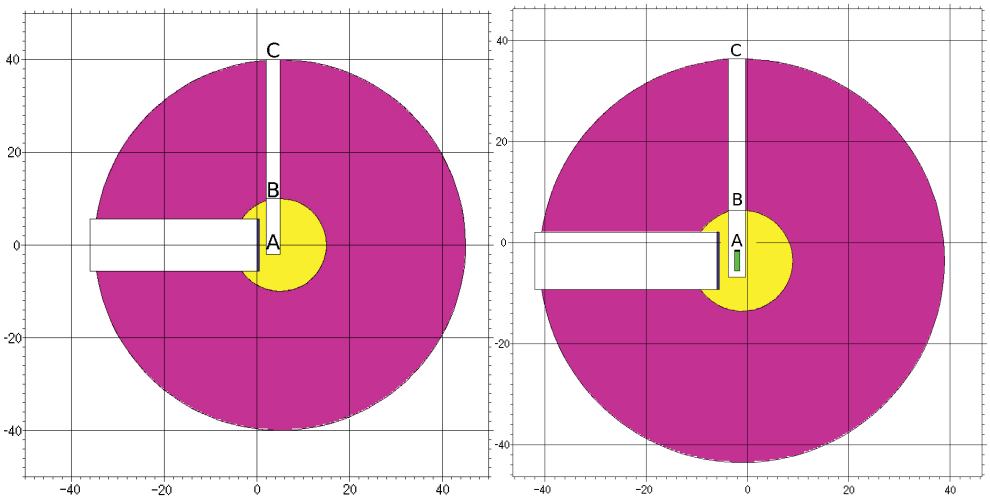

Figure A.5: *TMR Geometry used for the MCNP simulations. The energy, time and divergence resolved neutron spectra were recorded at surfaces A, B and C. Left: Thermal extraction channel. Right: Cryogenic extraction channel*

The geometry used for the MCNP simulations is presented in Figure A.5 for the thermal extraction channel on the left-hand side and for the cryogenic extraction channel on the right-hand side. It

consists of a Ta target (blue) with a surface area of 100 cm^2 and a thickness of 5 mm, a polyethylene moderator (yellow) with a radius of 10 cm, a Be reflector (purple) with a thickness of 30 cm and the LH2 or methane moderator (green) which is varied in length, diameter and position. The simulations were done with an instantaneous proton beam with an energy of 70 MeV hitting the center of the target. A convolution of the simulated spectra with a proton beam shape creates a realistic output. This approach allows to analyse different pulse structures relevant for different target stations with just one MCNP simulation.

The parameters of the neutrons passing the surfaces A (moderator surface), B (moderator/reflector interface) and C (reflector/shielding interface) normalized to the number of simulated primary particles are recorded in the standard MCNP output format in energy bins from 0.1 meV to 100 MeV in 10 bin per decade, in time bins from 5 μs to 5 ms in steps of 5 μs and in divergence bins from cos(0.5°) to cos(180°) with respect to the surface normal. The spectra have therefore the dimensions

$$d \in \mathbb{R}^{L \times M \times N}, \tag{A.2}$$

where L is the number of time bins, M is the number of energy bins and N is the number of divergence bins. $d_{i,j,k}$ is the number of neutrons in the $i\text{-}th$ time bin t_i, in the $j\text{-}th$ energy bin e_j and in the $k\text{-}th$ divergence bin $cos(\alpha)_k$.

Brilliance and normalization

The brilliance for the instantaneous proton pulse can be defined by the number of neutrons emitted from a surface with an area of A into a solid angle Ω inside a wavelength band $\Delta\lambda$ at a mean wavelength λ within a time Δt.

The brilliance therefore can be calculated from the MCNP output d which is normalized to the number of simulated protons mAs within the discrete three dimensional space by

$$B = \frac{d}{A\Omega(1\%\Delta\lambda/\lambda)\Delta t} \tag{A.3}$$

and therefore has the dimensions

$$[B] = \frac{1}{s\ sr\ cm^2(1\%\Delta\lambda/\lambda)(mAs)}. \tag{A.4}$$

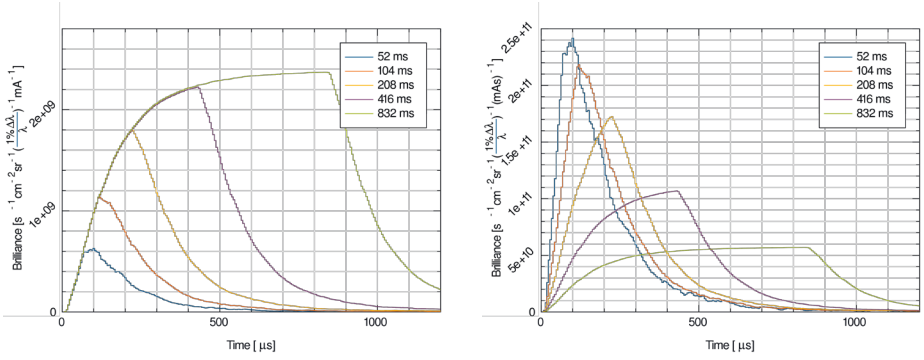

Figure A.6: *Left: Thermal neutron brilliance of a single pulse for different proton pulse lengths. Right: Thermal neutron brilliance for different proton pulse lengths multiplied with the respective proton pulse frequencies.*

Convolution

As the output was recorded for an instantaneous proton beam, the spectra need to be convoluted with the pulse width of the proton beam. With a proton pulse shape given by p with the same step size as defined by d, the discrete convolution is given by

$$(p * d)_{i,j,k} = \sum_{x=-\infty}^{x=\infty} p_x \cdot d_{i-x,j,k}. \tag{A.5}$$

This convolution is defined for a single proton pulse and the resulting normalization of the convolution depends on the definition of the proton beam shape. As the beam current is limited by the current technology, it is useful to set the proton beam intensity to 1 so that the integral is equal to the proton beam width. The convolution therefore is normalized to mA (Figure A.6 left).

A CANS will be operated as a pulsed source, so that the proton pulses arrive with a given frequency which is indirect proportional to the pulse width for a fixed duty cycle. In order to compare the performances of target stations operated at different frequencies and pulse widths, the repetition rate of the proton pulse needs to be taken into account. This is done by multiplying the frequency to the calculated convolution (Figure A.6 right) resulting in a normalization to mAs.

BIBLIOGRAPHY

[1] Neutrons for science and technology. Technical report, European Neutron Scattering Association, 2017.

[2] ESFRI Physical Sciences and Neutron Landscape Group Engineering Strategy Working Group. Neutron scattering facilities in europe: Present status and future perspectives. Technical report, ESFRI Scripta Volume I, 2016.

[3] `https://www.mlz-garching.de/englisch/neutron-research/neutron-source.html`.

[4] J. Womersley and A. Schreyer. Neutron users in europe: Facility-based insights and scientific trends. Technical report, ESS, 2018.

[5] M.B. Leuschner, D.V. Baxter, V.P. Derunchuk, H. Kaiser, C.M. Lavelle, H. Nann, N.B. Remmes, T. Rinckel, W.M. Snow, and P.E. Sokol. LENS: A new university-based neutron source for science and education. *Nuclear Instruments and Methods in Physics Research Section B: Beam Interactions with Materials and Atoms*, 261(1):956 – 959, 2007. The Application of Accelerators in Research and Industry.

[6] Y. Ikeda, A. Taketani, M. Takamura, H. Sunaga, M. Kumagai, Y. Oba, Y. Otake, and H. Suzuki. Prospect for application of compact accelerator-based neutron source to neutron engineering diffraction. *Nuclear Instruments and Methods in Physics Research Section A: Accelerators, Spectrometers, Detectors and Associated Equipment*, 833:61 – 67, 2016.

[7] M. Furusaka, H. Sato, T. Kamiyama, M. Ohnuma, and Y. Kiyanagi. Activity of Hokkaido University Neutron Source, HUNS. *Physics Procedia*, 60:167 – 174, 2014. 3rd International Meeting of the Union for Compact Accelerator-driven Neutron Sources, UCANS III, 31 July–3 August 2012, Bilbao, Spain & the 4th International Meeting of the Union for Compact Accelerator-driven Neutron Sources, UCANS IV, 23-27 September 2013, Sapporo, Hokkaido, Japan.

[8] K. Hirota, S. Imajo, G. Ichikawa, I. Itoh, M. Kitaguchi, H. M. Shimizu, Y. Tsuchikawa, Y. Kiyanagi, K. Tsuchida, A. Uritani, K. Watanabe, S. Yoshihashi, A. Yamazaki, Y. Iwashita, and Y. Yamagata. Development of Nagoya University Accelerator-driven Compact Neutron Source (NUANS). IPAC17, Copenhagen, Denmark, May 2017.

[9] S. Tasaki, T. Nagae, M. Hirose, Y. Yamashita, K. Hironaka, Y. Abe, Y. Yamagata, Y. Otake, and K. Hirota. Properties and possible applications of Kyoto University Accelerator based Neutron Source (KUANS). *Physics Procedia*, 60:181 – 185, 2014. 3rd International Meeting of the Union for Compact Accelerator-driven Neutron Sources, UCANS III, 31 July–3 August 2012, Bilbao, Spain & the 4th International Meeting of the Union for Compact Accelerator-driven Neutron Sources, UCANS IV, 23-27 September 2013, Sapporo, Hokkaido, Japan.

[10] J. R. Granada, R. E. Mayer, J. Dawidowski, J. R. Santisteban, F. Cantargi, J. J. Blostein, L. A. Rodríguez Palomino, and A. Tartaglione. The sciences and applications of the electron linac-driven neutron source in Argentina. *The European Physical Journal Plus*, 131(6):216, Jun 2016.

[11] A. Menelle, F. Ott, B. Homatter, B. Annighöfer, F. Porcher, C. Alba-Simionesco, N. Chauvin, J. Schwindling, A. Letourneau, A. Marchix, and N.H. Tran. Neutrons production on the IPHI accelerator for the validation of the design of the compact neutron source SONATE. *arXiv*, 1612.00237, 2016.

[12] P. Mastinu, J. Praena, G. Martìn-Hernàndez, N. Dzysiuk, G. Prete, R. Capote, M. Pignatari, and A. Ventura. Status of the LEgnaro NeutrOn Source facility (LENOS). *Physics Procedia*, 26:261 – 273, 2012. Proceedings of the first two meetings of the Union of Compact Accelerator-Driven Neutron Sources.

[13] U. Rücker, T. Cronert, J. Voigt, J. P. Dabruck, P.-E. Doege, J. Ulrich, R. Nabbi, Y. Beßler, M. Butzek, M. Büscher, C. Lange, M. Klaus, T. Gutberlet, and T. Brückel. The Jülich high-brilliance neutron source project. *The European Physical Journal Plus*, 131(1):19, Jan 2016.

[14] T. Gutberlet, D. Tunger, P. Zeitler, and T. Brückel. Do neutrons publish? A neutron publication survey 2005-2015. *arXiv*, 1804.07185, 2018.

[15] J. T. Cremer Jr. *Neutron and X-ray Optics*. Elsevier insights, 2013.

[16] K. Zeitelhack, C. Schanzer, A. Kastenmüller, A. Röhrmoser, C. Daniel, J. Franke, E. Gutsmiedl, V. Kudryashov, D. Maier, D. Päthe, W. Petry, T. Schöffel, K. Schreckenbach, A. Urban, and U. Wildgruber. Measurement of neutron flux and beam divergence at the cold neutron guide system of the new Munich research reactor FRM-II. *Nuclear Instruments and Methods in Physics Research Section A: Accelerators, Spectrometers, Detectors and Associated Equipment*, 560(2):444 – 453, 2006.

[17] P. Link. *Experimental Facilities: Forschungsneutronenquelle Heinz-Maier-Leibnitz (FRM II)*. TU München, 2010.

[18] G. Cicognani. *Guide to Neutron Research Facilities: ILL, The Yellow Book*. ILL Grenoble, 2006.

[19] `https://www.technologysi.stfc.ac.uk/Pages/ASD_HPT_ISIS-TS1.aspx,https://www.isis.stfc.ac.uk/Pages/Moderator.aspx`.

[20] L. Zanini. *Description and performance of the new baseline ESS moderators*. ESS-Report 0068256, 2016.

[21] T. Unruh and W Petry. Neutronenforschung für die wissenschaftlichen herausforderungen der zukunft. Technical report, Komitee Forschung mit Neutronen, 2013.

[22] `https://www.fz-juelich.de/jcns/jcns-2/EN/Forschung/High-Brilliance-Neutron-Source/HBS-Conferences/_node.html`.

[23] T. Gutberlet, U. Rücker, and T. Brückel. Towards compact accelerator driven neutrons sources for europe. *Neutron News*, 28, 2017.

[24] `http://www.strodel.info/research.php`.

[25] Helsinki Quantum Flagship Event. Exploring and making quantum technology. Technical report, Press Dossier, 2019.

[26] `https://www.fzj.de/pgi/EN/Leistungen/SchoolsAndCourses/SpringSchool/History/SpringSchool2009/_node.html`.

[27] Front cover. *J. Mater. Chem. A*, 4:3157–3158, 2016.

[28] E. Mauerhofer, U. Rücker, T. Cronert, P. Zakalek, J. Baggemann, P.-E. Doege, J. Li, S. Böhm, H. Kleines, T. Gutberlet, and T. Brückel. *Conceptual Design Report - NOVA ERA (Neutrons Obtained Via Accelerator for Education and Research Activities) - A Jülich High Brilliance Neutron Source project*, volume 7 of *Schriften des Forschungszentrums Jülich Reihe Allgemeines / General*. Forschungszentrum Jülich GmbH Zentralbibliothek, Jülich, 2017.

[29] G. Anderson, B. Schweitzer, R. Anderson, and D.A. Gómez-Gualdrón. Attainable volumetric targets for adsorption-based hydrogen storage in porous crystals: Molecular simulation and machine learning. *The Journal of Physical Chemistry C*, 123(1):120–130, 2019.

[30] A. M. Arévalo-López, G. M. McNally, and J. P. Attfield. Large magnetization and frustration switching of magnetoresistance in the double-perovskite ferrimagnet Mn2FeReO6. *Angewandte Chemie International Edition)*, 54(41):12074—12077, 2015.

[31] W.-T. Chen, H.-S. Sheu, R.-S. Liu, and J. P. Attfield. Cation-size-mismatch tuning of photoluminescence in oxynitride phosphors. *Journal of the American Chemical Society*, 134(19):8022–8025, 2012.

[32] M. Yang, J. Oró-Solé, J. A. Rodgers, A. B. Jorge, A. Fuertes, and J. P. Attfield. Anion order in perovskite oxynitrides. *Nature Chemistry*, 3:47, 2010.

[33] M. T. Sougrati, A. Darwiche, X. Liu, A. Mahmoud, R. P. Hermann, S. Jouen, L. Monconduit, R. Dronskowski, and L. Stievano. Transition-metal carbodiimides as molecular negative electrode materials for lithium- and sodium-ion batteries with excellent cycling properties. *Angewandte Chemie International Edition*, 55(16):5090–5095, 2016.

[34] Matthew Josh, Claudio [Delle Piane], Lionel Esteban, Julien Bourdet, Sherry Mayo, Bobby Pejcic, Iko Burgar, Vladimir Luzin, Michael B. Clennell, and David N. Dewhurst. Advanced laboratory techniques characterising solids, fluids and pores in shales. *Journal of Petroleum Science and Engineering*, 180:932 – 949, 2019.

[35] G. D. Gatta, P. Vignola, G. J. Redhammer, M. Meven, and G. J. Mcintyre. Single-crystal neutron diffraction and mössbauer spectroscopic study of hureaulite, (Mn,Fe)5(PO4)2(HPO4)2(H2O)4. *European Journal of Mineralogy*, 28(1):93–103, 2016.

[36] M.H. Köster, L.B. Williams, P. Kudejova, and H.A. Gil. The boron isotope geochemistry of smectites from sodium, magnesium and calcium bentonite deposits. *Chemical Geology*, 510:166–187, 2019.

[37] J. Gómez Barreiro, H.-R. Wenk, and S. Vogel. Texture and elastic anisotropy of a mylonitic anorthosite from the morin shear zone (Quebec, Canada). *Journal of Structural Geology*, 71:100 – 111, 2015. Special Issue: Deformation of the lithosphere - How small structures tell a big story.

[38] R. L. Paul. Prompt gamma-ray activation analysis for certification of sulfur in fuel oil srms. *Journal of radioanalytical and nuclear chemistry*, 311(2):1149–1154, 2017.

[39] C. Sieghorst, G. Hampel, B. Karches, P. Krenckel, P. Kudějová, C. Plonka, Z. Révay, S. Riepe, K. Welter, and N. Wiehl. Determination of boron and hydrogen in materials for multicrystalline solar cell production with prompt gamma activation analysis. *Journal of Radioanalytical and Nuclear Chemistry*, 317(1):307–313, 2018.

[40] H. Da-Qian, J. Wen-Bao, J. Zhou, C. Can, L. Jia-Tong, and W. Hong-Tao. Heavy metals detection in sediments using PGNAA method. *Applied Radiation and Isotopes*, 112:50 – 54, 2016.

[41] G. Requena, G. Garces, R. Fernandez, and M. Schöbel. Determination of internal stresses in lightweight metal matrix composites, in Neutron Diffraction, 2012.

[42] K. Everschor-Sitte, J. Masell, R. M. Reeve, and M. Kläui. Perspective: Magnetic skyrmions—overview of recent progress in an active research field. *Journal of Applied Physics*, 124(24):240901, 2018.

[43] E. Loureiro, I. R.-and Scoppola, L. Bertinetti, A. Barbetta, G. Fragneto, and E. Schneck. Neutron reflectometry yields distance-dependent structures of nanometric polymer brushes interacting across water. *Soft matter*, 13(34):5767–5777, 2017.

[44] M. Trunk, M. Wetjen, L. Werner, R. Gernhäuser, B. Märkisch, Z. Révay, H.A. Gasteiger, and R. Gilles. Materials science applications of neutron depth profiling at the PGAA facility of Heinz Maier-Leibnitz Zentrum. *Materials Characterization*, 146:127 – 134, 2018.

[45] G. Festa, C. Andreani, M. P. De Pascale, R. Senesi, G. Vitali, S. Porcinai, A. M. Giusti, R. Schulze, L. Canella, P. Kudejova, M. Mühlbauer, and B. Schillinger. A nondestructive stratigraphic and radiographic neutron study of Lorenzo Ghiberti's reliefs from paradise and north doors of Florence baptistery. *Journal of Applied Physics*, 106(7):074909, 2009.

[46] A. Schaeffer. LHCf sheds new light on cosmic rays. Rayons cosmiques: LHCf change la donne. *CERN Bulletin*, BUL-NA-2011-104. 17/2011:1, 2011.

[47] J. Denekamp. Neutron radiobiology revisited. *Acta Oncologica*, 33:233–240, 1994.

[48] W. W. Kühne, B. B. Gersey, R. Wilkins, H. Wu, S. A. Wender, V. George, and W. S. Dynan. Biological effects of high-energy neutrons measured in vivo using a vertebrate model. *Radiation Research*, 172:473–480, 2009.

[49] Cosmic rays, neutrons and the mutation rate in evolution. *MIT Technology Review*, 2014.

[50] G. Figueroa-González and C. Pérez-Plasencia. Strategies for the evaluation of DNA damage and repair mechanisms in cancer. *Oncol. Lett.*, 13:3982–3988, 2017.

[51] Universities Space Research Association (USRA), editor. *Proceedings of Workshop Predictions and Measurements of Secondary Neutrons in Space*, Houston, 1998.

[52] P. Jacobs, A. Houben, W. Schweika, A. L. Tchougréeff, and R. Dronskowski. A Rietveld refinement method for angular- and wavelength-dispersive neutron time-of-flight powder diffraction data. *Journal of Applied Crystallography*, 48(6):1627–1636, 2015.

[53] R. Bewley. FARO: A new type of neutron spectrometer with flux and resolution optimized. *Review of Scientific Instruments*, 90:075106, 2019.

[54] J.O. Birk, M. Marko, P.G. Freeman, J. Jacobsen, R.L. Hansen, N.B. Christensen, C. Niedermayer, M. Mansson, H. Ronnow, and K. Lefmann. Prismatic analyser concept for neutron spectrometers. *Review of Scientific Instruments*, 85(11):113908, 2014.

[55] R. Bewley. The Mushroom - a neutron spectrometer with a difference. In *International Collaboration on Advanced Neutron Sources (ICANS XXII)*, Oxford, 2017.

[56] G. Molnar, editor. *Handbook of Prompt Gamma Activation Analysis with Neutrons*. Kluwer, 2004.

[57] R. R. Greenberg, P. Bode, and E. A. De Nadai Fernandes. Neutron activation analysis: A primary method of measurement. *Spectrochimica Acta Part B: Atomic Spectroscopy*, 66(3):193 – 241, 2011.

[58] Z. Revay. PGAA: Prompt gamma and in-beam neutron activation analysis facility. *Journal of large-scale research facilities JLSRF*, 1, 08 2015.

[59] L. Szentmiklósi, T. Belgya, Z. Révay, and Z. Kis. Upgrade of the prompt gamma activation analysis and the neutron-induced prompt gamma spectroscopy facilities at the Budapest research reactor. *Journal of Radioanalytical and Nuclear Chemistry*, 286(2):501–505, Nov 2010.

[60] Z. Révay, T. Belgya, L. Szentmiklósi, Z. Kis, A. Wootsch, D. Teschner, M. Swoboda, R. Schlögl, J. Borsodi, and R. Zepernick. In situ determination of hydrogen inside a catalytic reactor using prompt γ activation analysis. *Analytical Chemistry*, 80(15):6066–6071, 2008.

[61] K. Sueki, K. Kobayashi, W. Sato, H. Nakahara, and T. Tomizawa. Nondestructive determination of major elements in a large sample by prompt γ ray neutron activation analysis. *Analytical Chemistry*, 68(13):2203–2209, 1996. PMID: 21619306.

[62] T.H. Randriamalala, M. Rossbach, E. Mauerhofer, Z. Révay, S. Söllradl, and F.M. Wagner. FaNGaS: A new instrument for (n,n'γ) reaction measurements at FRM II. *Nuclear Instruments and Methods in Physics Research Section A: Accelerators, Spectrometers, Detectors and Associated Equipment*, 806:370 – 377, 2016.

[63] F. Mildenberger and E. Mauerhofer. Cyclic neutron activation analysis of large samples with a pulsed 14 Mev neutron source. *Journal of Radioanalytical and Nuclear Chemistry*, 311(1):917–927, 2017.

[64] K. V. Tian, G. Festa, L. Szentmiklósi, B. Maróti, L. Arcidiacono, G. Laganà, C. Andreani, S. Licoccia, R. Senesi, and P. Cozza. Compositional studies of functional orthodontic archwires using prompt-gamma activation analysis at a pulsed neutron source. *J. Anal. At. Spectrom.*, 32:1420–1427, 2017.

[65] R. G. Downing, G. P. Lamaze, J. K. Langland, and S. T. Hwang. Neutron depth profiling: Overview and description of nist facilities. *Journal of research of the National Institute of Standards and Technology*, 98(1):109–126, 1993.

[66] J. F. Ziegler, M. D. Ziegler, and J. P. Biersack. SRIM - the stopping and range of ions in matter (2010). *Nuclear Instruments and Methods in Physics Research Section B: Beam Interactions with Materials and Atoms*, 268(11):1818 – 1823, 2010. 19th International Conference on Ion Beam Analysis.

[67] Petry, Winfried. Neutrons for industry. *EPJ Web of Conferences*, 104:01001, 2015.

[68] A. Senyshyn, M.J. Mühlbauer, O. Dolotko, M. Hofmann, T. Pirling, and H. Ehrenberg. Spatially resolved in operando neutron scattering studies on Li-ion batteries. *Journal of Power Sources*, 245:678 – 683, 2014.

[69] OECD and Nuclear Energy Agency. *Beneficial Uses and Production of Isotopes*. 2005.

[70] The Editors of Encyclopaedia Britannica. Brain scanning. *Encyclopædia Britannica*, October 2015.

[71] *Manual for Reactor Produced Radioisotopes*. Number 1340 in Technical Reports Series. International Atomic Energy Agency, Vienna, 2003.

[72] *Cyclotron Produced Radionuclides: Physical Characteristics and Production Methods*. Number 468 in Technical Reports Series. International Atomic Energy Agency, Vienna, 2009.

[73] Y. Nagai, K. Hashimoto, Y. Hatsukawa, H. Saeki, S. Motoishi, N. Sato, M. Kawabata, H. Harada, T. Kin, K. Tsukada, T. K. Sato, F. Minato, O. Iwamoto, N. Iwamoto, Y. Seki, K. Yokoyama, T. Shiina, A. Ohta, N. Takeuchi, and T. Igarashi. Generation of radioisotopes with accelerator neutrons by deuterons. *Journal of the Physical Society of Japan*, 83:JPSJ.82.064201, 05 2013.

[74] K. Abbas, S. Buono, N. Burgio, G. Cotogno, N. Gibson, L. Maciocco, G. Mercurio, A. Santagata, F. Simonelli, and H. Tagziria. Development of an accelerator driven neutron activator for medical radioisotope production. *Nuclear Instruments and Methods in Physics Research Section A: Accelerators, Spectrometers, Detectors and Associated Equipment*, 601(3):223 – 228, 2009.

[75] R. Seviour. Compact accelerator based neutron source for technetium-99m production. In *IPAC 16*, May 2016.

[76] Y. Nagai. Medical isotope production using high intensity accelerator neutrons. *Physics Procedia*, 66:370 – 375, 2015. The 23rd International Conference on the Application of Accelerators in Research and Industry - CAARI 2014.

[77] D. Dubbers and M. G. Schmidt. The neutron and its role in cosmology and particle physics. *Rev. Mod. Phys.*, 83:1111–1171, 2011.

[78] P. Schmidt-Wellenburg. The quest to find an electric dipole moment of the neutron. *arXiv*, 1607.06609, 2016.

[79] S. Ahmed, E. Altiere, T. Andalib, C. P. Bell, B.and Bidinosti, E. Cudmore, M. Das, C. A. Davis, B. Franke, M. Gericke, P. Giampa, P. Gnyp, S. Hansen-Romu, K. Hatanaka, T. Hayamizu, B. Jamieson, D. Jones, S. Kawasaki, T. Kikawa, M. Kitaguchi, W. Klassen, A. Konaka, E. Korkmaz, F. Kuchler, M. Lang, L. Lee, T. Lindner, K. W. Madison, Y. Makida, J. Mammei, R. Mammei, J. W. Martin, R. Matsumiya, E. Miller, K. Mishima, T. Momose, T. Okamura, S. Page, R. Picker, E. Pierre, W. D. Ramsay, L. Rebenitsch, F. Rehm, W. Schreyer, H. M. Shimizu, S. Sidhu, A. Sikora, J. Smith, I. Tanihata, B. Thorsteinson, S. Vanbergen, W. T. H. van Oers, and Y. X. Watanabe. First ultracold neutrons produced at TRIUMF. *Phys. Rev. C*, 99:025503, 2019.

[80] K. K. H. Leung, G. Muhrer, T. Hügle, T. M. Ito, E. M. Lutz, M. Makela, C. L. Morris, R. W. Pattie, A. Saunders, and A. R. Young. A next-generation inverse-geometry spallation-driven ultracold neutron source. *Journal of Applied Physics*, 126(22):224901, 2019.

[81] Y. C. Shin, W. M. Snow, D. V. Baxter, C.-Y. Liu, D. Kim, Y. Kim, and Y. K. Semertzidis. Ultracold neutron production at compact neutron sources. *arXiv*, 1810.08722, 2018.

[82] J. Eberth and J. Simpson. From Ge(Li) detectors to gamma-ray tracking arrays – 50 years of gamma spectroscopy with germanium detectors. *Prog. Part. Nucl. Phys.*, 60:283–337, 2008.

[83] W. Urban, M. Jentschel, Märkisch. B., Th. Materna, Ch. Bernards, C. Drescher, Ch. Fransen, J. Jolie, U. Köster, P. Mutti, T. Rzȩca-Urban, and G. S. Simpson. New instrumentation for precise (n,γ) measurements at ILL grenoble. *Journal of Instrumentation*, 8(03):P03014–P03014, 2013.

[84] P.M. Jones, L. Wei, F.A. Beck, P.A. Butler, T. Byrski, G. Duchêne, G. de France, F. Hannachi, G.D. Jones, and B. Kharraja. Calibration of the new composite "clover" detector as a Compton polarimeter for the EUROGAM array. *Nuclear Instruments and Methods in Physics Research Section A: Accelerators, Spectrometers, Detectors and Associated Equipment*, 362(2):556 – 560, 1995.

[85] J.-M. Regis, G.S. Simpson, A. Blanc, G. de France, M. Jentschel, U. Köster, P. Mutti, V. Paziy, N. Saed-Samii, T. Soldner, C.A. Ur, W. Urban, A.M. Bruce, F. Drouet, L.M. Fraile, S. Ilieva, J. Jolie, W. Korten, T. Kröll, S. Lalkovski, H. Mach, N. Märginean, G. Pascovici, Zs. Podolyak, P.H. Regan,

O.J. Roberts, J.F. Smith, C. Townsley, A. Vancraeyenest, and N. Warr. Germanium-gated γ–γ fast timing of excited states in fission fragments using the EXILL & FATIMA spectrometer. *Nuclear Instruments and Methods in Physics Research Section A: Accelerators, Spectrometers, Detectors and Associated Equipment*, 763:210 – 220, 2014.

[86] M. Jentschel, A. Blanc, G. de France, U. Köster, S. Leoni, P. Mutti, G. Simpson, T. Soldner, C. Ur, W. Urban, S. Ahmed, A. Astier, L. Augey, T. Back, P. Bączyk, A. Bajoga, D. Balabanski, T. Belgya, G. Benzoni, C. Bernards, D.C. Biswas, G. Bocchi, S. Bottoni, R. Britton, B. Bruyneel, J. Burnett, R.B. Cakirli, R. Carroll, W. Catford, B. Cederwall, N. Celikovic, I. Cieplicka-Oryńczak, E. Clement, N. Cooper, F. Crespi, M. Csatlos, D. Curien, M. Czerwiński, L.S. Danu, A. Davies, F. Didierjean, F. Drouet, G. Duchêne, C. Ducoin, K. Eberhardt, S. Erturk, L.M. Fraile, A. Gottardo, L. Grente, L. Grocutt, C. Guerrero, D. Guinet, A.-L. Hartig, C. Henrich, A. Ignatov, S. Ilieva, D. Ivanova, B.V. John, R. John, J. Jolie, S. Kisyov, M. Krticka, T. Konstantinopoulos, A. Korgul, A. Krasznahorkay, T. Kröll, J. Kurpeta, I. Kuti, S. Lalkovski, C. Larijani, R. Leguillon, R. Lica, O. Litaize, R. Lozeva, C. Magron, C. Mancuso, E. Ruiz Martinez, R. Massarczyk, C. Mazzocchi, B. Melon, D. Mengoni, C. Michelagnoli, B. Million, C. Mokry, S. Mukhopadhyay, K. Mulholland, A. Nannini, D.R. Napoli, B. Olaizola, R. Orlandi, Z. Patel, V. Paziy, C. Petrache, M. Pfeiffer, N. Pietralla, Z. Podolyak, M. Ramdhane, N. Redon, P. Regan, J.M. Regis, D. Regnier, R. J. Oliver, M. Rudigier, J. Runke, T. Rząca-Urban, N. Saed-Samii, M.D. Salsac, M. Scheck, R. Schwengner, L. Sengele, P. Singh, J. Smith, O. Stezowski, B. Szpak, T. Thomas, M. Thürauf, J. Timar, A. Tom, I. Tomandl, T. Tornyi, C. Townsley, A. Tuerler, S. Valenta, Vancraeyenest, V. Vandone, J. Vanhoy, V. Vedia, N. Warr, V. Werner, D. Wilmsen, E. Wilson, T. Zerrouki, and M. Zielinska. EXILL—a high-efficiency, high-resolution setup for γ-spectroscopy at an intense cold neutron beam facility. *Journal of Instrumentation*, 12(11):P11003–P11003, 2017.

[87] M. Lebois, J.N. Wilson, P. Halipré, B. Leniau, I. Matea, A. Oberstedt, S. Oberstedt, and D. Verney. Prompt γ-rays from the fast neutron induced fission on 235,238U and 232Th. *Physics Procedia*, 59:37 – 41, 2014. GAMMA-2 Scientific Workshop on the Emission of Prompt Gamma-Rays in Fission and Related Topics.

[88] C. Michelagnoli, A. Blanc, E. Ruiz-Martinez, A. Chebboubi, H. Faust, E. Froidefond, G. Kessedjian, M. Jentschel, U. Köster, P. Mutti, and G. Simpson. FIPPS (FIssion Product Prompt γ-ray Spectrometer) and its first experimental campaign. *EPJ Web Conf*, 193:04009, 2018.

[89] Y.H. Kim, M. Thomas, H. Faust, C. Michelagnoli, U. Köster, F. Kandzia, M. Jentschel, E. Ruiz-Martinez, P. Mutti, E. Lelièvre-Berna, H. Schwab, E. Froidefond, G. Kessedjian, O. Meplan, G. Simpson, A. Chebboubi, and T. Materna. Development of a gas filled magnet for FIPPS phase II. *Nuclear Instruments and Methods in Physics Research Section B: Beam Interactions with Materials and Atoms*, 463:269 – 271, 2020.

[90] T. Okudaira, S. Takada, K. Hirota, A. Kimura, M. Kitaguchi, J. Koga, K. Nagamoto, T. Nakao, A. Okada, K. Sakai, H. M. Shimizu, T. Yamamoto, and T. Yoshioka. Angular distribution of γ rays from neutron-induced compound states of ^{140}La. *Phys. Rev. C*, 97:034622, 2018.

[91] H. Rauch and S.A. Werner. *Neutron Interferometry*. Oxford University Press, 2015.

[92] J. Klepp. Viewpoint: Moiré effect could enhance neutron interferometry, March 2018.

[93] P. Zakalek, P.-E. Doege, J. Baggemann, E. Mauerhofer, and Th. Brückel. Energy and target material dependence of the neutron yield induced by proton and deuteron bombardment. *EPJ Web Conf.*, 231:03006, 2020.

[94] A.J. Koning and D. Rochman. Modern nuclear data evaluation with the TALYS code system. *Nuclear Data Sheets*, 113(12):2841 – 2934, 2012. Special Issue on Nuclear Reaction Data.

[95] P. Zakalek, P.-E. Doege, J. Baggemann, T. Cronert, Y. Beßler, M. Butzek, J. Wolters, E. Mauerhofer, U. Rücker, T. Gutberlet, G. Natour, and Th. Brückel. Temperature profiles inside a target irradiated with protons or deuterons for the development of a compact accelerator driven neutron source. *Physica B: Condensed Matter*, 551:484–487, 2018.

[96] H. Podlech. Superconducting versus normal-conducting cavities. In *CERN Accelerator School on High Power Proton Accelerators*, pages 151–170, 2012. ISBN 9789290833840.

[97] D. Mäder, H. Hähnel, H. Höltermann, D. Koser, K. Kümpel, U. Ratzinger, W. Schweizer, M. Busch, H. Podlech, C. Angulo, J. Belmans, L. Medeiros-Romao, and D. Vandeplassche. Construction of the MYRRHA Injector. In *Proc. of International Particle Accelerator Conference (IPAC'17), Copenhagen, Denmark, 2017*, number 8 in International Particle Accelerator Conference, pages 2221–2223, Geneva, Switzerland, May 2017. JACoW. https://doi.org/10.18429/JACoW-IPAC2017-TUPVA062.

[98] K. Kümpel, D. Koser, S. Lamprecht, N.F. Petry, H. Podlech, A. Schempp, and D. Strecker. Measurements of the MYRRHA-RFQ at the IAP Frankfurt. In *Proc. 9th International Particle Accelerator Conference (IPAC'18), Vancouver, BC, Canada, April 29-May 4, 2018*, number 9 in International Particle Accelerator Conference, pages 949–951, Geneva, Switzerland, June 2018. JACoW Publishing. https://doi.org/10.18429/JACoW-IPAC2018-TUPAF090.

[99] R. Gobin, P.-Y. Beauvais, R. Ferdinand, P.-A. Leroy, L. Celona, G. Ciavola, and S. Gammino. Improvement of beam emittance of the CEA high intensity proton source SILHI. *Review of Scientific Instruments*, 70(6):2652–2654, 1999.

[100] L. Celona, G. Ciavola, S. Gammino, F. Chines, M. Presti, L. Andò, X. H. Guo, R. Gobin, and R. Ferdinand. Status of the Trasco intense proton source and emittance measurements. *Review of Scientific Instruments*, 75(5):1423–1426, 2004.

[101] O. Meusel, M. Droba, D. Noll, K. Schulte, P. P. Schneider, and C. Wiesner. Beam transport and space charge compensation strategies. *Review of Scientific Instruments*, 87(2):02B937, 2016.

[102] C. Wiesner. *Chopping and transport of high-intensity ion beams*. PhD thesis, Frankfurt University, 2014.

[103] H. Podlech. *Entwicklung von normal- und supraleitenden CH-Strukturen zur effizienten Beschleunigung von Protonen und Ionen*. Habilitation, Frankfurt University, 2008.

[104] K. Schindl. *Space charge*. CAS - CERN Accelerator School: Intermediate Course on Accelerator Physics, Geneva, 2006.

[105] G.S. Bauer. Overview on spallation target design concepts and related materials issues. *Journal of Nuclear Materials*, 398(1):19 – 27, 2010. Proceedings of the Ninth International Workshop on Spallation Materials Technology.

[106] S. A. H. Feghhi, Z. Gholamzadeh, and C. Tenreiro. Investigation of the optimal material type and dimension for spallation targets using simulation methods. *Journal of Theoretical and Applied Physics*, 8(1):117, 2014.

[107] F. Cardarelli. *Materials Handbook*. Springer International Publishing, 2008.

[108] N. Simos, H. Ludewig, H. Kirk, E. Dooryhee, S. Ghose, Z. Zhong, H. Zhong, S. Makimura, K. Yoshimura, J. R. J. Bennett, G. Kotsinas, Z. Kotsina, and K. T. McDonald. Multi-MW accelerator target material properties under proton irradiation at Brookhaven National Laboratory linear isotope producer. *Phys. Rev. Accel. Beams*, 21:053001, 2018.

[109] H. Ullmaier and F. Carsughi. Radiation damage problems in high power spallation neutron sources. *Nuclear Instruments and Methods in Physics Research Section B: Beam Interactions with Materials and Atoms*, 101(4):406 – 421, 1995.

[110] J.M. Steichen. Tensile properties of neutron irradiated TZM and tungsten. *Journal of Nuclear Materials*, 60(1):13 – 19, 1976.

[111] X.-S. Kong, S. Wang, X. Wu, Y.-W. You, C.S. Liu, Q. F. Fang, J.-L. Chen, and G.-N. Luo. First-principles calculations of hydrogen solution and diffusion in tungsten: Temperature and defect-trapping effects. *Acta Materialia*, 84:426 – 435, 2015.

[112] J.-H. You. Mechanics of tungsten blistering: A finite element study. *Journal of Nuclear Materials*, 437(1):24 – 28, 2013.

[113] V.T. Astrelin, A.V. Burdakov, P.V. Bykov, I.A. Ivanov, A.A. Ivanov, Y. Jongen, S.G. Konstantinov, A.M. Kudryavtsev, K.N. Kuklin, K.I. Mekler, S.V. Polosatkin, V.V. Postupaev, A.F. Rovenskikh, S.L. Sinitskiy, and E.R. Zubairov. Blistering of the selected materials irradiated by intense 200 kev proton beam. *Journal of Nuclear Materials*, 396(1):43 – 48, 2010.

[114] M. Fukumoto, Y. Ohtsuka, Y. Ueda, M. Taniguchi, M. Kashiwagi, T. Inoue, and K. Sakamoto. Blister formation on tungsten damaged by high energy particle irradiation. *Journal of Nuclear Materials*, 375(2):224 – 228, 2008.

[115] S. A. Maloy, R. Scott Lillard, W. F. Sommer, D. P. Butt, F. D. Gac, G. J. Willcutt, and M. R. Louthan. Water corrosion measurements on tungsten irradiated with high energy protons and spallation neutrons. *Journal of Nuclear Materials*, 431(1):140 – 146, 2012. Special Issue of the Tenth International Workshop on Spallation Materials Technology, (IWSMT-10).

[116] J. Chen, G.S. Bauer, T. Broome, F. Carsughi, Y. Dai, S.A. Maloy, M. Roedig, W.F. Sommer, and H. Ullmaier. Summary of the results from post-irradiation examination of spent targets at the FZ-Juelich. *Journal of Nuclear Materials*, 318:56 – 69, 2003. Fifth International Workshop on Spallation Materials Technology.

[117] A. San-Martin and F. D. Manchester. The H-Ta (hydrogen-tantalum) system. *Journal of Phase Equilibria*, 12(3):332–343, June 1991.

[118] G. Cerbe and H.J. Hoffmann. *Einführung in die Wärmelehre: von der Thermodynamik zur technischen Anwendung*. Studienbücher der technischen Wissenschaften. Hanser, 1990.

[119] VDI Gesellschaft. *VDI Heat Atlas*. VDI-Buch. Springer Berlin Heidelberg, 2010.

[120] S. Kandlikar, S. Garimella, D. Li, S. Colin, and M.R. King. *Heat Transfer and Fluid Flow in Minichannels and Microchannels*. Chemical, Petrochemical & Process. Elsevier Science, 2006.

[121] S. G. Kandlikar and H. R. Upadhye. Extending the heat flux limit with enhanced microchannels in direct single-phase cooling of computer chips. In *Semiconductor Thermal Measurement and Management IEEE Twenty First Annual IEEE Symposium, 2005.*, pages 8–15, 2005.

[122] Mark E. Steinke and Satish G. Kandlikar. An Experimental Investigation of Flow Boiling Characteristics of Water in Parallel Microchannels. *Journal of Heat Transfer*, 126(4):518–526, 05 2004.

[123] I. L. Shabalin. *Ultra-High Temperature Materials I*. Springer Netherlands, 2014.

[124] GoodFellow. Molybdenum High Temperature Alloy TZM (Mo99/Ti0.5/Zr0.1). `http://www.goodfellow.com/E/Molybdenum-High-Temperature-Alloy-TZM.html`, 2018.

[125] Indium Corporation. Liquid metal - galium and gallium alloys. https://www.indium.com/products/metals/indium/#documents, 2018. Form No. 97826 (A4) R6.

[126] PLANSEE. Molybdenum. https://www.plansee.com/en/materials/molybdenum.html, 2018.

[127] JAHM Software, Inc. Materials Property Database MPDB. v8.97.

[128] S. Böhm, T. Cronert, J.-P. Dabruck, X. Fabrèges, T. Gutberlet, F. Mezei, A. Letourneau, A. Menelle, F. Ott, U. Rücker, T. Tran, J. Voigt, and P. Zakalek. Neutron scattering instrumentation at compact neutron sources. *arXiv*, 1809.02370, 2018.

[129] Patent EP 3 091 540 B1, 2017.

[130] G.W.C. Kaye and T.H. Laby. *Tables of physical and chemical constants. 15th Edition.* United States, N.b., 1986.

[131] K. B. Grammer, R. Alarcon, L. Barrón-Palos, D. Blyth, J. D. Bowman, J. Calarco, C. Crawford, K. Craycraft, D. Evans, N. Fomin, J. Fry, M. Gericke, R. C. Gillis, G. L. Greene, J. Hamblen, C. Hayes, S. Kucuker, R. Mahurin, M. Maldonado-Velázquez, E. Martin, M. McCrea, P. E. Mueller, M. Musgrave, H. Nann, S. I. Penttilä, W. M. Snow, Z. Tang, and W. S. Wilburn. Measurement of the scattering cross section of slow neutrons on liquid parahydrogen from neutron transmission. *Phys. Rev. B*, 91:180301, 2015.

[132] S. Eisenhut, M. Klaus, J. Baggemann, U. Rücker, Y. Beßler, A. Schwab, C. Haberstroh, T. Cronert, T. Gutberlet, T. Brückel, and C. Lange. Cryostat for the provision of liquid hydrogen with a variable ortho-para ratio for a low-dimensional cold neutron moderator. *EPJ Web Conf.*, 231:04001, 2020.

[133] S.J. Park, J.G. Jang, and H.K Lee. Computational investigation of the neutron shielding and activation characteristics of borated concrete with polyethylene aggregate. *Journal of Nuclear Materials*, 452(1):205 – 211, 2014.

[134] L. Coates, M. J. Cuneo, M. J. Frost, J. He, K. L. Weiss, S. J. Tomanicek, H. McFeeters, V. G. Vandavasi, P. Langan, and E. B. Iverson. The Macromolecular Neutron Diffractometer MaNDi at the Spallation Neutron Source. *Journal of Applied Crystallography*, 48(4):1302–1306, 2015.

[135] J. Stahn, P. Korelis, U. Filges, T. Panzner, E. Rantsiou, M. Cardenas, U. B. Hansen, and B. Klösgen. Estia a focusing reflectometer for small samples based on the Selene guide concept. European Spallation Source (ESS), 2014.

[136] Heinz Maier-Leibnitz Zentrum. REFSANS: Reflectometer and evanescent wave small angle neutron spectrometer. *Journal of large-scale research facilities*, 1:A9, 2015.

[137] Heinz Maier-Leibnitz Zentrum. MARIA: Magnetic reflectometer with high incident angle. *Journal of large-scale research facilities*, 1:A8, 2015.

[138] J. Voigt, N. Violini, and W. Schweika. Compact chopper spectrometers for pulsed sources. *Journal of Physics: Conference Series*, 746(1):012018, 2016.

[139] A. Vickery and P. P. Deen. Choppers to optimise the repetition rate multiplication technique on a direct geometry neutron chopper spectrometer. *Review of Scientific Instruments*, 85(11):–, 2014.

[140] S. F. Parker, A. J. Ramirez-Cuesta, P. W. Albers, and D. Lennon. The use of direct geometry spectrometers in molecular spectroscopy. *Journal of Physics: Conference Series*, 554:012004, nov 2014.

[141] E. Mamontov and K. W. Herwig. A time-of-flight backscattering spectrometer at the spallation neutron source, BASIS. *Review of Scientific Instruments*, 82(8):085109, 2011.

[142] N. Tsapatsaris, R. E. Lechner, M. Markó, and H. N. Bordallo. Conceptual design of the time-of-flight backscattering spectrometer, MIRACLES, at the European Spallation Source. *Review of Scientific Instruments*, 87(8):085118, 2016.

[143] G. Festa, L. Arcidiacono, A. Pappalardo, T. Minniti, C. Cazzaniga, A. Scherillo, C. Andreani, and R. Senesi. Isotope identification capabilities using time resolved prompt gamma emission from epithermal neutrons. *Journal of Instrumentation*, 11(03):C03060–C03060, 2016.

[144] E. Vezhlev, A. Ioffe, S. Mattauch, E. Hüger, I. Tomandl, V. Hnatowicz, C. Chen, P. Notten, S. Staringer, V. Ossovyi, C. Felder, and T. Brückel. A new Neutron Depth Profiling (NDP) spectrometer at the JCNS for a focused neutron beam. *Radiation Effects and Defects in Solids*, 175:342–355, 2020.

[145] G. Erdtmann. *Neutron Activation Tables*. Verlag Chemie, Weinheim, New York, 1976.

[146] `http://web.nuklide.de/`.

[147] D. Filges, R. D. Neef, and H. Schaal. Nuclear simulation and radiation physics investigations of the target station of the European Spallation Neutron Source (ESS). *Nuclear Technology*, 132, 10 2000.

[148] D.J.S. Findlay, G.P. Skoro, G.J. Burns, and S. Ansell. Experimental verification of spallation inventory calculations. *Applied Radiation and Isotopes*, 125:1 – 3, 2017.

[149] Z. Kókai, S. Török, P. Zagyvai, D. Kiselev, R. Moormann, E. Börcsök, L. Zanini, A. Takibayev, G. Muhrer, R. Bevilacqua, and J. Janik. Comparison of different target material options for the european spallation source based on certain aspects related to the final disposal. *Nuclear Instruments and Methods in Physics Research Section B: Beam Interactions with Materials and Atoms*, 416:1 – 8, 2018.

[150] J. S. Becker, W. Kerl, and H.-J. Dietze. Nuclide analysis of an irradiated tantalum target of a spallation neutron source using high performance ion chromatography and inductively coupled plasma mass spectrometry. *Analytica Chimica Acta*, 387(2):145 – 154, 1999.

[151] R. Moormann, K. Bongardt, and S. Chiriki. Safety aspects of high power targets for european spallation sources. *International Conference on the Physics of Reactors 2008, PHYSOR 08*, 4:2545–2552, 01 2008.

[152] Q. Z. Yu, T. J. Liang, and W. Yin. Activity and radiation protection studies for the W-Ta target of CSNS. *Radiation Protection Dosimetry*, 136(3):216–221, 09 2009.

[153] D. Ene, K. Andersson, Mi. Jensen, S. Nielsen, and G. Severin. Management of tritium in European Spallation Source. *Fusion Science and Technology*, 67(2):324–327, 2015.

[154] E. Mauro and M. Silari. Radiation protection studies for a high-power 160 MeV proton linac. *Nuclear Instruments and Methods in Physics Research Section A: Accelerators, Spectrometers, Detectors and Associated Equipment*, 605(3):249 – 265, 2009.

[155] J. Blaha, F.P. La Torre, M. Silari, and J. Vollaire. Long-term residual radioactivity in an intermediate-energy proton linac. *Nuclear Instruments and Methods in Physics Research Section A: Accelerators, Spectrometers, Detectors and Associated Equipment*, 753:61 – 71, 2014.

[156] *Decommissioning of Facilities*. Number GSR Part 6 in General Safety Requirements. International Atomic Energy Agency, Vienna, 2014.

[157] S. M. Schmidt, T. Brückel, S. Förster, and M. Müller. Strategy Paper on Neutron Research in Germany: 2020-2045. Jülich, 2019.

[158] https://www.fz-juelich.de/jcns/EN/Leistungen/ConferencesAndWorkshops/HBS-Workshops/HBS-Workshop2017/_node.html.

[159] K. Lieutenant, G. Zsigmond, S. Manoshin, M. Fromme, H. N. Bordallo, D. Champion, J. Peters, and F. Mezei. Neutron instrument simulation and optimization using the software package VITESS. In M. Sanchez del Rio, editor, *Advances in Computational Methods for X-Ray and Neutron Optics*, volume 5536, pages 134 – 145. International Society for Optics and Photonics, SPIE, 2004.

LIST OF FIGURES

FIGURE CREDITS

The following Figures displayed are used by permission as follows:

Figure IV.1 bottom right: Reproduced from Ref. [27] with permission from The Royal Society of Chemistry.

Figure IV.2: Reprinted with permission from G. Anderson, B. Schweitzer, R. Anderson, and D.A. Gomez-Gualdron. Attainable volumetric targets for adsorption-based hydrogen storage in porous crystals: Molecular simulation and machine learning. The Journal of Physical Chemistry C, 123(1):120–130, 2019. Copyright American Chemical Society.

Figure IV.5: Reprinted from K. Everschor-Sitte, J. Masell, R.M. Reeve, and M. Kläui. Perspective: Magnetic skyrmions—overview of recent progress in an active research field. Journal of Applied Physics, 124(24):240901, 2018, with the permission of AIP Publishing.

Figure IV.7: Reprinted from G. Festa, C. Andreani, M.P. De Pascale, R. Senesi, G. Vitali, S. Porcinai, A.M. Giusti, R. Schulze, L. Canella, P. Kudejova, M.Mühlbauer, and B. Schillinger. A nondestructive stratigraphic and radiographic neutron study of Lorenzo Ghiberti's reliefs from paradise and north doors of Florence baptistery. Journal of Applied Physics, 106(7):074909, 2009, with the permission of AIP Publishing.

Schriften des Forschungszentrums Jülich
Reihe Allgemeines / General

Band / Volume 1
Fundamentos de Ensaio de Vazamento e Estanqueidade
J. da Cruz Payão Filho, W. Schmidt, G. Schröder (2000), 340 pp
ISBN: 3-89336-278-9

Band / Volume 2
Nur das Geld zählt? Erfassung von Nutzenorientierungen bei der Zuteilung von Geld und materiellen Gütern
M. Ertinger (2003), 333 pp
ISBN: 3-89336-336-X

Band / Volume 3
Advances in Nuclear and Radiochemistry
Extended Abstracts of Papers presented at the Sixth International Conference on Nuclear and Radiochemistry (NRC-6), 29 August to 3 September 2004, Aachen, Germany
edited by S. M. Qaim, H. H. Coenen (2004), XXXII, 794 pp
ISBN: 3-89336-362-9

Band / Volume 4
Wissenschaft im Zeichen der Zeit
Preisträger des Leibfried-Preises im Forschungszentrum Jülich 2000 – 2005
herausgegeben von R. Ball (2005), ca. 185 pp
ISBN: 3-89336-411-0

Band / Volume 5
Proceedings of the 1st International Conference on Natural and Biomimetic Mechanosensing
edited by: J. Casas, G. Krijnen, M. Malkoc-Thust, J. Mogdans, A. Offenhäusser, H. Peremans (2009), ca. 80 pp
ISBN: 978-3-89336-583-8

Band / Volume 6
Leo Brandt (1908-1971)
Ingenieur – Wissenschaftsförderer – Visionär
Wissenschaftliche Konferenz zum 100. Geburtstag des nordrhein-westfälischen Forschungspolitikers und Gründers des Forschungszentrums Jülich
herausgegeben von B. Mittermaier, B.-A. Rusinek (2009), I, 121 pp
ISBN: 978-3-89336-602-6

Schriften des Forschungszentrums Jülich
Reihe Allgemeines / General

Band / Volume 7
Conceptual Design Report
NOVA ERA
(Neutrons Obtained Via Accelerator for Education and Research Activities)
A Jülich High Brilliance Neutron Source project
E. Mauerhofer, U. Rücker, T. Cronert, P. Zakalek, J. Baggemann, P.-E. Doege, J. Li, S. Böhm, H. Kleines, T. Gutberlet, and T. Brückel (2017), 68 pp
ISBN: 978-3-95806-280-1

Band / Volume 8
Conceptual Design Report
Jülich High Brilliance Neutron Source (HBS)
T. Brückel, T. Gutberlet (Eds.) (2020), 197 pp
ISBN: 978-3-95806-501-7

Allgemeines / General
Band / Volume 8
ISBN 978-3-95806-501-7

Mitglied der Helmholtz-Gemeinschaft

JÜLICH
Forschungszentrum